Cavity Magnon-Polariton Spectroscopy

Dissertation
zur Erlangung des Grades
„Doktor
der Naturwissenschaften“
am Fachbereich Physik, Mathematik und Informatik
der Johannes Gutenberg-Universität
in Mainz

vorgelegt von:

Isabella Rahel Boventer

geboren in: Cholargos, Athen (Griechenland)

Mainz, den 16. April 2019

Date of the oral examination: 02.07.2019

Für meine Eltern

Abstract

The work which has been conducted in the course of this doctoral thesis with the title "Cavity Magnon Polariton Spectroscopy" can be classified as part of the recent and active research area of cavity spintronics. Among others, cavity spintronics aims to study light-matter interaction by the examination of the properties of the cavity-magnon polariton (CMP) and harness the CMP for applications bridging concepts of cavity quantum electrodynamics (CQED) with spintronics. The CMP is the associated quasiparticle resulting from the hybridisation of strongly coupled cavity photon-magnon (quasiparticles from a collective spin excitation in a magnetic material) states. In close collaboration with co-workers from the Karlsruhe Institute for Technology (KIT) who provided for the millikelvin data at 30 mK, the work on the CMP started with conducting a study on the temperature dependence of key properties of the CMP such as the cooperativity C, that is, the coupling strength and the magnon linewidth from 30 mK to 290 K. This work connects the quantum regime at millikelvin temperatures with the classical regime at room temperature and shows the persistence of the strong coupling regime, that is the existence of a coherent exchange of information, as $C > 1$ for the entire temperature range. However, beyond the realisation of strong coupling, real applications using CMPs require the ability to tune and control of the key property, i.e. the coupling strength reliably and reproducibly. For instance, it is necessary to switch the coherent exchange of information on and off deliberately. Therefore, as the next step, a new experimental scheme allowing such control over the coupling strength has been developed in the course of this thesis. Instead of the generally used approach of a *single*-tone driven CMP in the field of cavity spintronics, an approach driving the CMP with two tones is realised. The coupling strength is controlled by the relative phase and amplitude between the intracavity fields from the two inputs. It is shown that the coupling strength can be increased, decreased to zero accompanied by a strong amplitude enhancement and the decrease of the signal's linewidth, or transferred to a regime of level merging where the coupling strength is a complex quantity. Also, that method does not require any intrusion into the experimental apparatus during measurements. Thus, by the combination of realising strong coupling and the control of the coupling of the CMP, this work contributes to cavity spintronics. Specifically, the control over the coupling strength opens an avenue for generalized control of the coupling of other solid-state polaritons towards the development of applications for data storage and information processing technologies.

Zusammenfassung

Die Experimente, die im Zuge dieser Doktorarbeit mit dem Titel "Cavity Magnon-Polariton Spectroscopy" durchgeführt wurden, können in das junge und aktive Forschungsgebiet von Kavitätsspintronik eingeordnet werden. Indem die Eigenschaften von Kavität Magnon-Polaritonen (CMP) spektroskopisch untersucht werden, zielt dieser Forschungsbereich unter anderem darauf ab, dadurch ein besseres Verständnis über die Licht-Materie Wechselwirkung zu erlangen. Darüber hinaus geht es um die Frage, wie man das CMP, das das Potential hat, die Forschungsbereiche der Quantumelektrodynamik und Spintronik zu verbinden, für Anwendungen z.b. in der Informationstechnologie nutzen könnte. Das CMP stellt das assozierte Quasiteilchen, das aus der Hybridisierung von stark, resonant gekoppelten Kavitätsphotonen und Magnon resultiert, dar, wobei das Magnon selbst das Quasiteilchen einer kollektiven Spinanregung in einem magnetischen Material ist. In enger Zusammenarbeit mit Kollegen von dem Karlsruhe Institut für Technologie (KIT), welche die Messungen bei einer Temperatur von 30 mK durchgeführt haben, startete die hier vorgestellte Forschung mit einer temperaturabhängigen Studie über das CMP. Im Zuge dessen wurden die zentralen Eigenschaften des CMPs, wie beispielsweise die Kooperativität C, und damit die Kopplungsstärke und Linienbreite des Magnons in einem Temperaturintervall von 30 mK bis 290 K untersucht. Diese Arbeit verbindet nicht nur das Quantumregime für kryogene Temperaturen im Millikelvinbereich mit dem klassischen Regime bei Raumtemperatur, sondern zeigt auch die Beständigkeit für ein Vorliegen eines stark gekoppelten CMPs mit $C > 1$. Dies bedeutet, dass für den gesamten untersuchten Temperaturbereich ein kohärenter Austausch von Information vorliegt. Nichtsdestotrotz, für die Entwicklung von realen Anwendungen reicht ein stark gekoppeltes System mit einem kohärenten Austausch von Information nicht aus. Vielmehr muss es auch möglich sein, diesen Informationsaustausch, der im Experiment durch die Kopplungstärke als die zentrale physikalische Größe quantifiziert wird, zu kontrollieren und nach Belieben ein- und ausstellen zu können. Deshalb wurde als nächster Schritt im Zuge dieser Doktorarbeit eine neue experimentelle Methode entwickelt, die eine derartige Kontrolle über die Kopplungsstärke zulässt. Im Forschungsbereich der Kavitätsspintronik wurden die meisten Experimente bisher mit einem CMP durchgeführt, dass mit einem *einzelnen* Mikrowellenton getrieben wird. Anstatt dieses alten Ansatzes, wird die Kontrolle über die Kopplungsstärke mittels eines CMPs, dass von zwei Mikrowellentönen getrieben wird, realisiert. Die Kopplungsstärke wird dabei durch die Möglichkeit, die relative Phase und das relative Amplitudenverhältnis zwischen den zeitabhängigen Magnetfeldern in der Kavität, die von den beiden eingespeisten Mikrowellentönen kommen, gezielt zu verändern, kontrolliert. Es konnte gezeigt werden, das es damit möglich ist, die Kopplungsstärke entweder zu vergrössern, auf Null zu verringern, was mit einer enormen Verstärkung der Signalamplitude und Verringerung der Linienbreite einhergeht, oder ein Regime namens "level merging" zu erreichen, wo die Kopplungstärke komplex wird. Zudem ist es mit dieser experimentellen Methode nicht notwendig, in das Experiment und dessen Einstel-

lungen während einer Messung direkt einzugreifen. Die Ergebnisse dieser Doktorarbeit aus der Kombination einer Realisierung der starken Kopplung von Kavitätsphotonen und Magnonen mit der Kontrolle über die Kopplungsstärke des daraus resultierenden CMPs tragen damit zur Kavitätsspintronik bei. Insbesondere durch die Kontrolle über die Kopplungsstärke eröffnen sich neue Perspektiven für eine Verallgemeinerung diese Kontrolle der Kopplungsstärke auf Systeme mit anderen Festkörperpolaritonen im Hinblick neuer Anwendungen für Datenspeicherung und Informationsverarbeitung.

Contents

Ενα ξέρω, ότι τίποτα δεν ξέρω
"I only know I know nothing"

Socrates, c. 470-399 BC.

Chapter 1

Introduction

Etymologically, spectroscopy is a combination from the Latin word "spectrum" referring to an appearance or an image and the Greek word "skopein", i.e. to look at something [1]. Accordingly, the term spectroscopy can be translated to "looking of the apparition of something", meaning that one observes an object indirectly through another tool. In science, spectroscopic measurements refer to the study of the structure and properties of matter by observing interactions, e.g. absorption or reflection, often with electromagnetic radiation such as light [2]. From antiquity to today, the study of light-matter interaction has contributed to the understanding of a vast variety of fields in physics [3]. That study spans diffraction studies on the wave or corpuscular (Newton) nature of light during the seventeenth century to the observation of single atoms interacting with a single photon in the field cavity quantum electrodynamics (CQED) [4, 5] to unveiling the nature of the strong and weak forces that make up the foundations of matter at the microscale by high energy particle collisions (c.f. for instance [6]). Thus, the examination of light-matter interaction forms the core for further understanding of the building blocks of matter and related effects such as internal interactions. However, in order to gain insight about matter's internal degrees of freedom, i.e. its fundamental excitations, the study of light-matter interaction during light propagation in the medium is of special interest. Since Maxwell's theory for electrodynamics, light can be considered as an electromagnetic wave with an oscillating (AC) electric and magnetic field [7]. As the light propagates through a solid, these fields can excite the internal degrees of freedom with a dipole moment by the coupling to the electric or magnetic field [8].

In his theory of special relativity, Einstein proved the equivalence of matter and energy [9]. His theorem states that energy can be converted into matter, as observed in high-energy experiments, where a cascade of new particles is created as a result of the collision of two particles near the speed of light (c.f. for instance [10]). These collective elementary excitations inside a solid can be treated as particles with properties such as energy and momentum. However, as they do not consist of matter, these elementary excitations are denoted as quasiparticles.
If the frequency of the incident electromagnetic wave is close to that of an existing quasiparticle state a coupling between the normal modes of the medium, thereby influencing the electromagnetic wave and polarising the medium, emerges [8]. In the strong coupling regime, where the coupling exceeds the individual dissipations, this leads to the emergence of a new quasiparticle, namely the polariton [11]. Consequently, the propagation of the quasiparticle refers to a hybrid between the light wave and the elementary excitation of

the medium [12].
Depending on the material, the electromagnetic wave, i.e. the light, can couple to different elementary excitations such as excitons, defined as bound electron-hole pairs in a semiconductor [13], or magnons, the quasiparticles associated with a spin wave [14, 15]. Accordingly, in the process of the coupling of cavity resonator photons to such an excitation, there are cavity exciton and cavity magnon-polaritons (CMP). Because of the increasing demands for faster information processing and higher and non-volatile data storage capabilities, classical electronics, which uses the electric charge as the basic information carrier, approaches its fundamental limits [16]. For instance, as electrical circuits became smaller and smaller, the impact of Joule heating and losses increase [17, 18]. In contrast, if the inherent angular momentum of the electron, namely its spin is used instead as the primary information carrier, information could not be only conveyed without charge transport but also stored in a non-volatile manner [19]. The discovery of spin-dependent transport in 1980 opened an avenue to manipulate spins with electric and magnetic field for advances in data storage and information processing. Nowadays, this field is part of spintronics [20]. Together with the new possibilities to generate, detect and manipulate magnons on the nanoscale, this allows one to go a step further by utilising spin waves as primary information carriers for future applications such as logic devices [21, 22]. In analogy with electronics and spintronics, this new field of research is called magnonics, indicating the magnon as the basic information carrier [23]. Magnonics could also replace part of the charge-based spintronic applications since using magnons, as it would allow one to process information completely charge free and, hence, can exhibit lower dissipation than, for instance, diffusive spin transport by charge motion [23, 24, 25, 26].
Moreover, since magnons are also referred to as the quanta of spin waves, they could be harnessed for quantum information processing. Hence, their capability to interact with a variety of different information carriers could bridge spin-based and quantum-based approaches for information processing and utilised for the realisation of quantum computing, which refers to the relatively young field of quantum magnonics [27, 28].
The idea to use the quantum properties for information processing is as old as quantum mechanics itself. In 1982, Feynman posed the question of whether a classical computer could efficiently simulate quantum mechanical systems and answered his question by proposing to use quantum computers as universal quantum simulators [29]. By using, for instance, the superposition principle of quantum mechanics, instead of N classical bits, 2^N qubits (quantum bits, realised by two-level systems (TLS) in experiments) can be processed simultaneously. Hence, systems based on the laws of quantum mechanics could process much more data in shorter time [30, 31]. A decade later, algorithms such as the Deutsch-Josza or Shor's algorithm were developed, demonstrating the first systems which can run more efficiently on a quantum computer than a traditional one [32, 33, 34]. In combination with the progress of quantum controllable systems such as trapped ions or neutral atoms in cavity resonators [35, 36, 37, 38, 39, 40], these developments proved the feasibility of the experimental systems able to perform quantum computation and information processing based on the laws of quantum mechanics. However, these systems suffered from several drawbacks. In a computer, the information needs to be efficiently processed, then stored in a memory unit and, after, the information must be transferred between the processor and the memory unit. Accordingly, atom-cavity or spin-cavity systems only interact weakly with their environment. Thus, they exhibit long coherence times, making them attractive for storage. However, they are comparably slow as they respond weakly to external fields and are less scalable than, for instance, superconducting

circuits (termed SC qubits). Thus, according to Di Vincenzo's criteria for efficient quantum computing, their lower scalability makes them less attractive for data processing [41].

On the other hand, SC qubits which are macroscopic systems exhibiting coherence, are highly tunable, scalable and flexible and as they interact strongly with each other. These properties make them suited as fast data processing units [42, 43, 44, 45, 46]. However, they are sensitive to direct coupling to the environment, and stored information is lost quickly. Thus, the idea of hybridised quantum systems, where fast processing units, such as SC qubits, are directly or indirectly coupled to atoms or spin ensembles to function as a memory unit has gained much interest (c.f. [46, 47] and references therein). In this context, mediating the coupling of SC qubits to spin ensembles by a cavity resonator to which each constituent is strongly coupled, represents one of the most promising approaches for future applications [46, 48]. There, the resonator would serve as the data bus which mediates the information between the memory (spin ensemble) and the processing (SC qubits) unit.

Therefore, the observation of strongly coupled SC qubits yields a possibility to achieve coherence within macroscopic systems and transfer the concepts of CQED to solid state systems into a new field, namely circuit QED [42, 49]. In this context, indirectly coupled hybrid quantum circuits (HQCs) of spin ensembles and SC qubits are especially interesting. Whilst the spin ensemble couples to the cavity resonator via its magnetic dipole moment, the SC qubits couple through the electric dipole moment [47]. As a result, these systems are insensitive to charge noise, and thus, provide much higher coherence times. However, for a feasible HQC there must not be only strong coupling, i.e. a coherent exchange of information, between the spin and the qubit but each component also needs to be individually strongly coupled with the cavity resonator. Although several groups could already show strong coupling of SC qubits to such resonators [42, 50, 46], reaching the strong coupling regime for spin ensembles took longer. In 2011, the strong coupling of NV centres with a resonator was demonstrated [51, 52]. However, the coupling strengths were still relatively low, and, correspondingly, also the system's cooperativity, i.e. the ratio between coupling and dissipation from the resonator and the spin ensemble. Thus, another route needed to be followed which was utilising the macrospin of a ferromagnet. Theoretically, it was shown, that it was possible to strongly couple Kittel mode magnons, which can be treated as macrospins, to photons of a single mode cavity resonator [53].

The first experimental demonstration was realised by Huebl *et al.* in 2013, where they coupled a gadolinium doped yttrium-iron garnet sphere to a coplanar waveguide (CPW) resonator and observed at $T = 50\,\mathrm{mK}$ a cooperativity almost 100 times higher than was achieved with other spin systems so far [54]. Now, by showing a coherent exchange of information between a magnon, which also represents the carrier of information in spintronics, the experimental ground for merging concepts for CQED with spintronics was given. These groundbreaking experiments resulted in the emergence of the young field of cavity spintronics where the following experimental work on the CMP conducted in the course of this thesis falls into [55]. Shortly after, strong coupling, and hence the existence of a CMP, of magnons in a YIG sphere with cavity photons of a three-dimensional microwave cavity resonator was shown at 10 mK. This temperature corresponds to the quantum regime where the average photon and magnon number is below one [56]. Also, this work confirmed the prediction from the quantum theory of the existence of a square

root dependence between the coupling strength and the number of contributing spins. The experimental demonstration of such strong coupling at millikelvin temperatures paved the way for the first experimental realisation of coupling an SC qubit via the cavity resonator to the magnons of the magnonic sample [27, 57]. Accordingly, such coupling opened a path towards quantum information processing. Simultaneously, Zhang *et al.* reported the observation of strong and ultrastrong coupling between a Kittel mode magnon and the TE101 mode of a three-dimensional cavity resonator at room temperature ($T = 300\,\mathrm{K}$) [58]. Despite being in an entirely classical regime, they demonstrated key features usually attributed to a purely quantum coherent system such as oscillatory energy exchange between the cavity photons and magnons which they termed (classical) Rabi-like oscillations. Furthermore, they observed magnetic induced transparency and the Purcell effect in the ultrastrong coupling regime [59]. The observation of these features at room temperature was astonishing as such observations were restricted to the quantum regime. Accordingly, as usual, it raised more questions and represented the starting point for the field of cavity spintronics. The main questions are:
What is the mechanism responsible for the observation of such classical coherence in a strongly coupled CMP at room temperature? What changes undergo characteristics of a CMP such as the coupling strength in the transition from the millikelvin temperature where quantum effects become important and room temperature? How is it possible to proceed towards applications and also achieve a dynamic control over the coupling strength, such that the coherent exchange of information could be deliberately switched on and off at any time? Although the first question on the mechanism for the classical coherence could be answered, the other ones were open questions at the beginning of this doctoral thesis. Bai *et al.* could attribute the origin of classical coherent cavity photon-magnon coupling to the corresponding classical coherence of the macroscopic electromagnetic fields as described by Maxwell's equations. They obtained this result by comparing the results from a CMP in the strong coupling regime with a study of the coupling by utilising the spin pumping measurement technique [60]. In particular, the CMP originates from the fixed phase correlation between the magnon and photon states, i.e. the time-varying magnetisation and the corresponding cavity's alternating current (AC) magnetic field due to Ampères law from Maxwell's equations [61]. Accordingly, the other open questions are studied and answered in the course of this thesis as will be shown later on.

Since 2014, numerous experiments about the properties and possible applications of CMPs both at millikelvin temperatures and room temperatures have been conducted for different experimental geometries, such as two-dimensional or three-dimensional systems or different samples [62, 63, 64, 65, 66], showing the enormous potential of cavity spintronics. Furthermore, a study performed in the course of this doctoral thesis from 30 mK to 290 K examined the temperature dependence of the coupling strength and linewidth. Thereby, the formerly distinct temperature regimes have been connected [67, 68]. In addition, there are other intriguing works such as demonstrating a gradient memory with CMPs [69], studying cooperative CMP dynamics in feedback coupled cavities [70], achieving the manipulation of distant spin currents by means of a cavity resonator [71], tripartite entanglement [72] or reporting about the experimental confirmation of an exceptional point of the CMP [73]. Moreover, because of the growing interest in antiferromagnetic spintronics, there are recent theoretical considerations aimed at extending cavity spintronics to antiferromagnets for example by coupling a ferro- to an antiferromagnet through cav-

ity resonator photons [74]. However, all these experiments employed a fixed coupling strength set by the resonator geometry and sample choice. Thus, achieving control over the coupling strength represents the next natural step. At the moment, only a few experimental works exist on this topic, and all of them require changes to the system, such moving a YIG sphere within a cylindrical cavity resonator and, hence, carefully tuning the magnetic bias field angle of the internal to the external static field [75, 76]. However, the phase correlation leads to the classical coherence implies that it should be possible to control the coupling strength only by carefully tuning this phase correlation [77]. After demonstrating the persistence of a strongly coupled CMP from room temperature to millikelvin temperatures [67], the first experimental demonstration of a completely externally tunable control over the CMP coupling strength at room temperature has been realised in the course of this doctoral thesis [78].

In the body of this thesis, the behaviour of a hybridised system consisting of a cavity resonator photon with magnonic excitations will be discussed. Hence, the properties and controllability of the CMP are investigated through spectroscopic techniques. This doctoral thesis is organised as follows: First, in Chapter 2, a theoretical, general overview of the utilised concepts for both the magnetic, i.e. magnonic system and the cavity resonator is given. The hybridised systems and the equivalent alternatives for the analytical description are then introduced in Chapter 3. As mentioned above, CMPs have already been studied both at room temperature and cryogenic temperatures, but none of these previous works studied the intermediate temperature regime. Accordingly, the temperature dependent study connecting the millikelvin with the room temperature regime has been conducted in close collaboration between the Johannes Gutenberg-University Mainz (JGU) and the Karlsruhe Institute of Technology (KIT) where the millikelvin temperature data has been measured. Hence, in Chapter 4, a complete study across the entire temperature range from 30 mK to 290 K is presented. It is studied in the "classical" case of a hybridised system with fixed coupling strength between a cavity resonator photon and a magnon exhibiting an avoided crossing at resonance. Properties such as the temperature dependence of the coupling strength, the linewidth of the magnons and thus the cooperativity of the associated new quasiparticle, the cavity magnon-polariton are discussed. Subsequently, the ability to achieve complete control over the coupling strength of a strongly coupled CMP, i.e. to change the dispersive behaviour at resonance from level repulsion to a coalescence of the avoided level crossing which is called "level merging", is presented in Chapter 5. In this particular case, the coupling strength is changed by introducing a second drive to the entire system which is shifted in phase and amplitude concerning the first drives. Thus, the coupling strength is controlled by carefully tuning the relative phase shift $\phi = |\phi_{\mathrm{1stdrive}} - \phi_{\mathrm{2nddrive}}|$ and amplitude ratio δ_0 of the internal AC magnetic fields induced from both drives. After describing possible follow-up experiments for example by shifting focus to antiferromagnetic cavity spintronics using the same experimental apparatus assembled for this thesis at the JGU, a summary of the results and a general outlook for this work in the context of cavity spintronics is given in Chapter 6.

Chapter 2

Theoretical Background

This thesis is devoted to the experimental study, characterisation and manipulation of cavity magnon-polaritons (CMPs), the associated quasiparticles of a hybridised system from cavity resonator photons and magnons. Specifically, the fundamental hybrid system is comprised of two constituents, a reentrant cavity resonator in the microwave frequency regime, and a sphere made from Yttrium-Iron-Garnet ($Y_3Fe_5O_{12}$, YIG) serving as the magnetic sample. In order to discuss the experimental findings in the subsequent chapters, this chapter deals with the theoretical background which is necessary for the description of the CMP. When the resonance frequencies of the cavity photons and magnons are approaching each other, hybridisation between both subsystems emerges. The hybridisation is observable by the opening of a gap at resonance, and there the formation of the CMP takes place. Since two different physical systems are hybridising at resonance, this chapter is comprised of two parts. Whilst the first considers the physical properties and dynamical processes of the magnon, i.e. the magnetic component, the second one deals with the microwave theory which is required for the description of the characteristics of (cavity) resonator photons. There, the models and tools used for the description of a cavity resonator are introduced. The chapter is concluded with the discussion of the system's microwave properties such as the central measurement quantity, the scattering matrix $S_{ij}\, i, j \in \{1, 2\}$.

2.1 Maxwell equations

Electrodynamics is described by a set of fundamental equations known as the Maxwell equations [79, 80]. They summarise the relationship between electric and magnetic fields and include the laws of electromagnetic interaction. Therefore, they are introduced before any detailed discussion on specific properties of the individual system's components is carried out. In matter, the generalised macroscopic Maxwell equations read as:

$$\nabla \times \mathbf{E} = -\frac{\partial \mathbf{B}}{\partial t}, \tag{2.1a}$$

$$\nabla \times \mathbf{H} = \mathbf{J} + \frac{\partial \mathbf{D}}{\partial t}, \tag{2.1b}$$

$$\nabla \cdot \mathbf{B} = 0, \tag{2.1c}$$

$$\nabla \cdot \mathbf{D} = \rho, \tag{2.1d}$$

where $\mathbf{J}$ represents the electrical current density and ρ the charge density. Further, $\mathbf{E}$ and $\mathbf{B}$ denote the electric field strength and magnetic flux density in vacuum, and $\mathbf{H}$ and

D the magnetic field strength and electric flux density in matter, respectively. The latter are also called displacement vectors because they take the modifications of the electric and magnetic field by the presence of charges and currents in the matter into account [81]. The relation between the electric field displacement vector and the electric field and the magnetic field and the magnetic induction, respectively, is formulated as

$$\mathbf{D} = \epsilon_0 \mathbf{E} + \mathbf{P}, \tag{2.2a}$$

$$\mathbf{H} = \frac{1}{\mu_0}\mathbf{B} - \mathbf{M}, \tag{2.2b}$$

where **P** describes the polarisation (density of the electric dipole moment) and **M** the magnetisation vector. In an isotropic medium, the magnetisation **M** can be expressed in terms of the magnetic field strength **H** as

$$\mathbf{M} = \frac{1}{\mu_0}\chi_{\text{mag}} \cdot \mathbf{H}, \tag{2.3}$$

where χ_{mag} is the dimensionless (volume) susceptibility, giving a measure for the magnetisation of a material when it is exposed to an external magnetic field. As a result, by introducing the relative permeability $\mu_r = 1 + \chi_{\text{mag}}$, the displacement field can be written as $\mathbf{H} = \frac{1}{\mu_0 \mu_r}\mathbf{B}$ [82]. Depending on the sign of the susceptibility, one can distinguish between two different types of magnetic properties of a material which is exposed to a magnetic field. For instance, for $\chi_{\text{mag}} < 0$, a material is called diamagnetic, and for $\chi_{\text{mag}} > 0$ paramagnetic [83]. Note, that for an anisotropic medium, the magnetic response depends on the orientation of the magnetisation to the external field in each direction. The magnetic susceptibility is then not a scalar but a tensor of rank 2. Thus, in the next paragraph, the origin and different effects resulting in a non-zero net magnetisation of a material with and without the application of an external magnetic field are discussed.

2.2 Magnetisation dynamics and magnons

Magnetism in solids originates from the spin and orbital angular momentum of electrons as they carry mass, charge and spin [84]. In a semi-classical, strongly simplified picture, electrons move in quantised orbits (Bohr-Sommerfeld atomic model) around the nucleus. The rotation of the particle with velocity **v**, results in an orbital angular momentum $\mathbf{L} = m(\mathbf{r} \times \mathbf{v})$ where m denotes the particles mass, and **r** the position vector [83]. The rotation of the electron with charge $q = -e$ on a closed circle with surface area A constitutes a current loop as it is shown in Figure 2.1. Known as Ampères law, a moving charge induces a current **I** and leads to a magnetic dipole moment $\boldsymbol{\mu} = \boldsymbol{I}A$, where the current can be written in terms of $\mathbf{I} = \frac{\mathrm{q}\mathbf{v}}{2\pi \mathrm{r}}$ with the loop's radius r and the area A enclosed by the loop [79, 85]. In combination, the magnetic moment can be expressed via the orbital angular momentum **L**:

$$\boldsymbol{\mu}_l = -\frac{e}{2m_e}\mathbf{L}. \tag{2.4}$$

The orbital magnetic moment of a single electron (angular momentum number l=1) is called the Bohr magneton $\mu_B = \frac{|-e|\hbar}{2m_e}$, and the magnetic moment is opposite to the angular momentum's direction [86]. Commonly, the net (total) magnetic moments of a solid, for which all individual atomic magnetic moments $\boldsymbol{\mu}_i$ are summed up to $\boldsymbol{\mu} = \sum_i \boldsymbol{\mu}_i$, are expressed in units of μ_B. As mentioned previously, besides charge and mass, electrons

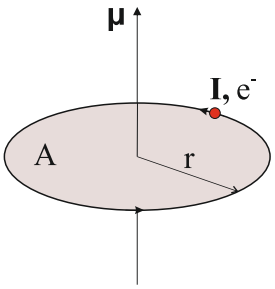

Figure 2.1: The current flow **I** of an electron e^- in a circular orbit, i.e. in a closed loop with surface area A, leads to a magnetic dipole with magnetic moment $\boldsymbol{\mu}$.

carry spin which is an inherent angular momentum [87, 88]. Therefore, a contribution from spin angular momentum to the total net atomic magnetic moment $\boldsymbol{\mu} = \boldsymbol{\mu}_l + \boldsymbol{\mu}_s$ needs to be considered, as well. It is expressed as

$$\boldsymbol{\mu}_s = -g\mu_B \mathbf{S} = -\gamma \mathbf{S}, \tag{2.5}$$

where g is the Landé or g-factor and γ refers to spin's gyromagnetic ratio in units of the Bohr magneton and **S** the spin angular momentum.

2.2.1 Magnetisation of isolated moments in a magnetic field

In order to determine the net magnetic moment of the electrons of a solid in a field, one can define the magnetisation as the net magnetic moment per unit volume, which is induced by the presence of an external magnetic field. Thus, for constant temperature and volume, the magnetisation can be calculated from the energy change of the system when it is exposed to an external magnetic field. Accordingly, it reads as:

$$\mathbf{M} = -\frac{1}{V}\left.\frac{\partial F}{\partial \mathbf{B}}\right|_T, \tag{2.6}$$

where F denotes the Helmholtz free energy [82, 89]. Classically, the Lorentz force acts perpendicular to the direction of the motion of a charged particle in a magnetic field. Thus, it changes the direction but there is no change in energy, and hence, with the above definition, the magnetisation is supposed to be zero. In other words, for an entirely classical system in thermal equilibrium and a uniform magnetic field, the net magnetisation is zero, which is known as the Bohr-van-Leeuwen theorem [90, 91]. As a result, magnetism is a pure quantum mechanical property of matter. Without a field, the bare Hamiltonian of the atom with Z electrons is defined as $\hat{\mathcal{H}}_0 = \sum_{i=1}^{Z}\left(\frac{\mathbf{p}_i^2}{2m} + V_i(\mathbf{r})\right)$, where $\mathbf{p}_i$ and $V_i(\mathbf{r})$ are the ith momentum and potential energy. The addition of a homogenous magnetic field, $\mathbf{B} = \nabla \times \mathbf{A}$ (thus with $A = -\frac{\mathbf{B}\times\mathbf{r}}{2}$ as a suited gauge) results a change of the kinetic energy of the i^{th} electron and is expressed in terms of the canonical momentum $[\mathbf{p_i} - q\mathbf{A}(\mathbf{r_i})]^2/(2m_e)$, where **A** is the magnetic vector potential, m_e the electron mass and $q = -e$ the electron's charge [82, 83]. Hence, taking both the influence of spin and orbital

angular momentum into account, the Hamiltonian of an isolated atom in a magnetic field reads as:

$$\hat{\mathcal{H}} = \hat{\mathcal{H}}_0 + \frac{\mu_B}{\hbar}(\mathbf{L} + g\mathbf{S}) \cdot \mathbf{B} + \frac{e^2}{8m_e}\sum_i^Z (\mathbf{B} \times \mathbf{r}_i)^2, \tag{2.7}$$

where the second term denotes the paramagnetic and the third the diamagnetic contribution, respectively [83]. If for the total angular momentum $\mathbf{J} = \mathbf{L} + \mathbf{S} \neq 0$, the first term dominates. However, for materials with closed atomic shells or ions it vanishes, i.e. $\mathbf{J} = \mathbf{0}$, and the diamagnetic moment is the remaining contribution. As a result, such materials exhibit a zero net magnetic moment in the absence of an external magnetic field. The Bohr-van Leeuwen theorem prohibits a purely classical explanation but still allows one to use a semi-classical approach which may be more intuitive. Hence, in a semi-classical picture, if one imagines an individual magnetic moment as a small circulating current, i.e. the electron moves in a circular orbit around the nucleus, the application of the external field induces a small magnetic moment opposite to the direction of the external magnetic field (Lenz' law). This represents the diamagnetic contribution. However, note that this only is an illustrative explanation and in line with the Bohr-van Leeuwen theorem, diamagnetism is of pure quantum mechanical origin. Quantum mechanically, one finds from first-order perturbation theory and using Equation (2.6) for $\mathbf{B}$ parallel to $\hat{\mathbf{z}}$, for the diamagnetic magnetisation $\mathbf{M} \propto -\mathbf{B}$ and $\chi_{\text{mag}}^{\text{dia}} < 0$ [86].

The situation is different for $\mathbf{J} \neq 0$, i.e. atoms with unpaired electrons, which results in non-zero individual atomic magnetic moments in the absence of an external magnetic field. However, as the moments are assumed to be independent of their neighbouring moments in the solid, the individual moments are randomly oriented at finite temperatures and there is no macroscopic order. Hence, the net magnetic moment of the respective solid is effectively zero [92]. The application of the external field aligns the unordered individual magnetic moments along the field's direction ($\chi_{\text{mag}}^{\text{para}} > 0$), yielding an effective macroscopic magnetisation. Thus, for a paramagnet, except for the much smaller diamagnetic contribution, the magnitude of the individual moments remains unchanged but the direction changes aligning them along the field's direction. Eventually, for a sufficiently high external magnetic field, all individual magnetic moments are aligned which results in the maximally achievable net magnetisation, called the saturation magnetisation [91]. Please note, that here the focus is on the atomic magnetic moments of localised electrons, which is also called Langevin paramagnetism [86]. For the description of the so-called Landau paramagnetism due to delocalised electrons in metals, the reader may refer to Ref. [83, 86] and the references therein. Focusing on the Langevin paramagnetism, the following expression can be derived for the magnetisation and the susceptibility of a paramagnet:

$$\frac{M}{M_s} = B_J(y) = \frac{2J+1}{2J}\coth\left(\frac{2J+1}{2J}y\right) - \frac{1}{2J}\coth\left(\frac{1}{2J}y\right), \tag{2.8}$$

where $M_s = Ng_J\mu_B J$ denotes the saturation magnetisation, $B_J(y)$ the Brillouin function and $y = x \cdot J = \frac{g_J\mu_B J B_{\text{ext}}}{k_B T}$ [15, 83]. Accordingly, the susceptibility reads as:

$$\chi_{\text{mag}}^{\text{para}} = \frac{C}{T}, \tag{2.9}$$

where this is also known as the Curie law with the Curie constant $C = \frac{\mu_0 N J(J+1) g_J^2 \mu_B^2}{3k_B}$. To some extent, all materials show diamagnetic behaviour but since the diamagnetic contribution is much weaker ($\chi_{\text{mag}}^{\text{dia}} \propto -(10^{-6} - 10^{-4})$) than the paramagnetic contribution($\chi_{\text{mag}}^{\text{para}} \propto$

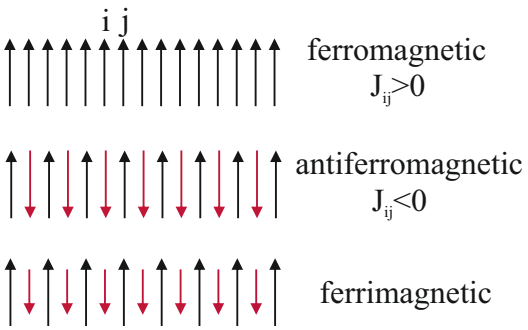

Figure 2.2: Illustration of the main types of (collinear) magnetic order in one dimension. J_{ij} is the exchange constant [86]. Ferromagnetic ordering denotes a parallel alignment of neighbouring spins, antiferromagnetic ordering an antiparallel spin alignment with an equal magnitude on both sublattices, and ferrimagnetic ordering is antiferromagnetically ordered but with a different magnitude of the net magnetic moment of each sublattice. This magnitude difference leads to a residual non-zero effective magnetisation of the material.

$10^{-5} - 10^{-3}$), it is mostly veiled by the dominating paramagnetic interaction such as in the presence of unfilled electron shells [82].

2.2.2 Spontaneous net magnetisation: Interacting spins

The above considerations can explain the observation of a non-zero net magnetisation under the application of an external field, but they do not account for the existence of materials with a spontaneous non-zero net magnetisation at zero applied magnetic field. Hence, in addition to the different response in an external magnetic field of diamagnets and paramagnets, there is also a class of materials with a spontaneous net magnetisation in the absence of an external magnetic field [15, 84]. However, for this kind of magnetic materials, another force, i.e. interaction between individual magnetic moments must exist which is stronger than a paramagnetic ordering at finite temperatures. This interaction then leads to an alignment of these moments without an additional field even at higher temperatures. In his original theory from 1907, P. R. Weiss proposed the addition of a large localised molecular field, which acts on each magnetic moment [93]. Assuming a homogeneous system and uniform magnetisation $\mathbf{M} = \frac{\mathbf{m}}{V}$, defined as the net magnetic moment per unit volume, he parametrised the strength of this molecular field via $\mathbf{B}_{\text{loc}} = \lambda \mathbf{M}$, where he introduced a phenomenological constant λ. Following a similar approach as for the Langevin paramagnetism, he obtained a modified expression of the susceptibility:

$$\chi_{\text{mag}}^{\text{ferromagnet}} = \frac{C}{T - T_C}, \tag{2.10}$$

where $T_C = \lambda C$ is the Curie temperature. This is also known as the Curie-Weiss law [91]. Thus, the spontaneous net magnetisation occurs only for temperatures $T < T_C$. For higher temperatures, the thermal fluctuations which counteract the formation of a macroscopic order exceed the strength of the aligning interaction. Again, the individual

magnetic moments are randomly oriented, and the material behaves as a paramagnet to a good approximation [83]. Magnetic materials which show this behaviour are called ferromagnets. However, in Weiss' original theory, the origin of this molecular field could not be explained. Classically, one could attribute this molecular field to magnetic dipolar forces, i.e. the magnetic dipole-dipole interaction. This interaction would lead to values of $\lambda \approx 4$, which cannot account for the observation of ferromagnets with critical temperatures in the order of $10^2 - 10^3$ K, requiring rather $\lambda \approx 10^4 - 10^5$. Thus, the origin of a spontaneous net magnetisation, i.e. macroscopic order, cannot be explained by dipole-dipole interactions [94].

Exchange interaction

The physical reason for the appearance of spontaneous magnetisation is due to the presence of yet another interaction of pure quantum mechanical origin, the (Heisenberg) exchange interaction. The origin of the exchange interaction is a combination of the Coulomb repulsion between the electrons and Pauli's exclusion principle for the antiparallel orientation of two adjacent spins [83, 94]. This additional interaction, i.e the related exchange energy between two neighbouring spins at lattice sites i and j with spin angular momentum operators $\hat{\mathbf{S}}_i$ and $\hat{\mathbf{S}}_j$, respectively, can be written as:

$$\hat{\mathcal{H}} = -\frac{1}{2}\sum_{ij} \mathrm{J}_{ij}\hat{\mathbf{S}}_i \cdot \hat{\mathbf{S}}_j, \tag{2.11}$$

where $\mathrm{J_{ij}}$ denotes the exchange integral and the factor 1/2accounts for avoiding double counting. Depending on the crystallographic structure, the sign of J_{ij} and the individual strength of the interactions leading to a spontaneous macroscopic magnetic moment of the solid, different types of magnetic order exist. For instance, if $J_{ij} > 0$, a parallel alignment of the neighbouring spins is energetically more favourable. Accordingly, this results in ferromagnetic order with a spontaneous net magnetisation at zero applied magnetic field. On the contrary, for $J_{ij} < 0$, an antiparallel alignment of two adjacent spins is the preferred final configuration. Materials which exhibit this type of antiparallel spin ordering are characterised as (Heisenberg) antiferromagnets. First introduced by L. Néel, one can model an antiferromagnet to a certain extent by two ferromagnetically ordered sublattices with a non-zero net magnetisation. In this model, the neighbouring antiparallel spins belong to the other sublattice. Both sublattices are aligned antiparallel to each other. If the net magnetic moment of each sublattice is equal, the spontaneous magnetisation of the material is zero (c.f. Figure 2.2). Analogously to ferromagnets, above a critical temperature the antiferromagnetic order vanishes and is replaced by a paramagnetic ordering. For antiferromagnets, this characteristic temperature is called the Néel temperature T_N. More information on antiferromagnets can be found in Ref. [15] and the references therein. However, the net magnetic moment from each sublattice may not be identical when, for instance, the material contains different ions in each sublattice. As a result, the material exhibits a residual, non-zero spontaneous net magnetisation at zero field which is the difference between the magnitude of both sublattices. Such partially compensated antiferromagnetic order refers to another type of magnetic order, describing ferrimagnetic materials [91, 94]. Note, that the above considerations are restricted to collinear ferro- and antiferromagnets, where the helix turn angle Θ is $\Theta = 0$ and $\Theta = \pi$, respectively [94].

Hence, the origin of the molecular field from Weiss' molecular field theory is the isotropic (Heisenberg) exchange interaction. For $T > T_c$ all ferromagnetic order is destroyed by the dominance of thermal fluctuations [80]. Below the Curie temperature, the material is ferromagnetically ordered, but thermal fluctuations decrease the number of aligned spins, i.e. the saturation magnetisation. As a result, the saturation magnetisation increases towards lower temperatures due to the decrease of thermal fluctuations. At very low temperatures ($T \ll T_c$), the contribution from these fluctuations is not strong enough to influence the ferromagnetic ordering any more. The value of the net magnetisation saturates at the saturation magnetisation value $M(T = 0) \equiv M_s$, i.e. the number of available spins reaches a maximum. Analytically, the temperature dependence of the saturation magnetisation can be approximated to first order by Bloch's $T^{3/2}$ law [83, 95]:

$$M \approx M_s \left(1 - \left(\frac{T}{T_c}\right)^{3/2}\right), \tag{2.12}$$

where the saturation magnetisation is proportional to the maximal number of available spins ($M_s \propto N$).
In all experiments conducted in the course of this thesis, the ferrimagnet Yttrium-Iron-Garnet (YIG, $Y_3Fe_5O_{12}$) has been utilised (c.f. Chapter 4, Section 2.3). YIG can be treated as a ferromagnet [96, 97, 98]. Thus, the focus will now lay on ferromagnetism and related effects, which will be now discussed in more detail. However, before, a short overview of YIG is given in the next section.

2.3 Yttrium Iron Garnet ($Y_3Fe_5O_{12}$ (YIG))

Although the ferrimagnetic insulator YIG does not grow naturally but has to be industrially fabricated, YIG exhibits the structure of a natural garnet. Due to its excellent magnetic properties YIG is now frequently used as the magnetic material of choice in the field of spin cavitronics [58, 56, 69, 61]. Among other properties, it so far has the smallest known linewidth in ferromagnetic resonance and magnetic damping of spin waves [91, 99, 100]. This low magnetic damping parameter makes YIG a well-suited candidate for experiments in magnonics and the development of applications based on magnons as storage units. Further, the net spin density ($2.1 \cdot 10^{22}\,\mu_B\,\mathrm{cm}^{-3}$ per unit cell, [100]) of YIG is comparably high which is advantageous for the coupling between a cavity resonator and a spin, i.e. the magnon [96]. From the early days of its discovery, this material has been used in applications of microwave technology such as filters in the high-frequency regime [99, 101]. The atoms arrange in a body-centered cubic (bcc) structure with a lattice constant of $a = 12.4\,\text{Å}$. The unit cell consists of 80 atoms and the Curie temperature is at $T_c = 560\,\mathrm{K}$ [98]. Magnetically, only the iron ions at different lattice sites, antiferromagnetically ordered in two sublattices, contribute to the net magnetic moment of the unit cell. As schematically pictured in Figure 2.3 for one unit cell, one sublattice is comprised of eight Fe^{3+} in an octahedral (a-sites) configuration with respect to the surrounding oxygen ions (O^{2-}) and the other of twelve Fe^{3+} ions in a tetrahedral (d-sites) configuration. Due to the different net magnetic moment from each sublattice, the unit cell exhibits a compensated non zero net magnetic moment of $\mu = 10\,\mu_B$ (at T=0 [98]) per unit cell, and in the limit of low energies, YIG can be treated as a ferromagnet [15]. As the material has been extensively studied in the decades since its discovery, numerous works

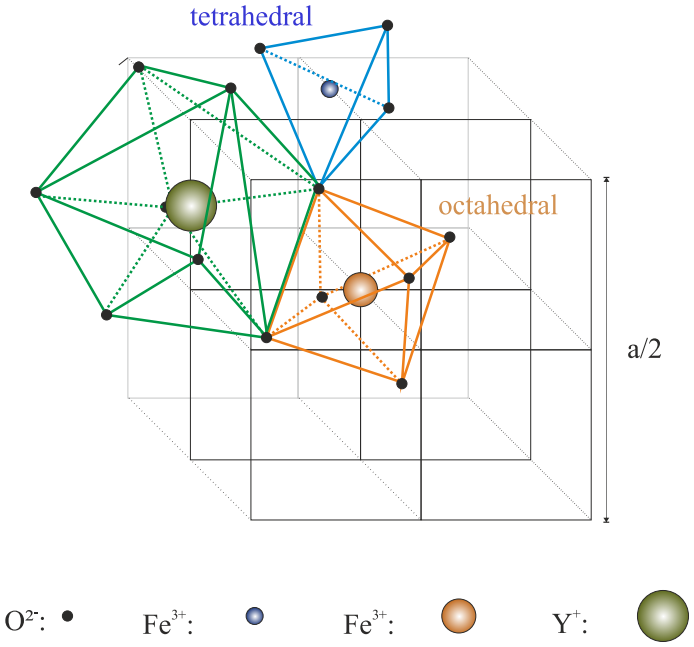

Figure 2.3: Schematical representation of YIG, showing the main characteristics for an octant of the body-centred cubic (bcc) unit cell, where the ions contributing to the magnetic properties of YIG are eight Fe^{3+} ions at the octahedral and twelve at the tetrahedral sites, respectively. The net magnetisation of this sublattices is aligned antiparallel. However, there is a non zero net magnetisation of $10\,\mu_B$ per unit cell, when adding both contributions. Thus, YIG is a ferrimagnet.

are dealing with the internal structure, the strength of the exchange interaction between the sublattices and the different spin wave branches of YIG such as Ref. [98, 99, 102]. However, this is out of the scope of this thesis, and the reader may refer to the literature and references therein for a more detailed description.

Note, that for the temperature dependent CMP study in this chapter a commercially [103] obtained YIG sphere with a diameter of $d = 0.5\,\text{mm}$ has been used. However, as pointed out later on in more detail in Chapter 5, it turned out that for "clear" avoided level crossings and the observation of level merging a smaller YIG sphere of $d = 0.2\,\text{mm}$ needed to be utilised. In addition, in order to discuss level merging for higher number of spins, i.e. larger spheres, few measurements were conducted with a YIG sphere of $d = 1\,\text{mm}$ (c.f. Chapter 5, Section 5.14).

2.4 Ferromagnetism

As stated before, in contrast to paramagnetism, ferromagnetic materials exhibit a spontaneous net magnetisation at zero fields [84]. Without the application of an external magnetic field, the ferromagnet is comprised of areas of spins in parallel alignment, called

magnetic domains. In order to minimise the potential energy of the ferromagnet, it is energetically more favourable to form such a multi-domain state [91]. The application of a sufficiently strong external field results in the formation of a monodomain state, where all spins, i.e. the individual magnetic moments, are all aligned along the external field direction. The ferromagnet is saturated now, and the magnetisation reached its maximum possible value, the saturation magnetisation M_s. All experiments which have been conducted in the course of this thesis and described in the following chapters, deal with a magnetically saturated magnetic specimen exposed to a correspondingly high, external magnetic field. Thus, the following discussion will focus on phenomena in a single domain state. For further information on contributions to the potential energy and formations, magnetic domains, in general, the reader may refer for example to [82, 91] and the references therein.
The energy of a magnetic dipole in a magnetic field is given by the Zeeman energy $E_Z = -\mathbf{m} \cdot \mathbf{H}$ and minimised for a parallel alignment of the magnetic moment $\mathbf{m}$ and the magnetic field, i.e. $\mathbf{m} \parallel \mathbf{H}$. When a magnetic moment (not yet aligned to the field's direction) is exposed to a magnetic field a torque $\tau = \mathbf{m} \times \mathbf{H}$ is exerted on the magnetic moment. If only orbital angular momentum and its relation to the magnetic moment is considered, this torque results in a classical equation of motion for a magnetic dipole, $\frac{\partial \mathbf{L}}{\partial t} = \mathbf{m} \times \mathbf{H}$. Thus, the direction of the magnetic moment starts to precess around $\mathbf{H}$ with an angular frequency of $\omega_L = -\gamma|\mathbf{H}|$. This behaviour is also known as Larmor precession and, correspondingly, ω_L the Larmor frequency [79]. If, in addition to the external, static magnetic field, an alternating current (AC) magnetic field $\mathbf{h}_{\mathrm{AC}}$ is applied perpendicular to this external field, another torque $\tau_2 = \mathbf{m} \times \mathbf{h}_{\mathrm{AC}}$ is exerted on $\mathbf{m}$. In case $\mathbf{h}_{\mathrm{AC}}$ is circularly polarised, matches the sense of the precession and the Larmor frequency, a constant torque is applied on $\mathbf{m}$. As a result, the magnetisation precesses in a cone with an angle Θ to the static field $\mathbf{H}$ (c.f. Figure 2.4). If the frequencies match, the energy absorption is maximal, and this results in magnetic resonance at this frequency [92]. Accordingly, if both the spin and orbital angular momentum are taken into account, the equation of motion of the magnetisation of a single domain ferromagnet can be derived similarly. It was derived for the first time in 1935 by L.Landau and L. Lifshitz and modified by Gilbert later on, in order to include damping by introducing a phenomenological parameter α. The spin dynamics will be discussed in the next section.

2.5 Spin dynamics

The presence of thermal fluctuations or other perturbations such as alternating frequency (AC) magnetic fields result in a deviation from the ferromagnetic ground state, where all spins are aligned parallelly. In such an excited state, different, time-dependent dynamical processes can take place, where the specific dynamics depend on the system under consideration. Thus, the Landau-Lifshitz-Gilbert equation (LLG) describes the corresponding dynamics, that is, the time dependent evolution of the magnetisation in an isotropic (single domain) ferromagnet for temperatures far below the Curie temperature [14]. Here, the continuum approximation is used. There, the magnetisation is defined as the net magnetic moment per unit volume whose length scale is above the one where the "granularity" of the individual magneti moments has to be taken into account [82]. This approach allows one to describe the magnetisation dynamics classically [14, 15]. It is written in the form

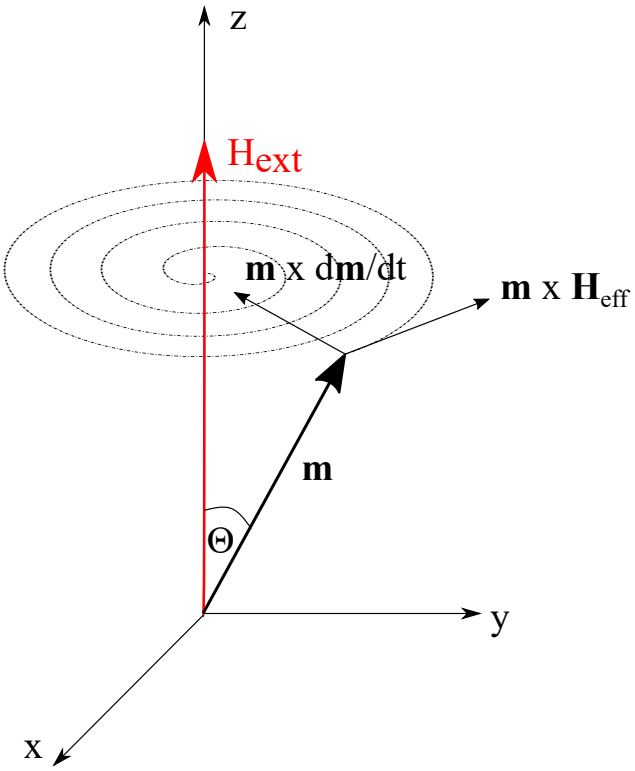

Figure 2.4: Graphical illustration of the precessional motion of a magnetic moment $\mathbf{m}$. The spin is moved from its equilibrium position by an alternating frequency (AC) magnetic field perpendicular to the external field $\mathbf{H}_{\text{ext}}$. Due to the non-linearity of the susceptibility tensor of a ferromagnet, only the component transverse to the direction of the effective field acts on the system, resulting in gyrotropy [15]. If not continuously driven, the precession is damped to equilibrium by an additional torque $\mathbf{m} \times (\partial\mathbf{m}/\partial t)$. As a result, the system relaxes back to equilibrium within a relaxation time τ.

proposed by Gilbert [104]:

$$\frac{\partial \mathbf{M}}{\partial t} = -\gamma \mathbf{M} \times \mathbf{H}_{\text{eff}} + \frac{\alpha}{M_s} \mathbf{M} \times \frac{\partial \mathbf{M}}{\partial t}, \tag{2.13}$$

where α denotes the dimensionless, phenomenologically introduced Gilbert damping parameter, $\mathbf{H}_{\text{eff}}$ refers to the effective magnetic field acting on the ferromagnetic sample andγ denotes the gyromagnetic ratio. Accordingly, the first term of Equation (2.13) describes the precessional movement of an excited spin around the equilibrium direction of the magnetisation. The second term describes the relaxation of the precession, as it is also schematically illustrated in Figure 2.4. The dissipation, included here via the second term, conserves the length of the magnetisation vector. However, this is not valid for all kinds of dissipation processes resulting in the relaxation of the magnetisation. Several dissipation processes are discussed in Section 2.9 in order to explain the experimental findings of the temperature dependence of the magnon linewidth.

To solve the LLG equation, both an internal static and a time dependent part for the effective field and the magnetisation are taken into account:

$$\mathbf{H}_{\text{eff}} = \mathbf{H}_{\text{eff},0} + \mathbf{h}_{\text{AC}}, \tag{2.14}$$

and

$$\mathbf{M} = \mathbf{M}_0 + \mathbf{m}_{\mathrm{AC}}. \tag{2.15}$$

The time dependent contributions ($\mathbf{m}_{\mathrm{AC}}$, $\mathbf{h}_{\mathrm{AC}}$) are assumed to be much smaller ($|\mathbf{H}_{\mathrm{eff},0}| \gg |\mathbf{h}_{\mathrm{AC}}|$, —$\mathbf{M}_0| \gg |\mathbf{m}_{\mathrm{AC}}|$) than the static ones ($\mathbf{M}_0, \mathbf{H}_0$), and the LLG is linearised [14, 15] by the method of successive approximations. If further the time dependence of the field is assumed to be harmonic (sinusodial), complex variables for both the magnetisation and the field can be obtained;

$$\frac{\partial \mathbf{m}}{\partial t} = \mathbf{m} e^{i\omega t} \tag{2.16}$$

and

$$\frac{\partial \mathbf{h}}{\partial t} = \mathbf{h} e^{i\omega t}, \tag{2.17}$$

where $\mathbf{m}$ and $\mathbf{h}$ are the complex amplitudes for the time dependent parts $\mathbf{h}_{\mathrm{AC}}$ and $\mathbf{m}_{\mathrm{AC}}$. They satisfy

$$i\omega\mathbf{m} + \gamma\mathbf{m} \times \mathbf{H}_{\mathrm{eff},0} = -\gamma\mathbf{M}_0 \times \mathbf{h} \tag{2.18}$$

which represents a linearised form of the LLG. For a sphere, the LLG can then be expressed as [15]

$$i\omega\mathbf{m} + \gamma\mathbf{m} \times \mathbf{H}_{\mathrm{eff},0} + \frac{i\alpha\omega}{M_0}\mathbf{m} \times \mathbf{M}_0 = -\gamma\mathbf{M}_0 \times \mathbf{h}. \tag{2.19}$$

Setting $\hat{\mathbf{z}} \parallel \mathbf{H}_{eff,0} \parallel \mathbf{M}_0$ yields the following solution for $\mathbf{m}$:

$$\mathbf{m} = \overleftrightarrow{\chi}\mathbf{h}, \tag{2.20}$$

where $\overleftrightarrow{\chi}$ is a nonsymmetric second rank tensor and denotes the high frequency susceptibility [105, 15].

2.5.1 The ferromagnetic ground state

Before it is possible to discuss any excitation of the system, it is necessary to first find the ferromagnetic ground state of the system. Hence, the goal is to find the ground state for the ferromagnetic, i.e. $J_{i,j} \geq 0 \,\forall\, \{i, j\}$, Heisenberg Hamiltonian shown in Equation (2.11). In order to show whether the spin operators $\hat{\mathbf{S}}_i$ and $\hat{\mathbf{S}}_j$ in the Hamiltonian are an eigenstate, it is convenient to use the circular, ladder operators [106]:

$$\hat{S}_i^{\pm} = \hat{S}_i{}^x \pm i\hat{S}_i{}^y, \tag{2.21a}$$

$$\hat{S}_i{}^{\pm} \left|S_i, m_i\right\rangle = \sqrt{(S_i \mp m_i)(S_i + 1 \pm m_i)} \left|S_i, m_i + 1\right\rangle. \tag{2.21b}$$

Then, Equation (2.11), can be written as:

$$\hat{\mathcal{H}} = -\frac{1}{2}\sum_{ij} J_{ij}\left(\frac{1}{2}(\hat{S}_i^+ \cdot \hat{S}_j^- + \hat{S}_i^- \cdot \hat{S}_j^+) + \hat{S}_i^z \cdot \hat{S}_i^z\right) \tag{2.22}$$

It can be seen, that the product states of a system with N spins, $\left|\hat{S}_1, m_1\right\rangle, \left|\hat{S}_2, m_2\right\rangle .. \left|\hat{S}_N, m_N\right\rangle$ are only diagonal for the last term in Equation (2.22). However, the first two change the quantum numbers m_i, m_j. Thus, $[\hat{\mathbf{S}}, \hat{\mathcal{H}}] \neq 0$, and the above states are not an eigenstate of the ferromagnetic Heisenberg Hamiltonian. Since $J_{ij} \geq 0 \,\forall\, \{i, j\}$ for a ferromagnet, the ground state energy is minimised when all N spins are aligned in parallel to each other, i.e. the maximal projection of the spins $S^z_{\mathrm{tot}} = -NS$ if the spins are considered to be

identical. Hence, one defines the total spin operator $\hat{\mathbf{S}}_{\text{tot}}$. Since $[\hat{\mathbf{S}}_{\text{tot}}, \hat{\mathcal{H}}] = 0$, it represents one good quantum number which could be used to find the simultaenous eigenstates, i.e. construct an eigenbasis for $\hat{\mathcal{H}}, \hat{\mathbf{S}} \cdot \hat{\mathbf{S}}$ and $\hat{S}^z$ [94, 107]. Therefore, if all spins are aligned to the same direction such as along the $\hat{z}$-direction, the ground state corresponds to:

$$|\psi\rangle \equiv |0\rangle = |S,S\rangle_1 |S,S\rangle_2 ... |S,S\rangle_N , \tag{2.23}$$

where the indices $1, 2, ..., N$ refer to the first, second and Nth spin, respectively. In addition, for the spins to take the maximal projection, $\hat{\mathbf{S}}_i^2 |S,S\rangle_i = S(S+1) |S,S\rangle_i$ and $\hat{S}_i^z |S,S\rangle_i = S |S,S\rangle_i$ are introduced. Utilizing Equation (2.22), shows that $|0\rangle$ is an eigenstate of the ferromagnetic Heisenberg Hamiltonian:

$$\hat{\mathcal{H}} |0\rangle = -\frac{1}{2} S^2 \sum_{ij} J_{ij} |0\rangle \equiv \hat{\mathcal{H}}_0 |0\rangle . \tag{2.24}$$

The exchange energy is a scalar and thus $\hat{\mathcal{H}}$ is rotational invariant, and the quantisation axis can be freely chosen which results in an infinite degeneracy in position space. There are $2\hat{S}_{\text{tot}} + 1$ ground states and, for $T = 0$, this relates to a spontaneously broken symmetry. Moreover, $\hat{\mathcal{H}}_0$ is the exact ground state for the Heisenberg ferromagnet because the respective energy is always lower or equal than the one from the expectation value $\langle\theta| \hat{\mathcal{H}} |\theta\rangle$ for an arbitrary product state [106]. Note, that it also corresponds to the minimal (classical) energy and the monodomain ferromagnetic phase of a sample described in Weiss' theory [94].

Furthermore, for short distances, in the presence of an external field and neglecting the weaker dipole-dipole interactions, the ground state energy is modified by the addition of the Zeeman energy. It minimises the energy for an alignment of all spins along the field, i.e. all parallel to each other, and reads:

$$\langle 0| \hat{\mathcal{H}} |0\rangle = -\frac{1}{2} S^2 \sum_{ij} J_{ij} - g\mu_B BNS, \tag{2.25}$$

, and one can now write the saturation magnetisation as $M_s = g\mu_B \frac{N}{V} S$. In contrast to the single exchange term, there is no spontaneous symmetry breaking in this case as this is already happening by the presence of the external magnetic field [15].

2.5.2 Excitations of the ferromagnetic ground state

The exact ground state applies only for $T = 0$. For $T \neq 0$, excitations caused, for instance, by thermal fluctuations, will result in deviating the system's state from the ground state. Thus, low-energy excitations of the ferromagnet have to be taken into account. Since the fully polarised ground state corresponds to a parallel alignment of N spins, one could imagine that "flipping" a single spin, i.e. reversing its direction (c.f. Figure 2.5 a.)), represents a fundamental excitation of the system. Accordingly, such excitation would correspond to a state of the form:

$$|\psi'\rangle = |S,S\rangle_1 , ..., |S,S-1\rangle_i , ..., |S,S\rangle_N , \tag{2.26}$$

, where $|\psi'\rangle$ denotes the states where the z-component is decreased by one unit. These states can be expressed in terms of a change of the ground state:

$$|\psi'\rangle = \frac{1}{\sqrt{2S}} \hat{S}_i^- |0\rangle \tag{2.27}$$

Comparing the energy difference between this state and the ground state, one finds $\Delta E = zJS$, where z is the coordination number. This leads to an exchange energy which is in the order of the critical temperature of T_C and corresponds to a very high energy for this system [106, 107]. Thus, reversing a single spin is not a good approximation for an eigenstate as the energy cost is too high. As a result, lower energy excitations should exist which represent the fundamental excitations of the ferromagnetic ground state.
In the limit of a large spin S, the quantum mechanical spin operator $\hat{S}_i$ can be replaced by a classical vector with a fixed length $|\hat{S}_i| = S$ and the classical approximation used [106, 107]. For such a system, it is assumed that the exchange integrals only depend on the difference of the different sites $\mathbf{R}_i$ and $\mathbf{R}_j$ of the Bravais lattice, i.e. $J_{ij} = J_{ji} = J(\mathbf{R}_i - \mathbf{R}_j)$. Correspondingly, the Hamiltonian has translational symmetry. Hence, utilising Bloch's theorem, it can be shown that a state constructed from linear combinations is an eigenstate of the excitation [94, 106, 108].

$$|\mathbf{k}\rangle = \frac{1}{\sqrt{N}} \sum_{\mathbf{R}_i} e^{i\mathbf{k}\cdot\mathbf{R}_i} |\psi'\rangle \,. \tag{2.28}$$

Thus, instead of a single "flipped" spin at site i, the low energy excitation corresponds to a translation of the excitation of a spin to a collective excitation of the system over the lattice sites $\mathbf{R}_j$. Passing from position to momentum space by a Fourier transformation, yields the spin operators [106].

$$\hat{S}^{\alpha}_{\mathbf{k}} = \frac{1}{\sqrt{N}} \sum_{\mathbf{R}_i} e^{-i\mathbf{k}\cdot\mathbf{R}_i} \hat{S}^{\alpha}_i, \tag{2.29a}$$

$$\hat{S}^{\alpha}_i = \frac{1}{\sqrt{N}} \sum_{\mathbf{k}} \hat{S}^{\alpha}_{\mathbf{k}} e^{i\mathbf{k}\cdot\mathbf{R}_i}, \tag{2.29b}$$

where $\alpha \in \{x, y, z, \pm\}$. These states have, up to an arbitrary vector of the reciprocal lattice, a well-defined momentum and energy $\hbar\omega(\mathbf{k})$. The associated quasiparticle to this collective spin excitation is called "magnon". Utilizing $J(\mathbf{k}) = \sum_i J(\mathbf{R_i} - \mathbf{R}_j) e^{i\mathbf{k}(\mathbf{R_i} - \mathbf{R}_j)}$, one obtains for the Hamiltonian in momentum space:

$$\hat{\mathcal{H}} = -\frac{1}{2} \sum_{\mathbf{k}} J(\mathbf{k})(\hat{S}^{+}_{\mathbf{k}} \hat{S}^{-}_{-\mathbf{k}} + \hat{S}^{z}_{\mathbf{k}} \hat{S}^{z}_{-\mathbf{k}}) - g\mu_B \sqrt{N} B_0 \hat{S}^{z}_0. \tag{2.30}$$

By expressing the state again in terms of ladder operators in momentum space $|\mathbf{k}\rangle = \frac{1}{\sqrt{2S}} \hat{S}^{-}_{\mathbf{k}} |0\rangle$ acting on the ground state and using $J(\mathbf{k}) = J(-\mathbf{k})$, shows that $[\hat{\mathcal{H}}, \hat{S}^{-}_{\mathbf{k}}] |0\rangle = [g\mu_B B_0 - S(J(\mathbf{k}) - J(\mathbf{k} = 0))] \hat{S}^{-}_{\mathbf{k}} |0\rangle$. Hence $|\mathbf{k}\rangle$ is an eigenstate of the system with an energy of the excited state, i.e. one magnon:

$$\mathbf{E}(\mathbf{k}) - E_0(B_0) = \hbar\omega(\mathbf{k}) = +g\mu_B B_0 - S(J(\mathbf{k}) - J(\mathbf{k} = 0)). \tag{2.31}$$

The calculation of the expectation value for the z-component of the flipped spin $\hat{S}^{z}_i$ on the state $|\mathbf{k}\rangle$ yields:

$$\langle \mathbf{k}| \hat{S}^{z}_i |\mathbf{k}\rangle = NS - 1 = S_{\text{tot}} - 1. \tag{2.32}$$

This shows, that the creation of each magnon lowers the total number of spins N in the ground state by one unit. Hence, magnons are bosonic quasiparticles where the actual excitation is distributed over the full lattice [15, 106]. Given the bosonic nature of the magnons, it should be possible to transform the spin momentum operator into a form

such that is expressed in terms of (bosonic) creation and annihilation operators. As a consequence, the magnon states could be written in the harmonic oscillator language, i.e. in form of $\hat{\mathcal{H}}_{\text{harm osc}} = \hbar\omega(\hat{a}_i^\dagger \hat{a}_i + \frac{1}{2})$. One widely used non-linear transformation to bosonic operators is called the Holstein-Primakoff transformation, which will be discussed in the following [25]. Please note, that this transformation is valid for a ferromagnet. However, under certain conditions the material used in this thesis, i.e. YIG, can be treated as a ferromagnet, therefore validating the following description.

2.6 Harmonic oscillator

The concept of spin is a purely quantum mechanical one, but by introducing a "classical" spin momentum operator $\hat{\mathbf{S}}_i$ assigned to each magnetic moment at a site i allows one to draw an analogy to the angular momentum $\mathbf{J}$ from classical mechanics [14, 94]. As it is demonstrated in the following this allows for a representation of the spin momentum in terms of raising and lowering operators. Consequently, a comparison to the harmonic oscillator reveals the possibility of describing (collective) magnetic excitations in terms of a harmonic oscillator.

For the case of an exchange interaction between two neighbouring spins at lattice sites i and j in an external magnetic field $\mathbf{H} = (0, 0, H_z)$, the Hamiltonian reads:

$$\hat{\mathcal{H}} = -\frac{1}{2}\sum_{i,j} J_{ij}\hat{\mathbf{S}}_i \cdot \hat{\mathbf{S}}_j - g\mu_B \mathbf{H}\sum_i S_i^z. \tag{2.33}$$

The summation over all individual spins can be expressed by an effective, total spin $S_0^z = \sum_i S_i^z$, such that for a system with N contributing spins the state with minimal potential energy for a ferromagnet ($J > 0$) is described by $S_0^z = -NS$. As shown above, this state denotes the ground state of a quantum Heisenberg ferromagnet [94]. In the Heisenberg model, the time dependent equation for the spin expectation value is written as

$$\frac{\partial < \hat{\mathbf{S}}_j >}{\partial t} = \frac{-i}{\hbar}[\hat{\mathbf{S}}_j, \hat{\mathcal{H}}], \tag{2.34}$$

where the spin is expressed as a classical vector as stated above. In order to decouple the spin operators at different site, a Fourier transformation is performed and the equation of motion can be written as:

$$\hbar\frac{\partial \hat{S}_{\mathbf{k}}^-}{\partial t} = iS[J(\mathbf{k}=0) - J(\mathbf{k})]\hat{S}_{\mathbf{k}}^- + ig\mu_B B_0 \hat{S}_{\mathbf{k}}^-. \tag{2.35}$$

Equation (2.35) shows, that the motion of each wave vector is decoupled from the others which resembles normal modes of a wave. If one considers a single excited mode, the solution of Equation (2.35) yields $\hat{S}_{\mathbf{i}}^x \propto \cos((\mathbf{k}\cdot\mathbf{R}_i + \omega(\mathbf{k}))t)$, $\hat{S}_{\mathbf{i}}^y \propto \sin((\mathbf{k}\cdot\mathbf{R}_i + \omega(\mathbf{k}))t)$ and $\hat{S}_i^z = S$. Thus, the real space spin components correspond to a plane wave and the the spins precess on a cone because the x- and y-components are shifted by $\frac{\pi}{2}$ as it is illustrated in Figure 2.5. Accordingly, this collective excitation is called a spin wave, where the magnons represent the spin wave quanta [15].

2.6.1 Holstein Primakoff transformation

If one considers the transition of a system of N spins from the ground to an excited state by lowering the total number of the spins in the ground state by, for instance, one unit,

this change can be described by the use of a number operator. This operator takes the spin deviations into account and at lattice site i is expressed by:

$$\hat{n}_i = \hat{S} - \hat{S}_i^z, \tag{2.36a}$$

$$\hat{n}_i = \hat{m}^\dagger \hat{m}, \tag{2.36b}$$

where in analogy to the photonic operators $\hat{a}^\dagger$, $\hat{a}$, $\hat{m}^\dagger$, $\hat{m}$ are the creation and destruction operator of the magnons. As mentioned previously, by considering the commutation relations for the spin, the Holstein-Primakoff (HP) transformation is a non-linear transformation which expresses the spin ladder operators in terms of $\hat{m}^\dagger$, $\hat{m}$. Then, the Hamiltonian from Equation (2.33) can be expressed in terms of raising and lowering operators. The spin operator is then transformed as [25]:

$$\hat{S}_i^z = S - \hat{m}_i^\dagger \hat{m}_i, \tag{2.37a}$$

$$\hat{S}_i^- = \sqrt{2S}\hat{m}_i^\dagger \sqrt{1 - \frac{\hat{m}_i^\dagger \hat{m}_i}{2S}}, \tag{2.37b}$$

$$\hat{S}_i^+ = \sqrt{2S}\sqrt{1 - \frac{\hat{m}_i^\dagger \hat{m}_i}{2S}}\, \hat{m}_i. \tag{2.37c}$$

It can be seen from the Equation (2.37a), that the number operator counts for the number of excitations, i.e. "flipped spins". However, due to its the square root dependence, the number operator has to satisfy the inequality $\hat{n} \leq 2S$ [94]. Further, the above transformation of the spin operators will not result in a Hamiltonian in terms of independent harmonic oscillators but rather interacting bosons. Hence, in order to also study magnon interactions, it would be convenient to reformulate the Hamiltonian such that it consists of a non-interacting and an interacting part. If $\sqrt{2S}\sqrt{1 - \frac{\hat{m}^\dagger \hat{m}}{2S}}$ is expanded to quadratic order at low temperatures, where the number of excitations is much smaller than the total number of spins, the ladder operators can be approximated (c.f. Equation (2.38)). This approximation is also known as the spin-wave approximation, and allows for decomposing the Hamiltonian as desired. In this approximation, $\hat{n} \ll \hat{S}$, and the ladder spin operators can be approximated by "real" harmonic oscillators [15, 106]:

$$\hat{S}_i^z \approx S, \tag{2.38a}$$

$$\hat{S}^- \approx \sqrt{2S}\hat{m}_i^\dagger, \tag{2.38b}$$

$$\hat{S}^+ \approx \sqrt{2S}\hat{m}_i. \tag{2.38c}$$

Diagonalising the Hamiltonian again in Fourier space, allows one to obtain the following expression for the Hamiltonian in the harmonic oscillator language.

$$\hat{\mathcal{H}} = \sum_{\mathbf{k}} \hbar\omega(\mathbf{k})\hat{m}_{\mathbf{k}}^\dagger \hat{m}_{\mathbf{k}} + \hat{\mathcal{H}}_0 \tag{2.39}$$

The propagation of this excitation is called a spin wave and, as mentioned, the corresponding spin wave quantum is called a *magnon*, the quasiparticle of such collective spin excitation. Correspondingly, a magnon represents a reversed spin which can be thought of a delocalised wave function of a one-dimensional ferromagnetic chain. In the number state representation, the magnetisation is the effective sum of all individual magnetic moments, where $M_s(T = 0) = g\mu_B \hbar S N$. Thus, the creation of one magnon lowers the total magnetisation value by one μ_B. Among other contributions, the previously mentioned

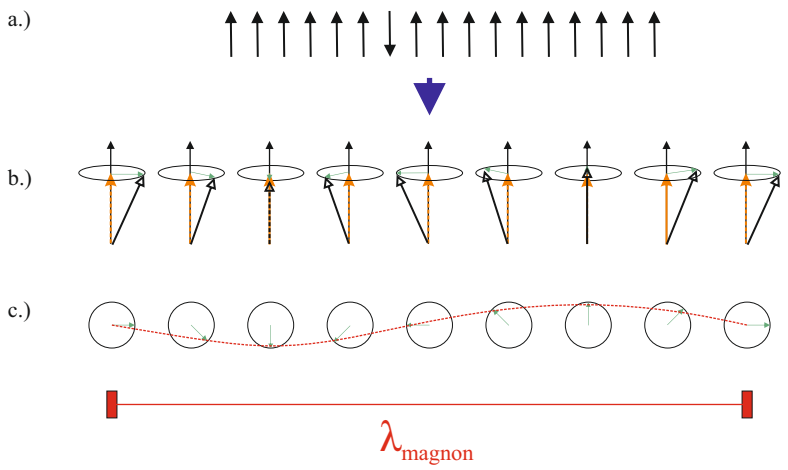

Figure 2.5: Illustration of a spin wave. a.) One dimensional ferromagnetic spin chain with one excited (reversed) spin as the first approach for an fundamental excitation. b.) The energy of flipping one spin is of the order to T_C and not a fundamental excitation of the system. Instead, the excitation is translated into a delocalised, collective excitation over the whole lattice chain. The magnetisation vector is precessing around the axis of saturation magnetisation, where the (phase) angle between adjacent spins differs. c.) Topview, showing the spin wave with wavelength $\lambda_{\mathbf{magnon}}$. Adapted from Ref. [82].

thermal fluctuations can result in the excitation of (thermal) magnons. The number of the magnons at certain temperature T can be expressed as [82]:

$$n_{\text{magnon}} = \left(\frac{k_B T}{\hbar}\right)^{3/2} \int_0^\infty \frac{\sqrt{x}dx}{e^x - 1} \propto T^{3/2}, \tag{2.40}$$

and it directly links Bloch's law in first order for the temperature dependence of the magnetisation to the number of magnons. As it is shown in Figure 2.5 for a one-dimensional chain of exchange coupled spins in a semi-classical picture and the limit for a large spin S, this operator can be described as a vector. In equilibrium, this vector is perfectly aligned along the z-axis, its axis of quantisation. If this vector experiences a small but uniform perturbation in a plane perpendicular to the z-axis, all spins will start to precess around the z-axis with different phases at each lattice site. This illustrates the propagation of the spin wave with wave vector $\mathbf{k}$.

The beforehand mentioned Kittel mode of a uniform precession of all spins in a uniformly excited magnetic specimen, represents a special instance of a spin wave, as it exhibits a wave vector of $\mathbf{k} = 0$.

2.7 Ferromagnetic resonance

The resonant absorption of energy typically in the microwave frequency regime of a magnetic moment of a ferromagnet is called ferromagnetic resonance (FMR) [91]. Nowadays,

FMR is a powerful spectroscopic technique which allows one for probing magnetisation dynamics, spin waves and, here, the CMP. In the following, the uniform precession mode, the Kittel mode and the linewidth in ferromagnetic resonance are further examined.

2.7.1 Effective magnetic field

In an experiment, the effective field $\mathbf{H}_{\text{eff}}$ in Equation (2.13) is a sum of both internal fields $\mathbf{H}_{\text{int}}$, such as demagnetisation fields or contributions from magnetic anisotropies and externally applied fields $\mathbf{H}_{\text{ext}}$, such as a constant field. The term is then expressed as an effective field $\mathbf{H}_{\text{eff}} = \mathbf{H}_{\text{int}} + \mathbf{H}_{\text{ext}}$. Taking into account the dominating contributions, the internal field of an anisotropic ferromagnet in an external field can be expressed as:

$$\mathbf{H}_{\text{int}} = \mathbf{H}_{\text{ex}} + \mathbf{H}_{\text{zeeman}} + \mathbf{H}_{\text{demag}} + \mathbf{H}_{\text{aniso}}, \tag{2.41}$$

where $\mathbf{H}_{ex}$ denotes the exchange field between two neighbouring spins S_i and S_j. The second term in Equation (2.41) refers to the Zeeman interaction of a spin with the external field, $\mathbf{H}_{\text{demag}}$ denotes the demagnetizing field (see below) and $\mathbf{H}_{\text{aniso}}$ refers to the net contribution from magnetocrystalline or shape anisotropy, for example [14, 91].

2.7.2 Kittel formula

In order to find a general expression for the dispersion of the uniform precession mode with zero wavevector, the demagnetising fields have to be considered as well. Demagnetising fields, described by the demagnetisation tensor $\overleftrightarrow{\mathbf{N}}$, lower the impact of an external field acting on the spins. The contribution strongly depends on the shape of the magnetic sample under observation. Adding this contribution to Equation (2.13) and solving the equation for the eigenfrequency ω yields an expression for the maximal absorption of energy by the ferromagnetic specimen at certain eigenfrequency for given field and magnetisation values. The first theory of ferromagnetic resonance was introduced in 1935 by Landau and Lifshitz and measured experimentally for the first time in 1946 by Griffiths *et al.* [109, 110]. The inclusion of a shape dependence was first described by Kittel in 1948 [111]. If one considers an external magnetic field applied along the z-axis, strong enough such that the sample is saturated ($M_0 \equiv M_s$), and the magnetisation vector is parallel to the external field, one obtains the dispersion relation of ferromagnetic resonance for an rotational ellipsoid

$$\omega_{\text{FMR}} = \gamma\sqrt{(H_z + (N_x - N_z)M_s)(H_z + (N_y - N_z)M_s)}. \tag{2.42}$$

Equation (2.42) can be further simplified, if the magnetic specimen is spherical, since then the contribution of the demagnetizing factors is equal in all three spatial directions with $N_x = N_y = N_z = \frac{1}{3}$. This gives the following expression for the Kittel formula [111]:

$$\omega_{\text{FMR}} = \gamma H_z, \tag{2.43}$$

where H_z denotes the effective sum of all external and internal field contributions along this direction.

2.7.3 Linewidth of ferromagnetic resonance

In typical FMR measurements, either the probing microwave frequency is kept constant, and the external static magnetic field is swept in a certain interval around the condition

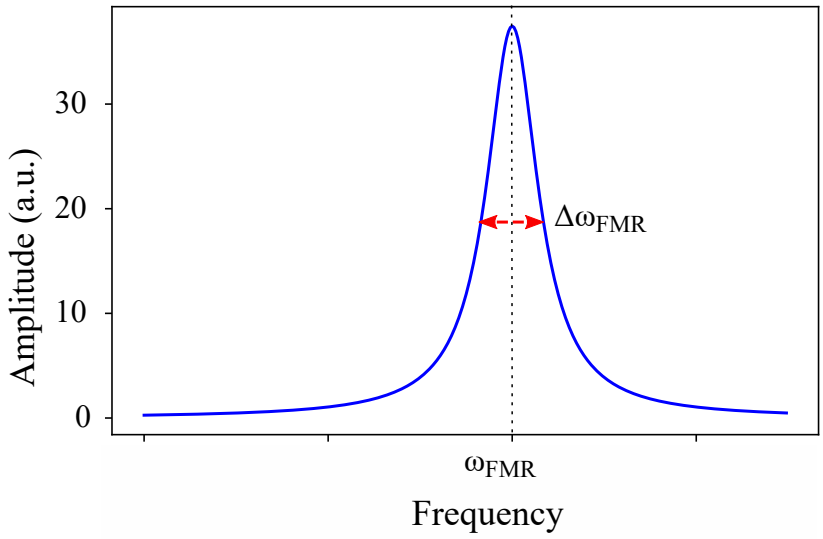

Figure 2.6: Schematical illustration of a typical (Lorentzian) line shape of the absorption amplitude measured in ferromagnetic resonance for the field-swept method. The amplitude is maximal at the resonance frequency ω_{FMR}, where the driving frequency and the natural frequency of the system such as the Kittel mode resonance frequency match. Dissipation processes lead to a broadening of the absorption, resulting in a full width at half maximum (FWHM, dotted red line) and finite absorption amplitude [92].

for resonance absorption or vice versa [112]. These methods are also called "field-swept FMR" or "frequency-swept FMR" [113]. Despite others, the measurement of the absorption of the respective magnetic sample as a function of a field or frequency represents a frequently used method to record ferromagnetic resonance [112, 114]. If the absorption is plotted as a function of the swept parameter, one obtains an absorption profile with resonance field or frequency where the absorption is maximal and a finite linewidth as it is schematically shown in Figure 2.6 for a typical FMR signal. Referring to the amplitude and linewidth, in an ideal system without any damping, the amplitude would diverge at resonance. However, different types of losses can exist. There can be either external losses of the whole system or internal losses such as scattering processes in the sample. As a result, they can lead to small, inhomogeneously distributed local shifts of the resonance frequency throughout the sample. Hence, instead of a single field or frequency value for a resonant absorption amplitude, there is a region of width ΔH (or $\Delta\omega$) where the amplitude is increased. Moreover, the divergence of the absorption amplitude has transformed into a finite but maximal amplitude at the original resonance frequency. Thus, the linewidth of a (ferromagnetic) resonance signal is defined as the full width at half maximum (FWHM) of the recorded line shape [92, 115, 116, 117, 118].
Note, that, in general, the field and the frequency swept methods yield comparable results and can be converted into each other [119, 120]. However, depending on the type of study to be conducted one might be more suited than the other. For instance, if one has to take the magnetic domain structure into account, the frequency-swept method with a fixed magnetic bias field is advantageous because the domain structure is not changed during the sweep. [121].
Thus, the measurement and study of the linewidth and the resonance lineshape allow for obtaining information about the internal processes resulting in damping in the studied

sample. As it has been formulated by the second term in Equation (2.13), where the Gilbert damping parameter α has been introduced, such dissipation processes eventually result in stopping the magnetisation precession if it is not continuously driven. Therefore, the linewidth ($\alpha \propto \frac{1}{\tau_{\text{magnon}}}$) is a measure for the (coherence) lifetime τ_{magnon} of the magnon. In view of the study of key properties such as the coupling strength of the strongly coupled cavity photon-magnon system, the magnon's lifetime is decisive for achieving a coherent exchange of information. Thus, the knowledge about the different contributions and then enhancing the lifetime is of prime importance regarding such hybridised systems and future applications. Depending on the specific properties of the magnetic sample under study and external parameters such as the temperature, different dissipation mechanisms with varying relative strength exist. Then, the total FMR linewidth is comprised of the sum from both intrinsic and extrinsic contributions. For instance, the intrinsic Gilbert damping due to spin-orbit coupling [122], or extrinsic ones such as scattering on sample defects [123, 124]. Accordingly, in the following typical mechanisms leading to a broadening of the FMR absorption are shortly discussed. However, the focus will be on effects related to rare-earth garnets because a bulk YIG sphere is used in all experiments conducted in the course of this thesis.

2.7.4 Precession frequency of Kittel mode

A perturbation from the ground state can occur either internally, from thermal contributions such as spin-lattice scattering processes, or extrinsically by the application of external radio-frequency (rf) fields. Since $[\hat{S}^z, \hat{\mathcal{H}}] = 0$, a spin aligned along the z-axis at equilibrium is only excited by an rf field with a perpendicular component. This sets the experimental condition for the observation of such excitation. For a small perturbation, the spin transforms into $\hat{\mathbf{S}}_j = (\hat{S}_i^x, \hat{S}_i^y, \hat{S}^z)$, where $\hat{S}_j^x, \hat{S}_j^y \ll \hat{S}^z$. By the transformation from a stationary to a rotating frame the circular spin components $\hat{S}^{\pm} = \hat{S}^x \pm i\hat{S}^y$ are introduced for which the following relations exist.

$$[\hat{S}_i^z, \hat{S}_j^{\pm}] = \hbar\delta_{ij}\hat{S}_i^{+}, \tag{2.44a}$$

$$[\hat{S}_i^{+}, \hat{S}_j^{-}] = 2\hbar\delta_{ij}\hat{S}_i^{z}, \tag{2.44b}$$

where one lattice site is considered. By means of the ansatz of complex variables as has been done for deriving Equation (2.19), the solution is:

$$\begin{gathered} S^- = S^-(0)\, e^{i\omega t} \quad \text{and} \quad S^+ = S^+(0)\, e^{i\omega t}, \\ \omega = \gamma H_z, \end{gathered} \tag{2.45}$$

where $\gamma = \frac{g\mu_B}{\hbar}$ is the gyromagnetic ratio. This equation is the frequency of a precessing spin and, since no shape considerations are taken into account for the derivation, it also denotes the resonance frequency for a ferromagnetic resonance (FMR) measurements for a sphere given by Equation (2.43).

2.8 Other spin wave modes: Magnetostatic modes

In general, magnetostatic waves represent a class of spin waves in the presence of bounded media where the exchange interaction is much weaker than the dipolar interaction, and the magnetostatic approximation can be applied [15]. The Kittel mode represents a special instance of a magnetostatic mode with wave vector $\mathbf{k} = 0$.

In order to describe the magnetisation dynamics, the magnetic field is written as the sum of both a static and a dynamic component ($\mathbf{H} = \mathbf{H}_0 + \mathbf{h}_{\mathrm{AC}}$). By substitution of that sum into the Maxwell equations (Equation (2.1)), this set of equations decomposes into two independent subsets, one for the DC and the other for the AC components. The static subset then contains two independent expressions, which are the electrostatic and the magnetostatic equations. They read:

$$\nabla \times \mathbf{H}_0 = \mathbf{J}_0 \qquad \nabla \cdot \mathbf{B}_0 = 0 \tag{2.46}$$

The dynamic components are expressed as:

$$\nabla \times \mathbf{e}_{\mathrm{AC}} + ik_0 \overleftrightarrow{\boldsymbol{\mu}} \mathbf{h}_{\mathrm{AC}} = 0 \qquad \nabla \times \mathbf{h} - ik_0 \overleftrightarrow{\boldsymbol{\epsilon}} \mathbf{e}_{\mathrm{AC}} = \mathbf{j}_{ext}, \tag{2.47}$$

where $\overleftrightarrow{\boldsymbol{\mu}}$ is the permeability and $\overleftrightarrow{\boldsymbol{\epsilon}}$ is the permittivity tensor [15]. In combination with the condition for the wave vector $\mathbf{k}, \mathrm{k}_z \ll \mathrm{k}_0 = \frac{\omega}{c}$, these equations set the conditions for the magnetostatic limit of the spectrum. The spectrum of the magnetisation oscillations can be divided into two parts. For high values of the wave vector $\mathbf{k}$, the short ranged exchange interaction, and in the limit for zero wave vector, long-range non-exchange (dipolar) interaction dominates, respectively. Spin waves and their associated quasiparticles belong to the former, the class of non-exchange spin waves and non-uniform magnetostatic modes is related to the latter [125, 126]. In this context, the Kittel mode represents a special instance of a magnetostatic mode.

2.8.1 Non-exchange (dipolar) spin waves

The wave vector interval, where non-exchange spin waves exist, is set by Maxwell's equations and the point where exchange interaction can no longer be neglected. It reads as

$$\mathrm{k}_{\mathrm{min}} = \mathrm{k}_0 \sqrt{\frac{4\pi M_s}{\Delta H}} < \mathrm{k} < \mathrm{k}_{\mathrm{max}} = \sqrt{\frac{\Delta H}{D}}, \tag{2.48}$$

where ΔH is the the linewidth of the resonance signal and D the nonuniform exchange constant. For YIG, $\mathrm{k}_{\mathrm{max}} \simeq 6 \cdot 10^3$ in an interval for $\mathrm{k} = 10^2$ to 10^4, the above magnetostatic approximations can be applied to calcuate the dispersion of the respective modes [15]. Depending on the relative orientation of the propagation direction (wave vector) and the saturation magnetisation, non-exchange spin waves can be either classified as volume modes or surface modes [23, 127]. As the names indicate, volume modes are propagating in the sample's volume and surface modes along the surface. The latter decay exponentially into the sample's volume. Figure 2.7 gives an overview of the different types of nonexchange modes including the functional dependence of the dispersion relation.

2.8.2 Nonuniform magnetostatic oscillations (in a sphere)

Since the mode with the strongest and most uniform magnetisation dynamics would be preferred for future applications, the temperature dependence of coupling strength of the

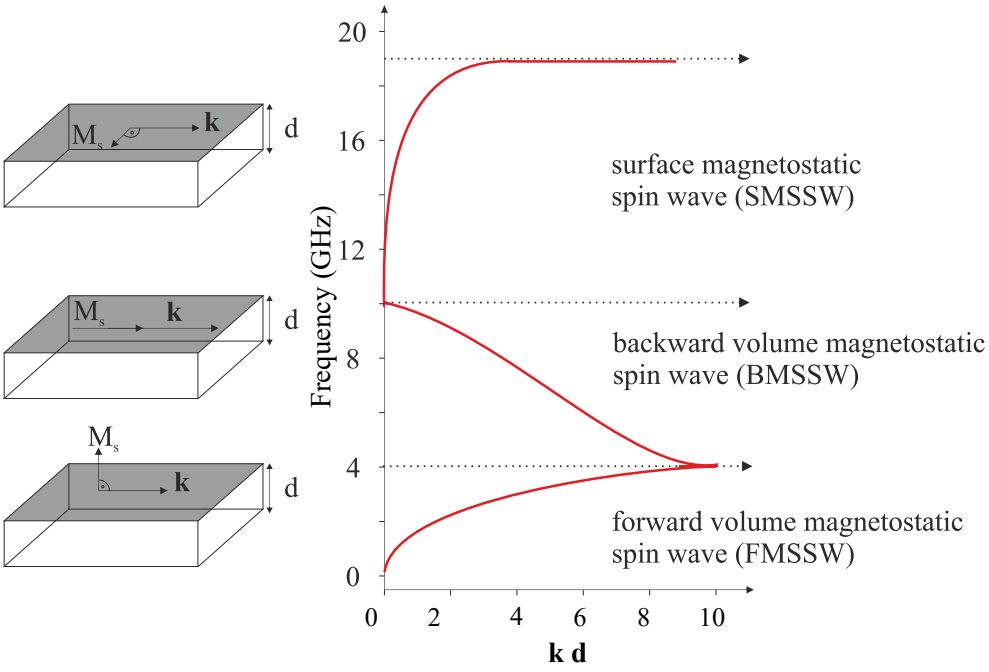

Figure 2.7: Overview over the main types of non-exchange dipolar spin waves. The specific type depends on the orientation between the wave vector **k** and the magnetisation M and results in different dispersions of these modes. Adapted from Ref. [128].

uniform magnetisation precession of the hybridised system is studied. As mentioned earlier, non-uniform magnetostatic modes also exist. Further, the existence of degenerate spin wave modes originates from the shape dependence of the dispersion (c.f. Equation (2.42)). The solutions for the eigenfrequencies of these modes are extensively studied by Walker *et al.* and Fletcher and Bell [125, 129]. The characteristic equation for a sphere can be written in terms of the associated Legendre function of the first kind with the associated Legendre polynomials $P_n^{m'}$, P_n^m as [126]:

$$n + 1 + \xi_0 \frac{P_n^{m'}(\xi_0)}{P_n^m(\xi_0)} \pm mv = 0, \tag{2.49}$$

where $\xi_0^2 = 1 + \frac{1}{\kappa}$ and $\kappa = \frac{\Omega_H}{\Omega_H^2 - \Omega^2}$, $v = \frac{\Omega}{\Omega_H^2 - \Omega^2}$ with $\Omega_H = \frac{H_0 - \frac{1}{3}4\pi M_s}{M_s}$ and $\Omega = \frac{\nu}{\gamma 4\pi M_s}$ in the form of the original papers. The eigenfrequencies do not depend on the radius of the sphere. Correspondingly, such magnetostatic modes are labelled as (n,m,r) modes, where $n \in \mathbb{N}$, $m = 0, \pm1, \pm2, ..., \pm n$, and r denotes the number of existing roots in the equations. Historically, for $m \leq 0$ it is r, and for $m > 0$ it is modified to $r+1$ [15]. In this context, the Kittel mode refers to the (1,1,0) mode. Lists of the different combinations of n, m, and r, and graphical illustrations for different spatial distributions of the nonuniform magnetostatic modes may be found in Ref. [126].

2.9 Relaxation of magnons

At equilibrium, the system is in its energetically most favourable state and configuration. Since in nature the state of lowest energy is the preferred one, an excited system will eventually relax back to equilibrium. If the excitation is continuously driven, the losses

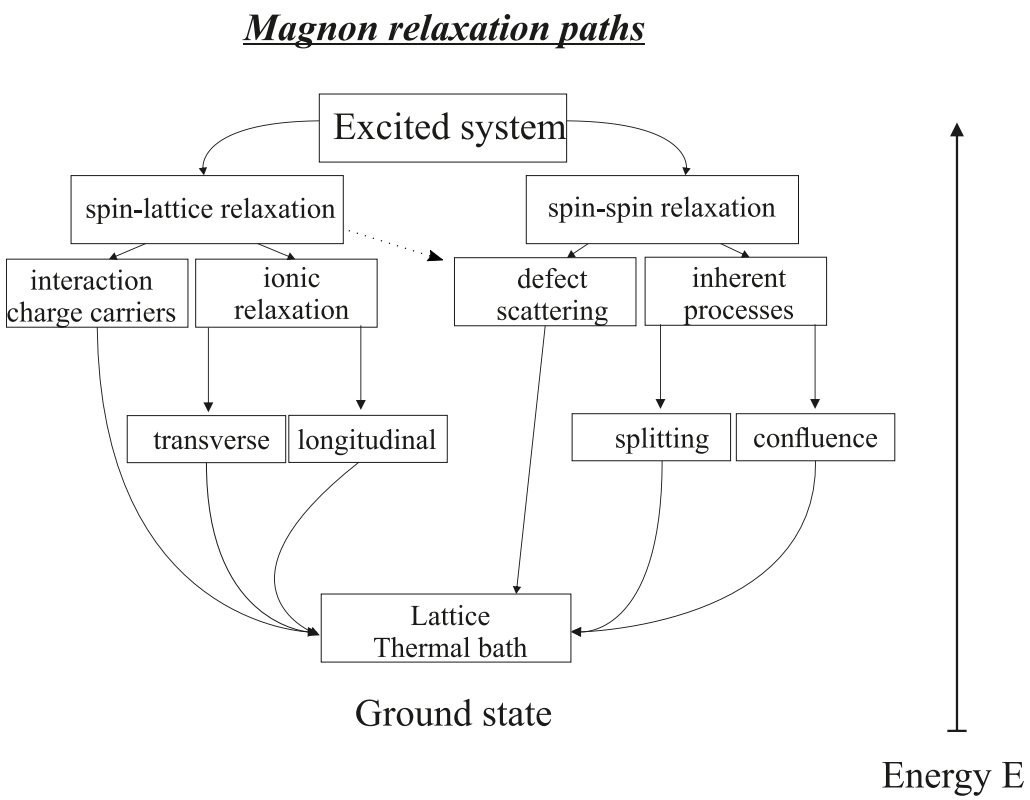

Figure 2.8: Block diagram showing different channels for magnon relaxation in an excited magnetic system coupled to the lattice. The specific relaxation path depends on the properties of the specific magnon state and material characteristics. Please note, that here spin-lattice relaxation refers to processes which result in an energy transfer from the spin to the lattice. Here, for instance, the defect scattering refers to the scattering of magnons with non-ideal crystals which contain impurity spins [15, 14]. However, general scattering due to lattice defects can result in defect induced spin-orbit coupling (as indicated by the dotted arrow).

due to energy dissipation into one or more relaxation channels will result in the observation of finite linewidths.
A magnon represents the quasiparticle associated with one excited spin which is translated in a delocalised collective excitation of the magnetic system (c.f. Figure 2.5). The single spin is coupled to other spins by interactions such as exchange coupling or dipolar interaction [15, 83]. Furthermore, individual spins and the whole magnetic system are not isolated from the environment. Rather, they can be coupled to the lattice or charge carriers which leads to different relaxation channels back to thermal equilibrium [14, 92]. To this end, the energy will relax back to the lattice either directly or indirectly. For instance, it may result in additional heating of the material by the energy transfer to the phonons. Whilst a direct energy transfer to the lattice denotes a group of different spin-lattice relaxation processes, the indirect relaxation by scattering to other spins refer to spin-spin relaxation processes [15]. Each of them is comprised of various types of relaxation as it is depicted in Figure 2.8. Instead of a sharp, δ-function resulting in a very sharp peak at one frequency in (ferro) magnetic resonance experiments, the signal is recorded with a finite linewidth. In the following, processes relevant in the explanation of the experimental findings will be introduced.

2.9.1 Spin-lattice relaxation processes

The relaxation of the excitation of the spins by a direct coupling to the (crystal) lattice, i.e. spin-orbit coupling, results in spin-lattice relaxation processes. In a crystal, the emergence of an inhomogeneous electrical field due to, for instance, unfilled 3d-electron shells in transition metals, results in another field, which is called the crystal field. The interaction of a (magnetic) ion with the crystal field lifts the degeneracy of the orbital terms via the Stark effect. If the contribution from the crystal field is stronger than the spin-orbit coupling, the orbital angular momentum number $\mathbf{L}$ is decoupled from $\mathbf{S}$, the total spin $\mathbf{J} = \mathbf{L} + \mathbf{S}$ no longer is a "good" quantum number, and the orbital angular momentum is quenched. As a result, the crystal field leads to a preferred direction of the orbital angular momentum and via the spin-orbit coupling to a preferred direction of the spin along a specific crystallographic axis. Therefore, the spin-orbit coupling leads to magnetocrystalline anisotropy. A crystal possesses a hard and easy magnetisation axis along which the magnetisation is harder or easier to obtain in the presence of an external magnetic field. Therefore, when a ferro- (ferri-) magnetic sample is placed in a magnetic field, apart from smaller contributions, the lattice ions are subjected to the exchange field, the crystal field and spin-orbit coupling. In view of their strong contribution to spin-lattice relaxation processes, the focus is on 3d and 4f ions with a strong spin-orbit coupling. The latter mostly emerge as impurities in the starting materials (see below). This way, ions in the S (l=0) states or ions with a quenched orbital angular momentum are excluded in the following [92]. The presence of the magnetic field lifts the $(2\mathbf{S}+1)(2\mathbf{L}+1)$ degeneracy of the ions' energy levels. Thus, the levels split further through the crystal field, exchange and spin-orbit interaction where the exact order depends on the relative strength of the interactions [15, 83, 85]. In this regard, the crystal field dominates for 3d-electrons because of their empty, outer electron shells which are not shielded as in the case of 4f ions [82, 92]. A splitting by exchange interaction takes place, and the resulting degenerate doublet is split by the spin-orbit interaction. Note that as a result, for 3d-electrons, $\mathbf{S}$ is a good quantum number because of the "quenching" of the orbital angular momentum L which lifts the $(2\mathbf{L}+1)$-degeneracy and where J=S. However, for 4f ions, $\mathbf{S}$ is not a good quantum number any more because the spin-orbit interaction is stronger than the crystal field's contribution. Instead, the quantum number $\mathbf{J} = \mathbf{L} + \mathbf{S}$ is utilised and spin-orbit interaction is the strongest one [92, 130]. Ions, which exhibit such strong spin-orbit coupling, mostly arise as rare earth (4f) impurities intermixing with the lattice during the growth process of the crystals [15]. As a result, the spin-lattice relaxation due to a coupling of the magnonic system with impurity ions with strong spin-orbit coupling can yield a significant contribution to the total linewidth in ferromagnetic resonance. The effect of ionic relaxation processes could be observed in low-temperature maxima of single YIG crystals [131, 132]. It was later explained by so-called "slow-relaxing impurities" and is discussed in the following [133, 134, 135].

Contribution to anisotropy in ferromagnetic resonance

The presence of anisotropy also influences the ferromagnetic resonance line shape and, hence, contributes to the linewidth. As it is out of the scope for the following discussion, for more detailed information on magnetic anisotropy and its implications, the reader may refer to Ref. [91] and references therein. Concerning the FMR linewidth, as previously mentioned, (impurity) ions with a strong spin-orbit coupling yield an angle dependent contribution to the total linewidth in FMR which denotes the sum of all possible con-

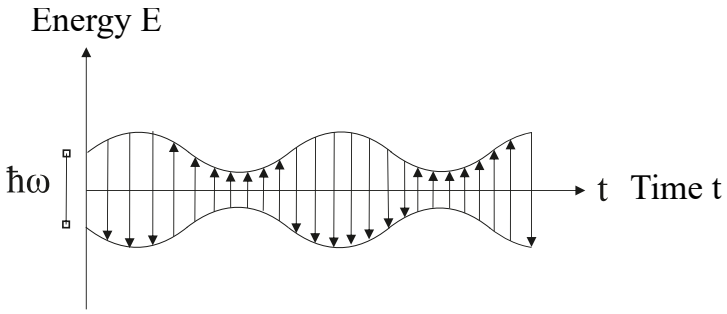

Figure 2.9: Modulation of the splitting, i.e. transition frequency ω of a two-level impurity ion in the presence of a magnetisation oscillation (such as a magnon). The finite impurity relaxation time results in retardation, which leads to energy transfer from the magnon to the crystal lattice via the impurity ion (Adapted from Ref. [15])

tributions. This leads to strong peaks at certain angles, where the exchange and crystal energy splittings are in the same order of the ion energy levels and so-called "near crossings" occur. [15, 131, 136].

Slow-relaxing impurities

Immediate, direct transitions of an excited ion to a lower energy level are fast relaxation processes and belong to the class of transverse relaxation mechanisms [15, 14]. Concerning rare earth garnets with impurity ions, it was first proposed by Kittel that the system can be divided into a magnetic and an ionic sublattice, with energy splitting ΔE [136]. For the description of this splitting, the two lowest ion energy levels are taken into account and represented as magnetically active, half-integer spin ($\frac{1}{2}$) states. The size of this splitting is temperature dependent, and the ferromagnetic resonance linewidth displays a maximum when the relaxation frequency is equal to the transition frequency, i.e. $\omega_{\text{ion}} = \frac{1}{\tau_{\text{ion}}} \equiv \Delta E$. Please note, that this sublattice representation of the ionic system is restricted to low temperatures and ions at dodecahedral lattice sites [136]. In this regard, a fast relaxation mechanism is unable to explain a peak of the ferromagnetic resonance linewidth at specific temperatures for reasonable values for the decay time τ_{ion} [135, 137].
Instead, a slow (longitudinal) relaxation mechanism is utilised to model the temperature behaviour of line broadening by rare earth impurities. A relaxation is called "slow" if the temporary variation of the magnetisation M is much smaller than the frequency equivalent to the splitting of the lowest ionic energy levels. The magnetisation change does not induce direct transitions, but it is still large enough to influence the energy splitting [138]. Therefore, as illustrated in Figure 2.9, the spacing of the levels is subjected to a time-dependent modulation by the variation in M. The splitting is modulated with a frequency ω which changes the thermal equilibrium population of each level. If this frequency matches the impurity relaxation frequency (inverse time), a transition between the levels takes place. Due to the finiteness of the relaxation time, this results in retardation leading to an energy transfer from the excited magnetic system, i.e. the magnons to the ion. In turn, the ion transfers energy to the lattice due to the strong spin-orbit coupling, and

the magnetisation oscillation relaxes back to thermal equilibrium. (c.f. Figure 2.8). This energy loss gives rise to a strong peak in the ferromagnetic resonance linewidth of the sample under study if the modulation frequency corresponds to the excitation frequency due to an external time-harmonic magnetic field. The relaxation time increases at lower temperatures. Therefore, for samples such as YIG, the contribution due to slow relaxing rare earth impurities plays an essential role in the temperature dependent evolution of the resonance linewidth. The temperature at which the peak occurs depends on the impurity relaxation time of the specific rare earth impurity ion. In the case of multiple different impurities, the resulting linewidth spectrum can show various peaks. The relative height of the peaks depends on the contributions from the respective impurity ion. A calculation based on rate quations for the populations of a modulated two-level (impurity) ionic system yields the following expression for the linewidth contribution ΔH_{sr}, where sr refers to the slow relaxing impurities [14]:

$$\Delta H_{\mathrm{sr}} \approx \frac{4 c_{\mathrm{imp}} S}{\hbar \gamma} \frac{(z_{\mathrm{imp}} B)^2}{k_B T} \frac{e^{\frac{\hbar\omega}{k_B T}}}{[e^{\frac{\hbar\omega}{k_B T}} + 1]^2} \frac{\omega_0 \Gamma_{||}}{\Gamma_{||}^2 + \omega_0^2}, \tag{2.50}$$

where c_{imp} denotes the impurity concentration, z_{imp} the average number of magnetic neighbours for a single impurity, ω the frequency of the ionic level splitting, S the value of the hosting spin, and $\Gamma_{||} = c_{||} T^2$ the longitudinal spin-lattice relaxation rate.

2.9.2 Spin-spin relaxation processes

Apart from Spin-Lattice relaxation processes, the spins can relaxate by scattering processes involving one or more spins. As illustrated in Figure 2.8, they can be divided into two groups. For instance, defect scattering emerges due to the presence of impurity spins. Inherent scattering processes refer to either splitting or confluence processes of the magnons. Thus, in the following, these processes are described.

Inherent scattering processes

- **Three-magnon scattering**
  The elementary processes in a three-magnon relaxation process are either confluence or splitting of magnons with different wave vectors $\mathbf{k}_1, \mathbf{k}_2$, and $\mathbf{k}_3$, where $\mathbf{k}_1$ denotes the decaying magnon under consideration. The magnetisation vector component M_z commutes with the Heisenberg exchange Hamiltonian and as such is a conserved quantity in the scattering process. Therefore, three-magnon relaxation processes cannot be caused by the exchange interaction between two neighbouring spins. Instead, the much weaker dipole-dipole interaction is responsible for such three-magnon processes. Due to its weakness compared to the exchange interaction, typically four-magnon processes, where M_z is conserved, contribute more to the total measured linewidth. However, in general, interactions with the lowest number of involved magnons are more probable. In the high temperature approximation $k_B T \gg \hbar\omega_1, \hbar\omega_2, \hbar\omega_3$ ([15]), and the linewidth contribution from splitting

via a three-magnon scattering processes reads as [15, 14]:

$$\left(\frac{2\Delta\omega_{r1}}{\gamma}\right)_{\text{3m:splitting}} = \frac{1}{4}\gamma^2 k_B T \omega_1 M_s \int_{k_2}\int_{\Theta_2=0}^{\pi}\int_{\phi_2=0}^{2\pi} \frac{|\sin(2\Theta_2)e^{-i\phi_2} + \sin(2\Theta_3)e^{-i\phi_3}|^2}{\omega_2(\omega_1-\omega_2)}$$

$$\times\, \delta(\omega_1-\omega_2-\omega_3)k_2^2\sin(\Theta_2)dk_2 d\Theta_2 d\phi_2,$$

where, $\Theta_2(\Theta_3)$ and $\phi_2(\phi_3)$ are the angles of the wave vector $\mathbf{k}_2(\mathbf{k}_3)$ and $\omega_{[1,2,3]}$ denotes the resonance frequencies of the respective magnons taking part in the scattering process. The contribution from confluence is:

$$\left(\frac{2\Delta\omega_{r1}}{\gamma}\right)_{\text{3m:confluence}} = \frac{\pi\gamma M_s k_B T k_1}{2D\omega_1}, \tag{2.51}$$

where $D = \frac{\eta}{\gamma}$ with the non-uniform exchange constant η [14, 15].

Three-magnon scattering processes do not conserve the length of the magnetisation vector along the externally applied static field at equilibrium. As a result, in a strict sense, the LLG equation in its linearised form is no longer valid. Nevertheless, for small amplitudes and small dissipation, it still represents a good approximation [15].

- **Four-magnon scattering**
  Depending on the material and the wave vector $\mathbf{k}$ of the corresponding magnon, four-magnon scattering processes can contribute both in the description the relaxation of primary and secondary magnons. Omitting dipole-dipole interactions, the contribution to the linewidth from four-magnon scattering can be expressed as [123, 139]

$$\Delta H_{\text{4m:scattering}} = \frac{1}{48\pi}\frac{\omega_1}{\gamma^2}\left(\frac{k_1 k_B T}{M_s D}\right)^2 F, \tag{2.52}$$

  where F is a factor depending on the frequency ω_1, k_1 the magnitude of wavevector k_1 and temperature T.

Scattering from defects: Two-magnon processes

Experiments with YIG samples of different surface quality and chemical purity yield linewidths of several MHz [140, 141]. Thus, in addition to linewidths due to inherent relaxation processes in the order of 1 MHz for YIG at room temperature, non-uniformities of either crystallographic, structural or geometrical origin contribute greatly to the line shape [117, 124, 142]. The first contribution includes polycrystalline samples with multiple, differently aligned crystal axes and imperfect single crystals, the second refers to inhomogeneous ion distributions over the crystal lattice, and the third is related to imperfections such as pores or rough surfaces [92]. The degree of such disorder may vary over the sample, slightly changing the conditions for resonance. Instead of measuring a sharp resonance frequency, a group of resonance frequencies close to each other is recorded and leads to the broadening of the line shape at resonance. These inhomogeneities lead to two-magnon scattering processes where one magnon with a specific eigenmode becomes coupled to another one due to these local distortions. Thus, one magnon with wave vector $\mathbf{k}_1$ is annihilated, and a new one with wave vector $\mathbf{k}_2$ is created. Due to the

presence of defects, the momentum is not a conserved quantity and then the momentum $\hbar\mathbf{k}_p = \hbar(\mathbf{k}_1 - \mathbf{k}_2)$ is directly transferred to the lattice. The general expression for the contribution to the linewidth is [15, 14]:

$$\Delta H_k = \frac{\gamma}{(2\pi)^2}\frac{V}{N}\int_{\mathbf{k}_2} H_{k_p}\delta(\omega_1 - \omega_2)k_2^2 \sin\Theta_2 dk_2 d\Theta_2 d\phi_2, \tag{2.53}$$

where V referes to the volume, N to the number of spins, H_{k_p} to the k^{pth} harmonic of the effective magnetic field, and Θ the angle between the degenerate spin waves with $\mathbf{k}_1$ and $\mathbf{k}_2$. There are two limiting cases which can be derived from this formula. First, for the case that the harmonics of the effective magnetic field can be described by the root-mean square effective field of non-uniformities ($\Delta H_k = \frac{\gamma}{\pi}a^3 H_p^2 \int_0^{\Theta_{\max}} \left(\frac{\partial\omega}{\partial k}\right)_{k=k_{d(\Theta)}} k_d^2 \sin(\Theta) d\Theta$). The resulting line shape is then broadened by the non-uniformities and "exchange narrowing" occurs due to the increasing strength of the exchange interaction for large wave vectors k. On the contrary, for small k magnitudes, the second case of large scale non-uniformities is present. For small k values, interactions of dipolar origin dominate, and the resonance lineshape is again broadened by the non-uniformities and undergoes now "dipole narrowing".

- **Polycrystalline broadening**
  In the independent grain model, a polycrystalline sample can be described as a set of independent, irregularly shaped small single crystals [143]. The space between such grains is modelled by spherical cavities in a theory from Sparks, Loudon, and Kittel (SLK model) and are commonly called pores [115]. In that framework the contribution to the linewidth was found:

  $$(\Delta H)_p = \frac{4\pi}{9}\frac{V_p}{V_0} 4\pi M_s \frac{3\cos^2(\Theta_{d0} - 1)^2}{\cos\Theta_{d0}}, \tag{2.54}$$

  where V_p denotes the volume of a single pore, V_0 the sample's volume, and $\Theta_{d0} = \arccos(\sqrt{N_z/4\pi})$, the polar angle of the degenerate spin waves with wave vectors k_1 and k_2.

- **Single crystal: Surface roughness**
  For single crystals, the linewidth due to two-magnon scattering processes is dominated by the contribution from surface roughness. According to the SLK model, the whole surface is covered with semi-spherical surface pits (c.f. Figure 2.10 a.)). Similarly to the previous expression, the line broadening due to a rough surface can be calculated via:

  $$(\Delta H)_{\mathrm{sp}} = \frac{\pi}{9}\frac{R_s}{R_0} 4\pi M_s \frac{3\cos^2(\Theta_{d0} - 1)^2}{\cos\Theta_{d0}}, \tag{2.55}$$

  where R_0 is the sample's radius and R_s the radius of surface pits.

2.9.3 Scattering processes for Kittel mode magnons ($\mathbf{k} = 0$)

The spectroscopic measurements studied in this thesis focus on the resonant coupling of a Kittel mode magnon to a standing wave mode photon of a cavity resonator. Therefore, the relaxation processes from Section 2.9.2 are discussed in the limit for $\mathbf{k}_1 \to 0$. If the

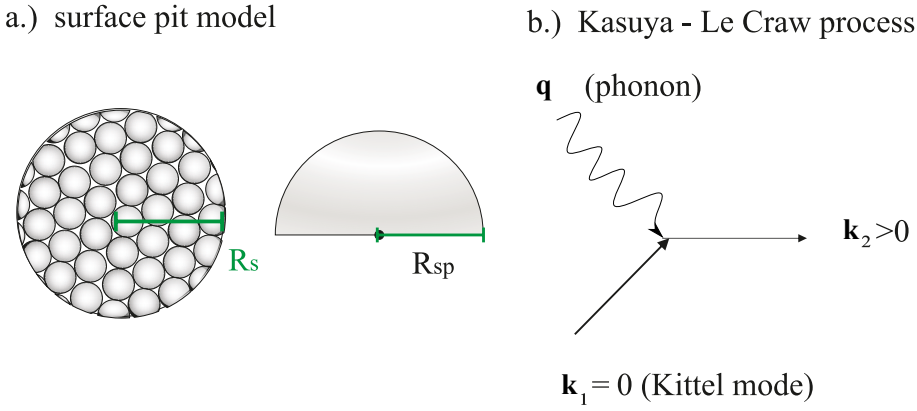

Figure 2.10: a.) Illustration of the surface pit model for the description of the line broadening due to rough sample surfaces. There, the whole surface of a sphere with radius R_s is covered by semispherical pits with radius R_{sp} [115]. b.) Schematic diagram for the relaxation of the uniform precession ($\mathbf{k} = 0$, Kittel) mode by means of magnon-phonon confluence. This is the so-called Kasuya-Le Craw process and explains the non-vanishing linewidth contribution in the limit for $\mathbf{k}_1 \to 0$ beyond low frequencies and temperatures [116].

effective field for the mode with $\mathbf{k} = 0$ is the root-mean square effective field of all non-uniformities H_p (chaotic non-uniformities), then one can write for the linewidth for an ellipsoid of revolution [15]:

$$\Delta H_0 = H_p \zeta_{\mathrm{ex}}, \quad \zeta_{\mathrm{ex}} \propto \frac{H_p}{H_{\mathrm{ex}}}, \tag{2.56}$$

where ζ_{ex} is the exchange coefficient and H_{ex} the exchange field. Correspondingly, for large scale non-uniformities, with $k_l \ll k_{\mathrm{max}}$, where l denotes a characteristic length scale of the non-uniformity,

$$\Delta H_0 = H_p \zeta_d, \tag{2.57}$$

where ζ_d denotes the coefficient for dipole narrowing. In this expression, the exchange interaction is neglected because the considered magnitudes are in the limit for low $\mathbf{k}$. When the exchange interaction is also taken into account, the singularity of ΔH_0 at the upper limit of the non-exchange spectrum ($\omega_0 = \frac{2\omega_M}{3}$) is replaced by a finite linewidth. The contributions from two-magnon scattering processes due to defects cannot explain the observed linewidths. In order to explain the linewidths of the Kittel mode, there must be a magnon relaxation process which does not vanish in this wave vector limit and is at frequencies below the exchange spin wave boundary. Three-magnon splitting only contributes at really low frequencies ($\omega < 2\omega_m/3$, where $\omega_m \equiv \gamma M_s$) whilst for higher frequencies the relaxation of the uniform precession mode was explained by a particular form of magnon confluence [15, 116]. For a ferrimagnet, such as YIG, magnon relaxation by confluence is possible, if the wave vectors $\mathbf{k}_2$ and $\mathbf{k}_3$ belong to a higher order, an exchange dominated spin wave branch. Known as the Kasuya-Le Craw process, the confluence of the magnon with small value of wave vector $\mathbf{k}$ with a phonon of an upper optical branch, results in the annihilation of the magnon with a low magnitude of the wave vector $\mathbf{k}$ and creates another magnon with a higher value of $\mathbf{k}$ (c.f. Figure 2.10 b.)).

2.10 Microwave theory

The previous discussion covered the "magnetic part" of the CMP. Therefore, in the following, an overview of the required microwave theory and the measurement parameter for the description of the "cavity part" of the CMP is given.

2.10.1 Wave equation

For an isotropic, linear and source free homogeneous medium, the wave equation for the propagation of an electromagnetic wave can be directly found as a solution from Maxwell's equations [99]. The application of a curl on both sides on Faraday's law (c.f. Equation (2.1)), utilising Gauss law, rewriting the left side of Amperes law, and equating both sides yields for an isolator:

$$\nabla^2 \mathbf{E} = \frac{1}{v_{\mathrm{ph}}^2} \frac{\partial^2 \mathbf{E}}{\partial t^2}, \tag{2.58}$$

where $v_{\mathrm{ph}} = \frac{\omega(\mathbf{k})}{k}$ is the phase velocity with the wave number $k = \frac{2\pi}{\lambda}$, where λ denotes the wavelength in the medium [79]. This equation, also known as the Helmholtz equation, links the time evolution of the electric field as being a vector quantity to the propagation of a wave with phase velocity v_{ph}, corresponding to the speed of light in a vacuum. Analogously, the equation for the magnetic induction $\mathbf{B}$ is:

$$\nabla^2 \mathbf{B} = \frac{1}{v_{\mathrm{ph}}^2} \frac{\partial^2 \mathbf{B}}{\partial t^2}. \tag{2.59}$$

The general solution for a plane wave can be written as a superposition of two waves, one travelling in a positive, the other one in a negative direction in space. The relative contribution of both components depends on the nature of the source and the boundary conditions which have to be applied. For instance, for a plane wave which propagates in a positive direction in space, the time evolution of the electric field can be found to be [99]:

$$\mathcal{E}(\mathbf{r}, t) = \mathbf{E}_0 \cdot \cos(\mathbf{k} \cdot \mathbf{r} - \omega t). \tag{2.60}$$

In general, an electromagnetic wave exhibits four characteristic properties [80]:

1. Both, the electric and the magnetic field components are directed transversely to the propagation direction of the electromagnetic wave

2. The electric and magnetic field components are aligned perpendicularly to each other.

3. The electric field is proportional to the magnetic induction or magnetic flux $\mathbf{B}$. ($\mathbf{E} = c\mathbf{B}$)

4. In a vacuum, the velocity of the wave corresponds to the speed of light, denoted by c. It can be expressed as the inverse square root product of the vacuum permittivity ϵ_0 and the permeability μ_0

$$c = \frac{1}{\sqrt{\epsilon_0 \mu_0}}. \tag{2.61}$$

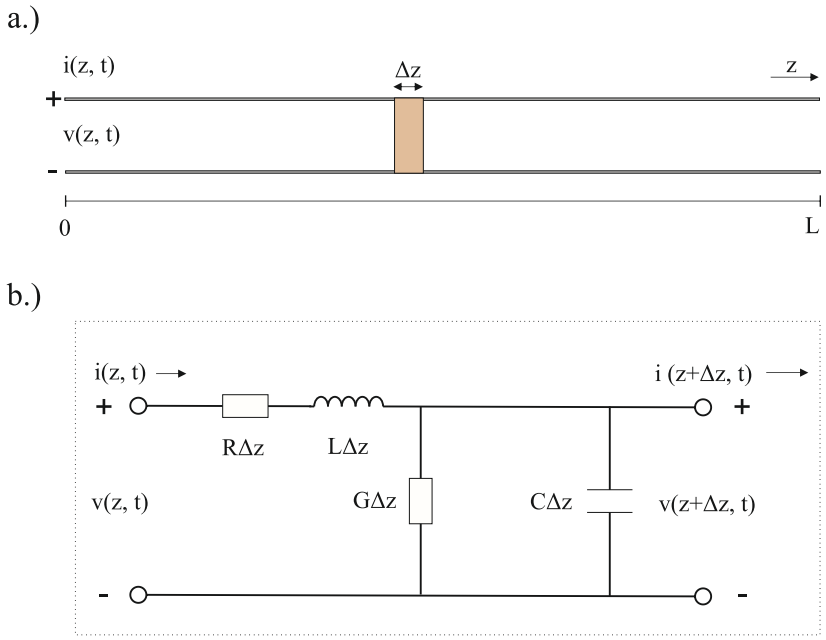

Figure 2.11: a.) Representation of a typical transmission line of length L by two conducting lines which are parallelly aligned. b.) The corresponding lumped element model representation for a small piece of length Δz. There, R and L are the series resistance and inductance, G and C shunt conductance and capacitance per unit length, respectively.

2.11 Transmission line

Typically, the frequency of ferromagnetic resonance is in the GHz-frequency range. Therefore, the cavity resonator or stripline or co-planar waveguide based approaches to measure the magnetic properties of a magnetic sample are employed in the microwave frequency range, as well [144]. Microwaves correspond to frequencies between $3 - 300\,\mathrm{GHz}$ and belong to the radio frequency (RF) regime which refers to AC signals in the range from $0.1 - 10^3\,\mathrm{GHz}$ [99]. The piece of signal line which conducts the microwave frequency signal is called the transmission line representing a distributed circuit element [145].
In the low-frequency range, the dimension of electrical circuits is typically much smaller than the wavelength. Thus, propagation effects such as losses along the transmission line or changes of the voltages and currents are negligibly small, and circuit theory and lumped element theory can be applied. However, when the dimensions of circuits are comparable to the wavelength or above, the effect of propagation along the circuit's transmission line has to be considered. Transmission line theory has to be utilised for the description, design, high fidelity usage of transmission lines in general, and specifically structures such as waveguides or cavity resonators in the microwave regime. Due to propagation effects, the voltages and currents may vary in both magnitude and phase along the transmission line. Therefore, the transmission line cannot be described by lumped elements, where both the magnitude and phase of voltages and currents do not vary over the circuit's dimension.

However, a transmission line element of length z can be divided into small pieces with infinitesimal distance Δz, and modelled by a successive combination of separate inductive, capacitative and resistive elements, if losses are included in the calculation. For a

transverse electromagnetic wave propagation which exhibits all the characteristics from Section 2.10.1 (TEM wave), there are at least two conductors modelling the transmission line. Thus, Figure 2.11 shows the typical representation of a transmission line by two parallelly aligned wires. By separating the transmission line into small pieces where the voltages and current spatial gradients are approximately zero over this infinitesmally small distance, each piece can be represented by means of lumped elements [99].

In the limit for $\Delta z \to 0$, the telegrapher's equations for the voltages and the currents can be derived under the application of Kirchhoff's laws. The expression for the voltages and currents is

$$\frac{\partial v(z,t)}{\partial z} = -Ri(z,t) - L\frac{\partial i(z,t)}{\partial t}, \tag{2.62a}$$

$$\frac{\partial i(z,t)}{\partial z} = -Gv(z,t) - C\frac{\partial v(z,t)}{\partial t}, \tag{2.62b}$$

where R denotes the series resistance, L the series inductance, G the shunt conductance and C the shunt capacitance of the transmission line per unit length. Solving the above equations by the ansatz of complex variables and the superposition principle for a linear system yields two wave equations for the voltages and currents,

$$\frac{\partial^2 V(z)}{\partial z^2} = \gamma^2 V(z), \tag{2.63a}$$

$$\frac{\partial^2 I(z)}{\partial z^2} = \gamma^2 I(z), \tag{2.63b}$$

where $\gamma = \alpha + i\beta = \sqrt{(R + i\omega L)(G + i\omega C)}$ is the complex propagation, α the attenuation, and β the phase constant. Once more, the solution of a travelling wave solution is the superposition of two wave packets propagating either in positive ($V_0^+ e^{-\gamma z}$) or negative direction ($V_0^- e^{+\gamma z}$). For instance, solving for the current $I(z)$ gives

$$I(z) = \frac{V_0^+}{Z_0} e^{-\gamma z} - \frac{V_0^-}{Z_0} e^{+\gamma z}, \tag{2.64}$$

where $\frac{1}{Z_0} = \frac{\gamma}{R+i\omega L} = \sqrt{\frac{G+i\omega C}{R+i\omega L}}$ denotes the inverse complex impedance of the transmission line per unit length. If the losses of the transmission line are really small and can be neglected in the calculation, the complex impedance simplifies to a purely real quantity $Z_0 = \sqrt{\frac{L}{C}}$ ($R = G = 0$, hence $\alpha = 0$). The equations for the voltage V and the current I are [99]

$$V(z) = V_0^+ e^{-i\beta z} + V_0^- e^{i\beta z}, \tag{2.65a}$$

and (2.65b)

$$I(z) = \frac{V_0^+}{Z_0} e^{-i\beta z} - \frac{V_0^-}{Z_0} e^{+i\beta z}, \tag{2.65c}$$

where $\beta = \omega\sqrt{LC}$ is the phase constant. The complex impedance in the presence of losses plays an important role in the design and characterisation of AC circuits. It is the frequency dependent, AC equivalent of the ohmic resistance $R = \frac{U}{I}$ in DC circuits. Nowadays, the industrial standard for radio frequency (RF) transmission lines is $Z_0 = 50\,\Omega$ and $Z_0 = 75\,\Omega$ in some areas of telecommunications. These values are mostly due to historical reasons and represent a good compromise between low attenuation values and usable power at different impedance values [146].

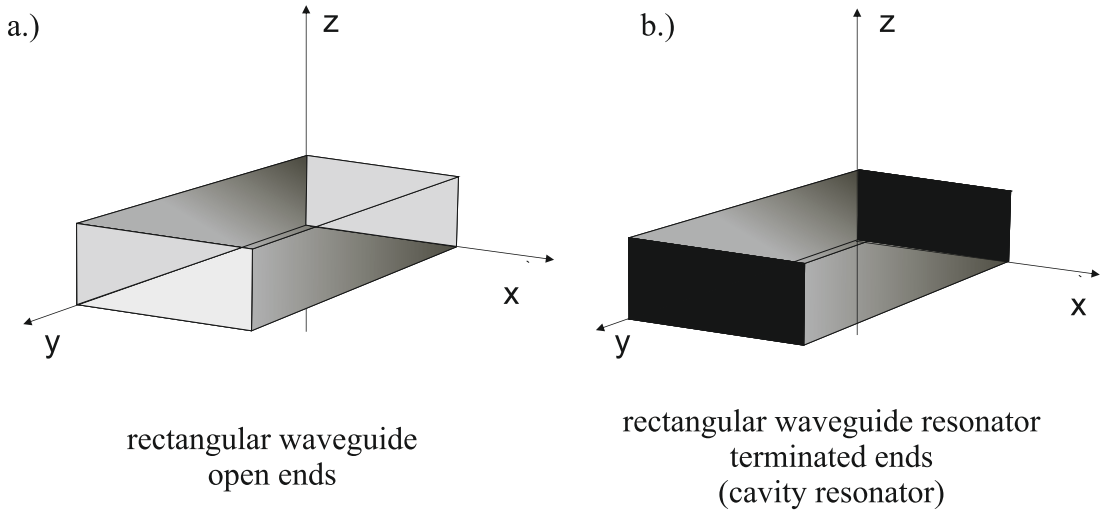

Figure 2.12: Difference between a rectangular waveguide which is a hollow tube with open ends (a.)) and a rectangular cavity resonator (b.)) where the open ends are now closed, i.e. terminated.

2.12 Waveguide resonators

The hitherto discussed model of a transmission line did not consider terminated ends with an arbitrary load and, thus, the reflection of the electromagnetic wave. In general, transmission lines terminated in two or three dimensions play a central role in a microwave network analysis and, specifically, in the description of the waveguide and cavity resonators. Both waveguide and cavity resonators represent a special type of a transmission line in the form of a hollow tube with open ends in case of a waveguide or closed ends in case of a cavity resonator (c.f. Figure 2.12) [99, 145]. Since all main experiments in this thesis are performed with cavity resonators, i.e. three-dimensional structures, the focus will be put on the description of such structures in the following. Therefore, some key aspects of such terminated lossy transmission lines will be discussed before.

2.12.1 The terminated transmission line

In the course of the physical description of cavity resonators with a small linewidth, i.e. small losses, the impedance can be approximately to be set real. The propagation constant γ remains complex. Figure 2.13 sketches a transmission line terminated with an arbitrary load, the impedance Z_l, which is the ratio of the voltage over the current at the load. If the transmission line and the load are not matched ($Z_0 \neq Z_l$), the mismatch of Z_l to Z_0 sets the parameters for the reflected wave such as its amplitude and phase. The reflected wave propagates opposite to the incident wave. This requires the introduction of a voltage ratio reflection coefficient Γ in Equation (2.65), since the ratio between the forward and backward propagating elements of the electromagnetic wave changes depending on the mismatch between Z_0 and Z_l. The voltage reflection coefficient Γ is expressed in terms of the two impedances Z_0 and Z_l:

$$\Gamma = \frac{V_0^-}{V_0^+} = \frac{Z_l - Z_0}{Z_l + Z_0} \tag{2.66}$$

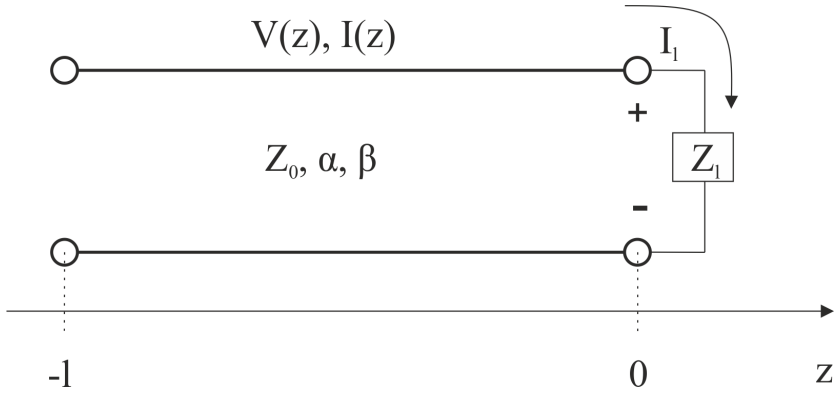

Figure 2.13: Transmission line which is terminated with an arbitrary load Z_l at z=0. I_l denotes the current at the load, $V(z)$ and $I(z)$, the voltage and current, respectively, at position z along the line. Z_0 is the transmission line's impedance, α the attenuation constant for a lossy transmission line and β the phase constant. If the transmission line is matched ($Z_0 = Z_l$), the reflection coefficient $\Gamma = 0$, for a mismatched transmission line $0 < \Gamma < 1$. (adapted from [99])

Then, new equations for the voltage $V(z)$ and the current $I(z)$ can be written as:

$$V(z) = V_0^+(e^{-i\beta z} + \Gamma e^{i\beta z}) \tag{2.67a}$$

$$I(z) = \frac{V_0^+}{Z_0}(e^{-i\beta z} - \Gamma e^{i\beta z}) \tag{2.67b}$$

The above expressions represent a superposition of the incident and reflected waves, which is the signature for the formation of a standing wave [79]. These standing waves result in different modes for a cavity resonator (c.f. Section 2.13.1).

The more the impedances match, the lower are the losses of the considered structure due to reflection. Therefore, reaching matching in the design is one important goal in the design of a structure such as a wave guide or a cavity resonator. If the mismatch of the transmission line's impedance, Z_0, to the load's one, Z_l, is increased, then $|\Gamma|$ increases. In contrast to the average power flow on such terminated transmission line, which is constant, the voltage of the standing wave oscillates between the values $V_{\min} = |V_0^+|(1 - |\Gamma|)$ and $V_{\max} = |V_0^+|(1 + |\Gamma|)$ becomes position dependent [99]. The ratio between the above voltages depends on the value of Γ and is called the (voltage) standing wave ratio ((V)SWR).

$$\text{(V)SWR} = \frac{1 + |\Gamma|}{1 - |\Gamma|} \tag{2.68}$$

This ratio is important in terms of microwave network analysis for the determination of the scattering matrix S_{ij} from a measurement with a vector network analyser (VNA). As such it is directly related to input-output theory applications in network measurements.

2.12.2 Modes of electromagnetic waves in transmission lines

Depending on the number of conductors, a transmission line can support different modes for the propagation of an electromagnetic wave. Transverse electromagnetic waves (TEM)

	E_z	H_z	$Z_i,\ i \in (\mathrm{TEM}, \mathrm{TE}, \mathrm{TM})$
TEM	0	0	$Z_{\mathrm{TEM}} = \eta$
TE	0	$\neq 0$	$Z_{\mathrm{TE}} = \frac{k\eta}{\beta}$
TM	$\neq 0$	0	$Z_{\mathrm{TM}} = \frac{\beta\eta}{k}$

Table 2.1: Overview of some characteristics for the three types of waves on a transmission line propagating along z-direction. Z_i denotes the wave impedance which is a ratio between the individual electric and magnetic field components [99]. Waveguide and cavity resonators are special cases of closed conductors. The variables η, β and k, represent the ratio between the magnetic permeability and permittivity, the phase constant and the wave number k, respectively.

do not have any longitudinal field component with respect to the propagation direction. Such waves are supported for transmission lines with two or more conductors such as coaxial cables, parallel plate waveguides or striplines [99, 147]. In addition to TEM waves, there are transverse electric (TE) and transverse magnetic (TM) waves, which have a longitudinal magnetic or electric field component. Typically, this kind of waves is supported in transmission lines with one conductor such as hollow waveguides [148]. Furthermore, for the latter two, the voltages, currents and characteristic impedances are no longer uniquely defined [99, 149]. If the wave propagates along the z-direction, the magnetic and electric fields are assumed to be time-harmonic, and the transmission line is source free, the equations for the transverse components a a function of E_z and H_z read as:

$$H_x = \frac{j}{k^2 - \beta^2}\left(\omega\epsilon\frac{\partial E_z}{\partial y} - \beta\frac{\partial H_z}{\partial x}\right), \tag{2.69a}$$

$$H_y = \frac{-j}{k^2 - \beta^2}\left(\omega\epsilon\frac{\partial E_z}{\partial x} + \beta\frac{\partial H_z}{\partial y}\right), \tag{2.69b}$$

$$E_x = \frac{-j}{k^2 - \beta^2}\left(\beta\frac{\partial E_z}{\partial x} + \omega\mu\frac{\partial H_z}{\partial y}\right), \tag{2.69c}$$

$$E_y = \frac{j}{k^2 - \beta^2}\left(-\beta\frac{\partial E_z}{\partial y} + \omega\mu\frac{\partial H_z}{\partial x}\right), \tag{2.69d}$$

where ω is the frequency, ϵ the electric permittivity, which is complex if attenuation losses are taken into account, μ the magnetic permeability and β the phase constant [99].
In Table 2.1, the main characteristics of TE, TM and TEM waves are summarised for a wave propagating in z-direction along a transmission line. The impedance shown in the table refers to the wave impedance, which describes the ratio between transverse electric and magnetic field components of the wave. This quantity is different from the characteristic impedance Z_0 of a transmission line, which is the ratio between the corresponding voltages and currents and does not directly relate the electric and magnetic field vector components.

For the design of a transmission line with the lowest possible losses, attenuation losses

should be taken into account. The loss contributions in a transmission line which do not originate from the impedance mismatches, are dielectric, ohmic conductor, and radiative losses which have to be considered in the calculation of the attenuation constant α [150]. Dielectric losses are included here, because dielectrics are often used to support the conduction of the wave and confine it. Each contribution has a different functional dependence on frequency and depends on the specific geometry such as stripline or coplanar waveguide as well as the material defining the dielectric. For more details on the origin and implications of the different loss contributions, the reader might refer to Ref. [99] or other books about microwave engineering.

2.13 Microwave cavity resonators

Planar transmission lines like striplines can be miniaturised and integrated into small scaled electrical circuits to a much higher degree than hollow waveguides. Although the latter are still utilised, nowadays, the majority of industrial applications employs planar transmission lines. Furthermore, they represent a good starting point for the introduction of closed waveguides in general, e.g. cavity resonators (Figure 2.12 a.) and b.)). Now, having previously introduced the general properties of transmission lines, cavity resonators and their characteristics can be described.
There are distinct geometries for cavity resonators such as rectangular or cylindrical or reentrant cavities [146, 151]. Please note, that if for simplicity reasons, the word cavity is used, it always refers to a cavity resonator. As it is depicted in Figure 2.12 b.) for the example of a rectangular structure, a cavity resonator describes a closed volume, which corresponds to a hollow waveguide with short-circuited, i.e. terminated ends. To this end, cavity resonators confine electromagnetic waves which can be injected by means of capacitive or inductive couplers. Accordingly, depending on the specific geometry such elements can support numerous TE, TM or TEM modes. Although, as shown in Table 2.1, such a rectangular waveguide only supports TE and TM wave modes [99, 152].

2.13.1 Modes of a cavity resonator

Among different types of existing cavity resonator geometries, rectangular or cylindrical cavity resonators are currently frequently used in the field of cavity polariton spectroscopy. Therefore, these two types are shortly introduced in the following.

Rectangular cavity resonator

A rectangular cavity resonator can be modelled by a pair of perfectly conducting, parallel plates in each spatial direction. Plane wave solutions, which can propagate through the cavity resonator are not solutions, because they do not satisfy the boundary conditions at the walls. Instead, standing wave modes can be excited in a cavity resonator as shown in Figure 2.12 b.) and the cavity resonator operates at certain, resonant frequencies which are set by the specific geometry and dielectric [153]. Assuming perfectly conducting walls, i.e. a dissipationless cavity resonator, the following boundary conditions for this example of a rectangular cavity can be formulated. As such, all field components must vanish

inside the conductor.

$$\hat{n} \cdot \mathbf{D} = \rho_s, \tag{2.70a}$$
$$\hat{n} \cdot \mathbf{B} = 0, \tag{2.70b}$$
$$\hat{n} \times \mathbf{E} = 0, \tag{2.70c}$$
$$\hat{n} \times \mathbf{H} = \mathbf{j}_s, \tag{2.70d}$$

where ρ_s denotes the (surface) electric charge density and $\mathbf{j}_s$ the (surface) current density at the conductor's surface. Hence, the tangential component of the electrical field E_t and the normal component of the magnetic field B_n to the cavity wall need to be zero. For example, the expression of the electrical field vector for a wave propagating in free space, $\mathbf{E}(\mathbf{r}, t) = \mathbf{E}_0 e^{i\omega t - \mathbf{kr}}$, changes to expressions comprised from a combination of cosinusoidal and sinusoidal components [81, 99],

$$E_x = E_{x0} \cos k_x x \sin k_y y \sin k_z z e^{i\omega t}, \tag{2.71a}$$
$$E_y = E_{y0} \sin k_x x \cos k_y y \sin k_z z e^{i\omega t}, \tag{2.71b}$$
$$E_z = E_{y0} \sin k_x x \sin k_y y \cos k_z z e^{i\omega t}. \tag{2.71c}$$

Another important implication of $E_t = 0$ is, that the wave vector $\mathbf{k} = (k_x, k_y, k_z)$ only takes on discrete values for which this boundary condition is satisfied. Like the field, the specified value may differ between the three spatial components. Maxwell's equation, $\nabla \cdot \mathbf{E} = 0$, relates all three wave vector components [80]. Then,

$$k_i = \frac{n_i \pi}{l_i} \quad i \in (x, y, z), n \in \mathbb{N}, \tag{2.72}$$

where l_i refers to the length of the cavity in the corresponding direction. Moreover, n is the mode number and specifies the spatial distribution of the electric and magnetic field per mode. Furthermore, the wave equation (Equation (2.58)) needs to be satisfied as well. This results in a relation between the wave vector components and the frequency of the standing wave in the cavity resonator. The wave vector only takes on discrete values, and hence does the frequency.

$$\frac{\omega}{c'} = \pi \sqrt{\frac{n_x^2}{l_x^2} + \frac{n_y^2}{l_y^2} + \frac{n_z^2}{l_z^2}}, \tag{2.73}$$

where $c' = \frac{c}{\sqrt{\mu_r \epsilon_r}}$ is the velocity of the electromagnetic wave in a medium. These frequencies are called the resonant frequencies of a cavity resonator for the TE_{xyz} or TM_{xyz} mode, respectively. For rectangular cavity resonators the dominant mode is the TE_{101} for $y < x < z$ or TM_{110} mode [99]. Referring to this they strongly depend on the final shape and dimensions of the cavity resonator.

Cylindrical cavity resonator

The cavity resonator which has been designed for the experiments conducted in this thesis is a reentrant double post cavity resonator consisting of two cylindrical resonators with a solid post in the centre. Thus, for completeness, the resonant frequencies of a cylindrical cavity resonator will also be given. Here, the dominant modes are the TE_{111} or TM_{010} mode, respectively. Accordingly, for TM modes the resonant frequencies can be expressed as [99] :

$$\frac{\omega}{c'} = \sqrt{\frac{p_{xy}^2}{x^2} + \frac{(z\pi)^2}{h^2}}, \tag{2.74}$$

where h denotes the height of the cylindrical cavity and p_{xy} the x-th root of the Bessel function.
Please note, that microwave resonators such as the cavity resonator representing a resonant circuit can also be modelled as an RLC circuit using lumped elements. Further information on this description can be found in Ref. [99, 153] and references therein. In the context of the description of the CMP, the RLC circuit approach is also discussed in Chapter 3.

2.14 Quality factor

In experiments, conductive and dielectric losses of the cavity resonator have to be taken into account. When the cavity resonator is excited, some energy is stored in the cavity's volume and oscillates between the electric and magnetic energy. Then, in the presence of losses, some of that stored energy in the cavity is dissipated per oscillation cycle. Unless the cavity is not excited continuously, eventually all stored energy will be lost. However, in view of applications, it is desirable that the amount of dissipation outside the cavity resonator is as low as possible. In order to quantify a measure for the amount of energy stored and that lost per oscillation cycle, the quality factor Q is used [154].

$$Q = 2\pi \frac{\text{energy stored in cavity resonator}}{\text{energy dissipated per oscillation cycle}}. \tag{2.75}$$

For an input microwave signal at the resonant frequency of a cavity mode, the energy stored in the cavity resonator is maximal. In addition, for a continuously driven cavity resonator, the resonator's linewidth $\Delta\nu$ refers to the cavity resonator losses per oscillation cycle. Thus, in the context of resonant circuits, the quality factor can be understood as the ratio between the resonance frequency and the linewidth (bandwidth) of the resonator

$$Q = 2\pi \frac{\nu}{\Delta\nu}. \tag{2.76}$$

This quantity is also called the unloaded quality factor Q_0, as it is an inherent property of the cavity itself; it does not include any coupling to any external circuitry. The addition of an external load, which may serve as a source for driving the cavity continuously, typically lowers the effective quality factor, also called the loaded quality factor, Q_l. This additional coupling to an external load opens further dissipation channels. Q_l is comprised of two contributions taking both wall and dielectric losses, i.e. internal ones (Q_i), and losses due to external coupling, Q_e, into account [99]. The loaded Q is expressed as

$$\frac{1}{Q_l} = \frac{1}{Q_i} + \frac{1}{Q_e}, \tag{2.77}$$

where, Q_i describes the sum of all internal losses and reads as $\frac{1}{Q_i} = \frac{1}{Q_d} + \frac{1}{Q_c} + \frac{1}{Q_r}$, where Q_d considers dielectric, Q_c conductive and Q_r radiative losses, respectively.
As mentioned, in the lumped element model, the cavity resonator can be modelled by a series or parallel RLC circuit and within that framework, can either be conductively or inductively excited [155].
When the cavity is coupled to an external load, one classifies the amount of coupling into three main categories. It is chosen depending on the desired application. In this regard,

the coupling efficiency κ is defined as the ratio between the internal Q_i and the external Q_e,

$$\kappa = \frac{Q_i}{Q_e}. \tag{2.78}$$

Correspondingly, the three coupling regimes are

$$\kappa < 1 : \textbf{undercoupled}, \tag{2.79a}$$
$$\kappa = 1 : \textbf{critically coupled}, \tag{2.79b}$$
$$\kappa > 1 : \textbf{overcoupled}. \tag{2.79c}$$

For capacitive coupling, the end of a transmission line carrying the microwave power is inserted into the cavity. For instance, for a maximal coupling, it may be placed at the antinode of the electric field of the chosen mode. Among other methods ([99]), the cavity resonator can be excited inductively, as well. This is realised by means of a small loop of metal wire with a single winding, where the microwave current from a source induces an AC magnetic field. If correctly aligned with respect to the field lines of the desired mode, the cavity resonator is excited. The coupling efficiency of both methods strongly depends on the exact position of this pin (loop) with respect to the electric (magnetic) field strength. Capacitive couplers may change the cavity's geometrical volume less than the inductive loops do but are more sensitive to temperature variations due to the change of the pin's position. Changes in the position, especially for a critically coupled cavity resonator, have a substantial impact in the coupling efficiency. Therefore, the quality factor can change significantly as a function of temperature. Consequently, the cavity resonator used in the experiments of this thesis employs inductive coupling of the microwave feed line.

2.15 Network analysis: Scattering matrix

A microwave network describes the usage of one or more connected microwave devices for the transmission of a microwave signal [99]. For many applications, the reflection, transmission and power properties are of central interest. The whole system is then treated as a microwave network with relative amplitudes relating output voltages, currents, and powers to those at the input. However, at high frequencies, network (circuit) analysis is only applicable to a small extent to distributed networks because both voltages and currents become strongly frequency and position dependent. In this case, the system cannot be simplified using passive lumped elements combined with active components and Maxwell's equations need to be solved. These solutions provide full information about the fields and currents at every point in space for the studied system. Because of this, they form the basis for solvers in the radio frequency (RF) regime, which are used for simulating the field and current distributions such as in the case of designing cavity resonators. However, for many applications, knowledge about the amount of transmitted and reflected power from the in- and outputs of the networks allows one to describe many electrical properties such as the power gain of a network. This results in the definition of scattering parameters (c.f. Figure 2.14 a.) for the example of a two-port network), which relate input and output power waves a and b, respectively [99, 154]. Therefore, the scattering parameters of this matrix relate the amplitudes and phases of the incident and outgoing waves from the device under test (DUT). Typically, the DUT is not directly connected to the signal source, but is separated by a distance l, originating, for instance, from connecting microwave

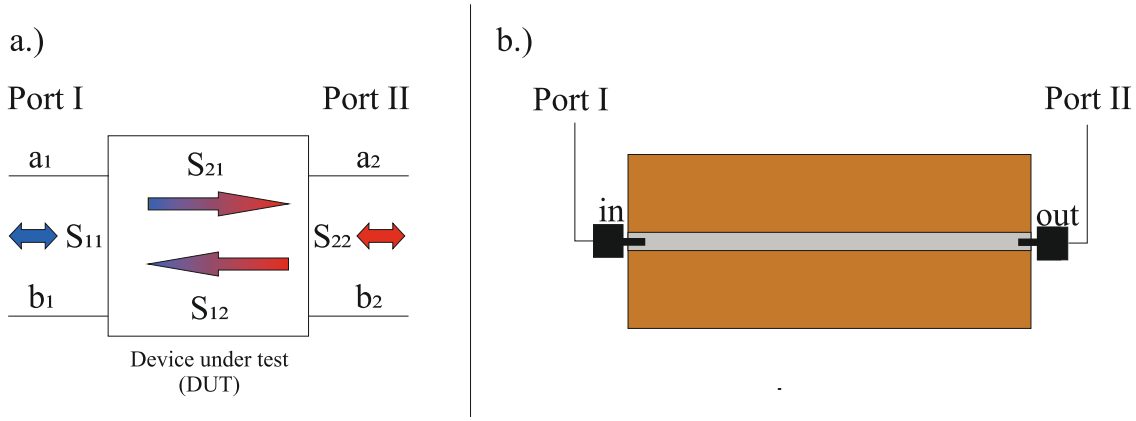

Figure 2.14: a.) Schematical illustration of the scattering matrix S_{ij} for a two-port network. There, S_{21} (S_{11}) and S_{12} (S_{22}) denote the forward or reverse transmission (reflection) parameter, respectively, if the forward direction is from Port I to Port II. b.) Example of a stripline which represents the device under test (DUT), illustrating a two-port network.

cables. It is shown in Figure 2.14 b.) for the example of a stripline for transmission measurements. In order to obtain information of the S-matrix directly at the DUT input and output, the reference plane for the phase needs to be shifted accordingly (c.f. Figure 2.15).

Now, instead of using inward and outward voltages, power waves which relate voltage and power,

$$a_i = \frac{V + Z_r \cdot I}{2\sqrt{R_R}} \tag{2.80a}$$

$$b_i = \frac{V - Z_R^\star \cdot I}{2\sqrt{R_r}}, \tag{2.80b}$$

can be defined, where $Z_R = R_R + iX_R$ denotes the reference impedance, which in the presence of losses may become complex. Equivalently, it is possible to define incident and reflected voltage waves such that $a_i = V_i^+$ and $b_i = V_i^-$. In Figure 2.14 a.) the parameters for a network with two ports are shown, typically used in the kind of hybridised cavity resonator magnonic sample systems, such as those studied in this thesis. The general relation of a network comprised from n ports can be expressed as,

$$\begin{pmatrix} b_1 \\ \vdots \\ b_n \end{pmatrix} = \begin{pmatrix} S_{11} & \cdots & S_{1n} \\ \vdots & \ddots & \vdots \\ S_{n1} & \vdots & S_{nn} \end{pmatrix} \cdot \begin{pmatrix} a_1 \\ \vdots \\ a_n \end{pmatrix} \tag{2.81}$$

For a two port network it simplifies to (c.f. Figure 2.14 a.)):

$$\begin{pmatrix} b_1 \\ b_2 \end{pmatrix} = \begin{pmatrix} S_{11} & \cdots & S_{12} \\ S_{21} & \vdots & S_{22} \end{pmatrix} \cdot \begin{pmatrix} a_1 \\ a_2 \end{pmatrix}, \tag{2.82}$$

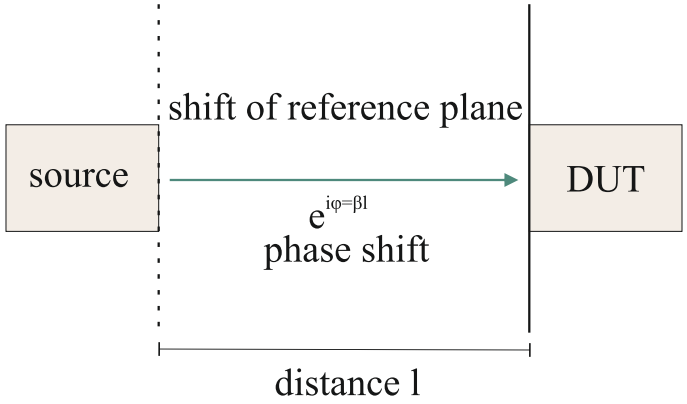

Figure 2.15: Shift of the reference plane for determination of the scattering parameters at the device under test (DUT) if the device has a distance l to the microwave source. This distance may be comprised by microwave cables, for instance. The phase shift is given by $e^{i\beta l}$, where β denotes the phase constant of the wave.

where, S_{12} (S_{21}) represents the parameter for reverse (forward) power gain and S_{11} (S_{22}) the inward (outward) loss. Since the S-Parameters are a measure for the ratio between input and output power at a specific port, these parameters are usually expressed in decibel (dB) power units. The conversion is:

$$|S_{ij}|^2\,(\mathrm{dB}) = -20\log_{10}(|a_{ij}|^2), \tag{2.83}$$

where $|a_{ij}|^2$ denotes the linear amplitude.

Chapter 3

Hybrid systems

3.1 Strongly coupled systems

In a general description, polaritons are the "particles" associated with a hybrid wave mode in a medium originating from the strong coupling between a propagating electromagnetic wave and an elementary excitation carrying a dipole moment [12]. As the electromagnetic wave propagates through the medium, the wave can couple to either the electric or magnetic dipole moment [8]. Further, there exist multiple excitations with a dipole moment in a medium of different origin which means one can distinguish between various types of polaritons. Among others, the coupling of photons to excitons (bound electron-hole pairs) results in exciton polaritons, surface plasmon (delocalised electron oscillations at an interface such as metal-dielectric) polaritons, and the coupling to magnons (quasiparticles associated to a collective spin excitation) to cavity magnon-polaritons (CMP) [156, 157]. The latter is subject of this thesis, but due to its general nature, some key aspects common to all types of polaritons are briefly discussed.

In the absence of a coupling between an electromagnetic wave, i.e. a photon, and another quasiparticle such as the magnon, the individual dispersions would cross at resonance where the value of an external sweeping parameter is set such that the individual eigenfrequencies match. However, in the presence of a CMP, the system's old eigenstates have to be replaced by the new, coupled ones. Semiclassically, light-matter interactions can be modelled by two coupled harmonic oscillators [11]. In the presence of coupling, the classical description of a system of two coupled oscillators results in the existence of a symmetric and antisymmetric solution, i.e. two frequencies ω_1, ω_2, respectively, at resonance in the dispersion spectrum [8]. They are separated by a gap of $\Delta\omega = \omega_1 - \omega_2$, and $\Delta\omega = 2g_{\text{eff}}$, where g_{eff} denotes the coupling strength. Here, strong coupling is reached when that frequency splitting exceeds the sum of the individual oscillator linewidths. In the quantum mechanical description of two coupled harmonic oscillators, the resulting eigenenergies of the coupled system differ by a characteristic frequency, called the Rabi frequency Ω [158]. The new eigenstates are now superpositions of the uncoupled, bare states, and often referred to as dressed states [11]. If the Rabi frequency exceeds the individual damping factors of each constituent, the system is in the strong coupling regime. In this regime, there is a coherent exchange of energy (information) between the system's constituents, which can be observed in the form of Rabi oscillations [158]. Hence, the size of the frequency gap in the spectrum corresponds to $\Omega = 2g_{\text{eff}}$ in a semi-classical description and, in turn, the size of the gap gives a measure of the coherent exchange of

information. The observation of such frequency gap results in an avoided level crossing in the spectrum and represents an experimental signature of a strongly coupled system. If the coupling refers to the coupling of a photon with a quasiparticle, for instance, the avoided level crossing is a characteristic signature for the presence of the resulting polariton. Referring to this, a characteristic dispersion spectrum with this avoided level crossing is schematically displayed in Figure 3.1. The small insets illustrate the symmetric (antisymmetric) solution in the framework of two coupled oscillators moving in (out) of phase which results in different frequencies of the coupled system.

As a quasiparticle of a coupled mode, the CMP can be partitioned into a photonic and magnonic part, whose relative contribution depends on how much the respective individual state fulfils the conditions for resonant coupling. Specifically, at resonance, the energies are equally distributed between both components [8, 61]. Therefore, it is necessary to quantify the strength of the exchange of energy, i.e. the coupling between the subsystems. If the coupling strength is stronger than the individual dissipation, i.e. loss, factors from photon (κ_r) and magnon (κ_m), i.e. $g_{\text{eff}} \gg \kappa_r, \kappa_m$, the "strong coupling regime" is present and this polariton is observable [158]. The stronger the interaction, the larger becomes the energy gap between the upper and lower branch of the polariton. Therefore, the gap is proportional to a macroscopic coupling strength which represents a measure of coherent information exchange [158]. By studying the dependence of the anticrossing's gap as a function of external parameters such as temperature or manipulating the internal phase relations between magnon or photon, it is possible to obtain information of the coupling strength [61], directly. Then, this allows one to extend the understanding of spin-photon coupling and develop methods to use such hybridised systems for applications in data storage or information technology such as mentioned in Chapter **??** and discussed in Ref. [46] (and references therein). Note, that the observed macroscopic coupling strength is the result from the simultaneous coupling of N spins to the photons which all exhibit a microscopic, single spin coupling strength g_0, leading to the effective coupling strength $g_{\text{eff}} \propto \sqrt{N} g_0$ [56].
Distinguishing between a microscopic and macroscopic picture already shows, depending on the kind of information one wishes to obtain over the system, either a classical or quantum mechanical approach can be more advantageous [61, 156]. In the studied CMP system, both the (cavity resonator) photon and the magnon can be described by harmonic oscillators [25, 14]. Therefore, modelling the polariton by two coupled harmonic oscillators is a general approach to understand the behaviour of the hybrid system in terms of forces acting on the single components and fundamental concepts [61]. However, this method does not reveal much information about the interaction concerning the single fields and dynamical correlations between magnons and photons such as the relative phase between the AC driving fields. Thus, utilising a combination from the LLG equation and Maxwell's equations (c.f. Chapter 2) represents another classical approach for the description of the coupling. This approach is especially useful for cavity resonator photons because a cavity resonator can be modelled by an RLC circuit, which mimics well the (microwave) properties of the system. For instance, understanding the influence of relative phases between different AC magnetic fields is more intuitive in this model. Thus, the existence of such a phase correlation will be important for the discussion of the experimental data in Chapter 5, where the relative phase between two coherent microwave feed lines is manipulated.

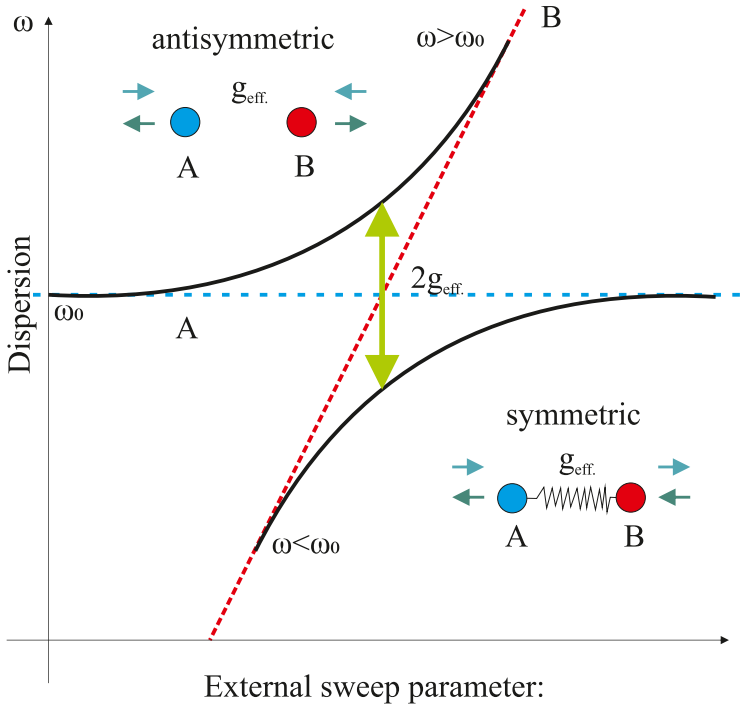

Figure 3.1: Sketch of the anticrossing in the presence of a polariton, the associated quasi-particle from the resonant coupling of a propagating electromagnetic wave to excitation with a dipole moment in a medium. Without coupling the individual dispersions would cross at resonance, i.e. $\omega_0 \equiv \omega_A = \omega_B$. For the coupled system, there are a symmetric and an antisymmetric oscillation with two solutions each, shown by the turquoise and blue arrow. As will be shown in the following sections, in the strong coupling regime the opening of the gap in the avoided level crossing corresponds to twice the value of the coupling strength.

In above (classical) descriptions, solely the macroscopic coupling strength of the N spin system is directly accessible. However, for a better understanding of the coupling on a more fundamental basis, the microscopic coupling strength which describes the interaction between a single photon and magnon needs to be also considered. At this small scale of low photon and magnon numbers, quantum effects come into play requiring the utilisation of the quantum mechanical approach for this case. Therefore, the central expressions and concepts of all three, both classical or quantum mechanical, approaches are introduced in the following. Accordingly, these different descriptions allow one to consider the hybridised spin-photon system from different perspectives which in combination complement each other and provide a more comprehensive framework. Additionally, this framework is later on used in the discussion of the experimental findings of the work presented in the following two chapters.

3.2 Driven, damped coupled harmonic oscillators

Typical experimental setups for (cavity resonator) photon magnon polariton spectroscopy consist of a cavity resonator and a magnetic sample [56, 58, 159]. Whilst the cavity photon is continuously driven by an external coupling to a microwave feed line, the magnetic

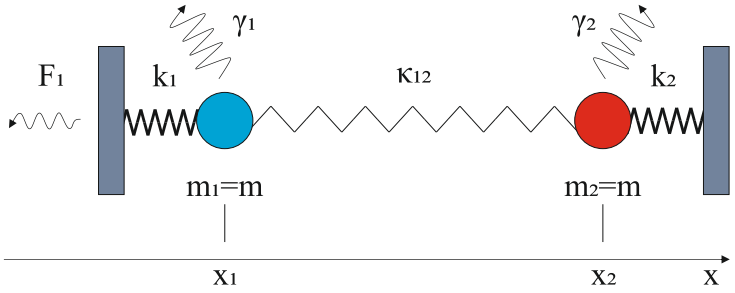

Figure 3.2: Illustration of a system of two coupled oscillators on three different springs and one driving force F_1 for the oscillator with spring constant k_1. Dissipation for each oscillator is included by the factors γ_1 and γ_2, respectively. The coupling constant between both oscillators is denoted by κ_{12}, and equal masses are assumed $m_1 = m_2 = m$.

sample is inserted into the antinode of the AC magnetic field of the cavity resonator mode of interest. Predominantly, this AC field drives ferromagnetic resonance in the sample and, hence, excites the (Kittel mode) magnons in the sample. Both the cavity photons and the magnons can be described as damped harmonic oscillators. Thus, in order to introduce the concept of the avoided level crossing as a signature for the CMP, one can describe the (strongly) coupled cavity photon-magnon system as a driven system of two damped, coupled harmonic oscillators. This system is illustrated schematically in Figure 3.2. A force F_1 drives the first oscillator at position x_1 and excites the second one by the coupling via the spring with a spring constant κ_{12}. This spring constant is a measure for the coupling strength of this system. If both oscillators are directly coupled to the environment, the corresponding external dissipation, i.e. loss, is indicated by the spring constants k_1 and k_2. Accordingly, the internal losses of each oscillator are given by γ_1 and γ_2, respectively. Correspondingly, the equations of motion (EOM) for each oscillator can be written in general form:

$$\ddot{x}_1 + 2\kappa_1\dot{x}_1 + \omega_1^2 x_1 + \frac{\kappa_{12}}{m}(x_1 - x_2) = \frac{F_1}{m} \tag{3.1a}$$

$$\ddot{x}_2 + 2\kappa_2\dot{x}_2 + \omega_2^2 x_2 - \frac{\kappa_{12}}{m}(x_1 - x_2) = 0, \tag{3.1b}$$

where $2\kappa_1 = \frac{\gamma_1}{m}$, $\omega_1 = \sqrt{\frac{k_1}{m}}$, $2\kappa_2 = \frac{\gamma_2}{m}$, $\omega_2 = \sqrt{\frac{k_2}{m}}$ denote the respective spring constants and F_1 the driving force [160]. After defining $\tilde{\omega}_1 = \sqrt{\frac{k_1+\kappa_{12}}{m}}$, $\tilde{\omega}_2 = \sqrt{\frac{k_2+\kappa_{12}}{m}}$, $g_{\text{eff}} = \frac{\kappa_{12}}{m}$, and similar to Ref.[61] writing the dissipation and coupling parameters in a dimensionless manner allows expressing the above equation in the following matrix form $\Omega\mathbf{x} = \mathbf{F}$, where $\mathbf{x} = (x_1, x_2)$ and $\mathbf{F} = (F_1, 0)$. Here, a time-harmonic ansatz $x_i = x_{0,i}e^{-i\omega_i t}$ has been used.

$$\begin{pmatrix} \omega^2 - \tilde{\omega_1}^2 + 2i\kappa_1\omega\tilde{\omega}_1 & g_{\text{eff}} \\ g_{\text{eff}} & \omega^2 - \tilde{\omega_2}^2 + 2i\kappa_2\omega\tilde{\omega}_1 \end{pmatrix} \cdot \begin{pmatrix} x_1 \\ x_2 \end{pmatrix} = \begin{pmatrix} -\frac{F_1}{m} \\ 0 \end{pmatrix} \tag{3.2}$$

By finding the frequencies for which $\det(\Omega) \equiv 0$, a characteristic equation is found

$$\tilde{\omega}_\pm = \frac{1}{2}[(\omega_A + \omega_B) \pm \sqrt{(\omega_A - \omega_B)^2 + g_{\text{eff}}^2}], \tag{3.3}$$

where $\omega_{\text{A}} = \tilde{\omega_1} - i\kappa_1\tilde{\omega}_1$, and $\omega_{\text{B}} = \tilde{\omega_2} - i\kappa_2\tilde{\omega}_1$.

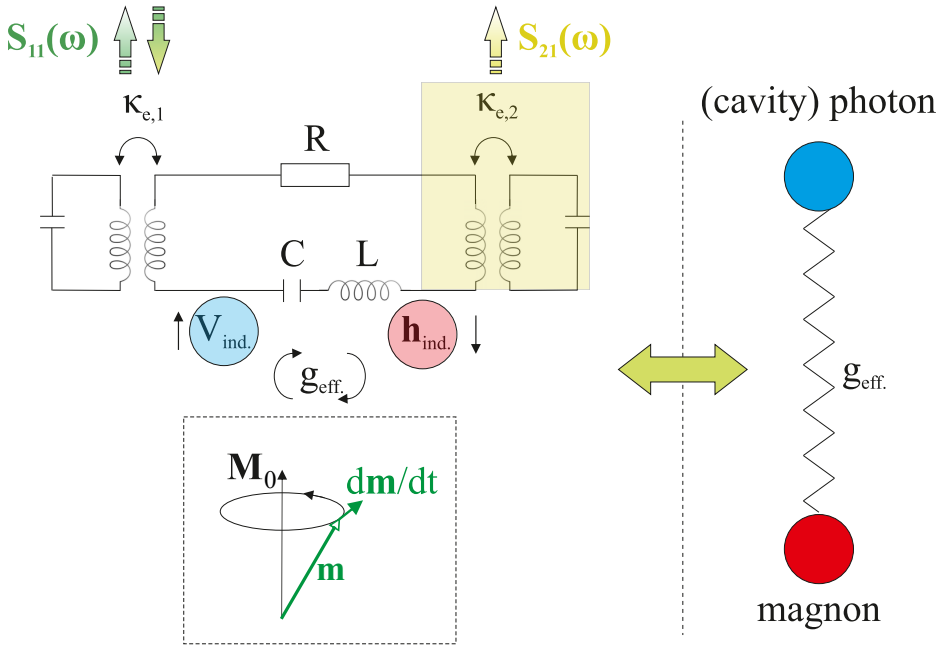

Figure 3.3: Schematical illustration of the interaction between the cavity resonator photons and magnons in a combination from Maxwell's equations and the LLG equation. The cavity resonator is modelled as a series RLC circuit, the inductive coupling to the cavity ports is denoted by $\kappa_{e,1}$ for a reflection resonator (e.g. $S_{11}(\omega)$ measurements) and the precessing magnetisation induces a voltage V_{ind} into the RLC circuit. On the other hand, the driving microwave induces an AC magnetic field to the magnonic system ($\mathbf{h}_{\mathrm{ind}}$). The shaded area denotes the second coupling with loss factor $\kappa_{e,2}$ to the environment. For instance, such second coupling is used for two-port transmission (e.g. $S_{21}(\omega)$) measurements), if the cavity exhibits two inductive couplings to an external microwave feed line. $\mathbf{M}_0$ denotes the magnetisation. This small inset sketches the precessional motion of the spins, i.e. represents the magnon in the RLC circuit approach. On the right, the analogy to the spring model between cavity photon and magnon is shown, where g_{eff} corresponds to the coupling strength in a.).

At resonance $\omega_{\mathrm{A}} = \omega_{\mathrm{B}}$, and subtracting the upper ($\tilde{\omega_+}$) from the lower polariton branch ($\tilde{\omega_-}$), allows one to find an expression for the frequency gap ω_{gap} in the avoided level crossing.

$$\omega_{\mathrm{gap}} = \tilde{\omega}_+ - \tilde{\omega}_- = 2g_{\mathrm{eff}} \tag{3.4}$$

This shows that the opening of the gap corresponds to twice the value of the coupling strength. If strongly coupled, this allows one to experimentally determine the coupling strength for a CMP system.

3.3 Resonator as RLC circuit: LLG and Maxwell's equations

The description of the CMP as a system of coupled damped harmonic oscillators does not give further insight about the phase relations and underlying magnetic fields leading

to the coupling [61]. As already mentioned, another classical approach is considering the (electro) dynamics of the system employing Maxwell's equations and the LLG for the magnetic system. In Figure 3.3, the correspondence between the system as two coupled harmonic oscillators and the RLC circuit - LLG system is shown. Since the CMP is a hybrid quasiparticle, the magnetisation dynamics for the magnons is covered by the LLG equation, and the cavity resonator is modelled by a resonant RLC circuit [61, 77, 161]. The coupling is comprised of two processes. First, the precessing magnetisation in the sample induces a voltage V_{ind} due to Faraday's law of induction into the RLC circuit. On the other hand, the microwave current $\mathbf{j} = (j_x, j_y, 0)$ in the circuit results in magnetic fields $\mathbf{h} = (h_x, h_y, 0)$ acting on the magnetisation due to Ampère's law [81]. In order to find an equivalent expression of coupled equations for the currents $\mathbf{j}$ and moments $\mathbf{m}$, the respective solutions of the linearised LLG and the induced voltage need to be found. Recall that, the solution of the linearised LLG equation using the complex expressions for the alternating current (AC) magnetisation $\mathbf{m}_{\mathrm{AC}}(t) = \mathbf{m}_{\mathrm{AC}} e^{i\omega t}$ and magnetic field $\mathbf{h}_{\mathrm{AC}}(t) = \mathbf{h}_{\mathrm{AC}} e^{i\omega t}$ yields:

$$\mathbf{m} = \overleftrightarrow{\chi}\mathbf{h}, \tag{3.5}$$

where $\overleftrightarrow{\chi}$ denotes the nonsysmmetric susceptibility tensor for the relevant frequencies [15]. This non-symmetricity of $\overleftrightarrow{\chi}$ leads to the property of magnetic gyration that is magnetisation precession around the axis of saturation magnetisation in the presence of a static field and a small transversal perturbation. In ferromagnetic resonance, the excitation frequency matches the natural frequency of one magnon mode (c.f. Chapter 2). Here, the focus is on the excitation of Kittel mode ($\mathbf{k} = 0$) magnons, which are precessing uniformly. However, ferromagnetic resonance is only possible under certain conditions. Ferromagnetic resonance only occurs when the perturbing AC field exhibits a circular component with a right-hand rotation relative to the axis of the external static field. Then, if the damping is assumed to be small, the time-dependent magnetisation and field vectors can be expressed in elliptically polarised (taking the sample's shape dependences into account) form [15, 61, 77]:

$$m_{\pm} = Dm_x \pm im_y, \tag{3.6a}$$
$$h_{\pm} = Dh_x \pm ih_y, \tag{3.6b}$$

wherein the following the ellipticity factor D is set to $D = 1$ because a spherical sample is used for all experiments conducted in the course of this thesis. In order to satisfy above condition for resonance due to the susceptibility tensor, the complex amplitude of the AC components have to correspond to the component m_+, h_+, i.e. $m_{\mathrm{AC}} = m_+$ and $h_{\mathrm{AC}} = h_+$. This results in [61]:

$$m_+ = \frac{-i\gamma M_s}{\omega - \omega_{\mathrm{FMR}} + i\kappa_m \omega} h_+, \tag{3.7}$$

where ω_{FMR} denotes the FMR frequency and M_s the saturation magnetisation. Now, this expression allows to express the voltage which is induced into the RLC circuit in terms of the time dependent magnetisation change via:

$$V_{+,\,\mathrm{ind}} = ig_c L \frac{\partial m_+(t)}{\partial t}, \tag{3.8}$$

where g_c denotes the coupling constant from the magnons to the cavity resonator photons in this RLC circuit picture, L the inductance (c.f. Figure 3.3) and $m_+(t) = m_+ e^{-i\omega t}$. This is the application of Faraday's law. The EOM for the microwave current of the RLC

circuit which also both takes the right hand rotation ($\mathbf{j}_+ = Dj_x(t) + ij_y(t)$) and time harmonicity ($\mathbf{j}_+(t) = \mathbf{j}_+ e^{-i\omega t}$) into account allows to find an equivalent expression for the voltage as

$$V_{+,\mathrm{ind}} = L\frac{\partial j_+(t)}{\partial t} + Rj_+(t) + \frac{1}{C}\int j_+(t)dt. \tag{3.9}$$

The microwave currents of the RLC circuit drive the FMR by inducing the magnetic fields $h_x = g_m j_{+,y}$ and $h_y = -g_m j_{+,x}$, where g_m denotes the coupling constant of the RLC circuit *to* the excitation of the magnetisation. Hence, combining Equation (3.8), Equation (3.9) and expressing the currents by the induced fields results in a set of two coupled equations describing the CMP. Similarly to the case of the coupled harmonic oscillators, they are arranged in a matrix form and read (derivation similar to Ref. [61] and Ref. [77])

$$\begin{pmatrix} \omega^2 - \omega_r^2 + 2i\omega\frac{R}{2}\sqrt{\frac{C}{L}} & i\omega^2 g_c \\ -i\gamma M_s g_m & \omega - \omega_{FMR} + i\kappa_m\omega \end{pmatrix} \begin{pmatrix} \mathbf{j}_+ \\ \mathbf{m}_+ \end{pmatrix} = 0. \tag{3.10}$$

The dispersion, i.e. the eigenfrequencies of the coupled system, can again be determined by finding the frequencies for which the determinant of the left hand matrix in Eq.(3.10) vanishes. A more detailed comparison of the correspondence between the harmonic oscillator and RLC circuit approach can be found, for instance, in Ref. [61, 162]. Since this approach considers different induced currents or fields present in the system, it could be, for instance, extended to a system with two AC magnetic fields with different amplitudes and phases. This will be used for finding one possible description for the experiment of the control and manipulation of the CMP coupling presented in Chapter 5 and theorised in Ref. [61, 77].

The combination of above approaches gives insight into the fundamental concept of the avoided level crossing, proving that the gap corresponds to twice the coupling strength, and allows to study phase and field relations from a combination of RLC circuit theory for the cavity resonator and the LLG for the magnons. However, this description only explains the coupling on a macroscopic basis since it is footed on a fully classical approach. For an understanding of the coupling on a microscopic basis, it is necessary to describe the coupled system based on quantum mechanics. In general, both the classical and the quantum approach yield the same results such as the dispersion spectra and the line shapes for the frequency swept spectra. Then, depending on the question which is addressed with the CMP either model may be more feasible. For instance, in the single photon regime at cryogenic temperatures, the quantum approach will be the preferred choice. This is now going to be discussed in the next section.

3.4 Quantum mechanical approach: Tavis-Cummings Hamiltonian

In order to derive a relation for the microscopic coupling strength between a single spin and one cavity photon, the well-known concepts from cavity quantum electrodynamics (CQED) can be used for the CMP in the strong coupling regime [11]. It provides a quantum mechanical framework for the description of the interaction between a single emitter

such as a two-level system, and a single mode field [158]. Accordingly, the Hamiltonian for the single emitter-field interaction can be written in generalised form:

$$\mathcal{H} = \mathcal{H}_{s.e.} + \mathcal{H}_F + \mathcal{H}_{\text{int}}, \tag{3.11}$$

where $\mathcal{H}_{s.e.}$, $\mathcal{H}_F$, and $\mathcal{H}_{\text{int}}$ denote the unperturbed, non-interacting single emitter , single mode field energy terms, and the interaction term, respectively. The magnons are precessing around the axis of saturation magnetisation in the presence of an external field. Thus, the interaction of each magnetic (dipole) moment contains the Zeeman term $\mathcal{H}_{\text{int}} = -\boldsymbol{\mu}\cdot\mathbf{B}$, where $\boldsymbol{\mu}$ denotes the total magnetic moment comprised of orbital motion and intrinsic electronic spin. Focusing on the spin part only, the equation reads as $\mathcal{H}_{\text{int}} = -\gamma\mathbf{S}\cdot\mathbf{B} = -\frac{\gamma}{2}\hbar\boldsymbol{\sigma}\cdot\mathbf{B}$, where σ denotes the spinor representation in form of Pauli matrices [11, 158]. First, the magnetic field is written in quantised form, where a large, but finite cavity resonator with running waves imposed with periodic boundary conditions are considered:

$$\mathbf{B}(\mathbf{r},t) = \sum_k \frac{\mathbf{k}\times\hat{\epsilon_k}}{\omega_k}\mathcal{B}_k a_k e^{-i\omega_{\mathbf{k}}t + i\mathbf{k}\cdot\mathbf{r}} + \mathcal{H}.c., \tag{3.12}$$

where $\mathcal{B}_k = \sqrt{\frac{\hbar\mu_0\omega_k}{2V}}$. Following the approach presented in Ref. [27], both operators are expressed in terms of raising and lowering spin operators $a^\dagger$ for the cavity photons ($m^\dagger$ for the magnons) and $a(m)$, respectively. They are multiplied by the corresponding mode functions $\mathbf{B}(\mathbf{r}_i)$ ($M_n(\mathbf{r}_i)$), which allows for writing the interaction term as

$$\mathcal{H}_{\text{int}} = g\mu_B\sqrt{2NS}\sum_i\sum_n M_n(\mathbf{r}_i)\frac{m^\dagger + m}{2}\mathbf{B}(\mathbf{r}_i)(a^\dagger + a), \tag{3.13}$$

where g denotes the gyromagnetic ratio, N the total number of spins, S the total spin number ($S = \frac{5}{2}$ for YIG, [100]) and $\mathbf{B}(\mathbf{r}_i)$ the linearly polarised microwave AC magnetic field for each spin i at position $\mathbf{r}_i$ in the sample. The sum is replaced by an integration over the mode's volume and the rotating wave approximation (RWA, [158]) applied, yielding

$$\mathcal{H}_{\text{int}} = \frac{g\mu_B}{2}\sqrt{2s}\sum_N\int_{V_{\text{mode}}} d\mathbf{r}M_n(\mathbf{r})\cdot\mathbf{B}(\mathbf{r}_i)(a^\dagger m + am^\dagger). \tag{3.14}$$

Since, here, the focus is on the properties and manipulation of the coupling to the spatially uniform Kittel mode ($\mathbf{k} = 0 \rightarrow \mathcal{B}_k \equiv B_0$) and the microwave AC magnetic field is perpendicular to the external field ($\mathbf{H}_{\text{ext}} = (0,0,H_{\text{ext},z})$), the interaction Hamiltonian is formulated as:

$$\mathcal{H}_{\text{int}} = \hbar\frac{\gamma}{2}B_0\sqrt{2NS}(a^\dagger m + am^\dagger), \tag{3.15}$$

Thus, the "frequency of interaction" which is the coupling strength g_{eff} for a system of N single spins simultaneously coupling to cavity photons can be written as:

$$g_{\text{eff}} = \eta\frac{\gamma}{2}B_0 = \eta\frac{\gamma}{2}\sqrt{\frac{\mu_0\hbar\omega}{2V_{\text{mode}}}}\sqrt{2NS}, \tag{3.16a}$$

$$= g_0\sqrt{2NS}, \tag{3.16b}$$

where g_0 denotes the single spin coupling strength, and the factor η is added, accounting for deviations in the experiment from a perfect mode overlap between magnons and photons [56, 58, 162]. Finally, the full Hamiltonian for the coupling of a single magnon and photon reads as

$$\mathcal{H} = \hbar\omega_r a^\dagger a + \hbar\omega_m m^\dagger m + \hbar g_0\sqrt{2NS}(a^\dagger m + m^\dagger a), \tag{3.17}$$

which in this form is also known as the Tavis-Cummings Hamiltonian for the coupling of a spin ensemble to a light field [11, 163].

As pointed out before, all three approaches give different pieces of information about the resonant spin-photon coupling mechanism. For instance, with an explicit expression for the coupling strength (Equation (3.16)), the temperature dependence can now be studied in detail. Besides, the dynamic approach from a combination of the LLG and an RLC circuit representation for the cavity photons allows understanding the experimental results on manipulating the coupling strength in the subsequent chapter more thoroughly.

3.5 The cooperativity C: Strong coupling in the presence of losses

In general, hybridised systems are a promising candidate for the implementation of quantum computing and new technologies in information processing, as has been previously mentioned. As previously mentioned in the discussion of the different models, the CMP is a linear system where the coupling strength represents a measure for the coherent energy exchange, i.e. the information exchange. This coherent information exchange becomes possible when the strong coupling regime is reached, where the coupling is much larger than both the cavity photon and the magnon losses. As indicated in the introduction of this chapter, the strong coupling regime is reached for:

$$g_{\text{eff}} \gg \kappa_r, \kappa_m, \tag{3.18}$$

where κ_r is the cavity resonator loss and κ_m the magnon loss parameter, respectively. However, if the losses are in the same range as the coupling strength, then there may be some coupling, but the coupling is almost immediately damped after that. As a result, there is no significant interaction between the individual subsystems. Therefore, the amount of coherent information exchange in the hybridised system needs to be quantified by considering both the coupling strength and the losses of the system which is described by the cooperativity C. Here, the cooperativity C of the system is defined as:

$$C = \frac{{g_{\text{eff}}}^2}{\kappa_r \kappa_m}. \tag{3.19}$$

Hence, if $C > 1$, the coupled system is in the strong coupling regime [4, 11]. Moreover, for cooperativities smaller than one ($C < 1$), the coupling of the system is in the weak coupling regime if and if the coupling energy is in the same order as the energy of the system and $C \gg 1$, the ultra-strong regime is reached [159]. First, the temperature dependence of the coupling strength and the magnon linewidth will be discussed in Chapter 4. This characterisation allows one then to examine the temperature dependence of the cooperativity and classify the coupling regime of the CMP for the experiments conducted in the course of this doctoral thesis.

Chapter 4

Temperature-dependent cavity magnon-polariton spectroscopy

This chapter is about the temperature dependent study of the main characteristics of a cavity magnon-polariton (CMP) from $T = 30\,\mathrm{mK}$ to $T = 290\,\mathrm{K}$. Here, the CMP is the associated quasiparticle from the resonant coupling of Kittel mode magnons in a Yttrium-Iron-Garnet sphere (YIG) and cavity photons of a three-dimensional (3D) reentrant cavity resonator. Correspondingly, the main characteristics are the macroscopic coupling strength $g_{\mathrm{eff}}(T)$ and the Kittel mode magnon linewidth $\kappa_m(T)$. Thus, their temperature dependence is examined in more detail in this chapter. In turn, the knowledge about $g_{\mathrm{eff}}(T)$, $\kappa_m(T)$ and the total cavity resonator loss corresponding to $\kappa_r(T)$, also allows determining the temperature dependence of the cooperativity C. If $C > 1$, there is a coherent information exchange between the magnon and the (cavity) photon including the presence of losses. As mentioned in the introduction, the existence, characterisation and control of such a coherent exchange of information are fundamental for any form of application such as in information processing. It requires the hybridisation of the magnons and cavity photons in the strong coupling regime, where the coupling strength exceeds the individual dissipation of both subsystems. In this regard, the creation of strongly coupled CMPs in a 3D resonator has been experimentally demonstrated both at millikelvin and room temperature. In the millikelvin temperature regime, one operates with low photon numbers or even in the single photon regime and the coupled system is described by quantum mechanics. However, the room temperature experiment corresponds to a demonstration of strong coupling including features similar to a Rabi-like oscillatory behaviour between magnon and photon in an entirely classical temperature regime. Thus, it is necessary to understand the transition from millikelvin temperatures, i.e. the quantum regime, to room temperature, i.e. the classical regime for the CMP. Accordingly, understanding that transition results in characterising quantities such as $g_{eff}(T)$ which give a measure for the coherent information exchange as a function of temperature.

In summary, the chapter is structured as follows. First, an overview of the whole experimental apparatus for a temperature dependent study of the CMP is given. Specifically, this includes the design of a dipstick for the measurements from $2\,\mathrm{K}$ to $290\,\mathrm{K}$, the construction of a suited cavity resonator, and the characterisation of the magnonic sample. Subsequently, the experimental data is presented and analysed where the temperature dependence of the effective coupling strength g_{eff} and of the magnon linewidth are individually analysed. The chapter concludes with discussing the system's cooperativity

showing the degree of coherence over the whole temperature range.

Due to technical constraints, the data below 2 K could not be measured with a standard continuous helium flow cryostat, but a dilution refrigerator located at the Karlsruhe Institute of Technology (KIT) had to be used. The corresponding data has been taken by my colleague Marco Pfirrmann with the same cavity resonator used in all of the other measurements I performed. Though, at this experimental setup, only reflection measurements could be conducted.

4.1 Components

In the beginning, before any experimental study on the temperature dependent behaviour of the CMP could be conducted, it has been necessary to design and set up an experimental apparatus for performing temperature-dependent measurements from 2 K to 290 K at the Johannes Gutenberg-University Mainz (JGU). Setting up the experiment includes the design of a new cryogenic rod for a continuous flow cryostat in the laboratory at the JGU, the implementation of electronic control, and measurement tools such as software for this type of cavity magnon-polariton spectroscopy. Furthermore, as a starting point, a suited cavity resonator meeting the physical conditions and experimental constraints for realising the study and manipulation of CMPs need to be designed and fabricated. The final design has been developed in active collaboration with Julius Krause from KIT who found the final design of this cavity resonator in the course of his Master's thesis [164]. Instead of a rectangular cavity resonator, a reentrant cavity resonator based on a proposal from Ref. [159] has been developed, since the initial design proved to be of poor quality for the spectroscopic measurements to be conducted.

4.1.1 The sample rod(s)

In order to measure at variable temperatures between 2 K − 290 K, it is necessary to insert the sample rod into a continuous helium flow cryostat. The cryostat is embedded approximately two meters into the ground and equipped with a superconducting magnet for the generation of a static, external field at the bottom. In combination with a heating wire which is controlled by a PID temperature control loop, the adjustment of the helium flow by remotely opening or closing a needle valve yields the control of the temperature in the sample space [165]. It connects the dewar filled with liquid helium with the inner sample space. The dipstick consists of a headpiece with the external wiring, a thin, hollow alumina rod, which serves as a container for the microwave and electrical connections to the sample, and a sample holder attached to the end of the alumina rod. It is inserted into the cryostat's sample space such that the sample at the sample holder is placed at the centre of the magnetic field.

In the course of this doctoral thesis, two rods with sample holders of similar design have been constructed. The second rod represents an improved version of the first one such as in terms of microwave transmission losses. However, the focus will be put on the primarily constructed sample rod, as this rod is utilised for the temperature-dependent spectroscopic experiment on the CMP from 2 K to 290 K. Nevertheless, some information about the second rod has been added for the sake of completeness and giving an overview of the specifications of the rods for later users. Both of them exhibit two microwave feed lines with SubMiniature version A (SMA) radio frequency (rf) cable connectors, schematically illustrated in Figure 4.1. In order to send a direct current (DC) signal to the sample, an additional DC connector with twelve pins is placed to the top of the headpiece. The DC cables are comprised of two twisted pairs of thin copper wire and connect the top part of the rod outside with the sample space at the other end which is immersed into the liquid helium. Whereas one pair serves as a reserve for broken connections of the first and, hence, is not in use, the other one connects an additional temperature controller.

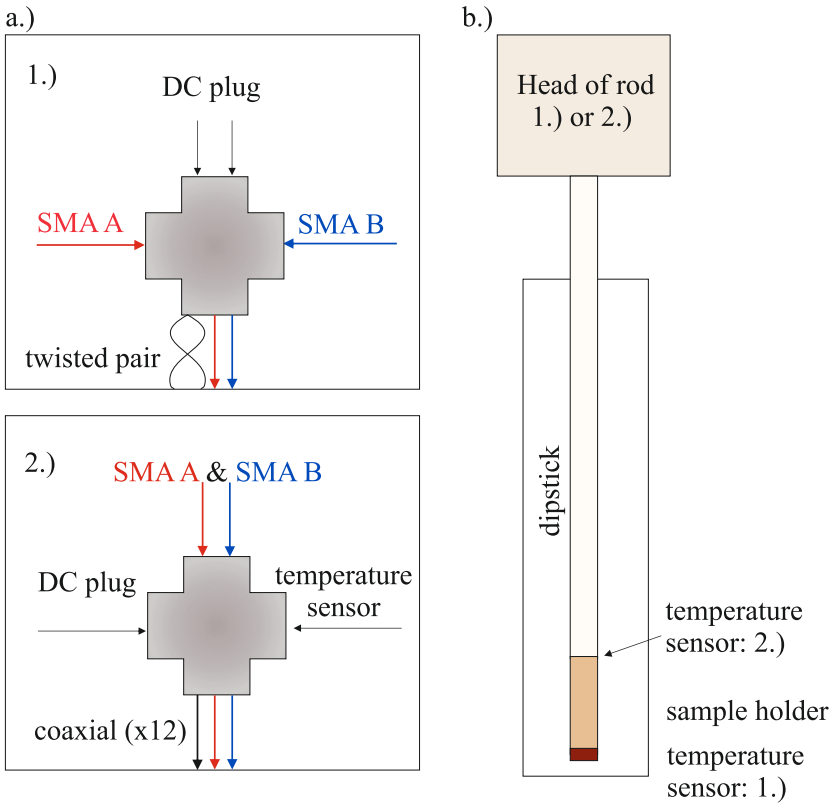

Figure 4.1: Sketch of the general design of the dipsticks. a.) Schematics of the headpieces for both rods. For the temperature-dependent measurements, the first rod (1.)) has been utilised whilst 2.) refers to the second rod. Two SMA cables A and B (c.f. Figure 4.3), are connected from the left and right side of the cross piece, and send the signal to the sample. A direct current (DC) plug with twelve connections is mounted at the top. It is connected to a temperature sensor (Cernox RTDS) placed at the bottom of the sample holder. Although both rods are identical when using them for the cavity magnon-polariton experiments, the second dipstick represents an improved version of the first one. It exhibits higher mechanical stability, increased microwave cable transmission and capability of both high frequency and additional DC measurements on bulk or thin film samples such as spin pumping experiments. Here, the SMA cables are mounted to the top, and the DC plug is attached to one side of the cross piece. Please note, that the second one has completely replaced the first rod and the temperature sensor has been added to the new rod, now. However, at the new rod, the temperature sensor is attached to the top of the sample holder because the remaining sample space below is needed for different types of waveguides, connectors and wiring. b.) Schematics of the entire sample rod, indicating the different positions of the temperature sensor for 1.) and 2.), respectively.

Before having been mounted to the sample holder, the temperature controller has been calibrated in a separate measurement, establishing the link between recorded two-point resistance and temperature. In order to put the temperature sensor as close as possible to the sample but leaving maximal flexibility for mounting different types of cavities, the temperature sensor is placed to the bottom copper plate of the first sample holder (Figure 4.1c.)). All cavities which have been used in the course of this thesis are made of solid copper. In combination with the sample holder whose material is copper as well,

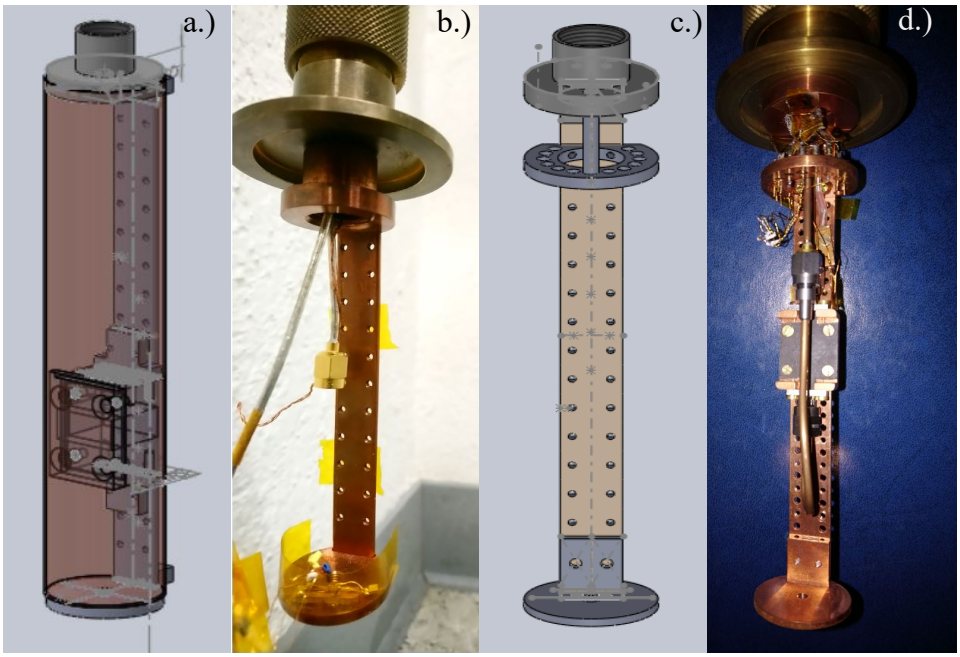

Figure 4.2: Sketch and corresponding photographs of the two different sample holders for the first (a.), b.)) and the second rod (c.),d.)), illustrating the final mount of the design shown in Figure 4.1. The Kapton foil is attached in order to both protect the cables and ensure that there is no electrical contact between the cables, the sample holder and a copper cap, which is placed later over the whole holder (not shown). For the last rod, a holder for in-plane ferromagnetic resonance (IP-FMR) measurements is attached. Technical drawings are found in the appendix.

all elements are thermally connected. When the temperature of the cryostat is changed, it is assumed that all components thermalise equally after a certain time interval which depends on the total difference between the initial and the set temperature. Moreover, the thermalisation process depends on the current level of liquid helium in the cryostat. This level sets a limit of how much each component is immersed in liquid helium or already in the area with gaseous helium further above. Later on, this sensor has been removed from the first and added to the second rod, which enables the same kind of spectroscopic measurements on the CMP like the first. Besides, through the second rod, experiments like spin pumping which require the application of a DC signal to the sample can be performed, now.

4.1.2 Design of sample holder

As it is illustrated in Figure 4.2, the sample holders of both rods differ in length and most importantly, in the way how the holder plate is attached to the rest of the rod. The first one is placed into a small recess of the part connecting the aluminium rod with the complete holder. It is fixed by small screws (M 1.5) from the top. The choice of such small screws turned out to become more and more unstable by time, especially when the attached piece is the heavy cavity resonator of solid copper. Consequently, the weight of the attached probes wore out the threaded hole. On the contrary, the second holder plate is attached sidewise. This modification allows for using stronger screws (M2 and M3) and a better translation of the attached weight. Thus, the second holder is much more

parameters	**sample holder I**	**sample holder II**
total length	95 mm	135 mm
vertical spacing	8 mm	8 mm
horizontal spacing	7 mm	7 mm
threaded holes	yes	yes
drilled holes	no	yes
temperature sensor	at bottom	at top
DC connections	4, twisted pair	12, coaxial

Table 4.1: Tabular overview over important specifications of both sample holders.

stable and robust. The instability of the first sample holder is yet another reason for the construction of the second rod, which incorporates all functions of the old one and adds some new features, as mentioned before. In this regard, an overview over the dimensions, general specifications and differences of the holder plate and the sample rod in general, can be found in Table 4.1.

4.1.3 First rod: Characterisation of SMA cables

In the course of the construction of the first rod, the corresponding SMA cables are pre-characterised in order to estimate the losses of microwave power from a vector network analyser (VNA) to the sample along the cables. They are self-assembled, measured in reflection, and then compared with standardised, commercially bought microwave cables. Figure 4.3 displays the result from the reflection ($|S_{11}(\omega)|$) measurement for the cables named A and B, respectively. The reflection loss increases linearly as a function of frequency and the amplitude fluctuations increase as well. For frequencies over $\omega/2\pi = 10\,\mathrm{GHz}$, the amplitude noise exceeds 3 dB, corresponding to a factor of 2 in reflection loss. In addition, a standing wave pattern is visible which is related to reflection loss by higher order standing waves. This results in the reduction of noise at certain points. The cables exhibit a length of 2.2 m, making a microwave reflection loss of the order of $\approx 5\,\mathrm{dB}$ per meter. For the commercially bought one, which is thicker and more rigid, the losses are expected to be lower as can be seen from the inset in Figure 4.3. The primary purpose for the first rod, where these cables are used, are spectroscopic measurements below 10 GHz, Because of high-frequency measurements of samples with small amplitudes, the design of the first rod is reconsidered, and hence the second one with much better cable transmission and lower losses has been constructed. The cables used in the second rod are semi-rigid but thin commercially bought ones. There, the general increase of reflection loss with increasing frequency is similar, but the signal to noise ratio (SNR) is orders of magnitude smaller, which allows for detection of signals with much lower amplitudes.

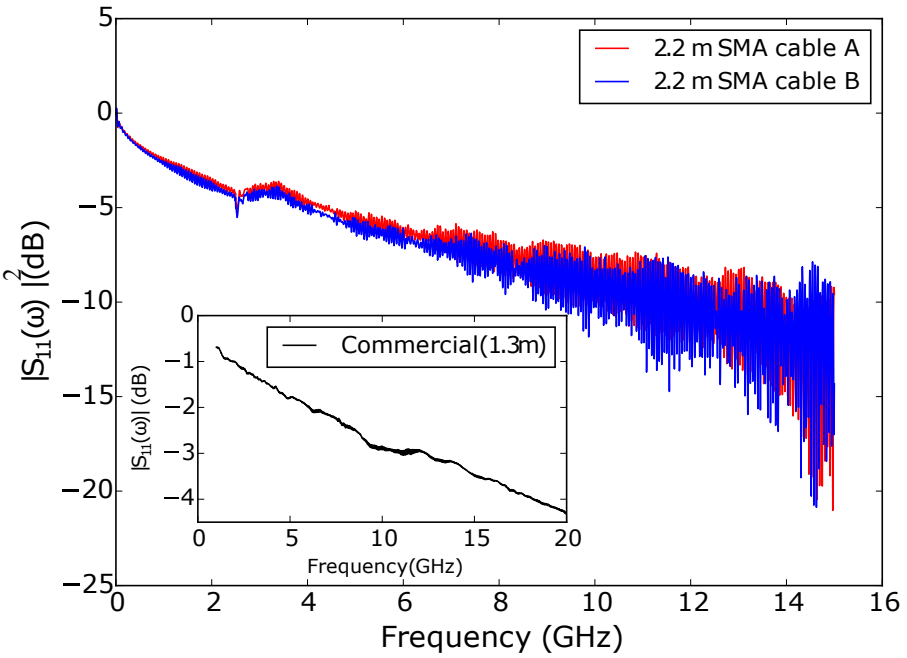

Figure 4.3: Characterisation of the inserted SMA cables a reflection measurement. For comparison, the result of both utilised cables is plotted in the same figure. The dominating contribution of the frequency loss is 1/f noise, lowering the reflection amplitude by in average 15 dB from 0 to 15 GHz with roughly 5 dB per meter. Both cables are well matched to the ports resistance (50 Ω) as the reflection starts from 0 dB. Further, despite small deviations, the cables show the same reflection behaviour. The amount of loss at higher frequencies is comparable to a commercially bought microwave cable which is shown for a cable of length $l = 1.3$ m. Please note, that the commercial cables in the laboratory are more rigid and thicker than the utilised ones, which normally results in less microwave transmission loss [99].

Before the characteristics of the reentrant cavity resonator are presented, possible sources for systematic errors given from the sample rod, and the cryostat construction need to be discussed. The identification and quantification of these errors allow confirming the reliability of the results concerning the experimental surroundings.

4.1.4 Sources for systematical errors

- **Field accuracy of the superconducting magnet** The externally applied magnetic field is the central sweep parameter for the cavity magnon-polariton system. Thus, before the first temperature-dependent measurements, the accuracy of the superconducting magnet has been measured by placing a hall probe sensor at the future sample's position. The field is both ramped up and down, the polarities changed, and the difference between the resulting values analysed. For field differences of 10 A an uncertainty of $\Delta H_{\text{ext}} = \pm 0.2$ mT is found. If the range of ramped current is much smaller, the error in the value of the externally applied magnetic is even lower (± 0.002 mT).

- **Temperature stability of cyrostat** In general, the exact temperature stability depends on the stability of the opening (given in units of a per cent from completely

closed (0%) to open (100%)) of the needle valve and the total current helium level, as well. Throughout the measurements, the temperature has been repeatedly recorded, and it is noted that in general the total temperature error is set at $\Delta T = \pm 1\,\mathrm{K}$ for higher temperatures. Unfortunately, in general, the pressure controlled by the needle valve is not stable. In a time interval of approximately 10 minutes, the valve closes (the pressure at the corresponding clock goes to zero) and then reopens to the remotely set value. This problem is not constrained to that specific cryostat, and the reason yet not found. So far, it is assumed by the persons responsible for the helium recovery cycle that the oscillation of the needle valve must be due to certain impurities in the liquid helium. As a result, the temperature error due to local temperature variations for different parts of the dipstick is increased by the temporal change in helium flow. For high temperatures ($T > 30\,\mathrm{K}$) the error bar is still in the order of $\pm 1\,\mathrm{K}$ but for lower temperatures, it quickly increases to $\pm 5\,\mathrm{K}$. Thus, the measurements at low temperatures have been conducted with high filling levels and immediate readjustment of the needle valve. Hence, this increase in temperature error could be controlled better, and the error put in the same range as for high temperatures.

4.2 The cavity photon: Design and simulation of reentrant cavity

Despite constructing the sample rod, the first step towards studying CMPs is finding a suited geometry for a cavity resonator, which meets both the physical conditions and experimental constraints. The first experimental works on strongly coupled cavity resonator photon- magnon system at cryogenic and at room temperature employed rectangular cavity resonators [56, 58, 69]. As it is also illustrated in Figure 4.4 a.) this type of cavity resonators is extended along two axes and strongly confined along the third spatial dimension [99]. Correspondingly, such a configuration allows to reach small mode volumes whilst the resonance frequency of the principal resonator mode can be kept easily below 15 GHz. As a result, it is possible to achieve a resonant coupling between the resonator and the inserted magnonic sample such as YIG with fields well below $\mu_0 H_{\mathrm{ext}} \equiv \mu_0 H_{\mathrm{res}} < 500\,\mathrm{mT}$. Therefore, a rectangular cavity resonator would represent the first choice for the temperature-dependent cavity magnon-polariton spectroscopy. Typically, such type of cavity resonators is excited in the mode with the lowest resonance frequency [99]. In the projection of the field distributions on the extended plane, the maximum of the electric field is located at the centre. Correspondingly, the magnetic field distribution describes a circumference along the cavity resonator walls, with maxima of the magnetic field in along the walls as can be seen in Figure 4.4 a.). In the case of a square, the magnetic field strength in the antinode is equal for all four sides.

The mode confined in the cavity resonator creates the time-dependent, alternating current (AC) magnetic field necessary for the excitation of spin waves. If both the cavity resonator is placed in a static external magnetic field such that this AC field points in a perpendicular direction and the magnetic specimen in one antinode of the cavity's resonator ground mode, the condition for ferromagnetic resonance is fulfilled. In this case, the Kittel mode magnons of the magnetic sample at the field's antinode can resonantly couple to the cavity resonator photons by sweeping the external magnetic field until the

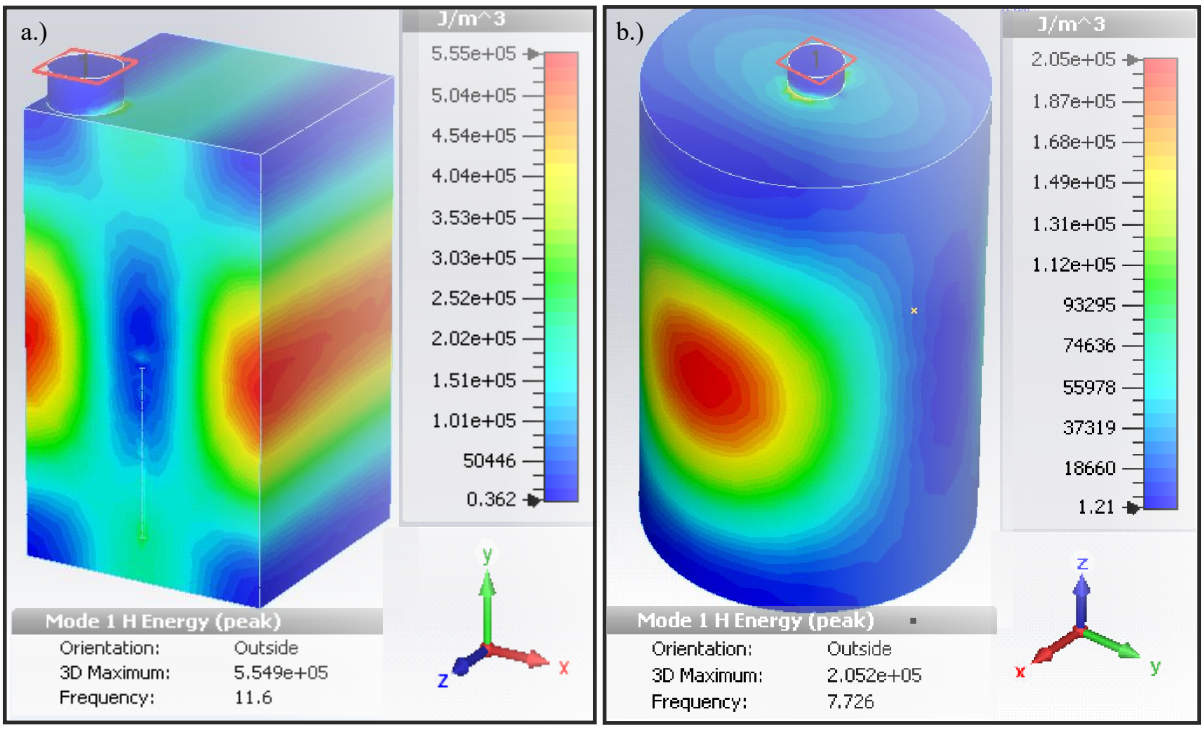

Figure 4.4: a.) Magnetic density for the lowest frequency mode of a primary design of a rectangular cavity resonator. b.) Magnetic density of the corresponding lowest mode for a cylindrical cavity resonator. These figures illustrate the mode distribution for other cavity types. They are the result of an eigenmode simulation with the CST™software [166].

magnons' and cavity photons' frequencies match. The necessity of a special alignment of magnetic DC and AC components and limited available space in the cryostat imposes constraints on the geometry and the utilised mode of the cavity resonator. Also, for the temperature-dependent study, one should operate in the strong coupling regime, i.e. when the coupling strength exceeds the individual linewidth of both the cavity resonator photons and magnons. Thus, a well-suited cavity resonator has to meet all experimental constraints, which are going to be discussed individually in the following.

1.) **Compactness**:
The maximally available sample space in the cryogenic rod built for the measurements performed at the JGU is given by the diameter of the cylindrical space in the cryostat. There, the sample, sample holder and a cap for protection of the samples have to fit in. The maximal diameter is $d = 29\,\mathrm{mm}$, which is the inner diameter of the cylindrical copper capping. In principle, the cavity resonator could be extended along the z-direction, but this is also limited. In order to apply the DC magnetic field as homogeneous as possible over the whole cavity resonator and especially the sample, the system should be as much as possible in the centre between the magnet's coils. In addition, a cavity resonator which is extended along the z-axis strongly increases the mode volume, leading to the next constraint.

2.) **Maximisation of coupling strength by resonator geometry**:
As previously stated, the coupling strength depends inversely proportional on the mode volume V_{mode} (c.f. Equation (3.16)). Thus, the cavity resonator should be

designed such that the coupling strength is maximised by minimising the mode volume. It had been shown in Chapter 3, Section 3.4, that the coupling strength scales linearly with the number of spins. However, merely choosing larger samples with a higher total number of spins does not represent a desirable general solution. This constraint is due to the premise that the cavity resonator should be usable for various sample shapes and sizes, i.e. also exhibiting reasonable coupling to the Kittel mode for samples with fewer spins. Furthermore, as the coupling strength also depends on the local strength of the applied magnetic field at the sample's position, a maximisation of the magnetic field strength would be beneficial.

3.) **Resonance frequency of chosen cavity resonator mode:**
The resonance frequency of the cavity resonator determines the frequency for the occurrence of the avoided level crossing between the magnons' and cavity photons' dispersions. Moreover, the resonance frequency determines the value for the externally applied static magnetic field to achieve a resonant coupling with the magnons in the sample. The relation between the frequency of the spins' precession around the axis of saturation magnetisation with the external field, i.e. the dispersion relation depends on the specific sample [15]. For a cavity resonator which is suited for various types of ferro- and ferrimagnetic samples, both bulk and thin film, and can also be measured at KIT the frequency of the chosen resonant cavity resonator mode should be in the order of 10 GHz such as the applied magnetic field can be kept relatively low. First, such choice of the cavity resonator's resonance frequency would enable both measurements for the cryostat located at the JGU, where field strengths up to 9 T can be applied and setups like the dilution refrigerator at the KIT, where the maximal strength of the magnetic field does not exceed 500 mT with the same cavity resonator. It could also be used for smaller magnets of room temperature setups with lower maximal field values ($\mu_0 H_{\text{ext}} < 1\,\text{T}$). Second, for measurements in the cryostat, over 10 GHz, the losses in the SMA cables greatly increase, which would complicate resolving signals with small amplitudes. Despite this, the corresponding external magnetic field should be still high enough to saturate the sample's magnetisation.

4.2.1 Coupling of the microwave feed line to the reentrant cavity resonator

In general (c.f. Chapter 2, Section 2.14), there are different means of coupling the microwave energy into a cavity resonator, i.e. exciting the standing wave photons. The insertion and the specific position of a cavity port where the microwave signal is coupled into the resonator may strongly influence the external quality factor Q_e. Therefore, the cavity resonance of one mode recorded transmission or reflection can change significantly concerning linewidth and amplitude. The excitation of the cavity resonator photons by the microwave is realised by either coupling to the electric or the magnetic field of the cavity mode. Independent from the type of coupler, as each cavity mode defines a certain spatial variation of the local amplitude with nodes and antinodes of the respective field, the coupling efficiency κ is heavily dependent on the local position of the coupler concerning the coupling field [99]. Since the linewidth of the cavity resonator's line shape determines the minimum coupling strength for which an avoided level crossing, i.e. the CMP, can be observed, the couplers should be kept fixed at the position where the linewidth of the

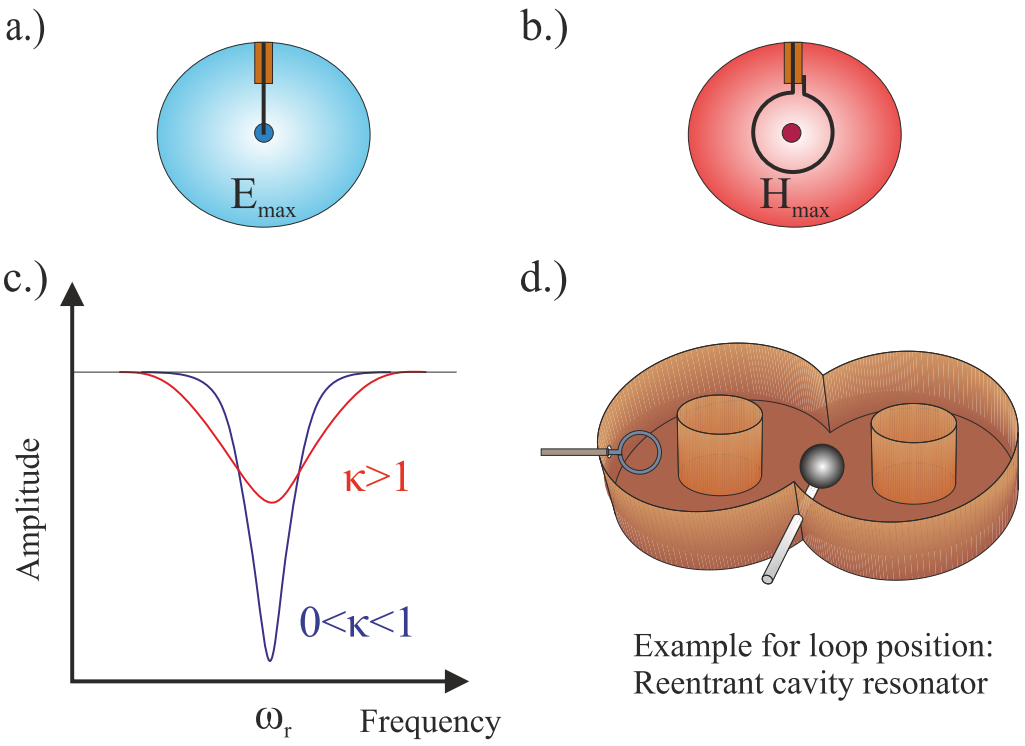

Figure 4.5: Schematical drawings of two different forms of coupling of microwave feed lines to the field of a cavity resonator mode to the antinode of the electrical (a.), capacitively) or the magnetic field (b.), inductively), respectively. c.) Change in resonance line shape of the cavity resonator for two different coupling efficiencies κ but fixed internal quality factor Q_i. ω_r is the resonance frequency of the chosen cavity resonator mode. d.) Illustration for an inductive coupling loop inserted into the final reentrant cavity resonator design which is used for the temperature dependent study of this chapter.

cavity resonance line shape is minimised.
There are two types of couplers, which either couple capacitively to the electric or inductively to the magnetic field component [99]. The capacitive coupler acts as a freely radiating dipole (antenna) and, in order to maximise the coupling efficiency, the coupler is typically placed at the electric field's antinode. Capacitive couplers typically consist of an unshielded, unterminated piece of metal wire. On the contrary, an inductive coupler in its simplest form refers to a piece of bent metal wire forming a loop with one winding. The end of the loop is soldered to the outer cable shielding which is equivalent to the ground of the corresponding cable. According to Faraday's law of induction, the current flow in the loop results in a magnetic field which leads to the inductive coupling. Figure 4.5 schematically shows capacitive and inductive means of coupling (a.) and b.)) and the change in line shape for different values of coupling efficiency κ but same internal quality factor Q_i. The loaded quality factor can be expressed in terms of κ, where $\kappa = \frac{Q_i}{Q_e}$ [99]:

$$(Q_l)^{-1} = \frac{1}{Q_i}(1+\kappa) \tag{4.1}$$

In case of inductive coupling of the microwave signal into the cavity resonator or excitation of magnons at resonance, due to the energy transfer, both processes would contribute

in locally distorting the same magnetic cavity resonator field. Thus at first, capacitive coupling would be more advantageous for such magnon polariton spectroscopy experiments because the coupler and magnetic specimen are not only spatially but also separated with respect to the electric and magnetic fields, and the mutual influence during coupling is reduced. Such coupling is less problematic for extended resonators with a large volume, but for small cavity volumes and higher resonance frequencies, it can be important to thoroughly separate the couplings of the microwave feed line and cavity photon to the magnons in the sample. However, this type of capacitive coupler as shown in Figure 4.5 is much more sensitive to temperature variations as the corresponding metal wire changes its length. As a result, the optimum position of the coupling loop concerning the field's antinode for a maximised coupling change, and the coupling loop no longer be located at the ideal position. Thus, that variation in position can induce a substantial change in the external quality factor, hence the loaded quality factor, and distort the desired cavity resonance of maximal amplitude and narrowest possible linewidth. Since the aim is to study the properties of the temperature dependence of the CMP, in the final design inductive coupling has been used exclusively. In order to minimise any cross-influence especially at resonance, the coupling loop for the excitation has been placed at the largest distance to the sample (c.f. Figure 4.5 d.))

4.2.2 Reentrant cavity resonator

If the above considerations are taken into account, another type of cavity resonator is much better suited for the experiments presented here, namely a reentrant cavity resonator [167]. Reentrant cavity resonators represent another class of cavity resonators that were first developed in the course of the construction of klystrons in the late 1930's [168, 169]. Since then, different types of reentrant cavity resonators for various applications such as particle accelerators, Gunn diodes have been developed and utilised [99, 146]. This type of cavities is also known under the term small-gap cavities since they exhibit a small gap or insertion of metalisation in the cavity's interactive region [170]. Accordingly, cylindrical reentrant cavity resonators constitute a particular type of small-gap cavities [171]. They exhibit a solid cylindrical post in the middle of the cylinder. Both the diameter and the height of that cylinder can be varied depending on the desired cavity properties but should not exceed the dimensions of the outer cylinder. Accordingly, the remaining free space creates the mode volume of the cavity. Despite new eigenfrequencies resulting from the different modes excited with other resonance frequencies, such cavities alone do not show a peculiar advantage to rectangular ones (especially for $\omega_r/2\pi < 10\,\mathrm{GHz}$). Just as rectangular cavity resonators do in the simple cylindrical configuration, they do not exhibit any unique property like additional enhancement of the absolute amplitude of the AC magnetic field. Further, the magnetic field distribution modes of the lowest resonance frequency are maximal at the circumference of the cylinder. Thus, samples such as spheres or thin films have to be attached as close as possible to the wall, which can be difficult for large samples due to the wall's curvature. Accordingly, such a curvature leads in locally, different distances of the sample to the magnetic field's antinode at the wall and strong amplitude gradients of the magnetic field strength along the sample. As a result, the magnetic field is inhomogeneous throughout the sample which increases the probability of exciting spatially non-uniform higher order magnetostatic modes next to the Kittel mode. The parasitic excitation of higher order modes should be avoided as much as possible because the dispersion spectra exhibiting an avoided level crossing for

each mode at the specific resonant coupling field will become much more complex. For instance, for simultaneous couplings of two magnon modes to the cavity resonator which are close in resonance frequency, the respective avoided crossings may influence each other. Correspondingly, this crosstalk could result in a distortion of the avoided crossings such as modifying the coupling strength. Consequently, the analysis will become more complicated and the separation of the respective contribution of every single mode to the other one will be aggravated. Thus, such utilisation of cylindrical cavity resonators can represent a disadvantage compared to a rectangular cavity resonator where it is easier to place the sample at a sufficiently homogeneous distribution of the magnetic field.

4.2.3 Double-post reentrant cavity resonator

For the final design of the cavity a slightly different approach has been pursued which combines advantages from both rectangular and cylindrical reentrant cavity resonators. Instead of one, two identical cylindrical reentrant cavity resonators with a solid post in their centre are put so close to each other, such that the outer cylinders overlap to a certain extent as can be seen from Figure 4.6 a.) - d.) [159]. Depending on the individual direction of the currents in the posts in the middle of each cylinder, the value of the effective magnetic AC field in the middle between both posts can be either set to zero (the currents are antiparallelly oriented) or maximised (currents are parallel) to twice the value of each individual field. These orientations refer to the first two principal modes at low frequencies which are called the "dark" and "bright" mode for the cancellation or enhancement of the magnetic field strength between the posts, respectively. Since the coupling strength depends on the amplitude of the AC magnetic field at the sample's position, this special configuration allows one to enhance the coupling strength.

4.2.4 Principal mode distribution of the reentrant cavity resonator

From simulations (c.f. Figure 4.6) and measurement of the "bright" mode (c.f. Figure 4.7) of the empty reentrant cavity resonator, the "dark" mode is found to be at $\omega_{r,\mathrm{dark}}/2\pi = 5.28\,\mathrm{GHz}$ and the "bright" mode at a resonance frequency of $\omega_{\mathrm{r,bright}}/2\pi = 6.48\,\mathrm{GHz}$. This number is sufficiently low to reach a hybridisation with YIG magnons at comparably low external magnetic fields but yet high enough that the magnetisation is saturated. The literature value of the saturation magnetisation of YIG is $\mu_0 M_s = 175\,\mathrm{mT}$ [98]. The saturation field is extracted from the plateau value of the hysteresis loop from a YIG sphere with diameter $d = 0.5\,\mathrm{mm}$ to be $\mu_0 H = 120\,\mathrm{mT}$ (c.f. Section 4.3), and the resonance frequency of the cavity resonator corresponds to a magnetic field of $\mu_0 H = 231\,\mathrm{mT}$. Therefore, the sample's magnetisation is fully saturated before any hybridisation with the Kittel mode can take place, and effects due to a non-saturated sample can be omitted for the following discussion. The resonance frequencies of the "dark" and the "bright" cavity mode differ by 1.2 GHz. In combination with the suppression of the magnetic field from the posts for the "dark" mode, the frequency difference to the "bright" is so large, that there will be no perturbation of the CMP spectrum at the "bright" mode's resonance frequency. Regarding possible coupling to higher order cavity modes, it is found from simulations that the next mode of the reentrant cavity resonates at a frequency of $\omega_r/2\pi = 18\,\mathrm{GHz}$. As a result, for the coupling of the Kittel mode's magnons to the cavity photons, there is no additional coupling to other cavity photons in a different resonator

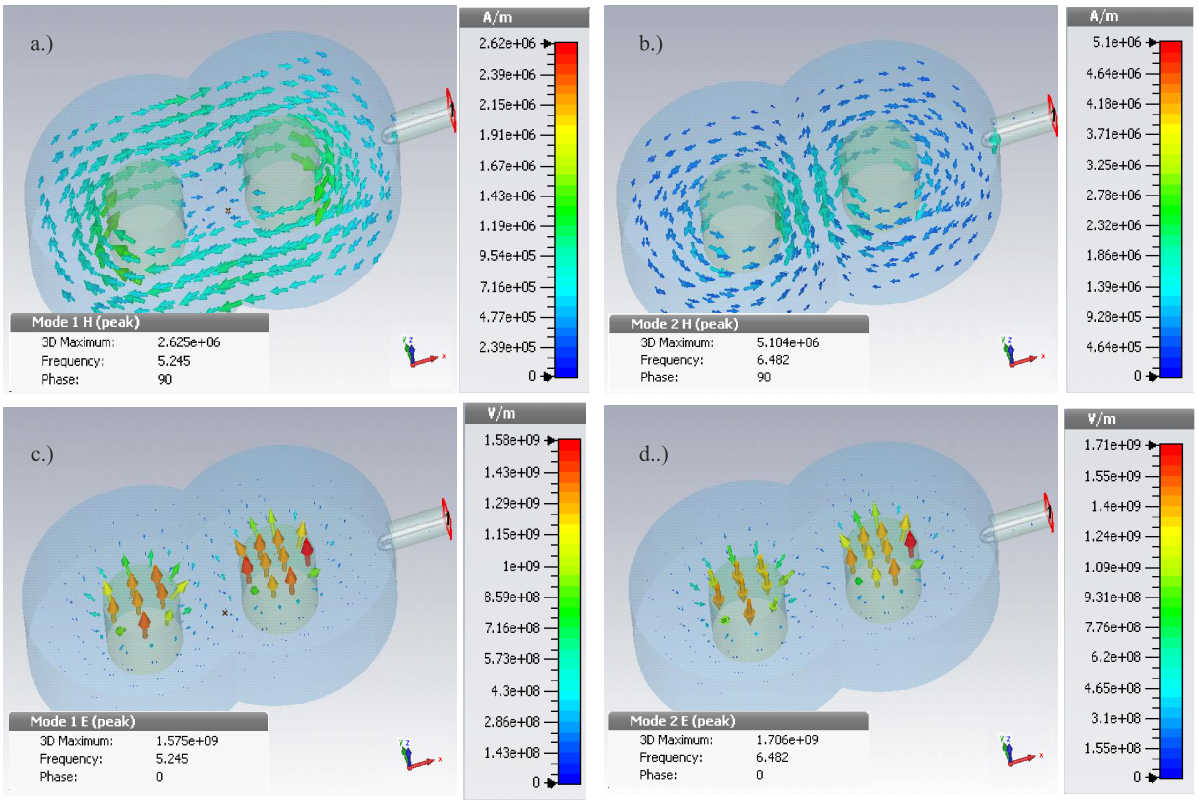

Figure 4.6: CST™(Computer Simulation Technology, [166]) simulations of the magnetic (a.) and b.)) and electric (c.) and d.)) field distribution for the "dark" cavity mode at $\omega_{\mathrm{r,\,dark}}/2\pi = 5.28\,\mathrm{GHz}$ and the "bright" cavity mode at $\omega_{\mathrm{r,\,bright}}/2\pi = 6.48\,\mathrm{GHz}$, respectively. In the experiment, the "bright" mode is utilised which exhibits an enhancement of the magnetic AC field amplitude in the antinode. As a result, the coupling strength can be further enhanced. (c.f. Equation (3.16))

mode. Thus, the observed spectra are not distorted by parasitic coupling to cavity modes below or above the resonance frequency of the empty cavity $\omega_{r,\mathrm{bright}}/2\pi = 6.48\,\mathrm{GHz}$.

4.2.5 Mode volume calculation and coupling strength

The coupling strength of the cavity photon-magnon interaction is inversely proportional to the mode volume of the cavity resonator ($g_{\mathrm{eff}} \propto \frac{1}{\sqrt{V_{\mathrm{mode}}}}$). For the calculation of the mode volume, the electric or magnetic field density distribution of the cavity mode of interest is integrated over the cavity resonator's volume, and normalised by the maximal value of the electric or magnetic field. Since the magnons in the YIG sample are excited by the AC magnetic field of the cavity resonator, i.e. coupling to the cavity photons, the coupling strength should depend on the magnetic field density as well. In the expression for the coupling strength, this link is given by the mode volume, which can be written in terms of the magnetic field density $\mathbf{B}$ [172].

$$V_{\mathrm{mode}} = \frac{1}{|\mathbf{B}_{\mathrm{max}}|} \int_{V_{\mathrm{cavity}}} |\mathbf{B}|^2 dV. \tag{4.2}$$

Thus, the coupling strength can be increased by increasing the maximum absolute value of the magnetic density distribution, because this reduces the mode volume. Referring

YIG sphere	cavity size (x,y,z) (mm)	V_{mode} (cm^3)	$g_{\text{eff}}/2\pi$ $\eta = 1$ (MHz)	$g_{\text{eff}}/2\pi$ $\eta = 0.58$ (MHz)
d=0.2 mm	32 x 32 x 5	2.304	10.06	5.836
	25 x 25 x 4	1.0421	14.96	8.677
d=0.5 mm	32 x 32 x 5	2.304	39.775	23.069
	25 x 25 x 4	1.0421	59.141	34.302
d=0.2 mm	Reentrant cavity	0.953	15.648	9.076
d=0.5 mm	h: 5.5 mm, r=10 mm	0.953	61.85	35.877

Table 4.2: Comparison of mode volume and expected coupling strength for two different sizes of the YIG sphere and the field's mode overlap η for different types and sizes of a cavity resonator. Rectangular resonators are compared to the reentrant cavity resonator. For this design, the mode volume is almost three times lower than for a comparable coupling strength in a rectangular resonator. The height h and the radius r correspond to one of the two cylindrical cavities from which the reentrant cavity resonator is formed. The final dimensions, are comparable to the rectangular cavity, although larger in the z-direction. The mode overlap value for the reentrant cavity resonator has been calculated by M. Denner in his Bachelor thesis where also technical drawings can be found [172]. Later on, these values allow a comparison with the experimentally measured values for the coupling strength.

to this, the particular design of the previously introduced reentrant cavity resonator is superior to a rectangular resonator of comparable dimensions. The enhancement of the magnetic field in the centre between both posts leads to an increment of $\sqrt{2}$ for the coupling strength. As shown in Table 4.2 the calculated mode volume yields a value of $V_{\text{mode}} = 0.953\,\text{cm}^3$ [164, 172]. Furthermore, η quantifies the mode overlap between the cavity photons in the respective cavity resonator mode and the magnons of a magnetostatic mode. Although, compared to a rectangular cavity resonator, the reentrant cavity resonator exhibits similar dimensions in the x-y plane and a reasonable extension in the z-direction, both its mode volume and the resonance frequency are much lower (c.f. Table 4.2). Thus, the values of the reentrant cavity resonator in Table 4.2 show that the compactness of this cavity leads to both a lower resonance frequency of the principal mode and higher values of achievable coupling strength for a YIG sphere of different size. Please note, that the mode volume can differ from the geometrical cavity volume which describes the enclosed volume between the cavity resonator's walls. More details and extensive simulations on the coupling of the microwave to the cavity resonator and the feed line can be found in Ref. [172].

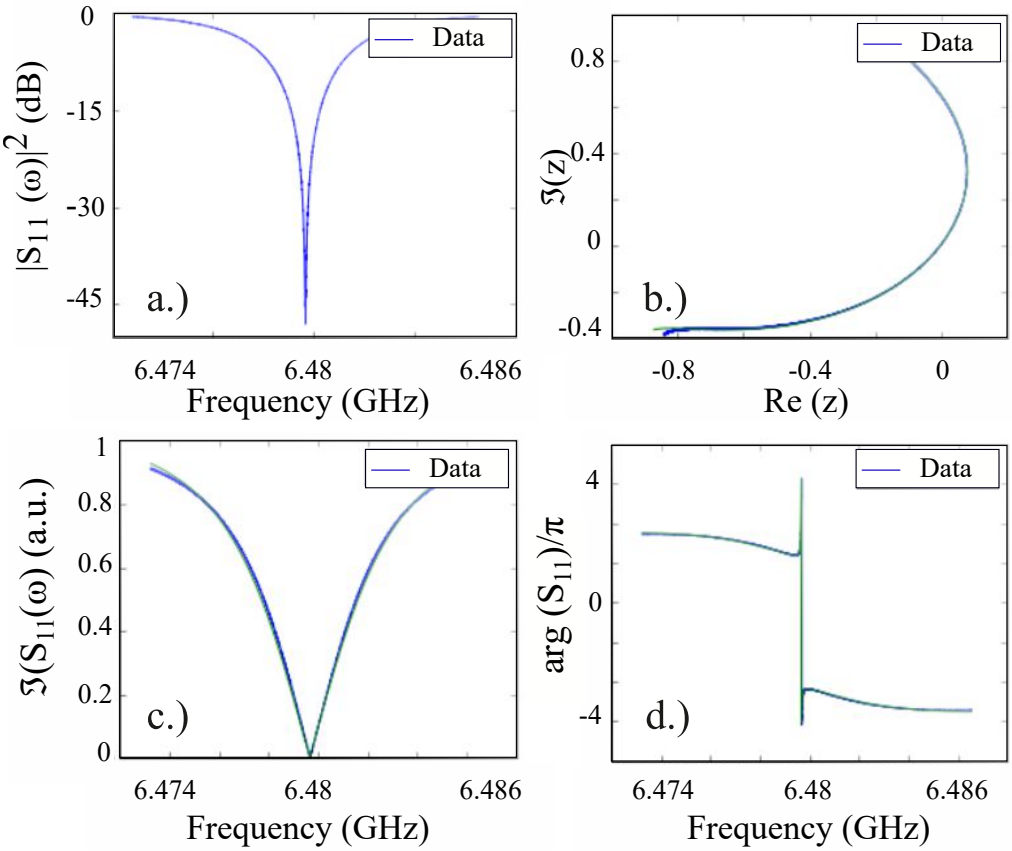

Figure 4.7: Characterisation of bare reentrant cavity resonator without any sample at room temperature through a reflection (S_{11}) measurement. a.) The cavity resonance in the "bright" mode is at approx. $\omega_r/2\pi = 6.48\,\text{GHz}$ and has an amplitude (in logarithmic units) of 48 dB. b.) - d.). The graphical illustration of the result of the circle fit in order to determine the values for the internal, unloaded and loaded quality factors Q_i, Q_0, Q_l, respectively. In b.) the data for $[z = \Re(S_{11}(\omega)) + i \cdot \Im(S_{11}(\omega))]$ and the corresponding fit in the complex plane are displayed. Accordingly, c.) and d.) show the amplitude and phase with the associated fit as a function of frequency. The values for the quality factors are given in Table 4.3.

4.2.6 Characterisation of the empty cavity

Before the insertion of a sample into the cavity resonator, it is necessary to characterise the response of the empty cavity. By doing so, the undistorted internal and external losses of the cavity resonator can be quantified. The resonance and the corresponding fit of the "bright" mode of the cavity are shown in Figure 4.7 a.). In b.), the result of from fitting a circle in order to determine the values of the internal, unloaded and loaded quality factor Q is graphically displayed. The underlying circle fit is based on code from the QKIT package and theory for modelling resonators in the complex plane [173]. Since the internal and external quality factor of the cavity differs only by 0.84 %, the cavity resonator is almost exactly critically coupled at room temperature [173, 174, 175]. The position of the inductive coupling loop has been optimised such that the cavity resonator response is maximised to an amplitude of 47 dB and linewidth of $\Delta\omega/2\pi \approx 2\,\text{MHz}$. This linewidth

Q_i	(1756 ± 2)
Q_0	(1771 ± 1)
Q_l	(881 ± 1)
$\omega_r/2\pi$	$(6.479 \pm 0.002)\,\mathrm{GHz}$
χ^2	0.00026

Table 4.3: Overview of the results from the fit of the resonator in the complex plane (Circle Fit) [173, 175].

sets a lower bound for the resolution of the cavity resonator, enabling the observation of avoided crossings with coupling strengths above the cavity resonator's linewidth. The full result from the circle fit is summarised in Table 4.3.

Nevertheless, the insertion of an additional component, such as the YIG sphere, into the cavity may change the resonance frequency as the filling factor of the cavity changes. The volume of the YIG sphere ($V = 6.54 \cdot 10^{-5}\,\mathrm{cm}^3$) which is used in the experiments of this thesis is small compared to the total geometrical volume ($V = 2.07\,\mathrm{cm}^3$) of the cavity. However, along the [110] crystal direction the YIG sphere a 1 cm long ceramic rod of beryllium oxide (BeO) is glued. Therefore, the cavity's volume will be decreased by the insertion of additional components with other dielectric constants, and the resonance frequency of the cavity resonator with the inserted sphere increases to $\omega_r/2\pi = 6.50\,\mathrm{GHz}$ at room temperature.

4.3 The magnons: Magnetic characterisation of the YIG sphere

In order to quantify the contributions of the magnonic subsystem when it is in a hybridised state with a cavity resonator photon, the magnetic sample has to be individually characterised as well before measurements on the CMP. Therefore, the saturation field and saturation magnetisation of the utilised YIG sphere of 0.5 mm diameter, the hysteresis loop of the sample is recorded at different temperatures.

4.3.1 Measurement of the hysteresis loop of the YIG sphere

The saturation magnetisation and its temperature dependence can be determined by using a superconducting quantum interference device (SQUID) where the SQUID itself has been invented in the 1960s by Ref. [176, 177]. A SQUID is comprised of a closed superconducting loop, split by a thin insulating barrier such that it forms two parallel Josephson junctions. The application of an external field leads to a change in magnetic field flux, which generates a voltage due to the Josephson effect. For more detailed information on the working principle of this device, the reader may refer to Ref. [178]. The sample is moved up- and downwards along a system of detection coils which are

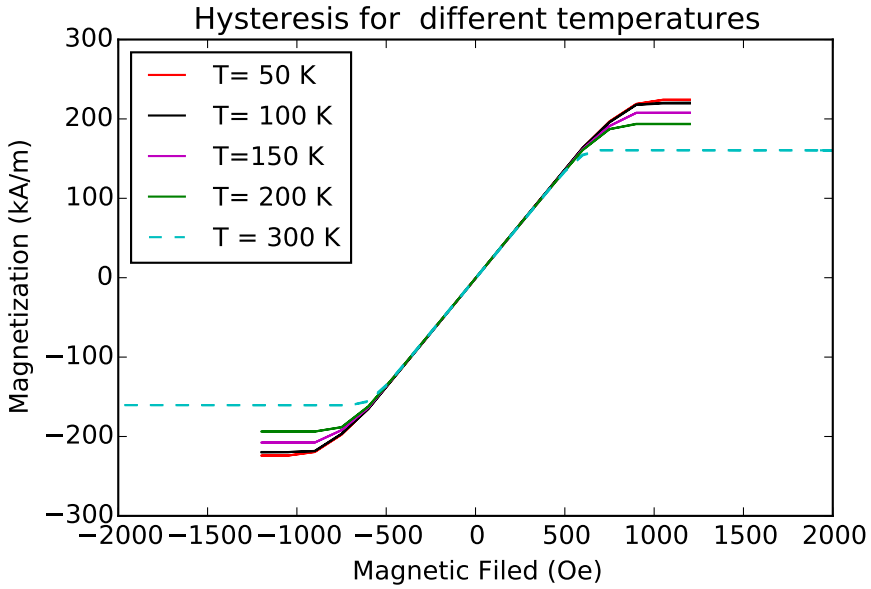

Figure 4.8: Measurement of the hysteresis for a YIG sphere of 0.5 mm diameter for temperatures from 50 K to room temperature. The saturation magnetisation corresponds to the value of the plateau both at a positive and negative polarity of the applied magnetic field.

connected to the SQUID sensor. Therefore, the movement induces a current in the coils, which is translated into a voltage at the SQUID, proportional to the magnetic moment of the sample, and the magnetisation values in the device are measured in units of emu, a short term for electromagnetic units [179].

The hysteresis describes the reversible and irreversible changes in the effective net magnetisation, measured along the z-axis of the SQUID, as the field is ramped with one polarity to saturation, then ramped to the saturation value at opposite field polarity and back. Important physical quantities here are the remanence field H_r, which denotes the magnetisation value at zero-field, the coercive field H_c, which is the field value where the magnetisation is zero and the saturation field value where the magnetisation reaches its maximal value. The hysteresis of the YIG sphere in Figure 4.8 is typical for a soft magnetic material, where the magnetisation gradually saturates as the applied field strength is increased [83]. The harder the magnetic material, the more the enclosed area of the loop increases and resembles a rectangular shape [82]. This property means that, when the saturation field is reached, all spins are aligned along this field and the maximal magnetisation is reached. The study of hysteresis loops represents a powerful and widely used tool for the characterisation and analysis of magnetic materials and the magnetisation properties under the influence of field and temperature variations (c.f. [82, 180, 181, 182, 183] and references therein).

The corresponding hysteresis loop of the YIG sphere is displayed in Figure 4.8 for different temperatures from $T = 50\,\mathrm{K}$ to $T = 300\,\mathrm{K}$ in steps of 50 K. The YIG sphere is fully saturated at a field of approximately $\mu_0 H \approx 100\,\mathrm{mT}$ with a saturation magnetisation of $M_s \simeq 160\,\frac{\mathrm{kA}}{\mathrm{m}}$ at room temperature.
Accordingly, the temperature dependence of the saturation magnetisation is extracted from the value at the plateaus at fields with different polarities and averaged. Since the saturation magnetisation depends on the total spin number N as it is the sum of individual

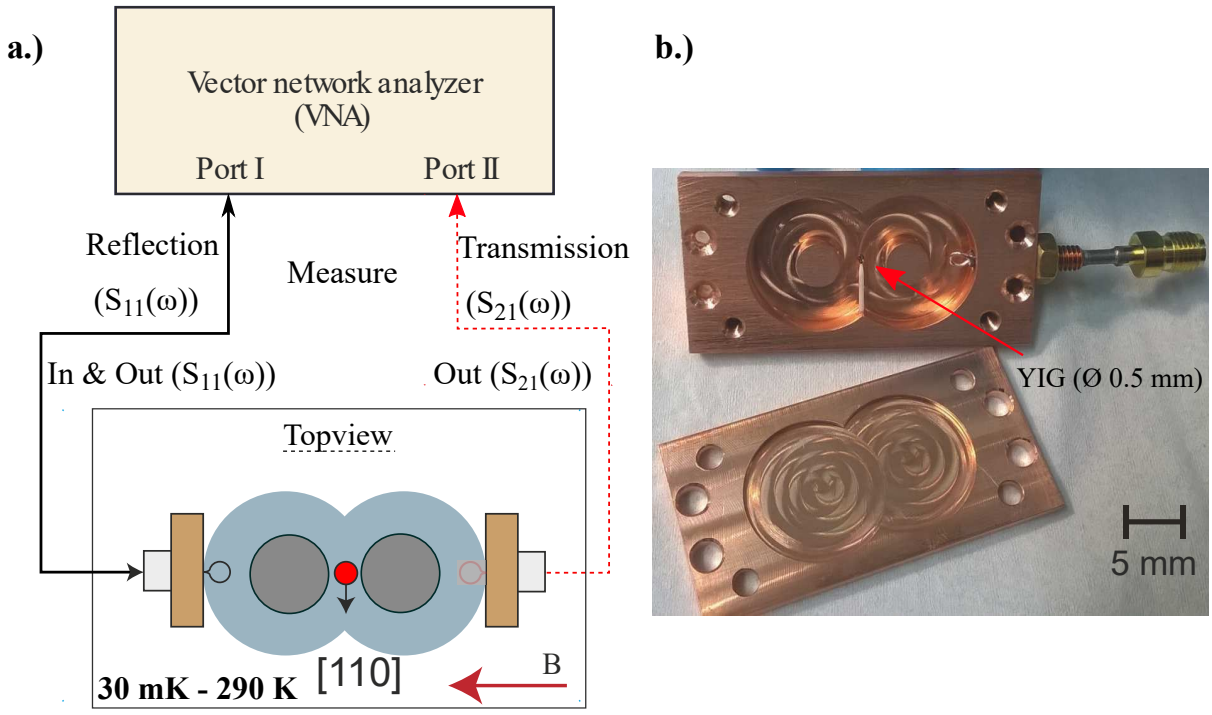

Figure 4.9: Experimental setup and position of the YIG sphere in the cavity resonator. a.) Schematics of the experimental setup. For reflection and transmission measurements the microwave signal from the VNA is inductively coupled into the resonator by means of one ($S_{11}(\omega)$) or two ($S_{21}(\omega)$) loops. The coupling loops (shaded for transmission, not mounted for reflection) are schematically drawn as circles. The YIG sphere (red) is placed in the magnetic field's antinode in the middle between the posts for enhanced coupling in the "bright" mode. b.) Photograph of the assembled YIG-cavity resonator system including an inserted inductive coupling loop.

magnetic moments [82], the changes of the saturation magnetisation are directly related to the temperature dependence of the coupling strength of the hybridised cavity photon-magnon system.

4.4 Experimental setup

After having introduced the important components individually along with the characterisation of both the photonic (cavity photon in resonator) and the magnonic (YIG sphere) part, an overview of the complete experimental setup for cavity magnon-polariton spectroscopy can be given. Schematically, the setup is displayed in Figure 4.9 a.) and, as denoted by the two microwave feed line ports in the figure, both reflection (left, bold) and transmission (right, dashed) measurements are conducted by using a two-port VNA where the output power level at the VNA is set to 0 dBm. The microwave signal travels along the SMA cables and reaches the cavity input port where it is inductively coupled into the cavity resonator. The YIG sphere is placed in the centre between the posts which corresponds to the antinode of the magnetic field in the "bright" cavity resonator mode. It has been commercially obtained from Ferrisphere Incorporated® and did not undergo any

further post-treatment before insertion into the cavity resonator. As mentioned before, the YIG sphere is glued along the [110] direction to a ceramic BeO rod of 1 cm length and inserted from the side of the cavity resonator (c.f. Figure 4.9 b.)) via a small drilling hole. The addition of holes and cuts to the cavity resonator without lowering the loaded quality factor Q_l and changing its properties is possible if the hole or cut does not interrupt the current flow of the cavity mode of interest. Furthermore, the lid of the cavity resonator does not interfere with the cavity's mode volume because the lid is placed in a parallel plane to the current and closes the resonating space. Correspondingly, this geometry avoids discontinuities of the cavity mode of interest by placing the lid wrongly such that there is an air gap between both halves, for instance. The external, static field is applied parallel to the long axis of the cavity resonator, along which it is also attached to the sample holder at the end of the cryogenic measurement rod for the temperature-dependent measurements.

4.5 Dispersion spectra

In order to study both the temperature dependence of the coupling strength and the magnon linewidth of the coupled cavity photon-magnon system, multiple dispersion spectra are taken for various temperatures. In Figure 4.10 a.) to d.) the signal amplitude including a field constant background signal (colour coded, $|S_{11}|$) of the reflection measurement is shown as a function of magnetic field and resonance frequency in steps of 50 K from 50 K to 200 K. Quantitatively, by comparing the individual figures, some aspects can Ã¶be already inferred from the raw data with the background oscillations themselves. In short, these are the changes in resonance frequency and field, variations in the width and amplitude of the signal, and the observation of additional avoided level crossings in a vicinity close to the Kittel mode's avoided level crossing. The initial observations are:

1. The resonance frequency decreases from 50 K to 200 K by approximately 20 MHz, from 6.5 GHz to 6.48 GHz.

2. The externally applied field for resonant coupling between cavity photons and magnons increases from 213 mT at 50 K to 219 mT for 200 K.

3. In all four plots from Figure 4.10 the dispersion spectra are shown for the same interval of the external field, frequency, and colour coding of the amplitude. However, the actual shape of the avoided level crossing is strongly temperature-dependent and undergoes visible changes. For instance, a comparison of the amplitudes of 50 K and 150 K shows that not only the linewidth is higher at lower temperatures, but the amplitude around the avoided level crossing changes as well.

4. For fields below the Kittel mode's avoided level crossing, additional small, field dependent, lines are occurring. At the resonance frequency of the cavity resonator's "bright" mode, they result in additional, weakly coupled avoided crossings. Correspondingly, their coupling strength is much lower than that related to the Kittel mode, as there is no clear frequency gap of the avoided level crossing to be seen. These features are clearly identifiable from 100 K to 200 K [Figure 4.11 b.) - d.)]. However, for lower and higher temperatures they cannot be directly seen from the raw data, and further data processing is necessary before the temperature dependence of the coupling strength and magnon linewidth can be extracted.

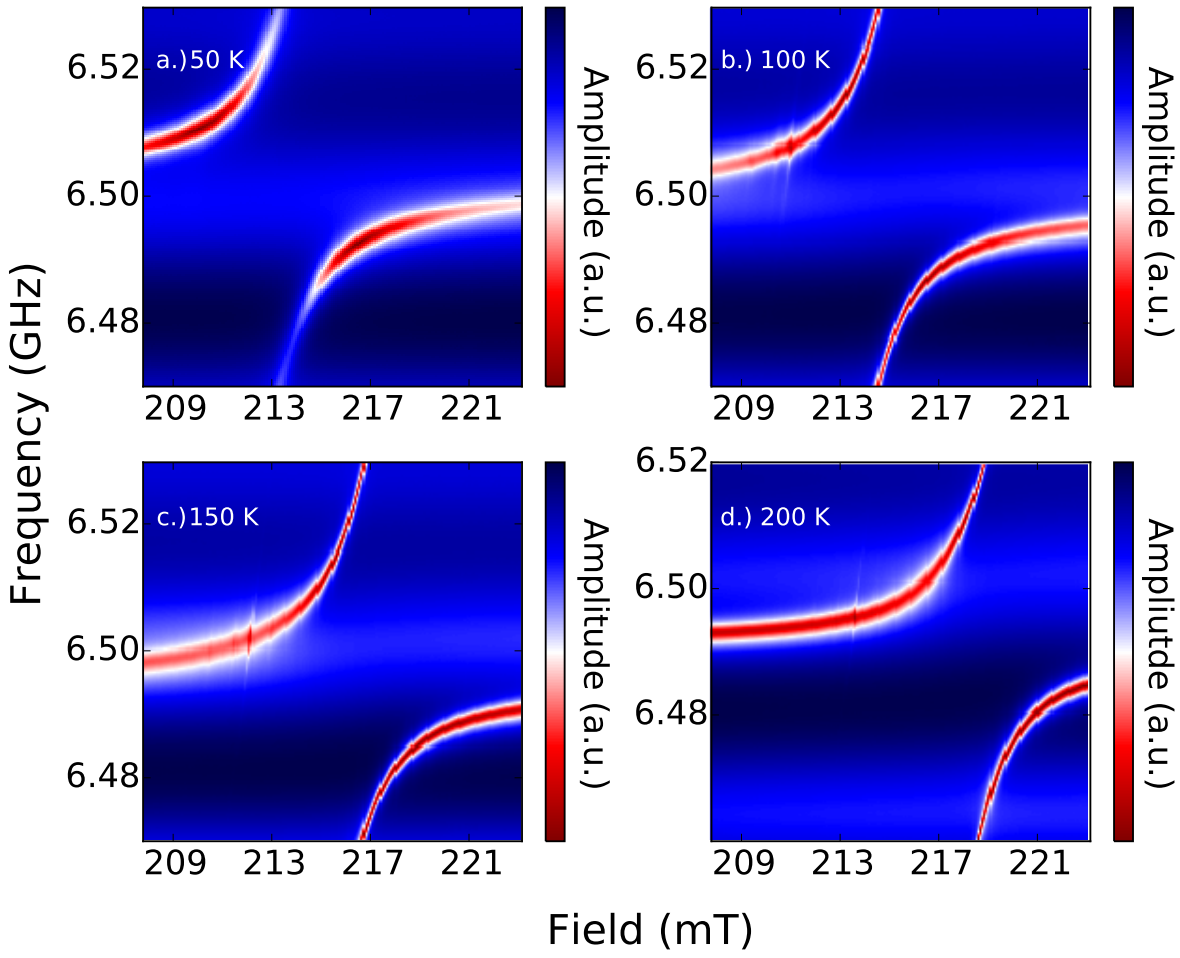

Figure 4.10: Raw data of a $S_{11}(\omega)$ measurement for four temperatures from a.) 50 K to d.) 200 K in steps of 50 K. These datasets include the field constant background (seen as the signal with periodic amplitude changes for different frequencies) and the signal of interest.

4.5.1 Data correction: Background oscillations

As illustrated in the previous discussion about the experimental setup, and the way the rods constructed, the microwave output signal has to travel along 4 m in total along the cables. The response of each cable (A and B) has been displayed in Figure 4.3. The occurrence of nodes and antinodes in the plot is a strong indication for oscillations of a certain fraction of the microwave signal within the cables. These oscillations contribute to the recorded signal at the VNA, which is a superposition from the microwave losses in the cables and the hybridisation of cavity resonator photon and magnon for certain applied magnetic fields. While the latter is strongly dependent on the effective magnetic field applied to the magnonic sample, the former represents standing wave modes in the cables and is field independent. This oscillatory signal serves as a finite background to the signal of interest, which is seen by the alternating blue and black lines in the background of the avoided level crossing in Figure 4.10. This contribution decreases the signal-to-noise ratio (SNR), meaning that signals with smaller amplitudes (SNR ≤ 1) are no longer

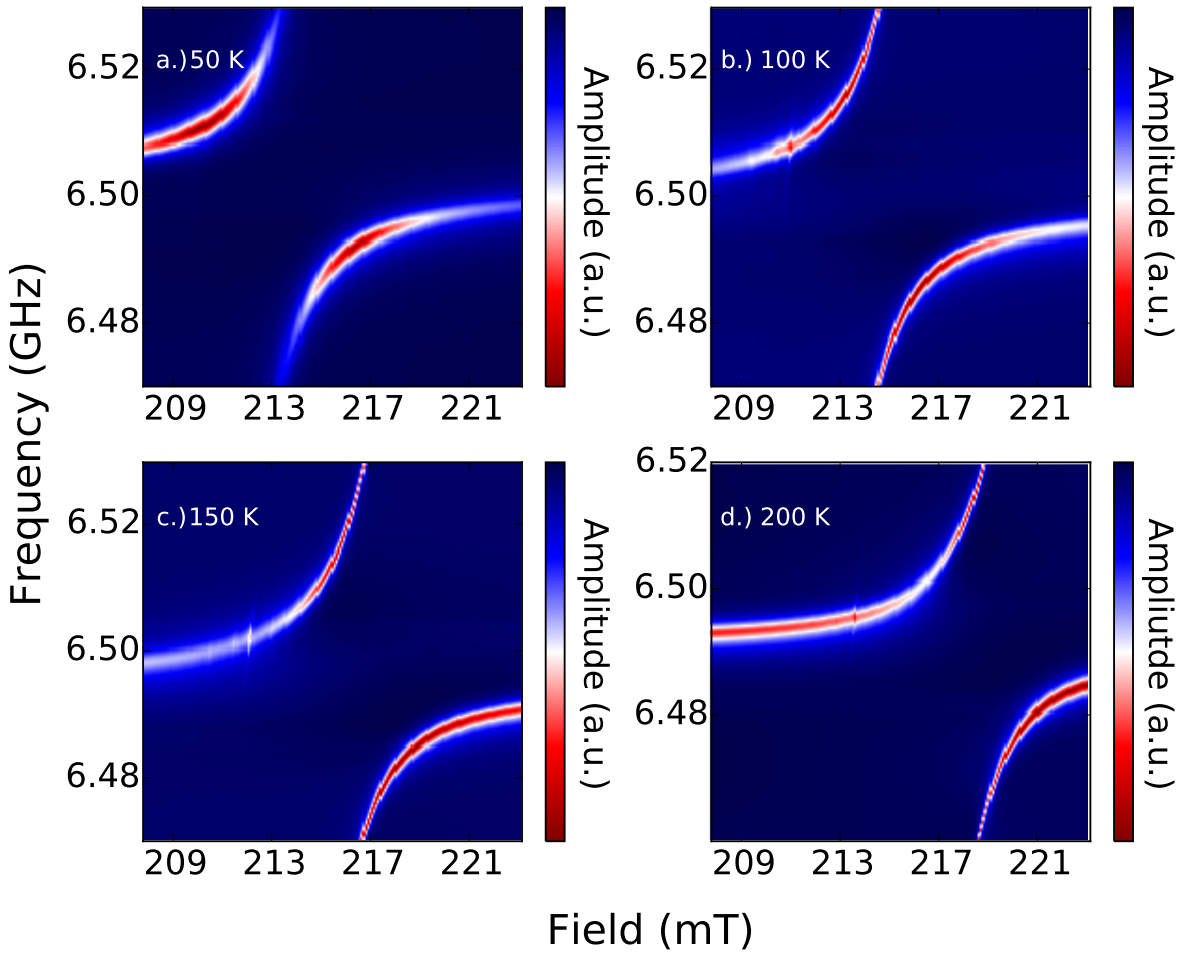

Figure 4.11: Background corrected dispersion spectra of the cavity magnon-polariton for four different temperatures for a $S_{11}(\omega)$ reflection measurement. The temperatures are a.) 50 K, b.) 100 K), c.) 150 K and d.) 200 K. The colour coded dimension refers to the amplitude ($|S_{11}|$) in linear units. From a.) to d.), both a shift towards a lower resonance in frequency and higher external field can be seen. In addition, at least one other avoided level crossing with a far smaller coupling strength is visible for 100 K and 150 K close to the Kittel mode's resonant coupling to the cavity photons. These avoided level crossings correspond to the hybridisation of cavity photons with a higher order magnetostatic mode (c.f. Section 4.6.7). The horizontal, black coloured lines, are an artefact of the background correction.

resolvable. Therefore, before performing any further data analysis regarding the initial observations, it is necessary to perform background subtraction, first. This background correction will be applied to all datasets and results in new spectra such as the ones in Figure 4.11, which are the same in Figure 4.10. However, the background correction, which was developed in the course of this thesis for this kind of spectroscopic data, has been applied. Correspondingly, the background oscillations can be successfully removed by this method, which is presented in more detail in the following.

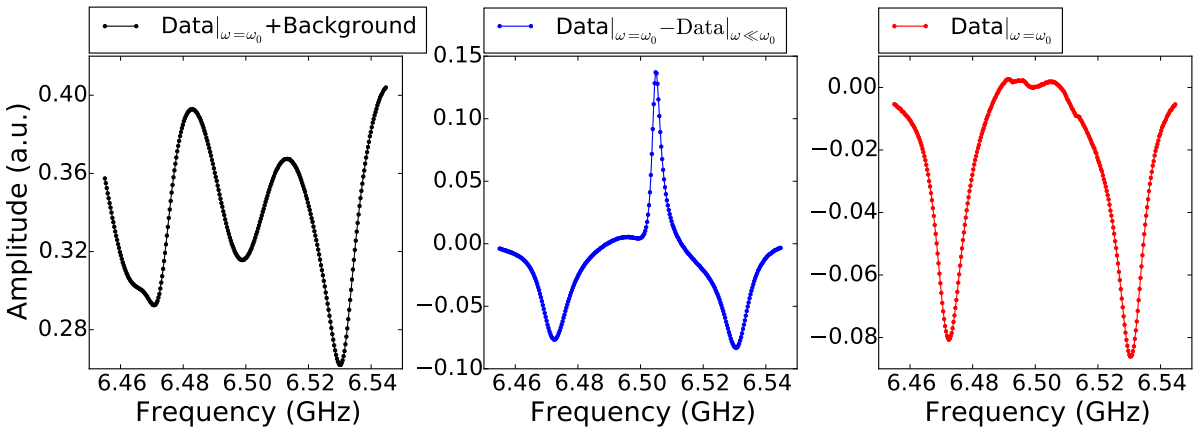

Figure 4.12: Demonstration of the fidelity of the background correction scheme for the data extraction of CMP signals with SNRs smaller than one. a.) This shows the avoided level crossing spectrum at 5 K. The background's amplitude is comparable to that of the signal. Thus, any fitting of the complex scattering parameter S_{11} will not work or give unreasonable results. b.) The result from a simple correction scheme. The fully off-resonant dataset is subtracted from the dataset at resonance ($\text{Data}|_{\omega=\omega_0}$.). The background is removed, but as an artefact, the off-resonant cavity response emerges with an inverted sign. This signal may distort the shape of one of the avoided level crossing dips and hence prevent reliable fitting of the linewidth. c.) CMP data after subtraction of the background. The avoided level crossing peaks, forming the gap of $2g_{\text{eff}}/2\pi$ are well visible. The small fluctuation in the middle is due to the chosen interval from which the cavity resonator's signal is removed and a finite region around it.

4.5.2 Background correction of CMP spectra

As previously mentioned, the background varies as a function of frequency but is constant for different magnetic field values. Hence, a simple, straightforward approach would be subtracting the first (last) data column from the whole dataset. The first (last) data column refers to one recorded frequency trace at the VNA interval with a certain frequency span for the lowest (highest) magnetic field value. Since this corresponds to an external magnetic field far from resonance, the magnons in the Kittel mode are not excited. Consequently, the signal consists of the undisturbed cavity resonance with amplitude and linewidth depending on the respective quality factors. In the hybridisation process the independent frequencies ω_1, ω_2 of the uncoupled system, i.e. its eigenvalues, are replaced by a new set of eigenvalues of the coupled system. At resonance $\omega_1 = \omega_2 = \omega_0 = \omega_r$,where ω_0 denotes the resonance frequency, and ω_r is the cavity resonator's frequency. A gap opens and the transition reads as $\omega_1, \omega_2 \rightarrow \omega_0 \pm g_{\text{eff}}$ In the avoided level crossing, there is now no signal amplitude, and the signal consisting of the background and the cavity resonator for an off-resonant field entry is subtracted from the data in the region of the avoided level crossing. Whilst the correct dips corresponding to the reflection (or peaks in transmission) measurement are displayed due to the subtraction of the background, the inverted cavity resonance signal occurs as an artefact. The cavity resonator resonant response is visible as a strong peak between the new eigenfrequencies that form the lower and upper branch of the avoided level crossing as shown in Figure 4.12 b.) for the dataset for $T = 5\,\text{K}$. One can infer from the figure that the cavity signal can distort the shape of the reflection data at resonance. For external fields close to resonance but

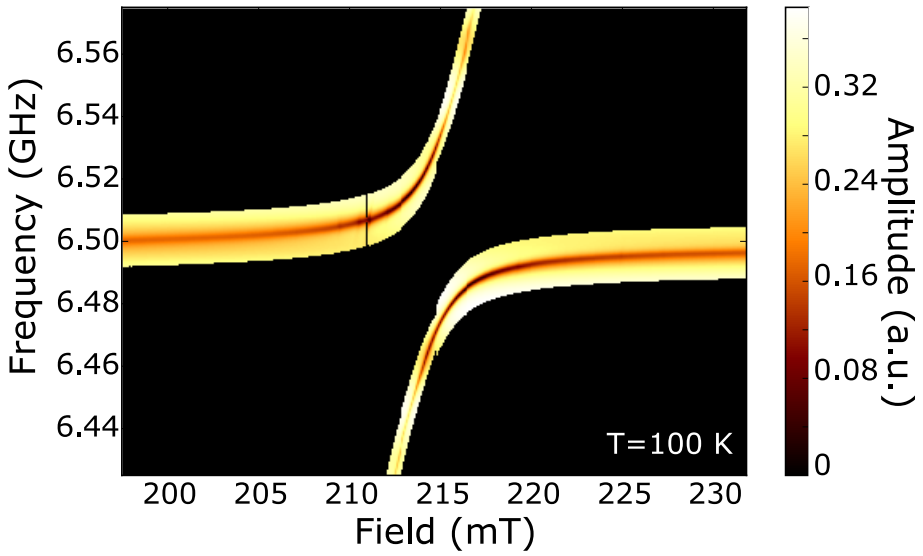

Figure 4.13: Illustration of the averaging process of the data at 100 K to exclude the contribution from the cavity's or magnons' response. The coloured area is given zero weight. Black shows the region of interest for the determination of the background and is given a weight of one in the averaging process. The small vertical black line is an artefact from the averaging process.

not at resonance, defined by $\omega_0 = \omega_r = \omega_m$, this may be an even bigger issue. In this region, the system is not fully hybridised but coupling sets in. Then the respective signal already shifts towards the new eigenfrequencies of the hybrid system, but still is close to the cavity's resonance frequency. As a result, the subtraction of the cavity resonance out of resonance can completely distort the actual signal's line shape, which calls for another correction scheme.

Correction scheme

In order to avoid the occurrence of artefacts such as the cavity resonance in the form of a peak, the contribution of the cavity has to be removed from the correction process. In other words, a background array free of any contribution of the constituents of the hybrid system has to be created. Due to the avoided level crossing at resonance, corresponding to the resonance frequency of the cavity, it is possible to find signal free regions for the whole dataset. However, for different frequencies, they are found at different values of the externally applied field. Thus, instead of taking into account the whole frequency interval at one magnetic field, each frequency entry is now considered as a function of the externally applied magnetic field. For each frequency entry, there is only a small region which does not correspond to a background signal, which is identified first. In this temperature-dependent data, the SNR is such that a simple peak search to identify the signal region is not possible. Instead, the position of the signal region is identified by calculating the gradient along the field axis. Around this position, an area corresponding to the linewidth of the signal, called the signal region, is defined. The definition of such area ensures that the complete signal is taken out in the following averaging process and no artefacts remain. Hence, the background at each frequency corresponds to the weighted

average of all field entries, where the weight of the signal region is set to zero and the rest to one, which is illustrated for 100 K in Figure 4.13. Through an iterative process, this is done for all frequencies, and the resulting background array is then subtracted from the raw data. The result from the background correction is shown in Figure 4.12 c.), exemplarily, for a temperature of 5 K. This background corrected signal is a clean, artefact free representation of the reflection data of the CMP at resonance.

Accordingly, the following analysis of the data will be based on datasets with this background correction.

4.5.3 Analytics and fitting

In order to find reliable results for the coupling strength and the magnon linewidth κ_m as a function of temperature, it is necessary to find an analytical expression for modelling the reflection $S_{11}(\omega)$ and $S_{21}(\omega)$ transmission parameter. Since many of the experiments with CMPs which have been conducted in the last years dealt with transmission measurements the expression for the transmission parameter has already been calculated [56]. The equation for $S_{21}(\omega)$ reads as:

$$S_{21}(\omega) = \frac{\sqrt{\kappa_{e,1}\kappa_{e,2}}}{i(\omega-\omega_r) - \frac{\kappa_i+\kappa_{e,1}+\kappa_{e,2}}{2} + \frac{g_{\text{eff}}^2}{i(\omega-\omega_m)-\frac{\kappa_m}{2}}}, \tag{4.3}$$

where $\kappa_{e,1}$ and $\kappa_{e,2}$ denote the losses due to the coupling to the microwave feed line of the input and output signals, κ_i is the internal cavity resonator losses, ω_r is the resonance frequency of the cavity resonator, ω_m is the frequency of the magnons, and κ_m is the loss parameter for the magnons corresponding to the magnon linewidth.

For the description of the reflection measurements an equivalent expression can be found in Ref. [58]. However, for the purpose of understanding and the derivation of a scattering formula for later experiments (c.f. Chapter 5), this expression will be derived here as well. The derivation is based on the Input-Output formalism within the framework of the Hamiltonian approach [11], where in general the Hamiltonian describing the whole system can be written as:

$$\mathcal{H} = \mathcal{H}_{\text{sys}} + \mathcal{H}_{\text{bath}} + \mathcal{H}_{\text{int}}, \tag{4.4}$$

where $\mathcal{H}_{\text{sys}}$ corresponds to the Tavis-Cummings Hamiltonian. Whilst $\mathcal{H}_{\text{sys}}$ refers to the intracavity interactions such as the coupling between cavity photon and magnon, $\mathcal{H}_{\text{bath}}$ describes the external environment, i.e. the bath, and $\mathcal{H}_{\text{int}}$ the interaction between the external field modes and the internal cavity photons. As a next step the equations of motion (EOM) for both the cavity photons $(a, a^\dagger)$ and the magnons $(s, s^\dagger)$, which include damping and diffusion, are written in the Langevin form, yielding [89]:

$$\frac{ds}{dt} = -\frac{i}{\hbar}[s, \mathcal{H}_{\text{sys}}] - \kappa_m \cdot s, \tag{4.5a}$$

$$\frac{da}{dt} = -\frac{i}{\hbar}[a, \mathcal{H}_{\text{sys}}] - \kappa_r \cdot a + \sqrt{2\kappa_e} b_{\text{in}}(t). \tag{4.5b}$$

An excellent derivation of a reflection or transmission parameter from Input-Output theory can be found in Ref. [11] and, here, the formulae for the scattering parameters are derived analogously to Ref. [11]). However, in order to adapt the general case to a CMP, the following assumptions and steps for the derivation of the final formula are made:

1. The magnons are not coupled to the external bath, but solely to the cavity photons.
2. The photons are coupled to the external bath which represents the input microwave field.
3. The following Input-Output relation between the signal entering and leaving the cavity resonator is utilised [11]: $b_{\text{out}}(\omega) + b_{\text{in}}(\omega) = \sqrt{2\kappa_{e,i}}a(\omega)$, where $b_{\text{out}}(\omega)$ and $b_{in}(\omega)$ denote the output and input from the microwave feed line to the cavity resonator port , respectively, and $a(\omega)$ is the internal cavity photon field.

The EOMs are solved and, by means of a Fourier transformation, expressed as functions of the frequencies ω. In correspondence to the transmission scattering parameter, this calculation results in:

$$S_{11}(\omega) = -1 + \frac{2\kappa_e}{i(\omega_r - \omega) + \kappa_r + \frac{g_{\text{eff}}^2}{i(\omega_m - \omega) + \kappa_m}}. \tag{4.6}$$

Depending on whether the experimental data refers to a reflection or transmission measurement, the data can be now fitted by means of Equation (4.6) or Equation (4.3), respectively. Referring to the fitting, generally, the free parameters are the external loss parameter κ_e from the coupling of the microwave into the resonator, the resonator frequency ω_r, the total resonator losses κ_r, the magnon frequency ω_m, the coupling strength g_{eff}, and the magnon linewidth κ_m. As a result, the total number of parameters used in the fitting process is comparably high, and the result of the fitting is highly sensitive to the precision of the input parameters. Therefore, the fitting procedure is performed in two steps. First, the coupling strength and resonance frequencies are determined by a fit to the avoided level crossing spectrum. Then, this is used as a precise input to the analytical expression for reflection or transmission. Such a two-step process has the advantage that the inputs could be given with higher accuracy. Specifically, the results such as the coupling strength for the parameters could be partially compared, and hence improving the quality of the final fit.

Fitting the avoided level crossing

In order to find a reasonable estimate for the frequencies ω_r and ω_m and the coupling strength g_{eff} the complete avoided level crossing is fitted. Accordingly, the frequency eigenvalues of the 2x2 matrix of the eigenmodes of the coupled system are determined which yield a solution for the symmetric and antisymmetric branch of the hybrid system's dispersion. Then, the spectrum of the avoided crossing is separated into the lower (symmetric) and upper (antisymmetric) frequency branches. Subsequently, a peak search algorithm is utilised to determine the dispersion, and each branch's dispersion is fitted in terms of a least-squares algorithm to the respective eigenvalue. In addition, the circle fit method is applied to the data entry far from resonance. In analogy to the case for the empty cavity, this allows for finding a good estimate of the quality factors Q_l, Q_i, and Q_e. The relation between the quality factors and the loss factors $\kappa_i, i \in (l, i, e)$ in Equation (4.6) and Equation (4.3), respectively, is:

$$Q_i = \frac{\omega_0}{2\kappa_i}, \tag{4.7}$$

where ω_0 denotes the corresponding resonance frequency of the considered quantity [67]. Thereby, it is possible to also find a good input value for the corresponding loss parameters of the coupling to the external feed line and the cavity resonator in the final fit of

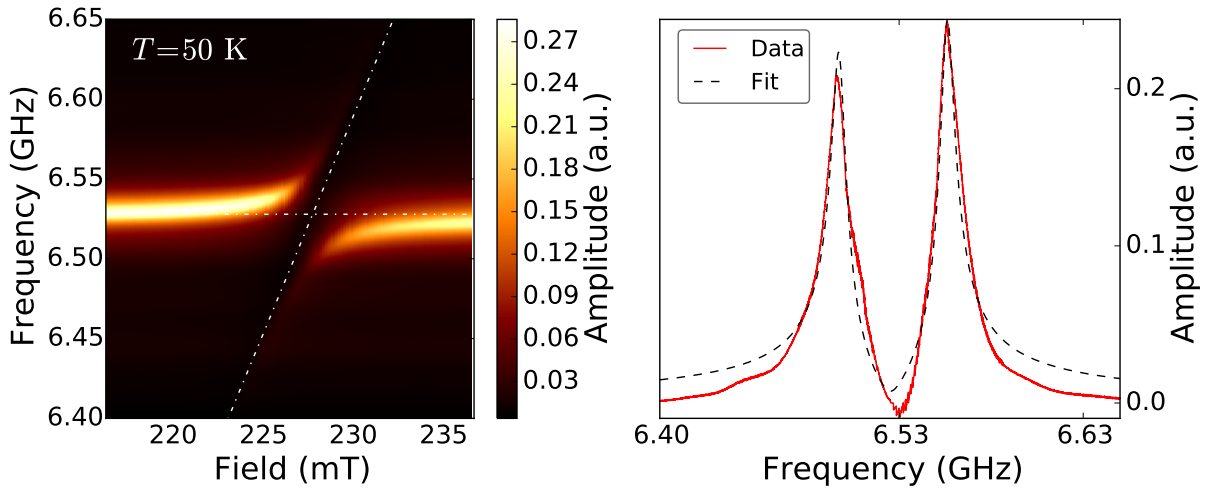

Figure 4.14: a.) Amplitude spectrum of a background corrected dataset for a transmission measurement at $T = 50\,\mathrm{K}$. The dotted lines (white) correspond to the individual dispersions of the cavity photons and the magnons. b.) Result of the fit of Equation (4.3) (black, dotted) to the data (red, solid line) as a function of frequency at resonance at $\mu_0 H_{res} = 228\,\mathrm{mT}$ from a.). The fit parameters are $\kappa_m/2\pi = (7.31 \pm 0.02)\,\mathrm{MHz}$, $\kappa_{e,1}/2\pi = \kappa_{e,2}/2\pi = (1.79 \pm 0.04)\,\mathrm{MHz}$, $\kappa_r/2\pi = (4.53 \pm 3.89)\,\mathrm{MHz}$, $\omega_r/2\pi = 6.528\,\mathrm{GHz}$, $\omega_m/2\pi = 6.525\,\mathrm{GHz}$, and $g_{\mathrm{eff}}/2\pi = (29.29 \pm 0.03)\,\mathrm{MHz}$. The error bars for ω_r and ω_m are of the order of 10^{-7}. The huge error on κ_r shows that the fit is rather sensitive due to the high number of parameters and is strongly dependent on the input parameters.

the experimental data.

Please note that Alexander Stehli from the KIT originally developed this method of fitting the avoided level crossing. For the data analysis of the measurements conducted at the JGU, I carried out small modifications to the code in order to adapt this code to the framework of our analysis. In addition, I used his ansatz only for pre-characterisation, the actual fitting of the data is based on an algorithm including the previous background correction scheme, I developed for data with partially bad SNR.

Fitting of the experimental data

The results from the fit of the avoided crossing and resonator comprise a set of starting parameters, which are used for a reliable fit of either scattering parameter for reflection ($S_{11}(\omega)$) or transmission ($S_{21}(\omega)$). Exemplary, Figure 4.14 a.) shows the transmission amplitude's dispersion spectrum of the background corrected dataset at $T = 50\,\mathrm{K}$, where the white, dotted lines indicate the dispersions of the uncoupled system constituents. If the coupling strength is zero ($g_{\mathrm{eff}}/2\pi \equiv 0$), the dispersions would cross at resonance. Accordingly, the absence of an avoided crossing means that there is either no or a strongly suppressed coherent information exchange. For instance, such suppression could be advantageous if one aims to store individual pieces of information deliberately in either the photonic or magnonic subsystem. Later, in Chapter 5, a method to control the coupling strength by enhancing or suppressing it is presented. The second part of Figure 4.14 displays the fit result (black, dotted line) together with the transmission amplitude (red, solid line) as a function of the frequency at resonance ($\mu_0 H_{\mathrm{ext}} = 228\,\mathrm{mT}$). The devia-

Parameter	Fitresult
κ_m	(7.31 ± 0.02) MHz
$\kappa_{e,1}/2\pi$	(1.79 ± 0.04) MHz
$\kappa_{e,2}/2\pi$	(1.79 ± 0.04) MHz
$\kappa_r/2\pi$	(4.53 ± 3.89) MHz
$\omega_r/2\pi$	6.528 GHz
$\omega_m/2\pi$	6.525 GHz
$g_{\text{eff}}/2\pi$	(29.29 ± 0.03) MHz

Table 4.4: Numerical result from the fit of Equation (4.3) to the data shown in Figure 4.14 b.)

tion of the fit from the data around the baseline can be attributed to residues from the background correction which remain in the signal and the small asymmetry between both peaks. Also, this small deviation explains the error in the loss parameter κ_i, i.e. the internal quality factor. The fit results are summarised in Table 4.4.

4.5.4 Error bars

At the beginning of this chapter, the sources for possible systematic errors are discussed. In addition to these, the uncertainties in the sample's exact volume, the filling factor and the resonance frequency, the applied field to name a few of them, result in error bars for both the magnetisation and coupling strength. These quantities can be directly inferred from the data without any modelling process. However, for the extraction of parameters such as linewidth of the magnons κ_m and the loss parameters κ_i in general, the analytical expression is used. Of course, these parameters also depend on "external" errors such as temperature instability, but without the knowledge of the temperature dependence of these values, the estimation of the uncertainty can be relatively imprecise. Hence, the error bars of the quantities obtained from the fitting process are the result of calculating the root mean square of the standard deviation of the model with the data. Computationally, in addition to the result on the parameters themselves, the least squares algorithm from the Python package SCIPY also returns the Jacobi matrix $\mathbf{J}$. If one assumes Gaussian errors, the Hessian matrix can be approximately computed by $\mathbf{H} \approx \mathbf{J}^T\mathbf{J}$ [184]. Then, from the Hessian matrix, the covariance matrix C can be obtained, which is needed for the final calculation of the error. The covariance matrix is expressed as $\mathbf{C} = \sigma^2\mathbf{H}^{-1}$, where σ^2 denotes the variance of the residuals. This gives for the calculation of the error $\Delta\mathbf{x}$ of a (vector) array $\mathbf{x}$ of length i, where i corresponds to the number of fit parameters:

$$\Delta\mathbf{x} = \sqrt{\text{diag}(\mathbf{C})} \tag{4.8}$$

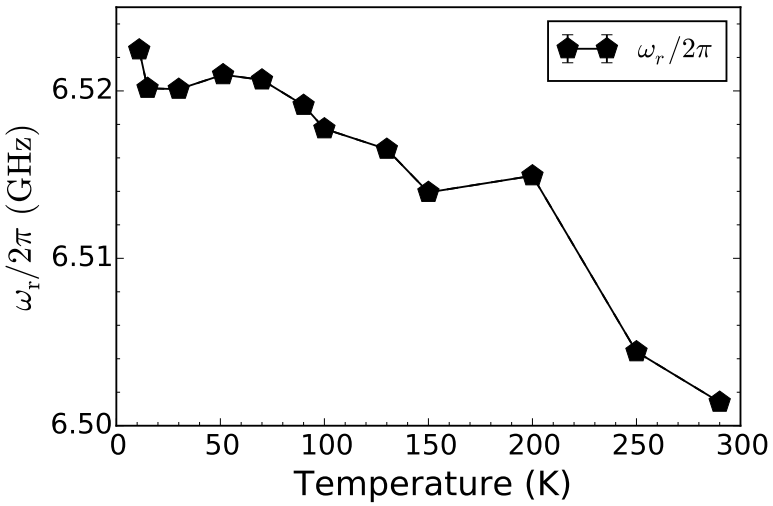

Figure 4.15: Temperature-dependent change of the resonance frequency of the bright mode of the cavity resonator. The resonance frequency changes in total by $\Delta\omega_r = 0.03\,\%$ over the full studied temperature range, which results in a total shift of $\Delta\omega_r/2\pi = 0.02\,\mathrm{GHz}$ The error bars are in the order of 0.01 and smaller than the data point symbols.

Now, with all tools for a quantitative data analysis at hand, the data can be background corrected and fits the expressions for reflection or transmission can be made. Then, the exact temperature dependence of the coupling strength, magnon linewidth and cooperativity can be obtained from the outcome of the fits. Based on this, the origin, influence and relative weight of the changes in these quantities are individually discussed in the following sections. First, the temperature dependence of the saturation magnetisation and its relation to the coupling strength is analysed.

4.6 Temperature dependence of the coupling strength

As denoted previously (c.f. Section 4.3.1), the macroscopic coupling strength depends on the resonance frequency of the coupled system, the gyromagnetic ratio and the total number of spins which, in principle, could all change as a function of temperature. Referring to the total number of spins, this quantity is directly related to the saturation magnetisation. The saturation magnetisation denotes the effective sum of all magnetic moments when they are all aligned along an external, static magnetic field. Each magnetic moment corresponds to one spin, thus $M_s \propto N$ and, in principle, $g_{\mathrm{eff}} \propto \sqrt{M_{\mathrm{s}}}$. In general, all these quantities can depend on temperature in different ways, and it is not clear from the beginning which contribution dominates the general temperature evolution of the effective coupling strength g_{eff} Thus, the individual contributions and the relative weights of these quantities to temperature-dependent changes of the coupling strength need to be discussed first.

4.6.1 Temperature dependence of the resonance frequency of the cavity resonator

The resonance frequency of the cavity resonator ω_r determines the centre frequency ω_0 of the avoided level crossing at resonance. At the resonant coupling field, the individual frequencies match, i.e. $\omega_0 = \omega_r = \omega_m$. Hence, any change in the cavity's resonance frequency results in a change of the resonance frequency of the avoided level crossing. The dispersion relation for a spherical sample, such as the YIG sphere relates the necessary external field to be applied for resonant coupling with the frequency of the cavity. In total, from 290 K to 2.4 K the resonance frequency increases by $\Delta\omega_r = 0.03\,\%$ (c.f. Figure 4.15) from $\omega_r/2\pi = 6.50\,\mathrm{GHz}$ to $\omega_r/2\pi = 6.52\,\mathrm{GHz}$. The increase itself is strongest between 250 K and 200 K. Presumably, this change of 0.02 GHz can be mainly attributed to the contraction of the cavity resonator at lower temperatures. The volume of the resonator decreases and hence the resonance frequency increases.
Please note that the simulated value is $\omega_r/2\pi = 6.48\,\mathrm{GHz}$ and is $\omega_r/2\pi = 0.02\,\mathrm{GHz}$ lower than the experimentally determined value of $\omega_r/2\pi = 6.50\,\mathrm{GHz}$ at room temperature. This increase can be attributed to the difference between the simulation and the experiment. Accordingly, in the simulations, the cavity resonator has been modelled without a YIG sphere inserted. The sphere's volume decreases its geometrical volume and results in the small increase of the resonance frequency of ω_r. In addition, small distortions and the finite precision of the machinery used in the fabrication process may lead to a deviation from the simulated cavity resonator resonance frequency.

4.6.2 Temperature dependence of external field applied for resonant coupling

The resonance frequency of the cavity determines the exact value of the external field which needs to be applied for a resonant coupling. Correspondingly, the magnon resonance frequency of the respective magnon mode is tuned towards the cavity resonator's frequency by the external field. Whilst the latter depends on the geometry, volume, and chosen cavity mode, the magnon frequency depends among other things on the sample's shape, wave vector, and mode of precession (c.f. Chapter 2). The complete studied temperature range spans $\Delta T \approx 290\,\mathrm{K}$, which means that parameters such that the cavity volume may also change as lower temperatures lead to a contraction of the material. Since the solid posts within the cavity resonator contract, the total volume may increase. However, it is also possible that the utilised YIG sphere deviates from a perfectly spherical shape and is an ellipsoid. As such, the Kittel mode's dispersion exhibits a small dependence on the saturation magnetisation via $\omega_m/2\pi \propto (H_{ext} - \frac{1}{3}(3N_z - 1)4\pi M_s(T))$, where N_z is the z-component of the demagnetizing tensor. Since the resonance frequencies have to match, and the resonance frequency of the cavity resonator only changes by 0.03% over the whole temperature range, the increase in $M_s(T)$ due to Bloch's law towards lower temperatures needs to be compensated by a lower value of the externally applied field for resonant coupling. Altogether, this results in a lower resonance frequency of the specific cavity mode, as shown in Figure 4.16. From room temperature ($T = 290\,\mathrm{K}$), the externally applied magnetic field, decreases from $H_{\mathrm{ext}} = 229.5\,\mathrm{mT}$ to $H_{\mathrm{ext}} = 221.5\,\mathrm{mT}$ at a temperature of $T = 2.4\,\mathrm{K}$. Therefore, the total change of the resonance frequency results in $\Delta H_{\mathrm{ext}} = 8\,\mathrm{mT}$, corresponding to a difference of 3.4 %.

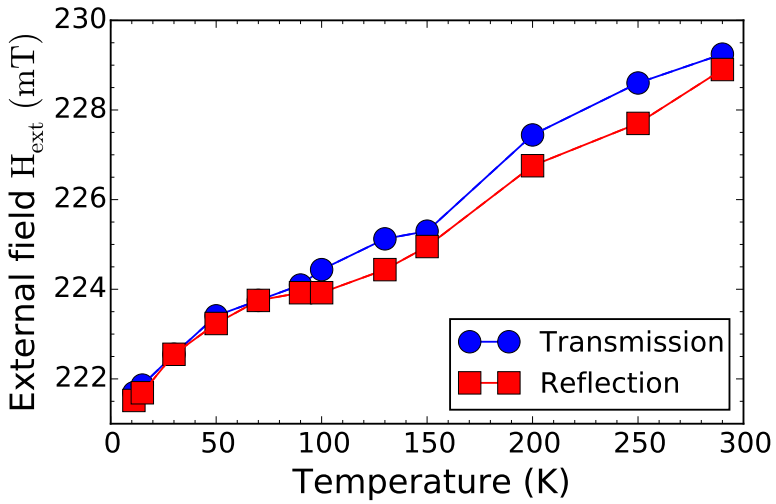

Figure 4.16: Temperature-dependent change of the strength of the external magnetic field value for resonant coupling measured in reflection (red) and transmission (blue). The decrease could be attributed to either a local increase of the mode volume or a small dependence of the saturation magnetisation for an imperfect spherical sample shape ($\omega_m \propto (H_{ext} + \frac{4\pi}{3} M_s(T))$). The cavity resonator's frequency only changes by 0.03%. The increase in saturation magnetisation results in a lower resonance field in order to obtain the same magnon resonance frequency. Hence, the value of the externally applied field for a resonant coupling between cavity photons and Kittel mode magnons decreases at most by 3.4 %. The reflection and transmission data differ only in the order of 0.5 mT, which can be attributed to the precision of setting the external magnetic field. The error bars are in the order of 0.01.

4.6.3 Temperature dependence of the gyromagnetic ratio

Since magnons are the quasiparticles associated to spin waves and describe collective spin excitations in a material, one deals with N electronic spins which are precessing with a certain frequency around the axis of saturation magnetisation. In general, the specific value of the precession frequency depends on the dispersion of the spin wave mode under consideration. However, for uniformly precessing Kittel mode magnons in a sphere, the resonance frequency only depends on the externally applied static field and the gyromagnetic ratio ($\omega_m/2\pi = \gamma H_{ext}$). It is shown in Figure 4.16 that the externally applied static magnetic field for a resonant coupling between the cavity resonator and the magnons changes by $\Delta H_{\text{ext}} = 3.4\,\%$ for the considered temperature range. In combination with the variation of the resonance frequency of the cavity resonator by $\Delta\omega_r = 0.31\,\%$ (c.f. Figure 4.15), the temperature dependence of the gyromagnetic ratio can be studied. From literature, the gyromagnetic ratio of the electronic spins is reported as $\gamma_{\text{lit}}/2\pi = 28\,\frac{\text{GHz}}{\text{T}}$ [92] and constant with temperature. In absolute numbers, the value for the gyromagnetic ratio in the temperature-dependent study of a cavity magnon-polariton system changes by $\Delta\gamma = 3.4\,\%$ as shown in Figure 4.17. Thus, one can see, that the change in the externally applied field due to slight deviations from a perfectly spherical shape or cavity volume variations (c.f. Figure 4.16) dominates. This dominance results in modifying the value of $\gamma(T)$ leading to a deviation from the value at room temperature. The deviation is within the error bars, in accordance with the literature value, and explains the deviation from the number in literature for lower temperatures.

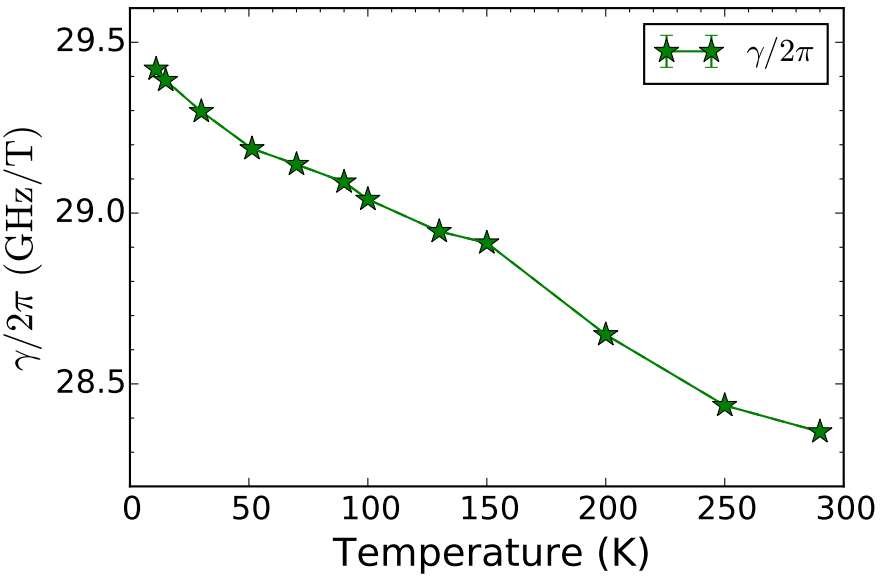

Figure 4.17: Temperature-dependent change of the gyromagnetic ratio $\gamma = \frac{\omega_r}{H_{\text{ext}}}$. The gyromagnetic ratio increases towards lower temperatures since the externally applied field needed for a resonant coupling decreases towards lower temperatures by $\Delta H_{\text{ext}} = 3.4\,\%$ (c.f. Figure 4.16). Moreover, the resonance frequency of the cavity resonator, ω_r varies by $\Delta\omega_r = 0.31\,\%$ (c.f. Figure 4.15). This difference is one order of magnitude below the total resonance field change. Thus, the gyromagnetic ratio is dominated by the variation of the value for the externally applied field and changes by the same amount as the external magnetic field. The error bars are in the order of 0.01, and covered by the data point symbols.

4.6.4 Temperature dependence of the saturation magnetisation

The macroscopic coupling strength $g_{\text{eff}}(T)/2\pi$ has a square root dependence on the total number of contributing spins and thus the saturation magnetisation. Accordingly, the influence of the saturation magnetisation on the coupling strength for different temperatures has to be quantified as well. The temperature dependence of the saturation magnetisation is experimentally determined from hysteresis measurements of the YIG sphere by means of SQUID (c.f. Section 4.3) and displayed in Figure 4.6.4 from $T = 10\,\text{K}$ to $T = 300\,\text{K}$ together with a fit to Bloch's $T^{3/2}$ law written in first order. The function for modelling the temperature dependence of the saturation magnetisation reads as:

$$M_s(T) = M_s(0) \cdot \left(1 - \left(\frac{T}{T_c}\right)^{\beta \cdot \frac{3}{2}}\right), \tag{4.9}$$

where $M_s(0)$ denotes the value at $T = 0\,\text{K}$, T_c the Curie temperature, and β a dimensionless fitting parameter. The fit yields $\mu_0 M_s(0) = (282 \pm 3)\,\text{mT}$, $T_c = (566 \pm 43)\,\text{K}$, and $\beta = (1.30 \pm 0.15)$. From the literature value of the spin net density per unit cell of YIG, $\rho_s = 2.1 \cdot 10^{22}\,\mu_\text{B}\,\text{cm}^{-3}$, the theoretically expected value for the saturation magnetisation for $T = 0\,\text{K}$ can be calulated [100]. The value is $\mu_0 M_s(0) = (245 \pm 40)\,\text{mT}$ ($M_s(0) = (194 \pm 32)\,\frac{\text{kA}}{\text{m}}$). Within the error bars, this is in accordance with the value from the above SQUID measurement. Including the error of $\Delta\mu_0 M_s(T) = \pm 40\,\text{mT}$ due to the uncertainty in spin number N originating from an error in the sphere's radius, the value of $\mu_0 M_s(T =$

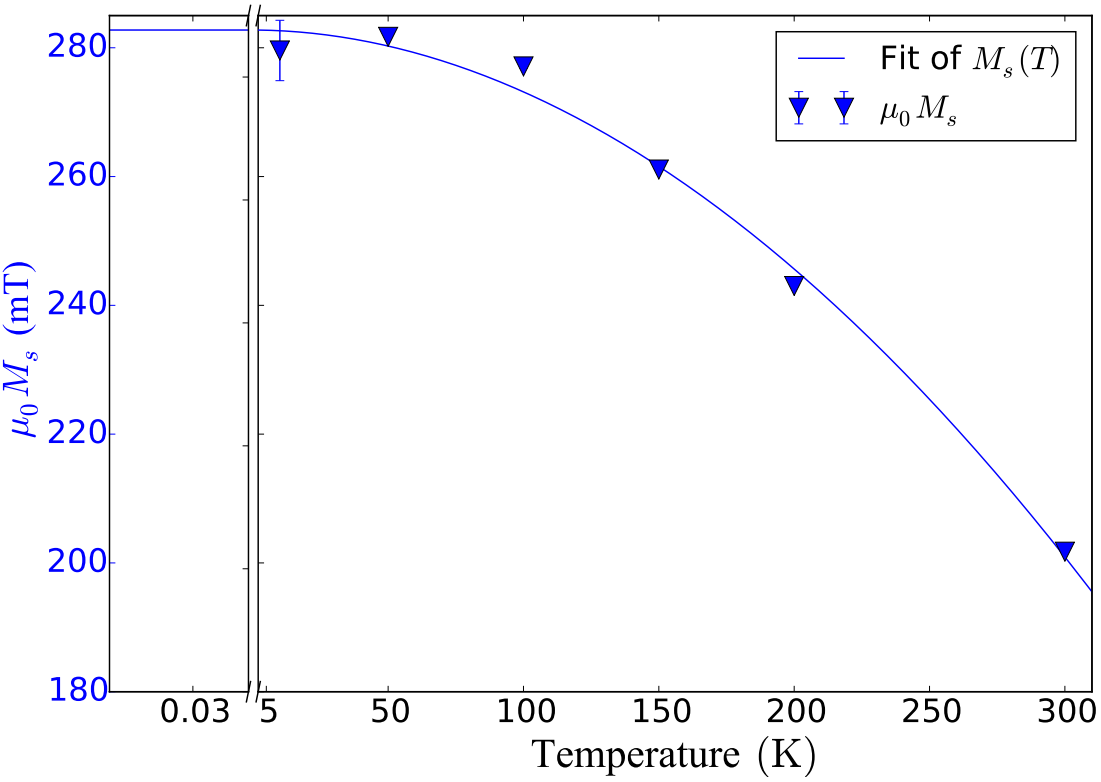

Figure 4.18: Temperature dependence of the saturation magnetisation $M_s(T)$ extracted from SQUID measurements of the YIG sphere. The saturation magnetisation increases towards lower temperatures according to Bloch's $T^{3/2}$ law, which is shown by the blue line. The fit yields $\mu_0 M_s(0) = (282 \pm 3)\,\mathrm{mT}$, $T_c = (566 \pm 43)\,\mathrm{K}$, and $\beta = (1.30 \pm 0.15)$, where $M_s(0)$ denotes the value at $T = 0\,\mathrm{K}$, T_c the Curie temperature and β a dimensionless fitting parameter.

$300\,\mathrm{K}) = (200 \pm 40)\,\mathrm{mT}$ matches the literature value of $\mu_0 M_s(T = 300\,\mathrm{K}) = 175\,\mathrm{mT}$ [98]. Here, the error bars are mostly attributed to the possible variation in the sphere's volume and thus the number of spins. In total, the saturation magnetisation increases from room temperature to $T = 10\,\mathrm{K}$ by $\Delta M_s = 35.71\,\%$. In comparison to contributions such as the externally applied field and the resonance frequency of the cavity resonator to $g_{\mathrm{eff}}(T)/2\pi$, the change in saturation magnetisation is at least one order of magnitude higher. Therefore, it is expected that the temperature-dependent evolution of the coupling strength is mainly governed by the temperature-dependent variation of the saturation magnetisation, via $g_{\mathrm{eff}}(T)/2\pi \propto \sqrt{M_s(T)}$.

Another indication, that the saturation magnetisation dominates the temperature-dependent changes of the coupling strength is displayed in Figure 4.19 by calculating the ratio between $g_{\mathrm{eff}}(T)/2\pi$ and $\sqrt{M_s(T)}$. If the change in saturation magnetisation indeed dominates the temperature dependence of $g_{\mathrm{eff}}(T)$, this ratio should remain constant for all temperatures as both quantities evolve proportionally to each other. This ratio is shown from $T = 50\,\mathrm{K}$ to $T = 300\,\mathrm{K}$ and peaks at $T = 150\,\mathrm{K}$. However, the maximal difference of the value does not exceed $5.3\,\%$ and, within the error bars, this decreases further. It

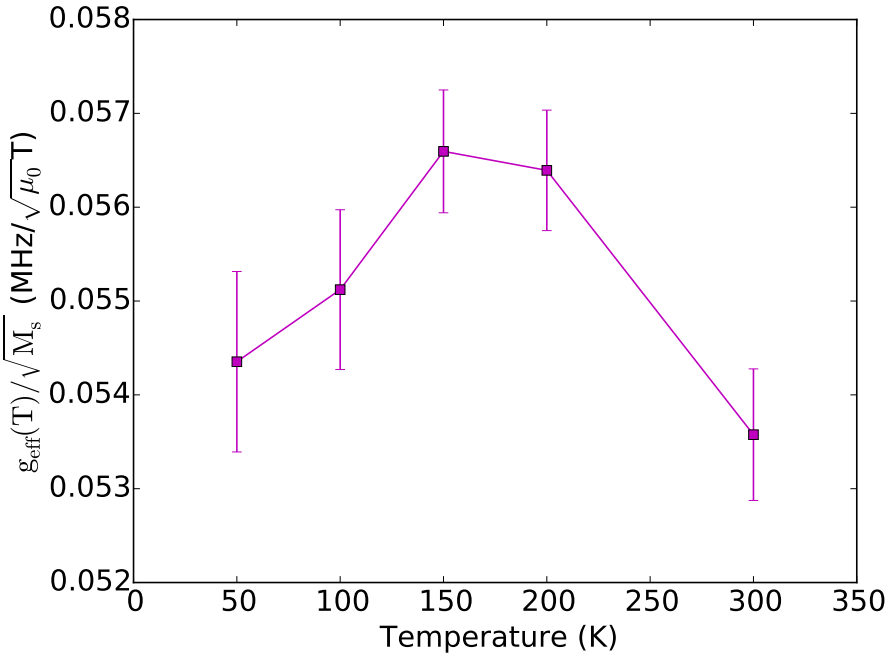

Figure 4.19: Proportionality ratio between the square root of the magnetisation and the coupling strength as a function of temperature. The magnetisation dominates the coupling strength's changes. Thus, the proportionality ratio does not change with temperature within the error bars. This constancy demonstrates the strong influence of the magnetisation on the coupling strength and justifies modelling it by a modified Bloch's $T^{3/2}$ law.

confirms the previous statement for the governing contribution to the temperature dependence of the coupling strength, but from the apparent variation, the other contributions also play a small role. Hence, taking these additional small changes such as the resonant applied field which decreases towards lower temperatures into account, the ratio can be considered constant within the given error bars. As a result, the continuity of this proportionality ratio over the full temperature range allows modelling of the coupling strength by the square root of the saturation magnetisation. Correspondingly, the temperature dependence of the coupling strength is modelled by Bloch's $T^{3/2}$ law as well, taking the relation $g_{\mathrm{eff}}(T)/2\pi \propto \sqrt{M_s}$ into account. This dependence is shown in the next section.

4.6.5 Expected maximum value of the coupling strength

In the previous section, it is shown that the change in saturation magnetisation is expected to govern the temperature dependence of the coupling strength. Thus, towards very low temperatures, the coupling strength should saturate at the maximum possible value for this reentrant cavity resonator-YIG sphere system. If one assumes, that all spins ($N = (1.37 \pm 0.15) \cdot 10^{18}$, c.f. Section 4.6.7) in the sample are contributing to the coupling, the maximal value of the coupling strength can be calculated through Equation (3.16) a.). Accordingly, for the coupling strength of a single spin, the calculation yields $g_0^{\mathrm{th}}/2\pi = (23.6 \pm 1.18)\,\mathrm{mHz}$ for perfect mode overlap ($\eta = 1$), and $g_0^{\mathrm{th}}/2\pi = (13.69 \pm 1.18)\,\mathrm{mHz}$ for $\eta = 0.58$ in the real experiment [172]. As a result, the maximum expected value of the macroscopic coupling strength for this system is $g_{\mathrm{eff}}(T = 0)/2\pi = (35.87 \pm 5.16)\,\mathrm{MHz}$ (c.f. Table 4.2). Despite smaller errors for the resonance frequency, the dominating

contribution to the error bar originates from an uncertainty of 0.05 for the exact value of the mode overlap factor η. For example, such uncertainty exists because the YIG sphere is not exactly located at the centre between both posts which already changes the mode overlap η. Furthermore, several measurement runs are performed with this setup and the YIG sphere removed and re-inserted to show the robustness and general reproducibility of this system. Therefore, the YIG sphere's exact position and thus the mode overlap may have slightly changed, leading to an error in the latter quantity. This value will be now compared to the experimental findings.

4.6.6 Experimental results

As indicated in the description of the cavity resonator and Figure 4.9, the temperature dependence of the coupling strength is studied both in transmission and reflection measurements. In order to show the reproducibility of the results independent from the cavity and measured scattering parameter type, the data is recorded twice as a function of temperature with two slightly different reentrant resonators. Whilst the first reentrant cavity resonator is equipped with only one port, a second one of precisely the same dimensions but with two inductively coupled microwave ports has been fabricated. As indicated in Figure 4.9, the ports are located at each end of the long axis of the reentrant cavity resonators. The addition of a second port enabled to record transmission and reflection spectra from each port. In order to minimise an error due to temperature fluctuations from cooling and warming and vice versa, the data is taken subsequently at each temperature point.
However, it is experimentally found, that the signal could not be simultaneously optimised both for a transmission or reflection measurement at each port. The cavity resonator ports are not accessible during the temperature dependent measurement as the setup is inserted into the cryostat. Furthermore, the position of the inductive coupler should not be changed because the coupling losses at the ports, i.e. Q_c, have to remain constant over the whole temperature range. Note that, remaining constant means here constant up to the inevitable changes due to a possible contraction of the material at different temperatures. Correspondingly, if they are not fixed, identifying the temperature dependent changes of the losses would be impossible. Thus, as a compromise, the ports' settings are optimised at room temperature such that the port for the $S_{11}(\omega)$ measurements is optimised for a reflection measurement and the other (used for the S_{22}) for the transmission measurement. As a result, the error bars of the S_{22} reflection measurement are expected to be comparably larger.

Figure 4.20 shows the temperature dependence of the coupling strength $g_{\text{eff}}(T)$ for a selected S_{11}, S_{22} (reflection) and S_{21} (transmission) measurement. In addition, the figure contains a red solid line corresponding to a fit to the coupling strength of Bloch's $T^{3/2}$ law via $g_{\text{eff}}(T) \propto \sqrt{M_s(T)}$. The fit yields $g_{\text{eff}}(T = 0)/2\pi = (30.65 \pm 0.5)\,\text{MHz}$, $\beta = (1.06 \pm 0.15)$, and $T_c = (566 \pm 43)\,\text{K}$. The latter two confirm the Bloch's $T^{3/2}$ nature of the temperature dependence and, within the error bars, in accordance with the Curie Temperature for YIG, respectively [92]. Qualitatively, all independent measurements show the same temperature dependence. As previously indicated, the differences, especially in the error bars, between the reflection and transmission curves can be attributed to finding a compromise in optimising the resonator ports for both measurements simultaneously. In Figure 4.20, the S_{11} (red circles) data corresponds to a measurement of

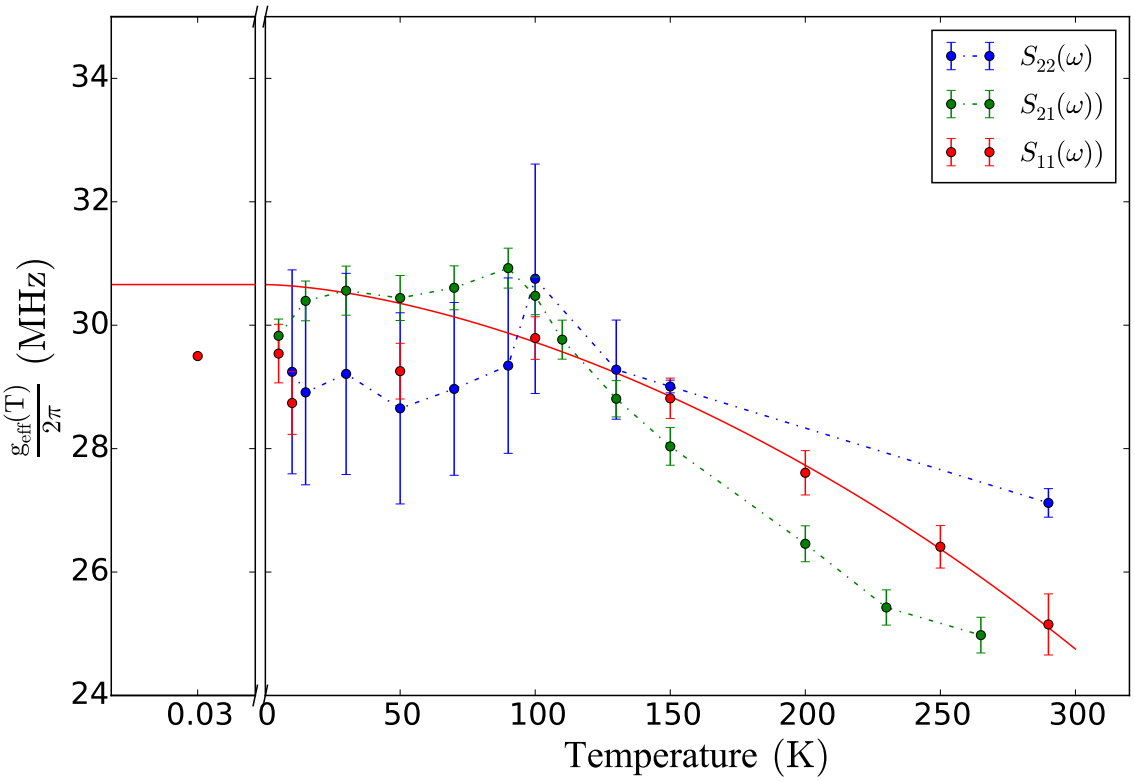

Figure 4.20: Temperature dependence of the coupling strength measured both for reflection (red $S_{11}(\omega)$) and blue ($S_{22}(\omega)$)) and transmission (green ($S_{21}(\omega)$)). There, two temperature regimes can be distinguished. From room temperature, the coupling strength increases from 25 MHz by $\approx 20\%$ at 100 K. As discussed previously, the square root dependence of the coupling strength on the saturation magnetisation is the dominant contribution. Thus, this temperature regime is modelled by Bloch's $T^{3/2}$ law. The fit (solid red line) yields $g_{\text{eff}}(T = 0)/2\pi = (30.65 \pm 0.5)$ MHz. However, for temperatures below $T = 100$ K the coupling strength decreases towards a minimum at $T = 10$ K and recovers to increase to a plateau-like value in the millikelvin temperature regime ($T = 30$ mK) of 29.5 MHz. This deviation from the evolution according to Bloch's $T^{3/2}$ law, is due to the additional excitation of a low number of spins in the YIG sphere in higher order, non-uniform magnetostatic modes. This excitation decreases the total spins precessing uniformly in the Kittel mode. Hence, the coupling strength is decreased. The large error bars for the $S_{22}(\omega)$ and its outlier at 290 K occur because the second cavity port was not optimised for a reflection measurement. The less pronounced decrease in the transmission data ($S_{21}(\omega)$) is due to the "worse" second port and a worse SNR which decreased the quality of the fits. Data at 30 mK taken at KIT by Marco Pfirrmann.

the first reflection cavity resonator and the other curves to a transmission (green circles) and reflection measurement (blue circles) from the second resonator. Since the repeated removal and insertion of the YIG sphere resulted in small position changes within the cavity resonator, the exact value of the coupling strength differs. Especially for temperatures below $T = 30$ K, the SNR of the transmission data is lower, and the value and correspondingly the error of the coupling strength is less accurate since the value of the

coupling strength has been extracted from fits to the avoided level crossing.

Concerning the temperature dependence of the coupling strength, one can identify two regimes with distinct temperature dependence, where different physical contributions seem to dominate the evolution of the coupling strength. The first refers to temperatures from $T = 290\,\mathrm{K}$ to $T = 100\,\mathrm{K}$, where the coupling strength increases towards lower temperatures. As already mentioned, this is in good accordance with the fit to the square root of Bloch's $T^{3/2}$ law, where the change in saturation magnetisation is the governing contribution. A comparison of both the experimentally found maximal value of $g_{\mathrm{eff}}(T = 30\,\mathrm{mK})/2\pi = 29.5\,\mathrm{MHz}$ and the value from the fit of a Bloch's $T^{3/2}$ like temperature behaviour of $g_{\mathrm{eff}}(T = 0\,\mathrm{K})/2\pi = (30.65 \pm 0.5)\,\mathrm{MHz}$ with the analytically calculated value of $g_{\mathrm{eff}}^{\mathrm{th}}(T = 0\,\mathrm{K})/2\pi = (35.87 \pm 5.16)\,\mathrm{MHz}$, shows, that within the error bars all values are in accordance with each other. However, for temperatures lower than $T = 100\,\mathrm{K}$, the previously used model of Bloch's $T^{3/2}$ law with an additional square root does not describe the temperature-dependent evolution of the coupling strength well. Instead of approaching a plateau value such as the saturation magnetisation does for low temperatures, the coupling strength decreases to a minimal value at $T = 50\,\mathrm{K}$ and then recovers to the plateau value for millikelvin temperatures. Despite the decrease which will be discussed in the following, the combination of the data point at 30 K and values for g_{eff} at higher temperatures confirm, that $g_{\mathrm{eff}}(T)$ is predominantly governed by the temperature dependence of the saturation magnetisation. Accordingly, the coupling strength evolves as $g_{\mathrm{eff}}(T) \propto \sqrt{M_s(T)}$. This dependence is shown in Figure 4.20, where it is seen best for the reflection data because of the data in the millikelvin temperature regime.

However, the said decrease of the coupling strength for temperatures between 30 K and 100 K, can be observed from both the reflection and the transmission measurements where for the latter the decrease is less prominent but still observable. Thus, it is not only an artefact but should be another temperature-dependent property of this hybridised system, which needs to be studied in greater detail in the following.

4.6.7 Decrease of the coupling strength: Magnetostatic modes

The coupling of the uniformly excited magnons, i.e. the Kittel mode magnons, is the most dominant contribution to the coupling with the cavity photons, and of central interest in this thesis. However, magnons in other modes with non-uniform precession patterns over the volume of the sample could also couple to the cavity photons if the resonance frequencies match. Similar to the Kittel mode with $\mathbf{k} = 0$, in the limit of small wave vectors, these non-uniform modes can be attributed to magnetostatic modes (c.f. Chapter 2, Section 2.8). In the following, the influence of higher order magnetostatic modes on the coupling strength is discussed.

Maximum number of spins for resonant coupling

The maximum number of available spins for resonant coupling to the cavity resonator photons is determined by the sample's volume, its geometry and the material specific properties such as the spin net density. For the sphere made of YIG, the reported value of the spin net density is $\rho_s = 2.1 \cdot 10^{22}\,\mu_{\mathrm{B}}\,\mathrm{cm}^{-3}$ [100]. Calculating the volume of the sphere with a diameter of $d = 0.05\,\mathrm{cm}$ yields $V_{\mathrm{sphere}} = (6.54 \pm 0.75) \cdot 10^{-5}\,\mathrm{cm}^{-3}$. The uncertainty

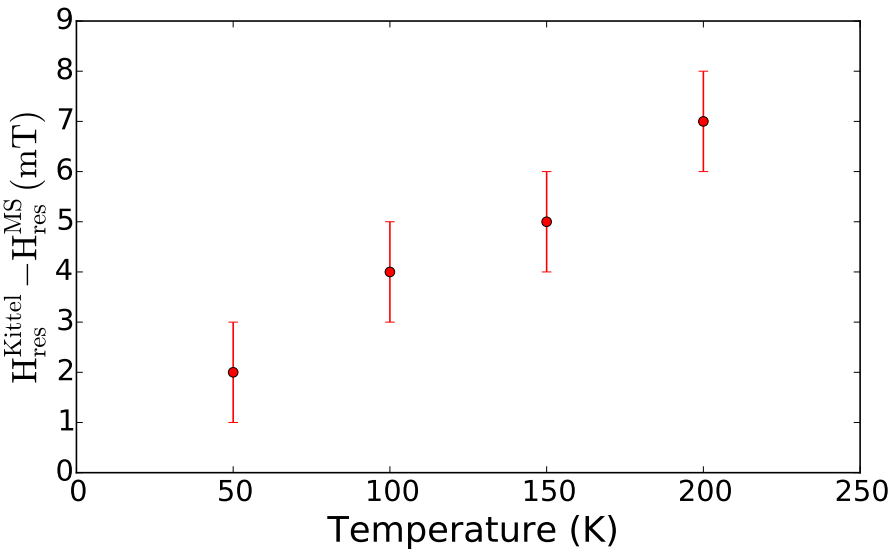

Figure 4.21: Difference between the magnetic field applied for the resonant coupling to the Kittel mode with coupling strength $g_{\mathrm{eff}}(T)/2\pi$, $H_{\mathrm{res}}^{\mathrm{Kittel}}$, and resonance with another magnetostatic mode of higher order, $H_{\mathrm{res}}^{\mathrm{MS}}$ with the highest observed gap. This difference decreases from 7 mT at $T = 200$ K to 2 mT at $T = 50$ K. Both for lower and higher temperatures than shown, the weakly coupled magnetostatic mode could no longer be resolved.

in the value of the volume is estimated from small deviations of the sphere's diameter on the order of $\Delta r = 0.001$ cm. As a result, the maximally available number of spins in the YIG sphere can be calculated to be $N = (1.37 \pm 0.15) \cdot 10^{18}$. The coupling strength exhibits a square root dependence on the number of spins such that $g_{\mathrm{eff}}(T)/2\pi \propto \sqrt{N}$.

The simultaneous excitation of two different magnon modes lowers the total number of available spins of each mode due to the conservation of the particle number [185]. Then, a decrease in the coupling strength of a magnetostatic mode corresponds to the parasitic excitation of magnons in other (magnetostatic) modes lowering the total number of spins precessing in the mode of interest. Therefore, in the temperature interval between $T = 10$ K and $T = 100$ K fewer spins are taking part in the resonant coupling of magnons in the Kittel mode to the cavity resonator photons due to the presence of other, parasitic excitations as illustrated in Figure 4.20.

Instead, the "non-Kittel" magnons are precessing non uniformly in other magnetostatic (MS) modes of higher order, whose resonance frequency is very close to that of the Kittel modes' resonant coupling to the cavity resonator photons. In the course of sweeping the external magnetic field in and out of resonance $\omega = \omega_m^{\mathrm{Kittel}} = \omega_r$, the condition for resonant coupling of the cavity resonator photons to magnons in other modes can also be fulfilled. If enough spins are taking part, i.e. the corresponding effective coupling strength $g_{\mathrm{eff}}^{\mathrm{MS}}$ is large enough ($g_{\mathrm{eff}}^{\mathrm{MS}} \gg \kappa_r, \kappa_m$), this coupling can be observed as another avoided level crossing in the dispersion spectrum of the hybridised system in close vicinity to the avoided level crossing of the Kittel mode's. However, each coupling is not an instantaneous event but gradually starts to set in at external fields in an interval around the resonance, where the probability for hybridisation increases towards the resonant coupling field.

Correspondingly, if the resonant coupling fields for magnons in either the Kittel ($\mu_0 H_{\mathrm{res}}^{\mathrm{Kittel}}$) or higher order MS mode ($\mu_0 H_{\mathrm{res}}^{\mathrm{MS}}$) are close, then the natural frequencies $\omega_0^{\mathrm{Kittel}}$ and ω_0^{MS} are also in a similar range. As a result, there is a non-zero probability for a parasitic coupling of the magnons of another MS mode to the cavity photons at the resonant coupling field $\mu_0 H_{\mathrm{res}}^{\mathrm{Kittel}}$ for the Kittel mode. Since the cavity photon frequency ω_r matches the Kittel mode frequency $\omega_0^{\mathrm{Kittel}}$ but $\omega_0^{\mathrm{Kittel}} \neq \omega_0^{\mathrm{MS}} \neq \omega_r$, the parasitic coupling to the MS mode is slightly off-resonant. Thus, at this specific field, the probability for a coupling of the cavity photons to another MS mode is lower than for the coupling to the Kittel mode magnons. Consequently, the number of spins precessing in the higher order MS mode is much lower than the one for the Kittel mode. Thus, the coupling strength of such additional avoided level crossings is in the weak coupling regime. However, due to the conservation of the maximum number of available spins, this parasitic coupling decreases the number of available spins for coupling to the Kittel mode. As a result, the observed macroscopic value of the coupling strength is also lowered. For temperatures above 100 K, the probability of decreasing the Kittel mode's coupling strength by a parasitic coupling to other higher order MS modes is still too low. The coupling strength increases to lower temperatures because of the difference between $\mu_0 H_{\mathrm{res}}^{\mathrm{Kittel}}$ and $\mu_0 H_{\mathrm{res}}^{\mathrm{MS}}$ decreases.

Although the simultaneous coupling of spins to different magnetostatic modes resolves the question of decreasing coupling strength in principle, it does not explain the decrease of the difference between the resonant coupling fields and the increase of the coupling strength to the plateau value $T < 5\,\mathrm{K}$. In short, said increase back to the value at $T = 100\,\mathrm{K}$ within the error bars can be attributed to the differently strong temperature-dependent shifts of the resonance frequency. For $50\,\mathrm{K} \leq T \leq 100\,\mathrm{K}$, the difference $\mu_0(H_{\mathrm{res}}^{\mathrm{Kittel}} - H_{\mathrm{res}}^{\mathrm{MS}})$ decreases which results in a higher number of spins in the parasitic coupling. Thus, the values for the coupling strength are further lowered. The temperature-dependent change of this difference between the external resonance fields is shown in Figure 4.21 for $T = 50\,\mathrm{K}$ to $290\,\mathrm{K}$. This change is discussed in the next subsection, including connecting this difference to the predicted occurrence of other modes close to the Kittel resonance.

4.6.8 Resonance frequency of magnetostatic modes

Identification of magnetostatic modes In contrast to broadband FMR spectroscopy, cavity resonators only operate at certain, fixed frequencies which depend on the selected cavity resonator geometry [112]. Each of them is attributed to a certain distribution of the magnetic and electric field components of the standing wave mode pattern inside the cavity resonator [c.f. Chapter 2].

Hence, it is not possible to extract the resonance frequency as a function of the external, static field, which is swept in the interval of interest. In other words, the dispersion cannot be determined. As a consequence, the specific magnetostatic mode in the spectrum cannot be identified unambiguously by cavity resonance spectroscopy measurements.

Please note, when the temperature-dependent spectroscopic data has been taken, no temperature-dependent, broadband setup for FMR spectroscopy was available since the

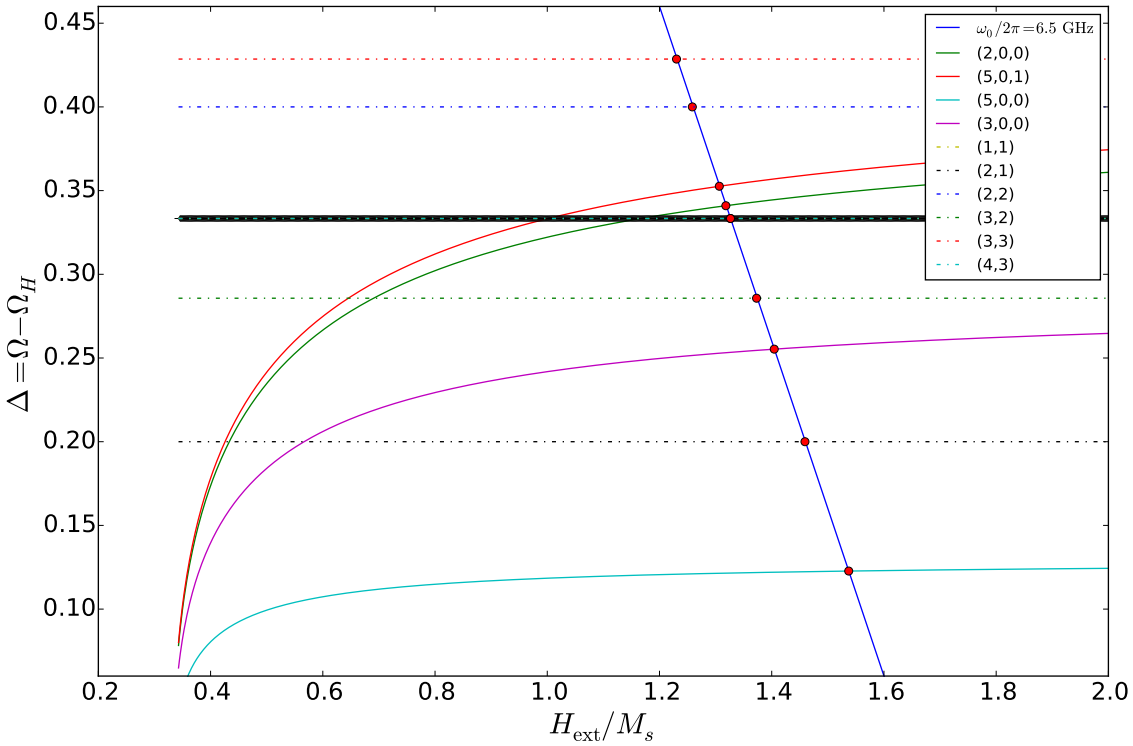

Figure 4.22: Dependence of the frequency difference $\Delta = \Omega - \Omega_H = \frac{\omega_0}{\gamma M_s} - \frac{H_i}{M_s}$, where $H_i = H_{\mathrm{ext}} - \frac{M_s}{3}$ on the external, static field normalised to the saturation magnetisation for a number of various magnetostatic modes (coloured lines). They exhibit a resonance frequency close to the one of the Kittel mode (solid black line). There, saturation magnetisation independent dispersions for modes of higher order (dotted, coloured lines) and dependent ones have to be distinguished (solid, thin lines). The blue line crossing all lines denotes the isoline where all different modes exhibit the same resonance frequency $\omega_0/2\pi = \omega_r/2\pi = 6.5\,\mathrm{GHz}$. A comparison with the distance of each mode to the resonance field of the Kittel mode (e.g. as shown in Figure 4.21) shows that the additional modes are higher order magnetostatic modes.

second measurement rod has been finished only recently. Therefore, measurements unambiguously identifying the individual modes as in Ref. [66] could not be conducted. Nevertheless, it is possible to further examine the absolute difference of the resonance frequencies between the Kittel mode and the other magnetostatic modes close to it. For modes, which do not differ much in frequency and nearly overlap, it is impossible to identify the exact mode number for the reasons given in the former paragraph. However, it can be confirmed, that the weaker avoided level crossings in the spectrum indeed refer other, higher order magnetostatic modes. Each magnetostatic mode is resonantly coupled to the cavity resonator photons if for its frequency $\omega_m^{\mathrm{MS-mode}} \equiv \omega_r \equiv \omega_0$ holds. Due to this relation, the observed avoided level crossings in the temperature-dependent study of the cavity magnon-polariton dispersion spectra occur at the crossing of the isoline with the frequency difference $\Delta = \Omega - \Omega_H$, where $\Omega = \frac{\omega_0}{\gamma M_s}$ with the resonance frequency $\omega_0 = \omega_r$ and $\Omega_H = \frac{H_{\mathrm{ext}} - M_s/3}{M_s}$ (c.f. Figure 4.22). As indicated by the red circles, the condition for a resonant coupling takes place at different field values for other modes. The horizontal projection of the fields on the x-axis, i.e. calculating the difference between the resonance fields for the Kittel mode and the respective MS mode, allows for a rough identification

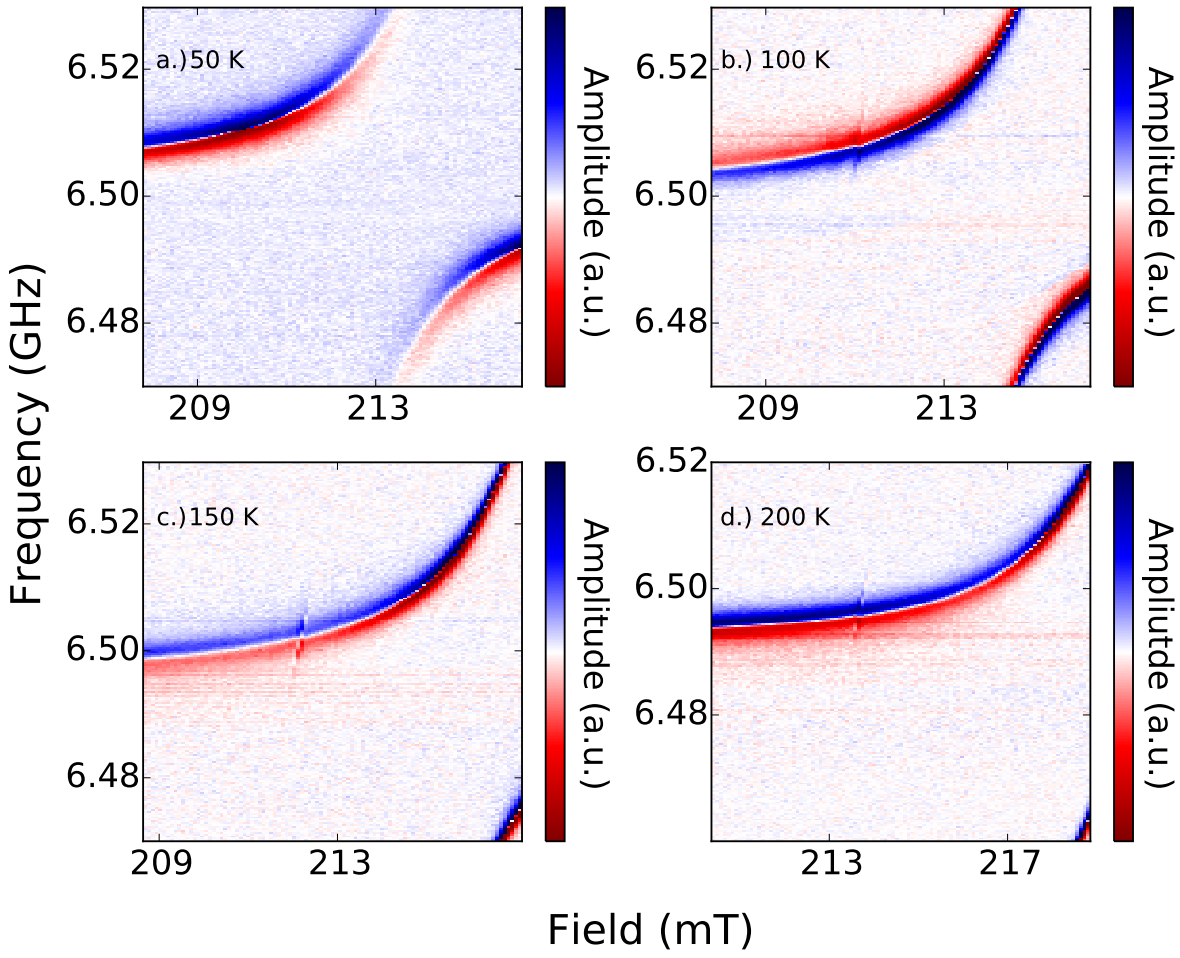

Figure 4.23: Background corrected amplitude gradient of a $S_{11}(\omega)$ reflection measurement, zoomed to resonance from $T = 50\,\mathrm{K}$ (a.)) to $T = 200\,\mathrm{K}$ (d.)) in steps of 50 K. The resonant field shifts due to the temperature-dependent change of the saturation magnetisation. The coupling to other magnetostatic modes is shown by the small avoided level crossings mostly in the weak coupling regime around 210 mT and 214 mT, depending on the temperature. Most importantly for the decrease of the coupling strength $g_{\mathrm{eff}}(T)$, the difference in terms of applied magnetic for resonant coupling with the specific mode and the Kittel mode decreases towards lower temperatures. For $T = 50\,\mathrm{K}$ this difference is not unambiguously resolvable any more within the avoided level crossing due to resonant coupling of the Kittel mode. The coupling strength of the Kittel mode decreases which is due to a simultaneous coupling to magnetostatic modes of higher order lowering the number of Kittel mode magnons.

of the mode given comparing this value with the observed distance in the spectra to the Kittel mode. Hence, Figure 4.23 shows the dispersion for four different temperatures from $T = 50\,\mathrm{K}$ to $T = 200\,\mathrm{K}$ in steps of 50 K. For better visibility of the weakly coupled avoided level crossings of other magnetostatic modes with the cavity photons, the amplitude gradient is plotted. Two features can be noted. First, the additional avoided level crossings of smaller coupling strength can be observed only for the temperature interval

between 50 and 250 K. Second, as previously mentioned, the difference concerning the applied external field for resonant coupling to each of these modes changes as a function of temperature. As the temperature is lowered, this difference decreases until the small avoided level crossings are not resolvable any more in the Kittel mode's avoided level crossing (c.f. Figure 4.21). Accordingly, this behaviour is attributed to the different dispersion relations for the Kittel mode and higher order MS modes [129].
Ideally, the dispersion relation for magnons in the Kittel mode for a sphere does not depend on the saturation magnetisation despite a constant term, which is denoted by Ω_H in the Walker equations [125]. Experimentally, as shown in Figure 4.16, the resonant coupling field changes by 3.4 % over a temperature difference of almost 300 K and for $50-100$ K by 0.4 % due to possible deviations from a perfect spherical shape. However, other magnetostatic modes can depend differently on the saturation magnetisation and consequently on temperature [129]. Thus, these modes also shift concerning the applied static field value for a resonant coupling. Towards lower temperatures, the observed mode's resonant field moves closer to the one of the Kittel resonance because of the temperature-dependent change in saturation magnetisation. At a temperature of ≈ 50 K, the modes are in such close vicinity to the Kittel mode, that they cannot be resolved any more in the avoided level crossing of that mode. For even lower temperatures the difference in the resonant coupling fields increases again and, hence, the coupling strength as well towards the value at 30 mK.

In summary, by separating the temperature dependence of the coupling strength into a "high" temperature ($T > 100$ K) and a "low" temperature regime, the observed changes in the coupling strength can be explained to full extent. For the first regime, the temperature-dependent variation in saturation magnetisation dominates the changes of the coupling strength, and allows to model the temperature dependence of the coupling strength via $g_{\text{eff}}(T)/2\pi \propto \sqrt{M_s} \propto \sqrt{N}$ by Bloch's $T^{3/2}$ law in the first order. On the other hand, the limited decrease and subsequent "recovery" to the cryogenic temperature value of the coupling strength can be attributed to the simultaneous coupling of the spins to higher order magnetostatic modes despite the Kittel mode's magnons at certain temperatures. As their resonance frequency shifts stronger than do the Kittel mode ones and increases again towards the cryogenic temperature regime, this parasitic coupling occurs with much lower probability. Hence, the coupling strength increases.
In order to quantify the coherent exchange of information in this cavity magnon-polariton system, it is necessary to study the dissipation of the magnons, as well. For instance, if the losses are considerably high, there may be a strong coupling between the cavity photons and the magnon, but the oscillation of energy, i.e. information exchange, between both components will soon be damped out. Hence, this system could not be used for a reliable source of coherent information exchange between magnons and cavity photons and possibly other components [56]. Thus, the temperature-dependent magnon dissipation in the Kittel mode is examined in the following section.

4.7 Temperature dependence of the magnon linewidth

Experimentally, FMR of a magnetic sample can be either measured via a stripline- or (coplanar) waveguide-based approach or employing the cavity-resonator-based FMR measurement technique [144]. The first type describes electrical measurements which can be recorded by different techniques such as VNA-FMR or pulsed inductive microwave mag-

netometry (PIMM), where VNA-FMR is currently mostly used [112]. For a more detailed description of these techniques, the interested reader can consult, for instance, Ref. [112] and [144] and references therein. These methods represent so-called broadband techniques which measure over a broad range of frequencies and, hence, are also suited for the frequency swept method at constant external magnetic field. On the contrary, the cavity resonator-based approach which has been used for the experiments discussed in this doctoral thesis is a single-band technique. The sample is inserted into the cavity resonator, and the FMR of the sample is measured as a function of an external magnetic field at a fixed frequency which corresponds to the resonance frequency of the cavity resonator (c.f. Equation (2.13.1)) by a microwave reflection or transmission measurement using a VNA, for instance.
As pointed out in Chapter 2, Section 2.7, FMR measurements record the line shape and also enable the study of the linewidth of the magnetic sample, which can be determined by associating the full width at half maximum (FWHM) to the resonant frequency or external magnetic field at resonance. Then, the linewidth, i.e. the total damping parameter can be extracted from the resulting slope [91, 112]. For the single-band cavity resonator based approach, however, the magnon linewidth is rather *indirectly* determined from the CMP's line shape. Depending on the measurement type, its line shape is modelled by Equation (4.6) (reflection) or Equation (4.3) (transmission). The early experiments on the study of the properties of YIG and other garnets employed ferromagnetic resonance as well to gain insights into the magnon linewidth. There are numerous works from this time, and the underlying processes are well understood nowadays. However, these experiments used direct, broadband FMR measurement techniques in order to study the magnon linewidth also as a function of temperature [137, 140, 186].
The magnon linewidth in the Kittel mode was not studied as a function of temperature for a CMP. Hence, in the following, the linewidth of a Kittel mode magnon strongly coupled to a cavity photon, i.e. in the presence of the CMP, is discussed as a function of temperature. In addition, in combination with the temperature dependence of the coupling strength, the determination of the temperature dependence of the magnon linewidth allows one to classify the coupling regime by calculating the cooperativity C for the entire temperature range.

4.7.1 Experimental data

The temperature dependence of the magnon linewidth $\kappa_m/2\pi$ is determined between 30 mK and 290 K. For each temperature, a fit according to Equation (4.6) or Equation (4.3) to the dataset at resonance yields the numerical values for the magnon linewidth. The functional dependence is displayed in Figure 4.24, where the triangles (blue) and circle (red) refer to the transmission and reflection data, respectively. For better clarity of the temperature dependence, solid lines, connecting the data points are drawn. Partially, the error bars of the transmission measurement are much higher than the corresponding points from the reflection data. As previously mentioned in the discussion of the coupling strength, the ports could not be simultaneously optimised for both reflection and transmission measurements (c.f. Section 4.6.6). Recall, that one cavity resonator port used both for recording the reflection data and as excitation port in case of the transmission measurement. In order to also obtain a good signal in reflection, the associated loop of that port is tuned such the signal there optimised for a reflection measurement. Only the second port of the resonator, used for the outcoupling of the signal, is optimised in

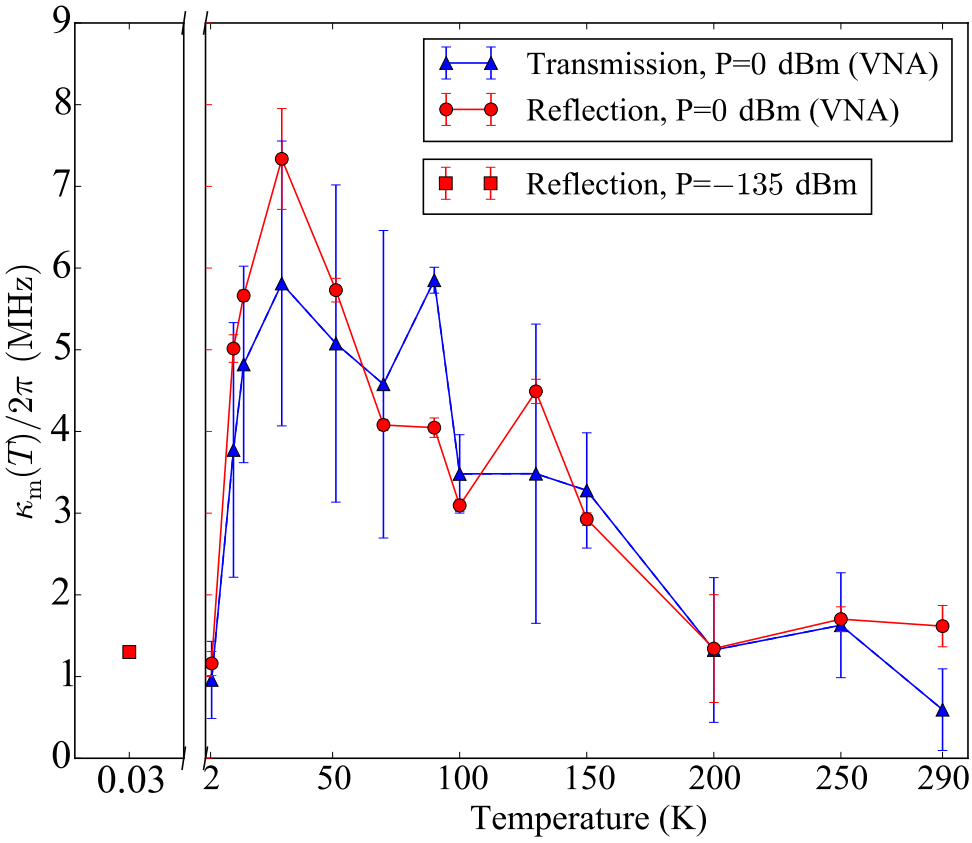

Figure 4.24: Temperature dependence of the magnon linewidth for reflection (red) and transmission (blue) measurements. In the cryogenic setup for millikelvin temperatures, transmission measurements are impossible; only the reflection result is shown. The solid lines are a guide for the eye. At room temperature, the linewidth κ_m is of the order of 1 MHz. Towards lower temperatures, the linewidth increases to a smaller broad peak at $T \simeq 90-120$ K. The linewidth reaches its maximum value at $T \simeq 40$ K with $\kappa_m \approx 7$ MHz. The linewidth decreases back to 1 MHz at $T = 30$ mK. Data at 30 mK taken from Marco Pfirrmann at KIT.

terms of the transmission. As a result, the SNR is worse in certain cases for the transmission measurement since one of the two ports used is not perfectly optimised for this transmission measurement. Thus, the error from the subsequent fit also increased for the determination of the value of the linewidth.
Both at room temperature and cryogenic temperatures ($T < 1$ K) the linewidth is of the order of $\kappa_m = 1$ MHz. However, starting from room temperature, the linewidth increases up to a clear peak at $T \simeq 40$ K. Afterwards, the linewidth rapidly decreases towards the lowest temperature value at $T = 30$ mK, which recovers the room temperature result. Besides, a second peak, or rather a broad plateau of less prominence, in the magnon linewidth can be observed around 100 K, i.e. in the intermediate temperature range. The error bar on the transmission measurement is comparably high, but within this error bar, the value is in accordance with the more evident second peak around this temperature. By these observations, the temperature dependence of the magnon linewidth $\kappa_m(T)$ can be decomposed into two parts: A temperature-dependent contribution leading to the peaks

around 40 K and 120 K and another one serving as a baseline of the order of 1 MHz. The occurrence of a finite width at half maximum, which is defined as the line width of the ferromagnetic resonance line shape, is due to the existence of various scattering processes. They are of different origins with different functional dependencies on the temperature. In Chapter 2, Section 2.9 various scattering processes have been introduced in a general manner. The different contributions and their relative weight to the total linewidth will now be discussed in the context of the experimental data.

Please note that, in this experiment, the total magnon linewidth is extracted from the cavity magnon-polariton line shape. Thus, the resulting value is comprising both intrinsic and extrinsic contributions. Extrinsic contributions such as defects result in a coupling of the spin dynamics to the lattice and augment the value from intrinsic dissipation processes. In the following, the contributions will be discussed individually.

4.7.2 The linewidth "baseline" of 1 MHz

Contribution from intrinsic Gilbert damping

Intrinsic Gilbert damping originates from spin-orbit coupling where the spin number is not a conserved quantity [122]. YIG is a ferrimagnetic insulator with a very low value of the intrinsic Gilbert damping parameter $\alpha = 10^{-4}$ to 10^{-5} which makes it a promising candidate for magnon based applications in data processing and information technology [24, 61, 187]. At room temperature, YIG exhibits linewidths in the order of $\Delta\omega/2\pi \approx 0.03$ MHz [15]. Studies on the temperature dependence of the Gilbert damping parameter reveal a decrease towards lower temperatures [66]. Consequently, from room temperature towards millikelvin temperatures, the value is at least two magnitudes lower. Further, this intrinsic contribution alone cannot account for the "baseline" linewidth in the order of 1 MHz, and other processes contributing must, therefore, exist.

Surface Pit Scattering (SLK)

The SLK linewidth is proportional to the saturation magnetisation. In the discussion of the temperature dependence of the coupling strength it has been shown that the saturation magnetisation is the dominating factor down to 100 K and changes significantly ($\Delta M_s \approx 35\%$). Since $\Delta\omega_{SLK}/2\pi \propto M_s(T)$, the SLK linewidth is also expected to follow Bloch's $T^{3/2}$ law as a function of temperature as mentioned before (c.f.Section 2.9.2) structural inhomogeneities of the surfaces can result in a substantial broadening of the measured linewidth. The surface roughness of the commercially purchased YIG sphere has been reported to be 50 nm by the company, which allowed for setting an upper estimate for the size of the surface pits of this order [103]. Inserting the other values for the saturation magnetisation from the experiment into Equation (2.55) yields the temperature dependence shown in Figure 4.25. The SLK linewidth increases from 0.95 MHz at room temperature to 1.1 MHz at 10 K. Compared to the total increase of the magnon linewidth (Figure 4.24), the SLK linewidth does not change significantly over the considered temperature range. Adding the Gilbert damping parameter to the SLK linewidth, these contributions make up the (almost) temperature-independent contribution to the magnon linewidth of the order of 1 MHz within the error bars. Thus, the "baseline" of the decomposed magnon linewidth can be explained by the presence of spin-orbit coupling and two-magnon processes. As explained in Chapter 2, Section 2.9.3 for the $\mathbf{k} = 0$ (Kittel

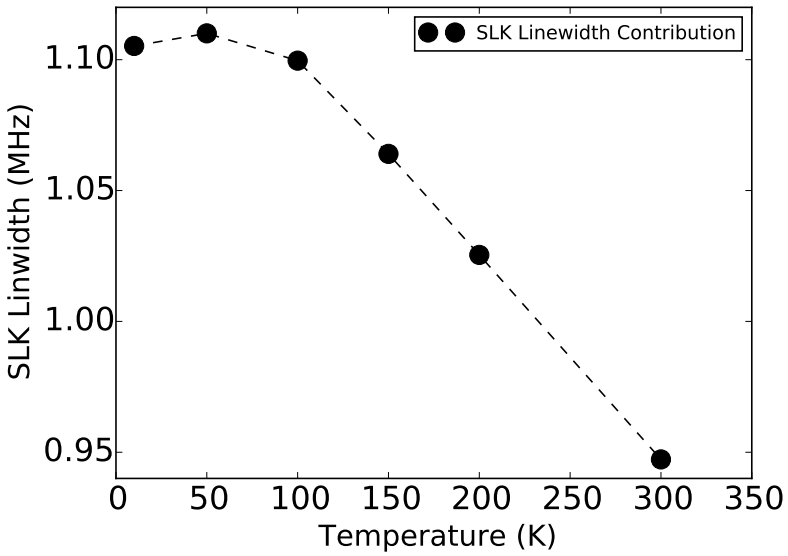

Figure 4.25: Modelled temperature dependence of the contribution to the Kittel mode magnon linewidth from surface pit scattering (SLK) based on a theory from Sparks, Loudon and Kittel [115] and Equation (2.55). Qualitatively, the SLK linewidth shows a similar temperature dependence as the saturation magnetisation, because the linewidth broadening due to a rough surface also depends on the saturation magnetisation. The linewidth increases from 0.95 MHz at room temperature to 1.1 MHz at lower temperatures. This value is in the order of 1 MHz over the whole temperature range. Thus, the linewidth due to a rough sample surface contributes to the "baseline" of the linewidth but does not explain the strong increase of the linewidth below 100 K. The error bars are smaller than the size of the data points.

mode) magnons, the intrinsic relaxation (spin-orbit coupling) is related to the Kasuya-Le Craw process.

4.7.3 Peaks: Rare earth impurity scattering

The sum of the intrinsic damping and the SLK scattering does not explain the peaks of the linewidth at specific temperatures. Hence, another mechanism must be present. As mentioned, YIG is a material which cannot be found as such in nature and belongs to the class of rare earth garnets [92]. Although high purity samples can now be fabricated, the inclusion of impurities cannot be wholly excluded during the growth process [188]. Specifically, it is known that the presence of other rare earth impurity ions in YIG can significantly increase the magnon linewidth [140]. As illustrated in the theoretical introduction, the presence of these rare earth impurity ions can change the temperature dependence of the linewidth. The splitting of the two lowest energy levels in the crystal field multiplett of the corresponding rare earth impurity ion is temperature dependent. If the resonance frequency of the system corresponds to a resonant transition from the upper to the lower energy level, another relaxation channel is opened. As a result, the linewidth is strongly enhanced at this temperature and observed in the form of a peak where the frequency of this energy splitting depends on the specific rare earth impurity ion in the sample. Moreover, if there are different rare earth impurities in the sample,

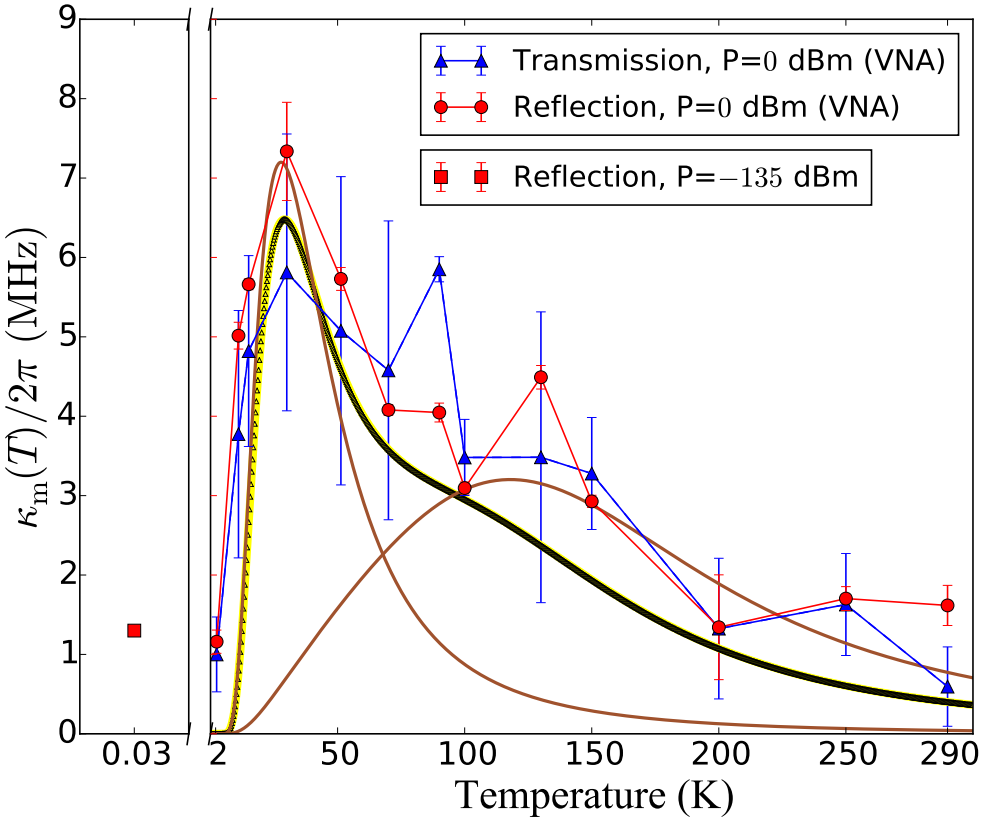

Figure 4.26: Temperature dependence of the magnon linewidth extracted from the polariton's line shape in reflection (red circles) and transmission (blue triangles). The solid red and blue line connect the data points and serve as a guide for the eye. Based on Equation (2.9.2), the green lines individually represent the peak of the linewidth due to scattering from at least two different types of rare earth impurity ions. The summation of both contributions (black curve), including the offset from line broadening due to intrinsic and surface scattering models the complete temperature dependence well. The parameters used for the model are given in Table 4.5. The solid brown lines model the individual identified peaks in the linewidth with parameters given in Table 4.5. The offset originating from intrinsic damping and surface pit scattering (SLK) has to be added to the modelled curves. The above-calculated offset is not included as this calculation represents a rough estimate. In addition, the solid lines seem to go to zero at 0 K because the fit result for the linewidth at 2.4 K is estimated too low, and is an outlier in the fit.

one will observe the peaks in the linewidth at different temperatures. Depending on the relative concentration of the rare earth impurity ion, the heights of the peaks at different temperatures may differ.

This kind of temperature-dependent behaviour could explain the observation shown in Figure 4.24. By means of Equation (2.9.2), it is possible to model each peak individually, as illustrated in Figure 4.26. In summary, by taking all the discussed contributions into account, it is possible to model the temperature dependence of the magnon linewidth by a combination of (dominating) rare earth impurity scattering, surface pit scattering,

	Peak at $T = 43\,\mathrm{K}$	Peak at $T = 90\,\mathrm{K}$
$c_{\|\|}\left(\frac{\mathrm{GHz}}{\mathrm{K}^2}\right)$	$0.2 \cdot 10^{-3}$	$29 \cdot 10^{-3}$
ς	15.2	9.1

Table 4.5: Table with the values of both peaks for the longitudinal spin lattice relaxation rate $c_{||}$, and the temperature independent scaling factor $\varsigma = \frac{4c_{\mathrm{imp}}Sz_{\mathrm{imp}}^2}{\hbar k_B}$ from Equation (2.9.2). The resonance frequency is taken to be $\omega/2\pi = 6.5\,\mathrm{GHz}$.

and intrinsic damping. The full temperature dependence is shown in the above figure through the solid black line. Please note, that this is a model based on Equation (2.9.2) with physically reasonable parameters and is not the result from a numerical fit. Due to the low number of available data points, the fit did not converge to reasonable values. Regarding a comparison of the absolute values from the SLK linewidth and the rare earth impurity scattering value at $T = 290\,\mathrm{K}$, one may argue about the discrepancy between the reflection and transmission data, which exceeds the respective error bars. However, since the error on the transmission data is much higher in general, the linewidth value at this temperature has to be estimated to be slightly higher, around 1.6 MHz. Furthermore, the contribution of 0.95 MHz from the surface scattering, represents a rough estimate, as the size of the pores in this model is taken to be the same as the surface roughness. Taking this into account, modelling the temperature dependence as displayed in Figure 4.26 and Table 4.5 shows reasonable agreement to the measured data.

Note, that regarding the qualitative behaviour and magnitude of the values, this temperature dependence is in good agreement with previous studies on the Kittel mode magnon's linewidth [131, 135, 136, 137]. Therefore, the existence of the cavity magnon-polariton does not significantly influence the damping of the magnon by the additional coupling to the cavity photons.

4.7.4 Temperature dependence of the quality factors

In order to discuss the temperature dependence of the cooperativity of the polariton, the total linewidth of the cavity resonator and the temperature dependence of the coupling parameter to the feed line also have to be examined. The temperature dependence of these parameters is shown for both reflection (coupling to the feed line κ_e (blue) and loaded cavity loss parameter κ_r(red)) and transmission ($\kappa_{e,(1,2)}$ for the first and second port) measurements. The external coupling parameters of the two measurement types do not undergo excessive changes over the whole temperature range investigated. They are in the range of 1 MHz to 2 MHz, whereas the external coupling parameter from the reflection measurement is slightly higher at room temperature but varies less. All the ports are optimised at room temperature. Towards lower temperatures, these values and fluctuations increase because the couplers could not be optimised once the measurement rod is inserted and cooled down. The cavity resonator's couplers are optimised such that the cavity resonance is at the maximal amplitude and the lowest linewidth, i.e. as close as possible to being critically coupled. Therefore, the relatively constant value as a function of the temperature is an indication that the coupling of energy from the feed line into the cavity resonator does not change drastically and the values can be directly compared.

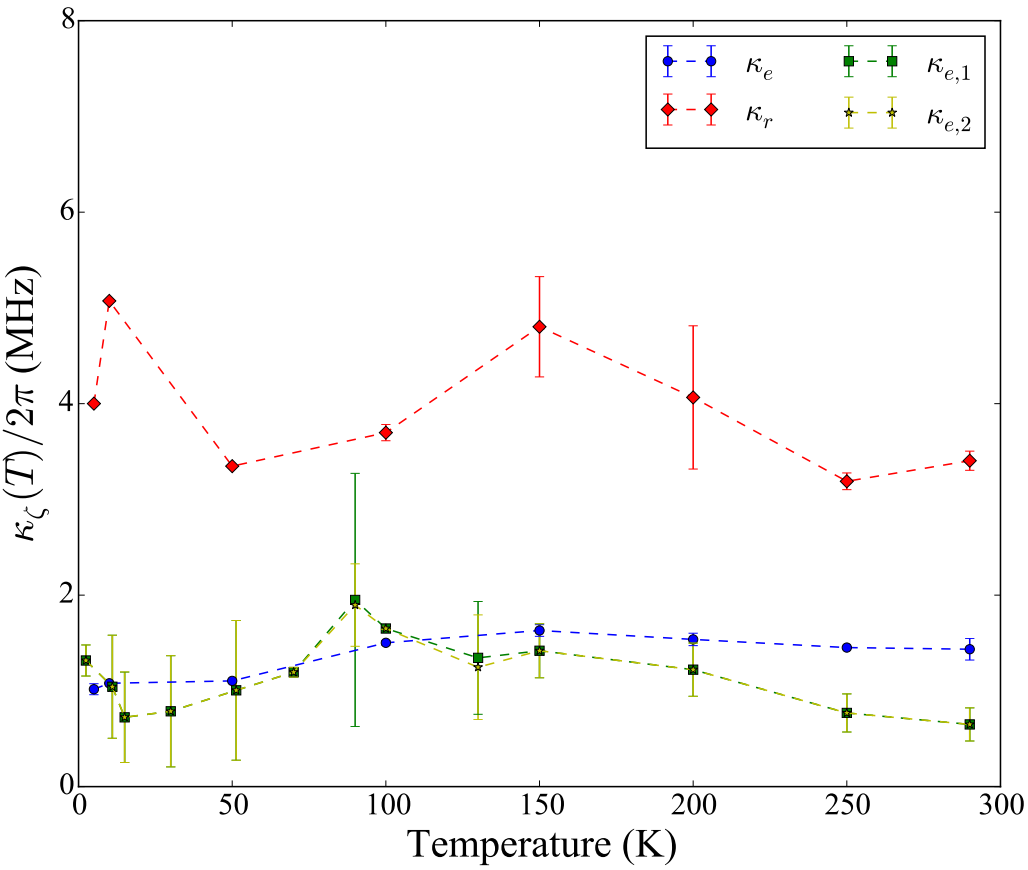

Figure 4.27: Temperature dependence of the coupling parameters κ_e (blue), κ_r (red), $\kappa_{e,1}$ (green), $\kappa_{e,2}$ (yellow) which are respectively the external reflection, loaded cavity loss parameter, the first and second cavity resonator port in transmission. Within the error bars, the value for the coupling parameters in the transmission measurement is, for both ports, on the order of 1 MHz over the whole temperature range. The resonator losses are of the order of 4 MHz for the entire temperature range. Towards lower temperatures, the errors and the values themselves increase, as the cavity resonator is optimised at room temperature and then inserted into the cryogenic setup.

In addition, Figure 4.27 displays the temperature dependence of the sum of internal and external loss factors, yielding the loaded loss parameter κ_r. Starting from 3.8 MHz, the linewidth slightly increased for intermediate temperatures (100 to 200 K) but remains on average on the order of 4 MHz. As this value also includes the internal dissipation, one can calculate this to be in the order of 2.5 to 3 MHz over the whole temperature range.

Change around resonance

In order to ensure that the above loss parameters do not undergo a strong change as they approach resonance, the dependence of the three coupling parameters, κ_e, κ_r, and κ_m has been studied as a function of the external static field around resonance. The result is shown for the respective values from an exemplary reflection measurement at $T = 50$ K in Figure 4.28. Starting from below the resonance field, both the magnon linewidth κ_m (red) and the external coupling parameter κ_e (green), do not significantly change as they pass resonance. The total cavity resonator losses, denoted by κ_r, increase as the applied

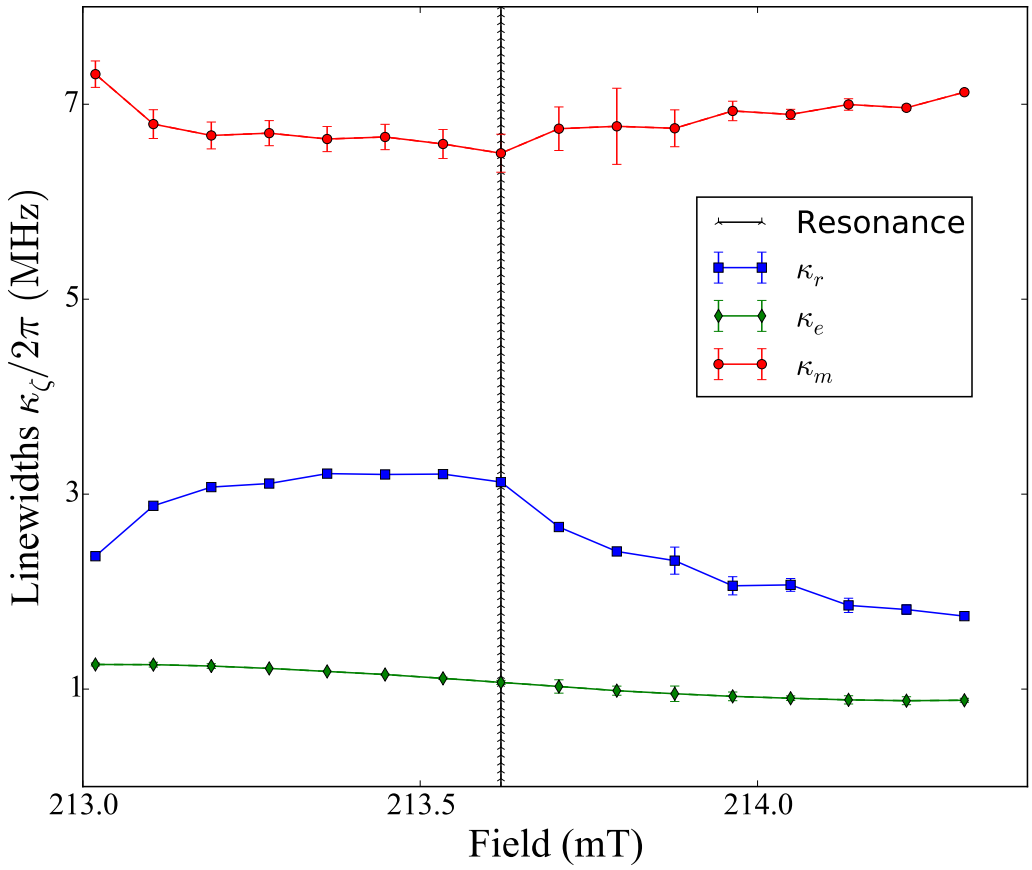

Figure 4.28: Dependence of the loss parameters on the external field for a measurement around the resonance frequency of the avoided crossing (vertical dotted black line) at $T = 50\,\mathrm{K}$. The magnon linewidth κ_m (red) is around 7 MHz, the total cavity resonator loss κ_r (blue) decreases from 3 MHz to 2 MHz when passing the resonant field towards higher field values and the coupling parameter to the feed line, κ_e remains as shown before, on the order of 1 MHz. The cavity resonator loss increases as the system approaches resonance by the external field, because of the enhanced coupling probability to the magnons, which absorb energy from the cavity mode. The error bars are on the order of the data points.

field approaches the resonance field. This linewidth enhancement can be attributed to the increased coupling of the cavity resonator photons to the Kittel magnons. Thus, additional energy is absorbed from the magnonic system as the cavity magnon-polariton is formed. With the full understanding of the cavity loss parameters and the magnon linewidth, the cooperativity of the hybridised system can now be discussed.

4.8 Cooperativity C

With the knowledge of the temperature-dependent magnon and total cavity resonator loss at hand, the coupling strength can be now compared to the product of the linewidths. Such comparison allows one to quantify the relative strength of the strong coupling regime, i.e. the amount of coherent information exchange including losses. As described in Chapter 3, Section 3.5, if $C > 1$ the coupling strength exceeds the system's damping, and such information exchange can take place. Based on Equation (3.19) and the previous

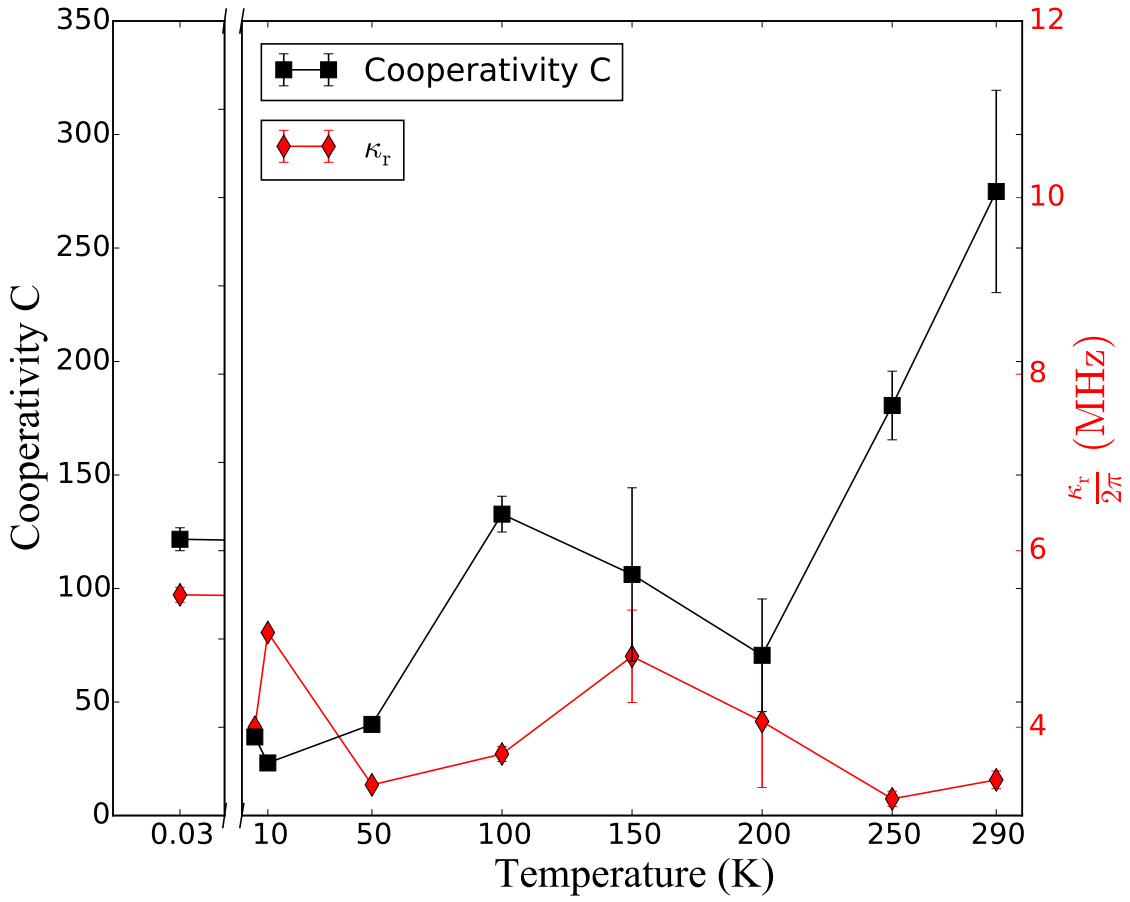

Figure 4.29: Temperature dependence of the cooperativity C (black, solid line) and the loaded linewidth of the cavity resonator κ_r (red, solid line). C is calculated according to Equation (3.19). As κ_m changes most as a function of temperature due to the rare earth impurity scattering and κ_r is almost constant within the error bars, the cooperativity shows an inversed temperature behaviour to κ_m. Numberwise, the cooperativity goes from 275 at room temperature down to 25 at 5 K. Despite the decrease, the cooperativity exceeds by at least one order of magnitude the minimal value of 1 for coherent information exchange.

discussion on the individual linewidths, the full temperature dependence of the cooperativity is displayed in Figure 4.29 (black squares). From a minimal value of 25 at 10 K the cooperativity reaches a maximum of 225 at $T = 290$ K. However, from $T = 30$ mK, C decreases by 75 % to the minimum at 10 K before C increases again. In addition, after another small peak at $T = 100$ K, C decreases for temperatures smaller than $T = 200$ K before C increases to the maximum value at 290 K. Besides $C(T)$, Figure 4.29 displays the temperature dependence of the total resonator losses (red diamonds) on which C also depends upon. This quantity shows a peak at $T = 150$ K and 10 K but does not exceed 6 MHz. As shown in Figure 4.26 the magnon linewidth exhibits peaks at 40 K with a total linewidth of ≈ 8 MHz and a smaller one at $T \approx 100$ K of ≈ 4 MHz due to rare earth impurity scattering. Thus, the magnon linewidth κ_m contributes most to the change in C by means of the strong peaks at certain temperatures. If the cavity resonator linewidth is comparably low (< 4 MHz), the cooperativity inversely reflects this increase in magnon linewidth. However, for the temperatures of increasing κ_r, the linewidth also increases

(c.f. Figure 4.26) which results in the observation of the local minimum for C at 200 K. Thus, the additional small peak is attributed to the decrease of κ_r whilst the magnon linewidth still increases at 100 K and the decrease at 40 K to the second, most dominant peak of κ_m (c.f. Figure 4.24 and Figure 4.26). Even the lowest value of the cooperativity is at least one order of magnitude higher than 1. Therefore, the coherent exchange of information by the resonant coupling between a cavity resonator photon and a magnon in the strong coupling regime is robust and prevails over the whole temperature range. Note, that the sample has been commercially obtained and did not undergo any post-treatment such as further refinement of the surface roughness. Thus, the cooperativity of this polaritonic system is robust even in the presence of strong peaks in the magnon linewidth. In addition, by increasing the purity of the sample, the cooperativity could probably be further enhanced.

4.9 Summary

In summary, this study on the temperature dependence of key properties of a hybridised cavity photon-magnon system gives a good characterisation and insight into the general behaviour of the coupling strength and the persistence of the cooperativity $C > 1$ for coherent information exchange. It is experimentally shown, that the temperature dependence of the coupling strength has to be divided into two regimes for $T > 100\,\mathrm{K}$ and for $T \leq 100\,\mathrm{K}$. Whereas for the first, the temperature-dependent changes of the saturation magnetisation due to Bloch's $T^{3/2}$ law govern the evolution of the coupling strength, the parasitic coupling to higher order magnetostatic modes results in a decrease of the coupling strength, which is minimal at $T = 40 - 50\,\mathrm{K}$. Further, it is shown that the temperature dependence of the CMP's linewidth is in agreement with the previously determined temperature-dependent linewidth of bulk YIG samples almost 50 years ago. Apart from small contributions such as SLK scattering due to rough surfaces, rare earth impurity scattering dominates the temperature dependence of the utilised YIG sphere. For this hybrid system, from the fitting, the linewidth has a large peak at 43 K and exhibits a second smaller and broad increase at 90K. In combination with the cavity resonators' loss $\kappa_r(T)$, it is shown that the coherent exchange of information is present over the entire studied temperature interval since the magnon and the cavity photon remain strongly coupled.

However, for possible future applications, it is not enough to be able to show that a coherent exchange of information of the cavity photons and the magnons does exist. Furthermore, it is even more important to be able to deliberately manipulate the system such as one can turn on or off the flow of information. Switching the information flow on or off at will could be achieved by controlling the coupling strength in such a way that, for full "transmission" of information, the gap of the avoided crossing is maximised. Correspondingly, also the gap should be manipulable such that it can close completely. If the gap could be changed, one could, for instance, observe by a complete collapse of the avoided level crossing; also called "level merging". In the course of this doctoral thesis, a new experimental scheme has been developed to enable steering the macroscopic coupling strength as it has also been theorised [77, 189]. In this experiment, the control over the coupling strength could be achieved by the introduction of a second microwave feed line.

This feed line serves as an additional drive to the excitation of magnons in the sample and differs in terms of amplitude and phase relative to the first, conventional microwave port. The experimental scheme, the results, and the subsequent discussion are the subject of the next chapter.

Chapter 5

Level merging

5.1 Introduction

The temperature dependent study on the properties of the cavity magnon-polariton (CMP) for a resonantly coupled hybrid system (c.f. Chapter 4) has been conducted for a fixed value of the coupling strength. In this experiment, the magnons are not directly coupled to the microwave feed line but are excited by the AC magnetic field of the standing wave mode of the cavity resonator, i.e. the cavity resonator photons. However, on the route towards applications in information technology or the implementation of hybrid cavity photon-magnon systems as the storage unit for quantum computers, the realisation of strong coupling between magnon and photon is not sufficient. Although the demonstration of strong coupling is an essential first step, it only proves that there is a coherent exchange of information between both subsystems. Hence, the next goal towards the realisation of applications is the control over the coupling strength. Specifically, this means that it is possible to manipulate the coupling at resonance such that the coherent information exchange can be either enhanced or fully suppressed. There are numerous works on the control of the coupling strength for other polaritonic systems, such as exciton (electron-hole pairs) or surface plasmon (excited surface electrons) polaritons, but for the CMP few works exist [156, 190, 191, 192] and the references therein. Instead of actively tuning the coupling strength itself, the coupling strength is varied by manipulation of the cavity resonator-YIG system itself. The position of the YIG sphere is changed and the angle between the AC magnetic field and static bias field varied [61, 73]. Recently, the control of the coupling of a two-dimensional (2D) setup, employing a split-ring-resonator (SRR) and thin YIG film geometry, has also been shown [193]. However, an active control over the coupling strength would leave the CMP system itself unchanged during a measurement and could enable the implementation of such control mechanism into other systems or structures. Such control for a three-dimensional system (3D) can be achieved by the addition of a second microwave input which differs in both amplitude and phase from the original input, as it has been recently theorised [77]. The coupling strength is controlled by externally tuning the *relative* phase ϕ and amplitude ratio δ_0 between both inputs which results in a modification of the intracavity ac-magnetic fields generated from both ports. However, in order to obtain control over the coupling and not just a disturbed avoided level crossing due to interference between both inputs, the second input has to be decoupled from the cavity resonator photons. Instead, the second input couples only directly to the magnons in the magnetic sample. In this chapter, the first demonstration of active control of the coupling strength of a 3D hybrid system with two

tones will be presented. It will be shown, that for particular combinations of ϕ and δ_0, the coupling strength can be either enhanced or suppressed such that the frequency gap of the avoided level crossing in the dispersion vanishes. Experimentally, this is observed as a level merging of the cavity photon's and magnon's dispersion in place of an avoided level crossing. After a general consideration of the impact of the additional second input, the experimental setup including the modification of the reentrant cavity resonator from the previous chapter is presented. Then, due to the addition of a second microwave tone, i.e. input signal on the magnons, the modifications on the "classical" analytical expression for the reflection scattering $S_{11}(\omega)$ (c.f. Chapter 4, Section 4.5.3) are discussed. This change results in a new analytical expression for the reflection parameter derived from the Input-Output theory. Subsequently, simulations based on the new expression for $S_{11}(\omega)$ are performed, and the expected behaviour of the system is analysed. Before the dependence of the coupling strength from the relative amplitude and phase is shown and analysed the possible, unwanted contribution from a direct coupling between both inputs is considered. In the following, this contribution is denoted as "crosstalk". The chapter concludes with an examination of the total signal's linewidth in the regime of level merging and the control of the coupling strength of higher order magnetostatic modes which are simultaneously excited.

Please note, that the initial work has been done together with Christine Dörflinger in the course of her Master's thesis which I co-supervised [189]. In the course of that work, we proved the general concept of this two-tone controlled coupling strength. With her help in recording the data, I analysed these data such as the phase and amplitude dependence of the coupling strength. I also derived the formula for the scattering parameter where I furthermore acknowledge discussions with the authors from Ref. [77].

5.2 Physical meaning of the phase of the CMP

As mentioned in the introduction, the coupling strength is controlled by tuning the relative phase and amplitude ratio between two microwave inputs, i.e. ports, at the cavity resonator. Each input is inductively coupled into the cavity resonator and generates an alternating current (AC) magnetic field. Since the AC magnetic field from the second input directly drives the magnons only and the other the cavity photons as previously, a change of the relative phase corresponds to altering the phase correlation between the magnon and the cavity photon. First, it is necessary to understand the dependence of this phase correlation on the coupling strength and the expected changes in the dispersion spectra after the manipulation of the coupling strength. Therefore, before the setup for the experiment on level merging is introduced, above dependence and expected changes are discussed in the following section.

5.2.1 Phase relation between the magnon and cavity photon

The CMP represents the associated quasiparticle from hybridisation of strongly coupled spins and photons. Hence, the CMP is comprised of a spin and photon part. At resonance, the ratio R between the contribution of the spin and photon is R=1. However, off-resonance, R differs from one and, depending on the frequency, either the spin or the photon part dominates. The contributions to the CMP from spin and photon can be

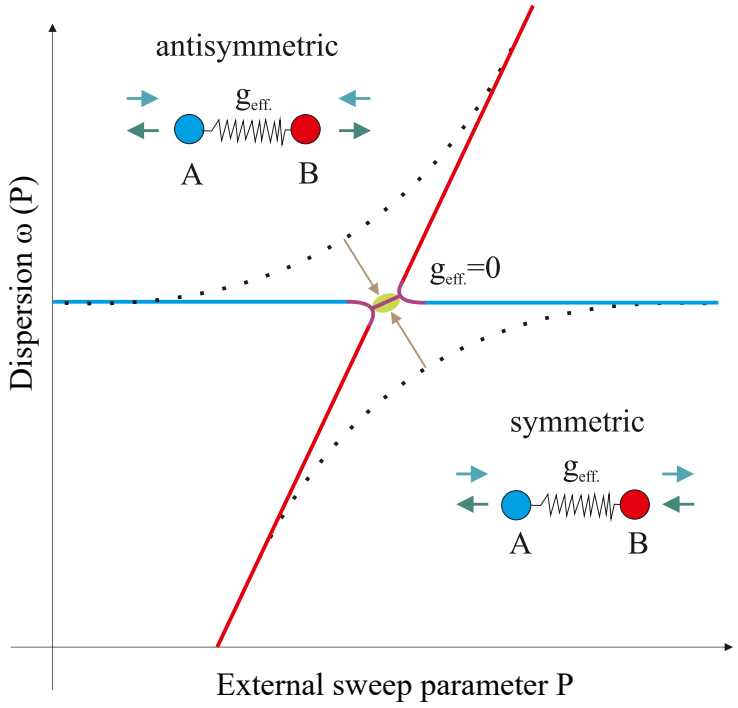

Figure 5.1: Schematical illustration of an attractive coupling and, hence, full level merging of spins (solid red line) and photons (solid blue line) at resonance. For the specific system discussed in the following, the frequency gap of the former avoided level crossing (dotted black line) closes due to the introduction of a second AC magnetic field driving only the spins, i.e. the magnons. The second tone exhibits a relative phase shift of π to the driving field induced from the microwave current of the cavity resonator. (c.f. RLC circuit model and LLG in Chapter 3). The upper left (antisymmetric) and lower right (symmetric) insets, show the solutions resulting in an avoided level crossing in the harmonic oscillator model. Depending on the value, the additional (phase dependent) input on B can change the symmetric and antisymmetric solution.

quantified in terms of a Hopffield transformation, which defines new polariton eigenstates X_+ and X_- instead of the uncoupled spin and photon states x_+ and x_- [61, 194]. It can be expressed as:

$$\begin{pmatrix} X_+ \\ X_- \end{pmatrix} = \begin{pmatrix} \zeta_- & \zeta_+ \\ -\zeta_- & \zeta_+ \end{pmatrix} \cdot \begin{pmatrix} x_1 \\ x_2 \end{pmatrix}, \tag{5.1}$$

where the individual fractions are denoted by the matrix elements $\zeta_\pm = \sqrt{\frac{g^2 \pm \Delta}{2g}}$) [194]. Neglecting damping and considering the on-resonant case with $R = 1$, shows that the repulsion of the two solutions leads to an avoided level crossing where the sign of the coupling strength is positive. In the Tavis-Cummings Hamiltonian, the coupling strength appears in the interaction term. The coupling strength is a real, positive valued quantity and the presence of the coupling can be understood an additional repulsive potential leading to hybridisation, i.e. the observation of an avoided level crossing in the dispersion spectrum [11, 163]. In the model of coupled harmonic oscillators, the upper polariton branch corresponds to an oscillation out of phase while the lower branch represents a

symmetric, in-phase relation. Thus, a fixed phase relationship between the spin and photon constituting the CMP exists.

5.2.2 Level merging: Changes in the dispersion spectrum

If the coupling strength can be changed by manipulating that fixed phase relationship such that the spin-photon system experiences an attractive rather than a repulsive potential, one would be able to manipulate the hybrid spectrum as illustrated in Figure 5.1. The coupling strength would become complex, and the squared value change sign (c.f. Chapter 3, Section 3.2) and the imaginary part which is typically attributed to losses the level attraction would dominate. Hence, the former avoided level crossing in the dispersion spectrum would collapse at resonance observed by the closure of the frequency gap. Such a coalescence of the symmetric and antisymmetric solution is referred to as "level merging". For $g_{\text{eff}} = 0$, the spin and photon dispersions cross and the coherent information exchange would be completely suppressed. Furthermore, for $g_{\text{eff}}^2 < 0$, the spin and photon states are attracted. In a narrow frequency range centred around the resonance, they may oscillate with the same frequency, i.e. that of the single remaining solution. The addition of a second AC magnetic field ($\mathbf{h}_{\text{AC}}^{\text{magnon}}$) to drive the spin part of the hybrid system can lead to control over the magnitude and sign of the coupling strength as it has also recently been theorised by Grigoryan *et al.* [77]. Therefore, the coupling strength is controlled by tuning the *relative* phase ϕ and amplitude δ_0 of the cavity's AC field $\mathbf{h}_{\text{AC}}^{\text{cavity}} = (0,\, h_{\text{AC}}^{\text{cavity}},\, 0)$ and $\mathbf{h}_{\text{AC}}^{\text{magnon}} = (h_{\text{x, AC}}^{\text{magnon}},\, 0,\, h_{\text{z, AC}}^{\text{magnon}})$ for the second tone, where $\delta_0 = \frac{|h_{x,AC}^{\text{magnon}}|}{|h_{\text{AC}}^{\text{cavity}}|}$ is defined as the ratio of the cavity magnetic AC field strength and x-component from the magnon port's AC magnetic field at the sample's position. As shown schematically in Figure 5.1, the prediction is that when $\phi = \pi$, the coupling strength will go to zero. From the cavity photon's perspective, the coupling to the spin represents another channel for energy dissipation. The relative phase change compensates for this dissipation and results in the spins acting as an additional drive for the cavity photons. Instead of a level repulsion, a level merging between spin and photon branch should then be observable. Consequently, this would allow one to study the dependence of the coupling strength on the relative phase and amplitude. It has been shown in the past, that for frequencies close to resonance, the coupling between spin and photon part has a substantial impact on the FMR linewidth [195]. Therefore, the influence of the level merging on the signal's amplitude and the associated linewidth is studied. According to the theoretical expectation, the amplitude of the crossing point at resonance should be greatly enhanced and the linewidth should decrease [77].

In order to experimentally realise the control over the CMP's coupling strength and study the previously mentioned features, the "classical" cavity driven polariton system with one external coupling to a microwave feed line is replaced by a two-tone CMP spectroscopy experiment. The idea for a realisation of this experiment and the different internal and external couplings is schematically drawn in Figure 5.2 by modelling the cavity photon and the magnons as two coupled harmonic oscillators. Here, the spring constants $\kappa_{e,1}$ and $\kappa_{e,2}$ respectively denote the coupling of the cavity resonator photons to microwave photons of the first microwave feed line ("cavity port"), and the magnons to the microwave photons from the second feed line ("magnon port"). Whilst the first corresponds to the same inductively coupled input of the previous chapter, the second one should ideally exclusively couple to the magnonic sample. Due to experimental constraints such as cor-

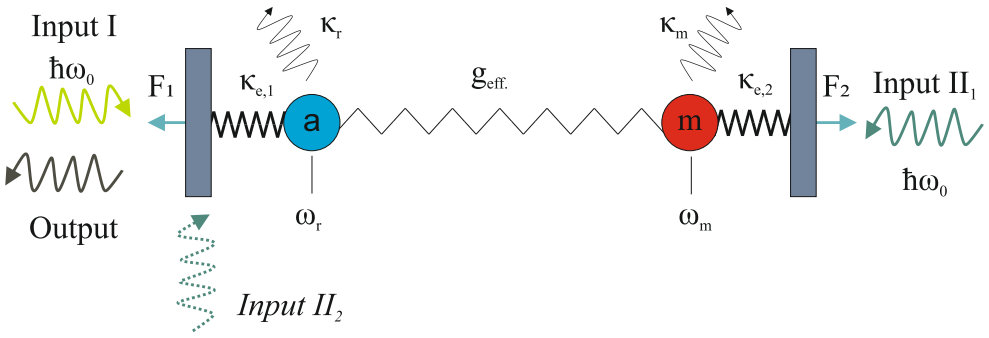

Figure 5.2: Schematic illustration of the system with two microwave signal inputs displayed in the framework of driven, coupled harmonic oscillators. The second input ("magnon port") ideally only drives the magnonic system. However, experimentally there is a small contribution from a parasitic excitation of cavity photons through the second port and is called "crosstalk", indicated by *Input* II_2 in the figure (Input II=Input II_1+Input II_2) in order to distinguish the (unwanted) crosstalk from the other inputs. The crosstalk is a parasitic contribution which should be suppressed as much as possible. The measurements are conducted in reflection from Input I, referred to as "cavity port" in the discussion.

rect alignment of the couplers (c.f. Section 5.5.3), the crosstalk cannot be suppressed completely, and a small fraction of Input II (Input II_2 in Figure 5.2) is directly coupled to the cavity photons. Since it can strongly influence the dispersion spectra obtained through a S_{11} reflection measurement (reflection at Input I in Figure 5.2) and presumably distort the signal's line shape and amplitude, the crosstalk has to be suppressed as much as possible. The (unwanted) contributions to the crosstalk are identified and discussed in Section 5.7 before the experimental results are shown. As before, the cavity photon, magnon dissipation factors and their resonance frequencies are respectively denoted by κ_r, κ_m, and ω_r, ω_m. After having introduced the type of dispersion spectra which are associated with controlling the coupling strength such as entering the regime of level merging, the experimental setup is going to be discussed.

5.3 Experimental setup

Before the implications of adding a second microwave excitation signal into the system such as the influence of the signal shape measured in reflection are discussed separately, the complete experimental setup is presented.

As displayed in Figure 5.3, a two-port VNA is used for all measurements. For the demonstration of level merging for a CMP, the microwave photons on either path have to be coherent up to this relative phase. Therefore, the first port of the VNA serves as the single microwave source for the system. If not mentioned otherwise, an output power level of $P_{\mathrm{out}} = -5\,\mathrm{dBm}\,(0.3\,\mathrm{mW})$ is set for the data presented in the following. The outgoing signal is then split by means of a power divider. The interference between both paths is of the order of $-20\,\mathrm{dBm}$. However, this contribution is negligibly small and can be neglected from now on. Please note, that in the entire experimental apparatus, commercially bought cables are utilised. The total cable length per signal path is of the order of 2 m before

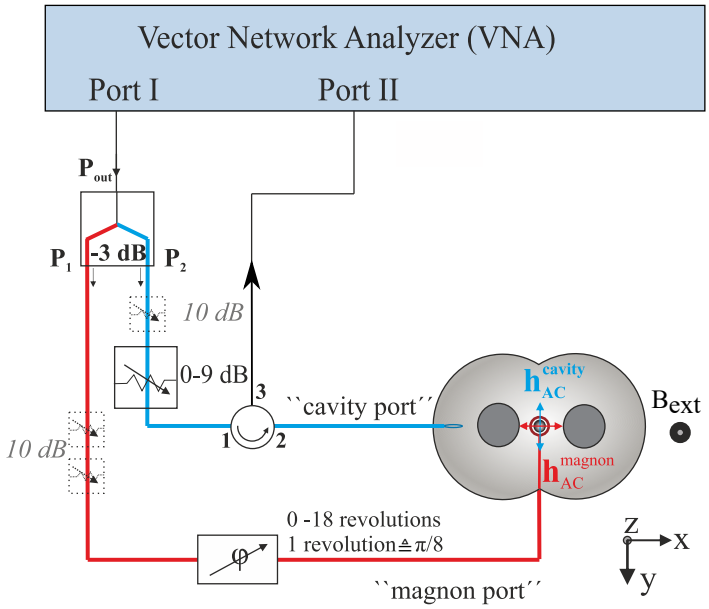

Figure 5.3: Sketch of the experimental apparatus including the position of the second inductive loop in the cavity resonator. In order to realise a relative phase shift, a power splitter divides the signal coming from Port I serving as the single microwave source into two paths, denoted by P_1 to the magnon and P_2 to the cavity port, respectively. The relative amplitude ratio is tuned by both a variable (0 to 9 dB) attenuator permanently put into the path of the cavity and fixed value (dotted) attenuators (10 dB each) insertable into P_1 and P_2. The fixed ones allow for extending the available range of the relative amplitude ratio between both inputs. The conversion of the attenuation to the relative amplitude ratio δ_0 is given in the appendix (c.f. Table 8.1). A mechanically tunable phase shifter modulates the phase from zero to $2.25\,\pi$ and is placed into P_1. The readout at Port II is from a reflection measurement ($S_{11}(\omega)$) at the cavity port. Here, the cavity is illustrated schematically, the position of the coupling loops and ports are shown in Figure 5.4 and 5.6 b.). In the experiment, the magnon port's loop is tilted by 45° towards the long cavity axis. The external magnetic field is applied along the z-direction.

arriving at the second VNA port, yielding an additional attenuation of approximately -3 dB of the signal along the whole path. Due to the different components in the path to the magnon (P_1) or cavity port (P_2), the individual powers, i.e. squared amplitudes at each resonator port, are already intrinsically different. Moreover, both signals travelling along the cables collect a certain phase which is related to the travelled distance. Thus, the different cable lengths result in a constant phase difference between both the cavity and the magnon port. However, in this experiment for the observation of level merging solely the *relative* amplitude and phase of the internal, AC magnetic fields of the magnon and cavity port are of importance. Therefore, tuning the relative phase and amplitude suffices for this experiment. The relative phase is modulated by the addition of a mechanically tunable phase shifter in the path P_1 to the magnon port. Concerning the phase shifter, it comprises 18 revolutions in total which allows one to change the phase by $12.25\,\pi$ in total, where one revolution corresponds to a phase shift of $\phi = (1 \pm \frac{1}{8})\pi$. The error denotes the shift of the phase going over the entire range back and forth repeatedly and measuring the phase difference with an oscilloscope. On the contrary, the relative

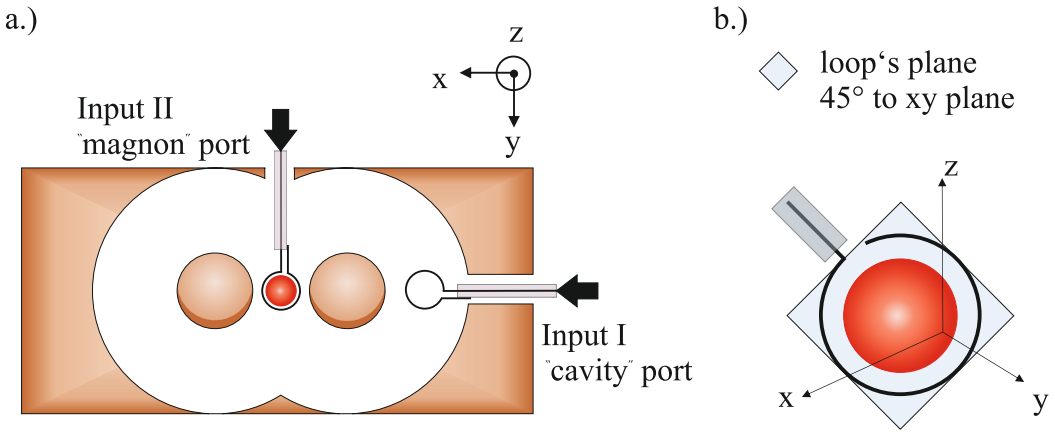

Figure 5.4: a.) Schematic drawing of the modified reentrant cavity illustrating the position and alignment of the two ports. Both consist of a loop with a single winding which couples inductively to either the cavity photons at the cavity port or the magnons at the magnon port. The magnon port consists of a metallic loop (cooper wire) which encloses the YIG sphere (red, $d = 0.2\,\mathrm{mm}$). b.) Actual alignment of the sphere enveloped by the loop of the magnon port. This loop makes an angle of 45° between the loop's plane and the xy-plane of the reentrant cavity resonator. It has been experimentally found, that this orientation represents the best compromise between the spatial limitations and minimisation of the crosstalk.

amplitude is controlled by attenuators in both paths. Whilst in the signal path P_2 to the cavity port a variable attenuator from 0 to 9 dB is permanently inserted, those with a fixed attenuation of 10 dB can be inserted in both paths (c.f. Figure 5.3). Depending on the desired regime of the amplitude ratio, i.e. whether the contribution from the cavity port or the magnon port should dominate, the attenuators are either placed into path P_1 or P_2, respectively. As mentioned, the dispersion spectra for sweeping the relative phase while keeping the relative amplitude ratio fixed and vice versa are recorded through a reflection measurement at the cavity port. The circulator in P_2 prevents any backflow into the feed line from reflections at the cavity port and directs the signal to Port II of the VNA. Most of the measurements presented in this chapter have been performed at the room temperature setup for ferromagnetic resonance at the KIT. This setup is comprised of a small coil magnet with a controlling voltage source, the VNA and the driving software. That experimental apparatus has been set up previously, and more details can be found in Ref. [189]. However, the reentrant cavity resonator has been brought and modified by myself for the experiment, which is discussed in the next section and also schematically illustrated in Figure 5.4 a.).

5.4 The reentrant cavity resonator for two-tone spectroscopy

For this spectroscopic study of the CMP employing two inputs with shifted phase and amplitude, the reentrant cavity resonator utilised in Chapter 4 required modifications. In order to meet both the condition of minimised crosstalk and of a tunable relative phase

and amplitude between $\mathbf{h}_{\mathrm{AC}}^{\mathrm{cavity}} = (0,\, h_{\mathrm{AC}}^{\mathrm{cavity}},\, 0)$ and $\mathbf{h}_{\mathrm{AC}}^{\mathrm{magnon}} = (h_{\mathrm{x,\,AC}}^{\mathrm{magnon}},\, 0,\, h_{\mathrm{z,\,AC}}^{\mathrm{magnon}})$, the following conditions and constraints exist:

- **Field alignment**
  In order to obtain FMR in the magnonic sample, i.e. excite the Kittel mode magnons, both of the time-harmonic AC fields need to exhibit a transversal component perpendicular to the external, static field $H_{\mathrm{ext}} = \mathbf{H}_{\mathrm{ext}}\hat{\mathbf{z}}$. Therefore, the magnetic fields have to be aligned such that $H_{\mathrm{ext}} \perp h_{\mathrm{AC}}^{\mathrm{cavity}} \perp h_{\mathrm{x,\,AC}}^{\mathrm{magnon}}$. At the magnetic field for a resonant coupling $\mathbf{H}_{\mathrm{res}}$, it yields $\mathbf{H}_{\mathrm{ext}} = \mathbf{H}_{\mathrm{res}}$ and $\omega_r = \omega_m$. Note, that the orientation of the inductive loop of the magnon port of 45° to the xy-plane of the cavity resonator results also in a component $h_{\mathrm{z,AC}}^{\mathrm{magnon}}$. This component is parallel to the external field and does not contribute to exciting the magnons in ferromagnetic resonance in the current setup.

- **Limited space and geometry**
  As shown in Figure 5.4, the magnon port consists of a circular metallic (made out of copper) loop with one winding around the spherical sample. If not otherwise stated, for most of the following measurements a YIG sphere ($r = 0.1\,\mathrm{mm}$), commercially bought from Ferrisphere Inc.™ [103], is used. As before, the sphere is glued to a thin, beryllium oxide (BeO) rod of 1 cm length and inserted into the cavity resonator such that the BeO rod is parallel to the z-axis. As a result, the orientation of the loop's plane (shaded blue in Figure 5.4 b.)) relative to the xy-plane of the cavity resonator (xy-plane) cannot arbitrarily be chosen to minimise the crosstalk.

- **Dimensions and position of the couplers**
  The magnetic field distribution of the cavity resonator's "bright" mode which will again be used exhibits the highest homogeneity in the centre between the posts. Thus, the YIG sphere is placed in this position to ensure a uniform excitation of the Kittel mode over the entire sample's dimension. The shape of the enveloping loop needs to be as circular as possible and with the smallest diameter without touching the sample. As discussed for the temperature dependence of the magnon linewidth of the Kittel mode's in YIG, additional inhomogeneities can drastically increase the linewidth. The larger the total dissipation factors κ_r and κ_m become, the harder it is to reach the strong coupling regime with this smaller sphere. Thus, e.g. lowering the surface quality such as by accidental scratches, needs to be avoided. In addition, together with the relative orientation to the xy-plane of the cavity resonator, the radius of the magnon port's loop determines the initial amplitude ratio δ_0 between the fields (c.f. Figure 5.6 b.)). Furthermore, the specific choice of the loop's geometry sets the accessible regime of relative amplitudes and whether it is possible at all to obtain level merging. Moreover, in the beginning, all couplers have to be carefully set and then remain fixed for the rest of the experiment.

5.5 Impact of the second microwave port

The addition of the second microwave port to the system enables tuning the coupling strength by means of ϕ and δ_0. However, this second microwave port represents a major change to the previous system from Chapter 4. Thus, the impact on the signal recorded in reflection at the cavity port needs to be discussed. Moreover, since δ_0 is defined as the ratio between the intracavity AC magnetic fields which are perpendicular to the external

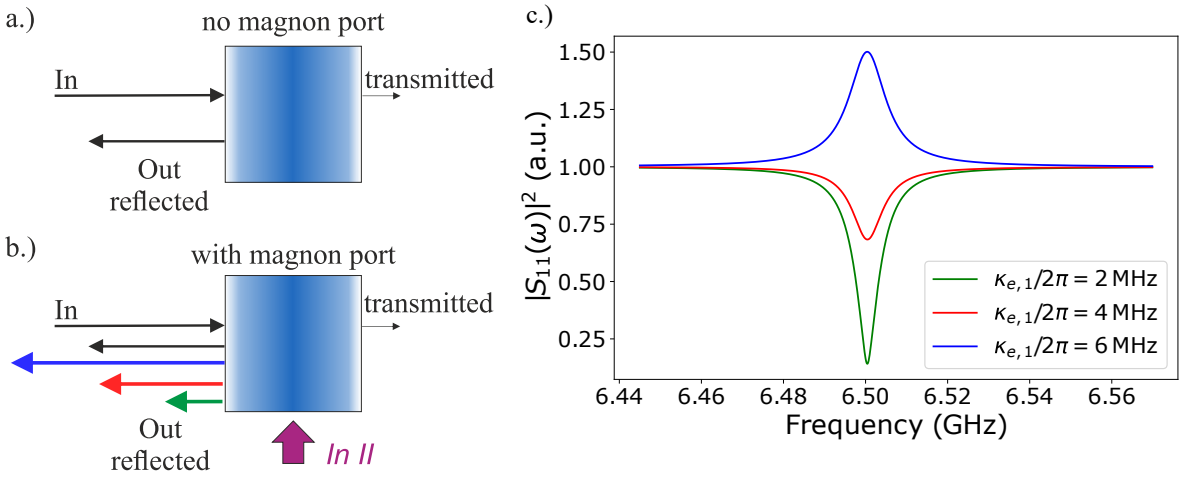

Figure 5.5: a.) Standard situation of a reflection measurement of a cavity resonator-sample system with one input signal. In reflection, losses are recorded and observed in the form of a resonance dip. b.) Change in contributing signal amplitudes if another input (In II) is added which only couples to the cavity resonator via the coupling of the magnons and cavity photons. For certain configurations, the second input serves as another drive to the cavity photons, and the input losses from the first port can be partially compensated or even exceeded. Then, either the amplitude of the reflection dip decreases to the reflectionless baseline value of one or for the case of gain, the cavity resonance transformed to a peak. On the basis of the modified $S_{11}(\omega)$ expression this is illustrated in c.) for three different values of coupling factors, i.e. strengths of the value for $\kappa_{e,1}$ for $\phi = 0, g_{\text{eff}}/2\pi = 5\,\text{MHz}$ and $\delta_0 = 1.23$ ($\kappa_m/2\pi = 1\,\text{MHz}, \kappa_r/2\pi = 5\,\text{MHz}, \omega_r/2\pi = 6.50\,\text{GHz}, \omega_m/2\pi = 6.37\,\text{GHz}, \kappa_{e,2}/2\pi = 1\,\text{MHz}$).

magnetic field of each port the (internal) amplitude ratio δ_0 cannot be directly determined. Therefore, the change of $S_{11}(\omega)$ due to the second port and the determination of δ_0 are discussed in the following.

5.5.1 Influence of second microwave port on the $S_{11}(\omega)$ response

The addition of the magnon port to the reentrant cavity resonator can have a substantial impact on the recorded microwave signal in the reflection measurement. First, there is the suppressed crosstalk which is always adding energy to the cavity photons by the direct coupling to the cavity photons. However, for certain values of the relative phase and amplitude, the indirect energy transfer of the magnon port via the coupling of the magnons to the cavity photons can become important. The signal from the second port directly driving the magnons serves as another drive for the cavity photons and partially compensates or even exceeds the "losses" which refer to the absorbed energy in the cavity and leading to a dip in the reflection spectrum at the respective frequency. However, this either decreases the amplitude of the signal recorded towards the background, i.e. baseline or even transforms the dip to a peak. Based on Equation (5.7), different cases have been plotted for typical experimental, off-resonant values of the variables. The difference between the inputs and outputs of a setup for a single tone and two-tone CMP spectroscopy is also shown in Figure 5.5 a.) and b.). In the transition region between a dip and a peak where most of the signal's amplitude is hidden within the background, this effect compli-

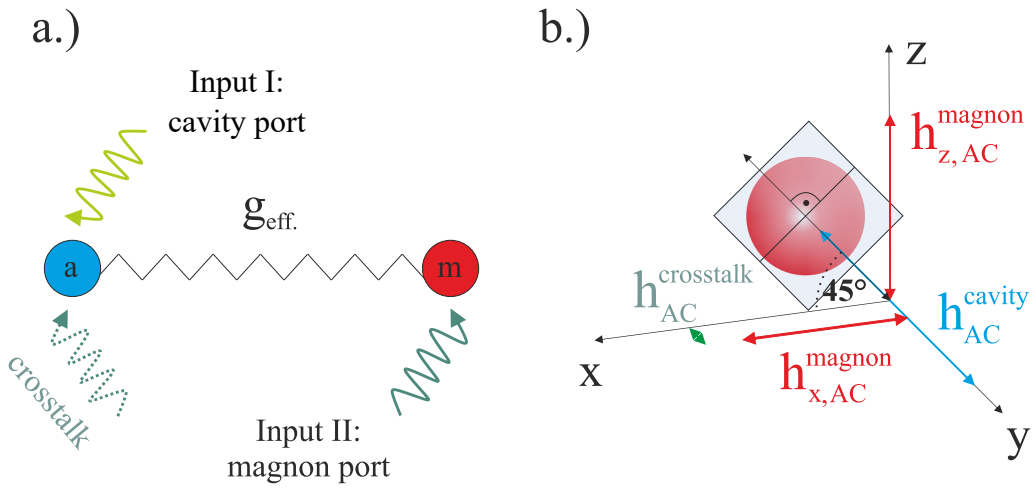

Figure 5.6: a.) Different inputs and couplings from the two-port system including the crosstalk which, in order to observe level merging and not direct interference effect between both ports, should be suppressed as much as possible. b.) Illustration of the alignment of all contributing AC magnetic fields in the coordinate system of the cavity resonator from Figure 5.4 a.). Due to the angle of 45° between the magnon port's inductive loop and the cavity resonator's xy-plane, there is a small, unwanted contribution along the y-axis capable of exciting the cavity resonator photons. This is the crosstalk field $\mathbf{h}_{\mathrm{AC}}^{\mathrm{crosstalk}}$ (shaded green as the contribution is much weaker and should be suppressed). The component along the x-direction is the necessary component of $\mathbf{h}_{\mathrm{AC}}^{\mathrm{magnon}}$ (red) which has the relative phase and amplitude relative to $\mathbf{h}_{\mathrm{AC}}^{\mathrm{cavity}}$ (blue). In the current understanding, the z-component of $\mathbf{h}_{\mathrm{AC}}^{\mathrm{magnon}}$ does not result in driving the magnons as the perpendicular alignment of the AC to the DC field for FMR is not given.

cates the analysis of the data. Therefore, for the final data analysis, it is not sufficient to consider only the amplitude of the complex signal. Instead, the phase has also to be considered, which is not done in most single tone CMP spectroscopic experiments. For a collection of other works in the field, the reader may refer to Ref. [61] and references therein. The details of the data analysis are discussed in Section 5.6.
Before a new expression for the reflection parameter $S_{11}(\omega)$ can be derived, it is necessary to further quantify the quality factor of the coupling of the microwave signal into the cavity. In addition, the amplitude ratio δ_0 cannot be directly determined from the experiment. Thus, the next section considers the quality factors and a general method to obtain δ_0 from either determining a conversion factor between internal and external amplitude ratio or the knowledge of the quality factors associated to the coupler's position.

5.5.2 Coupling regime of the microwave ports and amplitude ratio

As indicated before and sketched by the intracavity AC fields from the magnon and cavity port (c.f. Figure 5.4), it is not possible to measure the magnitude of the oscillating, time-dependent magnetic field components directly *at* the sample's position. Thus, with the current experimental setup, one cannot directly obtain values for the amplitude ratio

	cavity port	magnon port
$Q_i \pm \Delta Q_i$	(1925 ± 119)	(1699 ± 46)
$Q_e \pm \Delta Q_e$	(2573 ± 83)	(7704 ± 123)
$Q_l \pm \Delta Q_l$	(1101 ± 49)	(1392 ± 34)

Table 5.1: Result for the quality factors from a circle fit of an individual measurement on the cavity and magnon port in reflection. Whilst the cavity port is slightly undercoupled, the magnon port is strongly undercoupled as $Q_i \ll Q_e$. The values given are from an attenuator value of 8 dB along the path to the cavity port. The error bars originate from the fitting algorithm and are calculated from the covariance matrix.

of δ_0. Instead, it is only known to what extent the external power ratio between the two microwave feed lines (c.f. Figure 5.3) is changed using the attenuators.

As a result, solely the change in the external amplitude ratio between the two signal lines P_1 and P_2, denoted by δ_{ext} can be measured. The relative amplitude ratio at the sample's position in the cavity resonator is then denoted as the internal relative amplitude ratio δ_0. By introducing a factor ζ, which considers the amplitude change from coupling of the microwave signal into the cavity resonator at both ports, δ_0 can be calculated.

$$\delta_0 = \delta_{\text{ext}}\zeta,\ \zeta < 1, \tag{5.2}$$

such that $\delta_0 < \delta_{\text{ext}}$. Please note, that δ_{ext} is the product of the known change in amplitude ratio and the intrinsic amplitude ratio in the order of 1 as there are only small differences in the paths until the signal reaches the cavity ports such as in cable lengths ($\approx \pm 20$ cm) and different signal losses, for instance, at the inserted phase shifter or circulator. However, as this difference is small and the change of the amplitude ratio dominates, δ_{ext} is approximated by the ratio at the attenuators.

5.5.3 An alternative method to determine δ_0

Despite the above method for determining δ_0 which is obtained from fitting, the internal amplitude ratio δ_0 could, in principle, be experimentally found from the individual characterisation of the two cavity resonator ports' settings in an off-resonant measurement. Then, the individual loaded quality factors, i.e. the coupling efficiency of the respective feed line into the cavity resonator, can be found. If both δ_{ext} and the coupling parameters at the ports are known, it is possible to make a rough estimate about the "true" value of the amplitude ratio. In addition, this characterisation of the cavity and magnon port allows one to determine the coupling regime of each port. Similar to the previous characterisation of the empty reentrant cavity resonator, the respective quality factor, i.e. the couplings are found by performing a circle fit to the data [174, 175]. The resulting values, can be found in Table 5.1. Combining these coupling coefficients with the value at the attenuators, the internal amplitude ratio can be calculated, where the magnon port is approximated to also be a resonator port. From $A = 10\log_{10}(\chi)$, the linear change in relative power is found, where χ denotes the attenuation value in dB. Here, the path to the cavity

port is attenuated, thus the power entering at the magnon port is $P_{\text{magnon port}} = \frac{Q_{l,\text{magnon}}}{Q_{e,\text{magnon}}} \cdot A$. Hence, the power entering at the cavity port is $P_{\text{cavity port}} = \frac{Q_{l,\text{cavity}}}{Q_{e,\text{cavity}}}$ [196]. As a result, the internal amplitude ratio can be estimated via

$$\delta_0 = \sqrt{\frac{P_{\text{magnon port}}}{P_{\text{cavity port}}}}, \tag{5.3}$$

where the square root originates from the relation $P \propto |\text{amplitude}|^2$. As will be shown later, the onset of level merging ($\delta_0 = 1$ expected, c.f. Section 5.5.6) is observed for an attenuation of 8 dB $\equiv \delta_0 = 1.02 \pm 0.09$. For this value and $\phi = \pi$, the frequency gap of the avoided level crossing decreased to zero within the error bars (c.f. Section 5.8). Inserting these values into the above equations yields a relative amplitude ratio of $\delta_{0,\text{exp}} = 1.95 \pm 0.04$, which is higher than the expected value (within the error bars). However, as illustrated in Figure 5.6 b.), the above calculation does not take into account the tilt of the coupling loop to the resonator's xy plane. This would result in $\delta_{0,\text{exp}} = \delta_{\text{exp}} \cos(45°)$ and a value of $\delta_{0,\text{exp}} \approx 1.38 \pm 0.12$, where a conservative error on the relative angle of 5° is taken into account. In the follow-up experiments, the Q-factors of both ports have been slightly changed such that the cavity port is closer to being critically coupled and the other better matches an angle of 45°. Unfortunately, the dataset for the magnon port shown in Table 5.1 is the only usable one. Despite minimally changed parameters, the claim to use this estimate for the order of magnitude of δ_0 in the other measurements can be justified. In order to change the relative amplitude ratio significantly, one would require a completely different attenuation value along the cavity port's path. However, with the previous settings, the onset of level merging is observed for an attenuator value of 9 dB, which corresponds to an increase of $\Delta\delta_0 = 0.13$. If the uncertainties and similarity of the values for δ_0 are taken into account, the above calculation represents a reasonably good estimate for the subsequent datasets. Nevertheless, as previously mentioned, this calculation represents a rough estimate for the internal value of the relative amplitude ratio and is only reliable if more datasets which measure exclusively at the magnon port were taken. Here, for the datasets, which are discussed in the following, the above estimation confirms only that the experimental and expected values are of the same order of magnitude. However, in general, this way of determining δ_0 represents an experimental method to determine the internal amplitude ratio δ_0 for future experiments. Due to the limited amount of data with the settings of the following datasets, the above calculation only represents a rough estimate here and will not be used as it is too imprecise.

In conclusion, the conversion factor ζ can be estimated from the analysis of the data for the changes of the coupling strength and associated fits. The relationship between δ_{ext} and δ_0 is shown in Table 8.1. For the following discussions, this analytically determined value of the relative amplitude ratio δ_0 will be used as it represents the relevant quantity in understanding the changes of the coupling strength as a function of the relative amplitude. Having discussed the determination of δ_0, one can now derive a new expression for the reflection parameter of the measurement.

5.5.4 Scattering parameter $S_{11}(\omega)$

The addition of a second cavity resonator port driven at the same microwave frequency as the first port but with a different phase and amplitude results in a change for the

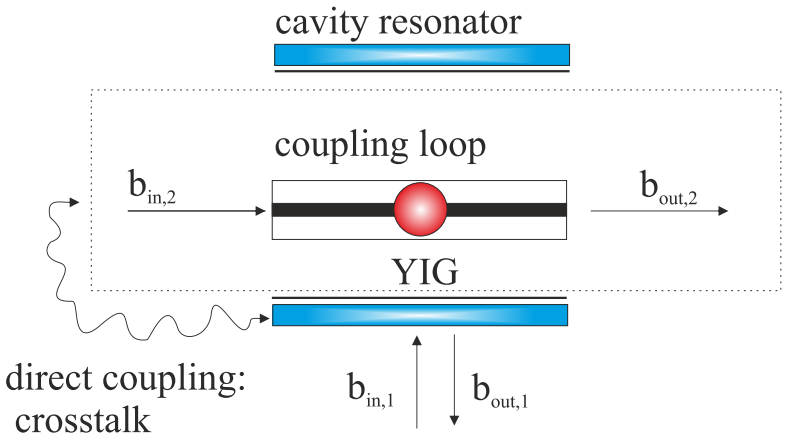

Figure 5.7: Sketch illustrating the different roles of the ports and thus their influence into the coupled system. The cavity resonator is sketched as the blue bars, the coupling loop of the second input as a "stripline", the YIG (red) placed in the centre. Whilst $b_{in,1}$ represents the microwave photon input field from the signal line directly exciting the cavity photons and it is the port where one measures the back-reflected signal, $b_{in,2}$ is the input signal from the second input with the additional phase shifter inserted. A direct coupling between $b_{in,2}$ to $b_{in,1}$ is the crosstalk. The fields $b_{out,1}$ and $b_{out,2}$ are the outputs of the first and second input, respectively.

analytical expression of the reflection scattering parameter $S_{11}(\omega)$. As before in Chapter 4, a quantum mechanical approach based on a modified interaction Hamiltonian, also called system Hamiltonian is utilised for the derivation of a new expression for $S_{11}(\omega)$ (c.f. Chapter 2). The VNA serves as the single microwave source of the system as illustrated in Figure 5.3. In the following derivation of the new scattering formula, the input from the microwave feed line which couples to the cavity port is denoted by $b_{in,1}$ and the second which exhibits the relative phase shift, by $b_{in,2}$. The resulting spectrum is recorded at the second port of the VNA which is configured for a transmission measurement. However, the signal there corresponds to the back-reflected signal from the cavity port, denoted in the following by $b_{out,1}$. In order to clearly distinguish the different roles and clarify the labelling of both feed lines in our systems, please refer to Figure 5.7. Schematically, this figure shows the cavity resonator with the inserted YIG sphere. Considering only $b_{in,1}$, this corresponds to the classical cavity photon magnon-polariton experiments where both subsystems hybridise at resonance and form an avoided level crossing in the dispersion (c.f. Chapter 4, [56, 58]). The situation changes when the additional loop enveloping the YIG sphere is inserted into the cavity such that there is no direct interaction with the cavity photon field. Experimentally, there is crosstalk which is as mentioned the small amount of direct interaction with the cavity resonator photons. It will be shown in Section 5.7 that the contribution is small and does not have a substantial influence on the two-tone cavity resonator-YIG system and can be neglected in the following derivation.
As previously mentioned, only the microwave photons from the cavity port excite the cavity resonator photons. This excitation is expressed by the photon creation and destruction operators a and $a^\dagger$, respectively. The inductive loop representing the magnon port does not lead to additional cavity photons because crosstalk is neglected here. Thus, the AC

magnetic field generated from the current in the loop acts solely as a direct input for the magnons. However, as the external field is swept and hybridisation sets in through the strong coupling of magnons to cavity photons, another channel for energy transfer opens. The magnons then serve as another drive for the cavity photons via this coupling.

The second driving field acts on the magnetisation and, hence, exerts an additional torque on the magnetisation [77]. If the phase and amplitude of this torque are chosen correctly, this torque compensates all dissipation channels including the coupling of the magnons to the cavity photons, and the avoided level crossing of the CMP coalesces, i.e. level merging can be observed.

Therefore, the classical Tavis-Cummings Hamiltonian for a coupled system with N constituents is extended to a *driven* form. As the drive takes place via the coupling of the magnons to the cavity photons, the driving frequency, denoted by Ω, corresponds to the coupling strength g_{eff} modulated by the relative phase ϕ and amplitude δ_0 from the contribution of the second port. It is key that the second port is not just another microwave port of the cavity resonator but acts *indirectly* on the cavity resonator photons via the coupling of the magnons. Otherwise, the effect of a relative phase and amplitude would result in interference effects and not level merging of the CMP's dispersion.

In the limit of small δ_0, i.e. $\delta_0 \to 0$, the contribution from the magnon port is much weaker than the one from the cavity port and the system can be effectively described as a single port hybrid system. Thus, if only one port is considered, this would result in an identical Tavis-Cummings Hamiltonian $\mathcal{H}_{\text{one port}}$:

$$\mathcal{H}_{\text{one port}} = \hbar\omega_r a^\dagger a + \hbar\omega_m m^\dagger m + \hbar g_{\text{eff}}(m^\dagger a + a^\dagger m), \tag{5.4}$$

where $m^\dagger$ and m denote the magnon creation and annihilation operators, respectively. In the above equation, there is no relative phase or amplitude as only one port is active. However, this changes for the two-tone driven system, where the system Hamiltonian $\mathcal{H}_{\text{sys}}$ has to be modified to take into account this new contribution. The total number of particles is conserved and thus the first two terms respectively denote the total number of cavity photons $\hat{n}_{\text{ges}}^{\text{photons}} = a^\dagger a$ and magnons $\hat{n}_{\text{ges}}^{\text{magnons}} = m^\dagger m$ in the system. In contrast to Equation (5.4), there are now two interaction terms. As previously, $H_{\text{int,1}} = \hbar g_{\text{eff}} \left(m^\dagger a + a^\dagger m\right)$ describes the interaction with coupling strength g_{eff} of the cavity resonator photons with the magnons and vice versa. The addition of a second interaction term $H_{\text{int,2}} = \hbar g_{\text{eff}} \delta_0 e^{i\phi}(a^\dagger m)$ considers the impact of the magnon port on the hybrid system via the coupling strength g_{eff}.

As a result, the new system Hamiltonian reads as:

$$\mathcal{H}_{\text{sys}} = \hbar\omega_r a^\dagger a + \hbar\omega_m m^\dagger m + \hbar g_{\text{eff}} \left(m^\dagger a + a^\dagger m\right) + \hbar\Omega \left(a^\dagger m\right), \tag{5.5}$$

where $\Omega = g_{\text{eff}} \delta_0 e^{i\phi}$. The last term is now interpreted as an additional drive of the cavity photons through the coupling to the magnons which are excited by magnon port.

The complex conjugated term of the last term is not included because this would correspond to the crosstalk, the direct interaction between the creation operator of the cavity resonator and the magnon lowering operator m. The addition of a second microwave

input to the hybrid system leads to an additional torque exerted on the precessing magnetisation due to the induced change in the x- and z- components of the AC magnetic fields.
It is experimentally found, that the tilt of 45° as illustrated in Figure 5.6 b.) of the coupling loop minimises the crosstalk of the system. Depending on the magnitude and the orientation of this torque which is determined by δ_0 and ϕ, the system's dissipation can be compensated if $\delta_0 = 1$ or even result in an additional drive for $\delta_0 > 1$. In this picture, the coupling strength represents yet another dissipation channel which is then also compensated. Thus, tuning ϕ and δ_0 allows for a control of the coupling strength of the CMP in this specific system.
However, in order to include dissipation in the system, the above Hamiltonian needs to be non-Hermitian. Also, considering the 2×2 matrix in the classical approach (c.f. Chapter 3), with the off-diagonal elements representing the coupling terms, level merging is only possible if the product of the off-diagonal terms is negative. It cannot be a positive, real valued quantity because the interaction potential would be repulsive. Thus, this means that the sign of the off-diagonal product has to change.

Now, the equations of motion can be written down in Langevin form [197] as:

$$\frac{\partial m(t)}{\partial t} = -i\omega_m m(t) - ig_{\text{eff}} a(t) - \kappa_m m(t) + \sqrt{2\kappa_{e,2}} b_{in,2}(t), \tag{5.6a}$$

$$\frac{\partial a(t)}{\partial t} = -i\omega_r a(t) - ig_{\text{eff}}(1 + \delta_0 e^{i\phi}) m(t) - \kappa_r a(t) + \sqrt{2\kappa_{e,1}} b_{in,1}(t), \tag{5.6b}$$

where ω_m denotes the magnon precession frequency, g_{eff} the effective coupling strength, $\kappa_{e,2}$ the coupling factor to the magnon port, ω_r the cavity photon frequency, κ_r the total resonator losses and $\kappa_{e,1}$ the coupling factor of the cavity port. After a Fourier transformation and employing the Input-Output relation for a system with one external port and a reflection measurement $b_{out,1} + b_{in,1} = \sqrt{2\kappa_{e,1}} a$ ([11]) the scattering parameter $S_{11}(\omega)$ can be expressed as :

$$S_{11}(\omega) = -1 + \frac{2\kappa_{e,1}}{-i(\omega - \omega_r) + \kappa_r + \frac{g_{\text{eff}}^2(1+\delta_0 e^{i\phi})}{X}} - \frac{2ig_{\text{eff}}\delta_0 e^{i\phi}(1 + \delta_0 e^{i\phi})\sqrt{\kappa_{e,1}\kappa_{e,2}}}{X\left(-i(\omega - \omega_r) + \kappa_r + \frac{g_{\text{eff}}^2(1+\delta_0 e^{i\phi})}{X})\right)}, \tag{5.7}$$

where $X = -i(\omega - \omega_m) + \kappa_m$. The first two terms can be mapped to Equation (4.6) except a change in the term for the coupling strength from $g_{\text{eff}}^2 \rightarrow g_{\text{eff}}^2(1 + \delta_0 e^{i\phi})$. In contrast, the term considering the coupling strength in the expression for Equation (4.6) for the CMP driven with a single tone is purely real. This would be the full expression for the scattering parameter in the case of a single tone CMP. However, the additional input via the magnon's coupling to the cavity resonator photons has to be considered for the two tone experiment. Hence, the third term considers this contribution. As the additional drive is mediated by the coupling to the cavity photons, it is proportional to g_{eff}, i.e. the coupling in the limit $\delta_0 \rightarrow 0$ for different phases ϕ.

Non-Hermitian Hamiltonian and PT symmetry: Impact on $g_{\text{eff}}(\delta_0, \phi)$

In quantum mechanics, an observable denotes a physical, measurable quantity [185]. In this framework, the values from a measurement denote the eigenvalues of the corresponding operator $\hat{O}$. This operator refers to the solutions of the eigenvalue equation

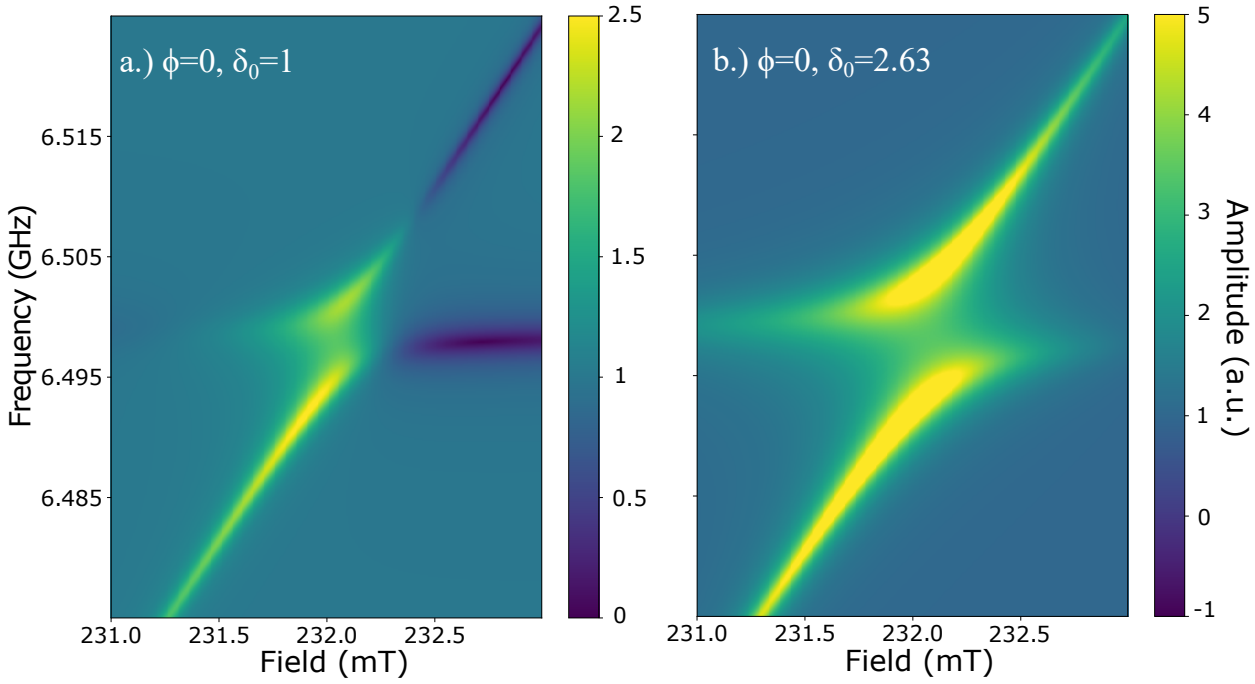

Figure 5.8: Simulations for $\phi = 0$ and $\delta_0 = 1$ (a.)) and $\delta_0 = 2.63$ (b.)) based on Equation (5.7) with parameters as close as possible to the experiment. The parameters used for this plot are $\kappa_m/2\pi = 1\,\mathrm{MHz}$, $\kappa_{e,1}/2\pi = \kappa_{e,2}/2\pi = 1.58\,\mathrm{MHz}$, $\kappa_r/2\pi = 2\,\mathrm{MHz}$, $\omega_r/2\pi = \omega_m/2\pi = 6.4985\,\mathrm{GHz}$. The gap of the avoided level crossing increases towards larger δ_0. The amplitude changes in a.) are attributed to considering additional phase changes in the course of the coupling and also depends on δ_0 and ϕ (c.f. Figure 5.5, Section 5.10.3). The relationship between the experimentally set attenuation, the external and internal amplitude ratio is given in the appendix in Table 8.1.

$\hat{O}\psi_l = O_l\psi_l$, where ψ_l denotes the eigenfunction of O_l. Since physical observables are real in the common formulation of quantum mechanics, the corresponding operator $\hat{O}$ needs to be Hermitian, i.e. only has real eigenvalues O_l, such that the product with the Hermitian conjugate $O^\dagger$ yields $O^\dagger O = 1$ [185]. However, in the case for that experiment of level merging, the system Hamiltonian is non-Hermitian but depending on the phase and amplitude configuration can still result in real eigenvalues of the CMP. This can be possible because, first, the introduction of a non-Hermitian term into the Hamiltonian denotes the allowance for an open system, i.e. dissipation is now included which is also referred to as approximate non-Hermiticity in the literature [198, 199] and references therein. For instance, this also describes radioactive decay or the introduction of dissipative systems in semiconductor physics. In addition, the existence of non-Hermitian systems with real-valued spectra has been proposed [200]. However, even for non-Hermitian systems, the spectra can be real if the system is $\mathcal{PT}$ symmetric, i.e. is invariant under parity and time reversal transformations such that $[H, \mathcal{PT}] = 0$. $\mathcal{PT}$ symmetric systems are studied in many different fields such as in quantum mechanics [200], optical microcavities [201] or magnetism and magnonics [202]. This symmetry also starts to receive interest in spintronics and for CMPs where the spectra and behaviour of $\mathcal{PT}$ symmetric CMPs have recently been discussed [73, 203, 204]. As shown in Ref. [73], the $\mathcal{PT}$ symmetric state is achieved by carefully engineering the losses from the cavity resonator and the magnons such that $\gamma_a = \kappa_r = \kappa_m$. Then, the coupling strength is tuned by moving the position

of the YIG sphere in the cavity resonator. In case of $g_{\text{eff}} = \gamma_a$, the two separate eigenmodes of the coupled system coalesce to one point. This singularity in the eigenvalues represents the hallmark of a non-Hermitian system and this point is called an exceptional point (EP). If $g_{\text{eff}} > \gamma_a$, the $\mathcal{PT}$ symmetry is broken and the eigenfrequencies are complex.

In contrast, for the level merging experiment discussed here, a new two-tone driven CMP is harnessed. The transition from avoided level crossing to level merging is achieved by tuning the relative orientation and amplitude of the additional torque added to the system. However, neither the dissipation nor the magnon dissipation are directly accessed and tuned such as has been done in Ref. [205]. The connection and incorporation of the experimental results from this two-tone driven system to the above discussion of $\mathcal{PT}$ symmetry and singularities such as EPs requires further in-depth theoretical studies. For instance, in the current model, the z-component of the magnon port does not contribute to drive the magnons as FMR is not possible for $h_{z,\text{AC}}^{\text{magnon}} \parallel H_{\text{ext}}$. In addition, this component is perpendicular to $h_{\text{AC}}^{\text{cavity}}$ and does not directly couple to the cavity photons as required. However, in a follow-up time-resolved experiment (Tim Wolz, KIT) on the same system, but replacing the inductive loop of the magnon port with a stripline, no level merging but only a cancellation, i.e. rather resembling destructive interference, of the signals of the avoided level crossing at resonance can be observed so far. Nevertheless, the system has been changed by the insertion of the stripline. Thus, despite that probably further measurements are required to confirm the observations of the time-resolved measurement, the exact role and the interplay of all fields also needs further investigation. This would allow a generalisation of the various experiments with different geometries and methods to manipulate the CMP's coupling strength. However, this is ongoing work and due to limited time out of the scope of this thesis.

For the experimental work discussed here, level merging is achieved by tuning the coupling strength from a real to a complex quantity. Thus, for this two-tone driven system, in the presence of coupling and the external control of ϕ and δ_0 one deals with an open system resulting in a non-Hermitian Hamiltonian.
An explicit study on the $\mathcal{PT}$ symmetry of CMPs has not been conducted in the course of this thesis, but it might be subject to future, follow-up experiments.

Before the experimental data are discussed, Equation (5.7) can be utilised to perform simulations on the dependence of the coupling strength on ϕ and δ_0. The result from these is shown in the next section.

5.5.5 Simulations on level merging

The comparison of simulations based on the model equation, the Equation (5.7) with the experimentally obtained results would confirm the utilised model. In addition, further insight into the coupling process and influence of the relative phase and amplitude ratio can be gained. Thus, in Figure 5.8 for $\phi = 0$ and Figure 5.10 for $\phi = \pi$, calculated dispersion spectra at the onset of level merging ($\delta_0 = 1$) and in the regime of full level merging ($\delta_0 = 2.63$) are shown. In case of a fixed phase $\phi = 0$ and increasing δ_0, the frequency gap of the avoided level crossing at resonance ($\mu_0 H_{\text{ext}} \equiv \mu_0 H_{\text{res}}$ such that $\omega_r \equiv \omega_m$), increases according to the change in δ_0. Note, the change from dip to peak in Figure 5.8 a.). This change can be attributed to the additional microwave port. In the

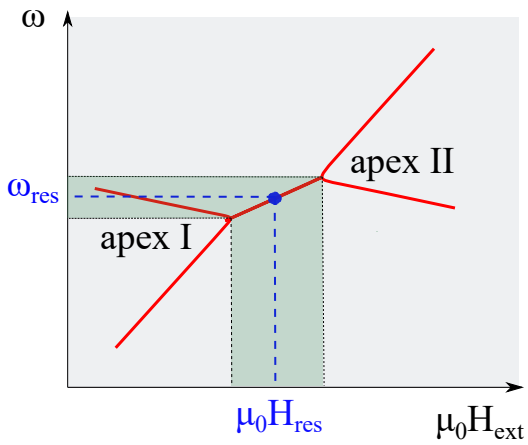

Figure 5.9: Schematical illustration of the dispersion spectrum in the regime of level merging for the description of the formation of two triangles where the apexes point to each other and move away from each other as δ_0 is increased.

presence of coupling, where the change is visible, the cavity resonator photons can receive "gain" from the Kittel mode magnons. As the experimental data and thus the formula refers to a reflection measurement, this energy input compensates for the resonator losses due to the absorption of microwave energy at the cavity's resonance frequency. The reflection dip may then vanish or even turn into a peak, both of which can be seen in this figure. By increasing the value of the relative amplitude ratio, more energy can be transferred to the cavity resonator photons via the coupling with the Kittel mode magnons. As a result, the area with a change from resonance dip to peak also increases.

These features can also be observed when the relative phase is changed to $\phi = \pi$ (c.f. Figure 5.10). As graphically illustrated in Figure 5.9, the spectrum consists of two triangular shaped curves to the left and right of the resonant field. At the resonance field and frequency, the signal's amplitude is much smaller than at the apex of either triangle, where it is strongly enhanced because at this point the dispersions of the cavity photon and the magnons coalesce (c.f. Section 5.29). In the transition from $\delta_0 = 1$ (a.)) to $\delta_0 = 2.63$ (b.)), one can infer from the figure, that the distance of these apexes grows as δ_0 is increased. However, the dispersion spectrum changes from an avoided level crossing at resonance to level merging. Now, the hybridised system exhibits only one solution in an area around resonance. This attraction takes place within a certain region around the resonance frequency and the externally applied magnetic field. Referring to the latter, this width corresponds to $\mu_0 \Delta H_{merging} = 4\,\Im(g'(\delta_0, \pi))/\gamma$ in magnetic field units. In the dispersion spectrum, this is observed in the formation of two triangular shaped areas with signal intensity, called "forks", whose apexes point toward each other. As shown in Figure 5.10 for $\delta_0 = 1$ (a.)) and $\delta_0 = 2.63$ (b.)), this distance grows and the "forks" move away from each other.

The extension of this region concerning an interval of the externally applied field depends on the size of the imaginary part of the coupling strength. In contrast to an avoided level crossing in a single tone experiment, the coupling strength is now a complex quantity. In order to further understand the impact of the complex coupling strength on the shape of the dispersion spectrum, the dependence on ϕ and δ_0 is discussed in the next section.

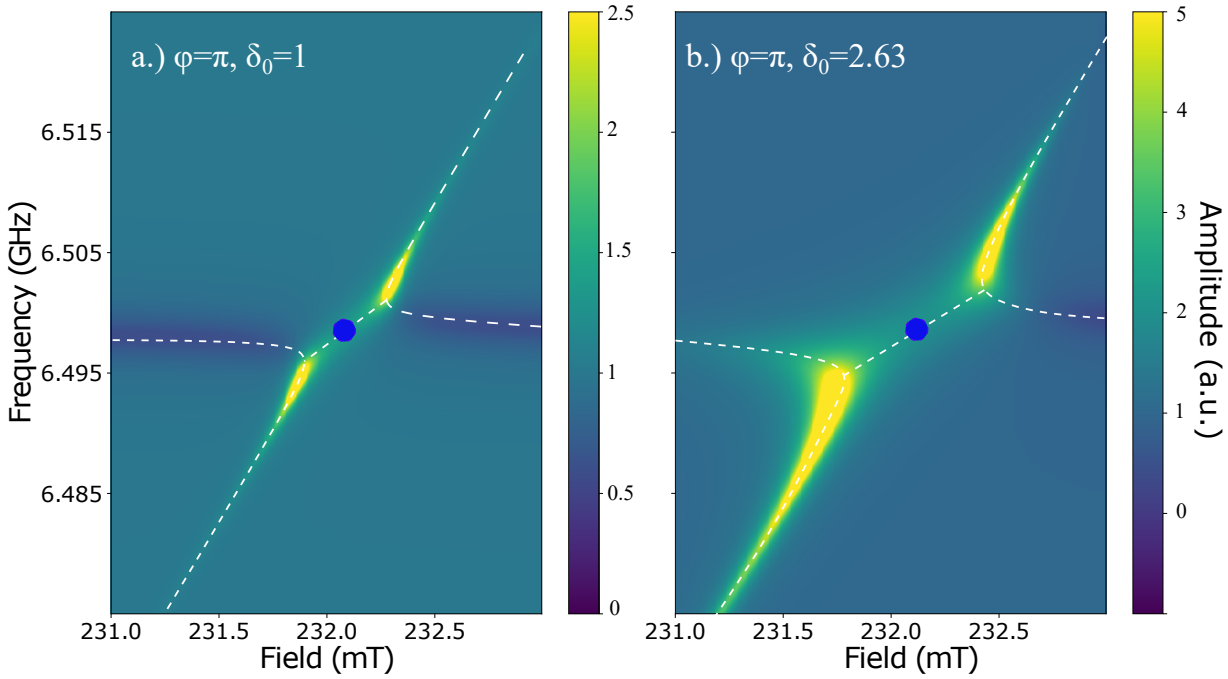

Figure 5.10: Simulation for $\phi = \pi$ and $\delta_0 = 1$ (a.)) and $\delta_0 = 2.63$ (b.)) based on Equation (5.7) with parameters as close as possible to the experiment. The parameters used for this plot are $\kappa_m/2\pi = 1\,\text{MHz}$, $\kappa_{e,1}/2\pi = \kappa_{e,2}/2\pi = 1.58\,\text{MHz}$, $\kappa_r/2\pi = 2\,\text{MHz}$, $\omega_r/2\pi = \omega_m/2\pi = 6.4985\,\text{GHz}$. a.) This spectrum displays the behaviour of the CMP under the influence of the magnon port at the transition from avoided level crossing to level merging for $\delta_0 = 1$. The white dotted lines serve as a guide for the eye for the dispersion. b.) The distance of the apexes with the maximal intensity grows both in resonance frequency and the applied magnetic field for an increase of the relative amplitude ratio. The horizontal distance corresponds to $\mu_0 \Delta H_{\text{merging}} = 4\,\Im(g'(\delta_0, \pi))/\gamma$ as discussed in Ref. [205]. Except for the relative phase ϕ, the same set of parameters is used as in Figure 5.8. The blue point denotes the resonance.

5.5.6 Complex coupling strength

As it can be seen from Equation (5.7), the purely real quantity g_{eff} for a "single-tone" driven CMP, has to be replaced by a new expression $g'(\delta_0, \phi)$ which is expressed as

$$g'(\delta_0, \phi) = g_{\text{eff}} \sqrt{1 + \delta_0 e^{i\phi}}, \tag{5.8}$$

where g_{eff} corresponds now to the "single-tone" coupling strength, i.e. the coupling strength in the limit for $\delta_0 \to 0$. For $\delta_0 = 1$ and $\phi = \pi$, the term in the square root vanishes and a complete merging of the frequency gap of the avoided level crossing in the dispersion spectrum is expected. Hence, this combination of relative phase and amplitude denotes the onset of level merging. If the relative phase is kept constant at $\phi = \pi$ and δ_0 is further increased, the term $g'(\delta_0, \phi)$ describing the coupling between the cavity photons and the magnons becomes purely imaginary. As a result, the antisymmetric and symmetric dispersion branches are attracted to the same frequency. Hence, in Figure 5.11, the expected dependence of the complex coupling strength on δ_0 (a.) and b.)) and ϕ (c.) and d.)) is displayed for the real (a.) and c.)) and imaginary part (b.), d.)). The first column shows the real and imaginary part of the coupling strength as a function of the relative

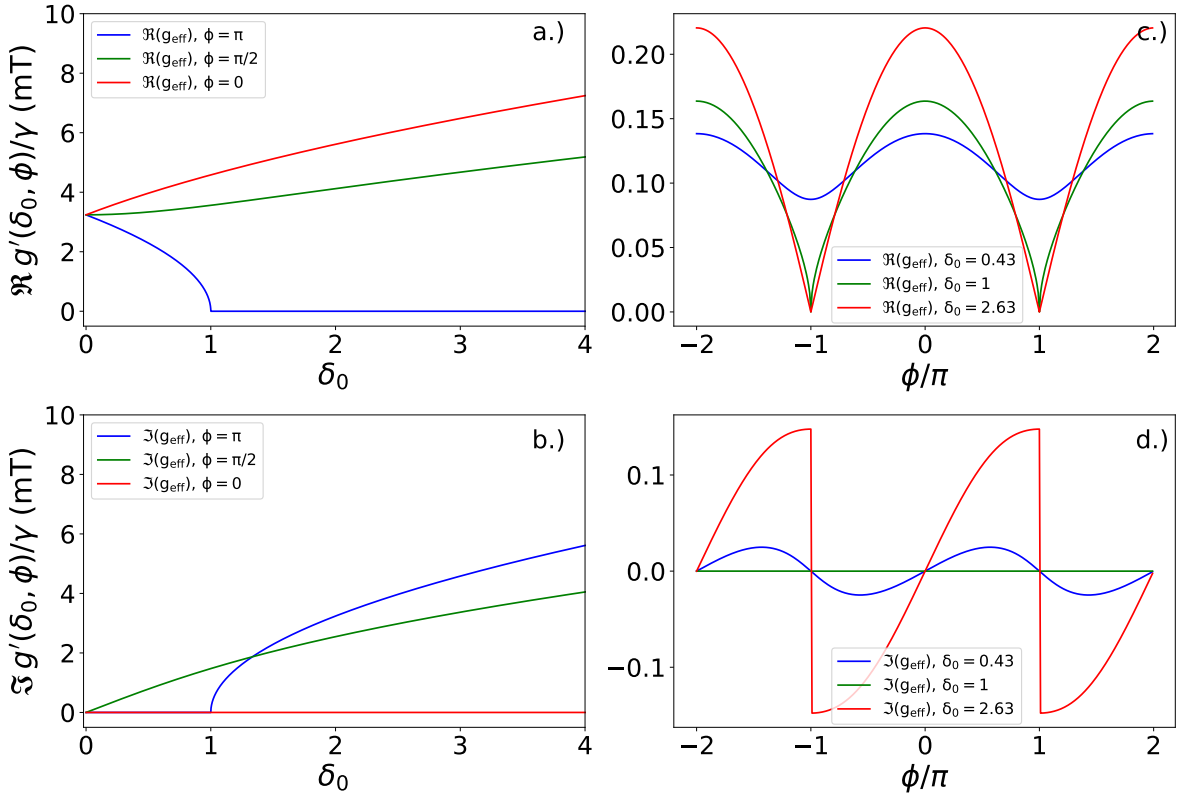

Figure 5.11: Simulations of the dependence of the real and imaginary part of the complex coupling strength on the relative amplitude ratio δ_0 (a.) and b.)) and phase ϕ. (c.) and d.)). a.) Dependence of the real part of the coupling strength for three different values of the relative phase ($\phi \in (0, \pi/2, \pi)$). For $\phi = \pi$, the real part goes to zero for $\delta_0 \geq 1$ whilst for $\phi = 0$, the real part continues to increase. At the intermediate phase value of $\phi = \pi/2$, the coupling strength also increases but with a smaller gradient compared to $\phi = 0$. b.) Dependence of the imaginary part of the coupling strength for three phase values. Compared to a.) the imaginary part is always zero for $\phi = 0$, non-zero only when $\delta_0 \geq 1$ for $\phi = \pi$ and constantly increasing for all values of δ_0 for $\phi = \pi/2$. c.) The real part of the coupling strength as a function of $\phi \in (-2\pi, 2\pi)$ for three values of δ_0 below, at the onset of, and in the regime of level merging. The dependence is periodic for all δ_0, with increasing maxima of the coupling strength for $\phi = 0$ and a sharp minimum at $\phi = \pi$ for $\delta_0 > 1$. Below $\delta_0 = 1$, the coupling is always suppressed. However, the slope for values close to π inccreases for higher δ_0. d.) Imaginary part from the spectrum shown in c.). Above $\delta_0 = 1$, the plot becomes more and more antisymmetric in the sense of a "smooth" continuous transition at $\phi = 0$ and an increasing discontinuity, i.e. sign change, at $\phi = \pi$.

amplitude ratio δ_0 for three fixed values of the relative phase ($\phi \in 0, \pi/2, \pi$). Whilst for $\phi = 0$, the coupling strength remains purely real for all values of δ_0 and increases with δ_0, the real part vanishes for $\phi = \pi$ and $\delta_0 \geq 1$. Instead, the coupling strength is imaginary and increases for higher values of δ_0. A relative amplitude ratio of $\delta_0 = 1$ constitutes the transition from level repulsion to level merging for $\phi = \pi$, because the sign of $g'(\delta_0, \phi)$ in Equation (5.8) changes from positive to negative. Hence, within the framework of two coupled harmonic oscillators, the repulsion between the antisymmetric and the symmetric mode is changed to an "attraction of the eigenvalues" of the coupled system. The relative

phases of $\phi = 0$ and $\phi = \pi$ represent two special cases. Since either the imaginary ($\phi = 0$) or the real part ($\phi = \pi$) for $\delta_0 = 1$ are zero, these cases allow to attribute the real part of the coupling strength to level repulsion and the imaginary part to attraction, respectively. In this regard, for intermediate relative phase values, the coupling strength is comprised of both a repulsive and attractive contribution. The final shape of the spectrum then depends on whether for a specific relative phase the real or imaginary part is the dominant contribution. However, due to the non-zero contribution of the other, the dispersion spectra are slightly distorted by the coexistence of both repulsion and attraction. The case for $\phi = \pi/2$ is shown in Figure 5.11 a.) for the real and c.) for the imaginary part. The non-zero imaginary part acts to "damp" the increase of the coupling strength towards higher values of δ_0. At this relative phase, both contributions are comparable in magnitude. Hence, compared to the increase (decrease) for $\phi = 0\,(\phi = \pi)$ one should expect a strongly suppressed dependence of the coupling strength on δ_0 for $\phi = \pi/2$.

In addition, the relative amplitude ratio can be kept fixed and the coupling strength studied as a function of the relative phase. The dependence on ϕ is illustrated for three different values of δ_0 in Figure 5.11 c.) for the real and d.) for the imaginary part, respectively. Regarding the real part, $g'(\delta_0, \phi)$ displays a periodic dependence on the relative phase in an interval from -2π to 2π. For $\delta_0 < 1$ and looking a the phase dependence of $g'(\delta_0, \phi)$, the coupling strength increases equally for $\phi = 0$ as it decreases for $\phi = \pi$ for the same value of δ_0. Hence, the coupling is modulated, but for the regime of level merging the relative amplitude ratio δ_0 needs to be altered. If $\delta_0 \geq 1$ (green and red solid line in Figure 5.11 c.)), the enhancement of the coupling strength at $\phi = 0$ increases. However, at $\phi = \pi$, level merging sets in and the real part of $g'(\delta_0, \pi)$ decreases to zero. At this point, the difference between the real part of $\delta_0 = 1$ and $\delta_0 = 2.63$ is tiny. However, this changes when the contribution from the imaginary part is also considered. For $\delta_0 < 1$, the coupling strength $g'(\delta_0 = \text{const}, \phi)$ is a continuous function for $\phi \in (-2\pi, 2\pi)$. However, at the transition to level merging, i.e. $\delta_0 = 1$, it becomes discontinuous at $\phi = \pm\pi$. At this point, the value of the imaginary part of the coupling strength is no longer uniquely defined. When the relative amplitude ratio is further increased, the jump, i.e. the discontinuity increases both in slope and magnitude. Just as in the previous description (a.) and b.)), the magnitude of the imaginary part is zero for all values of δ_0 when $\phi = 0$.
In the course of conducting the experiment, various dispersion spectra have been recorded by keeping either the relative phase constant and sweeping the relative amplitude ratio or vice versa. These datasets allow one to extract the experimentally determined dependence of the coupling strength $g'(\delta_0, \phi)_{|\phi=\text{const}}$ and $g'(\delta_0, \phi)_{|\delta_0=\text{const}}$, respectively. Here, the eigenvalues of the hybridised system are complex. Hence, only the modulus of this complex quantity, i.e. the coupling strength can be directly extracted from the experimental data.

One aim of this experiment is to be able to switch the coherent exchange of information deliberately on and off. For a coherent exchange of information, the hybridised system needs to be in the strong coupling regime where the individual dissipations are much smaller than the coupling strength. Hence, before a discussion on the data and the methods used for the data analysis, the presence of the strong coupling regime, i.e. the CMP, needs to be confirmed, as it is shown in the following paragraph.

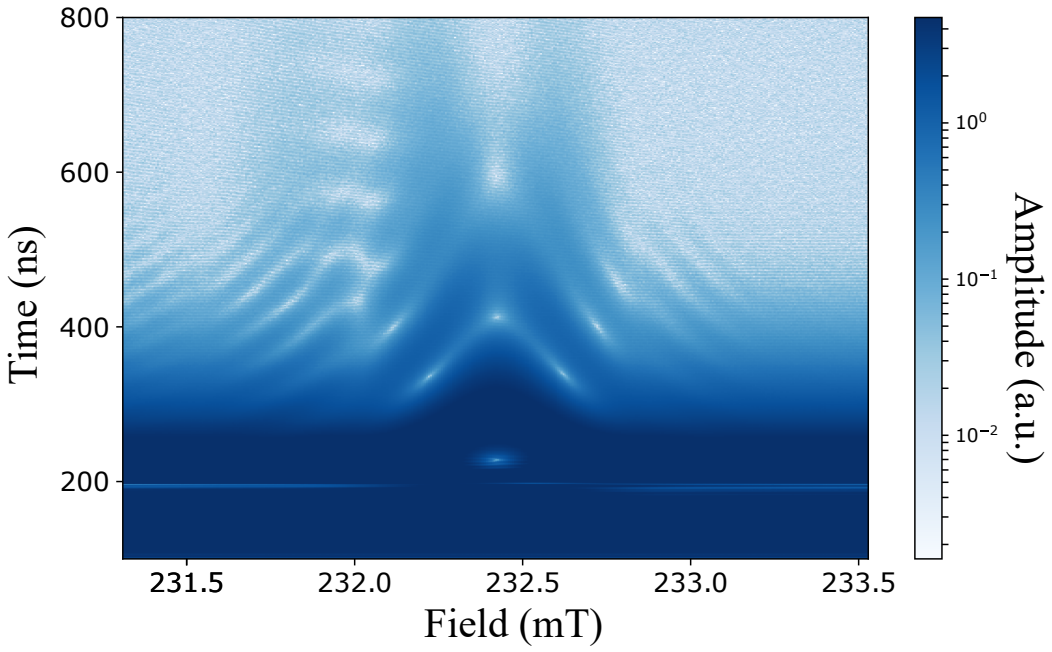

Figure 5.12: Classical Rabi-like oscillations for a comparable setting of the two tone driven CMP conducted with the same setup (the magnon port was left open for this measurement) in a later measurement run. The signal until $t = 200\,\text{ns}$ represents the time length of the excitation pulse on the cavity port. Following this, the coupling sets in and the freely decaying Rabi oscillation is recorded as a function of the externally applied field. The coupling strength can be estimated from the duration of one oscillation period and corresponds to $2g_{\text{Rabi}}/2\pi \simeq 5.4\,\text{MHz}$. Please note, that this dataset corresponds to a measurement at a frequency of $\omega/2\pi = 6.5\,\text{GHz}$. The data for this figure has been taken with the time-domain setup at KIT and is shown by courtesy of Tim Wolz.

5.5.7 Classical Rabi-like oscillations

The strong coupling regime refers to the frequency of the coherent energy exchange between both subsystems and yields the time for one oscillation period $\frac{2g_{\text{eff}}}{2\pi} = \frac{\Omega_{\text{Rabi}}}{2\pi} = \frac{1}{\tau_{\text{Rabi}}}$, where Ω_{Rabi} is the Rabi frequency. By studying the decay of the excitation of a two-level system (TLS), this kind of oscillation is also called a Rabi oscillation [11]. However, as detailed in Chapter 3 for the two-tone driven CMP at room temperature, the origin of the macroscopic coherent oscillation is given by the phase correlations in Maxwell's equations [61]. Therefore, in order to distinguish, the term classical Rabi-like oscillations has been introduced to quantify the strong coupling regime for this CMP [58]. As shown in Figure 5.12 for a time interval of approximately $400 - 500\,\text{ns}$, there are Rabi-like oscillations at the resonance frequency of the cavity resonator photons at 6.5 GHz. One oscillation period corresponds to a coupling strength of $\simeq 5.4\,\text{MHz}$, which is in line with the values from spectroscopic measurements. The existence of such Rabi-like oscillations indicates the presence of the strong coupling regime for this system [11, 58]. Thus, controlling the coupling strength of the CMP as previously discussed represents a novel method to deliberately turn on or off the coherent information exchange for CMPs. This time-resolved data has been taken at the time-domain setup at KIT which recently moved to the University of Glasgow by my colleague Tim Wolz. A sketch of the time domain setup can be found in master's and doctoral thesis from the KIT group such as in Ref. [206]. Having

examined the change and its consequences of the second port on the system Hamiltonian, i.e. the reflection parameter from Input-Output theory and the coupling strength via simulations, the experimental data and related schemes for the data analysis are going to be discussed in the following.

5.6 Data analysis

Although this experiment has been conducted outside a cryostat at room temperature where the microwave losses along the cables between source and receiver are greatly decreased, the cables contribute by an oscillatory background signal to the data. Analogously to the situation of the temperature dependent measurements of Chapter 4, these oscillations are not a function of the external magnetic field. However, the previous algorithm used for the removal of the background cannot be applied to the data of level merging. For the previous algorithm, the existence of a signal free region in the avoided level crossing at the frequency of the cavity resonator is a central feature for the background analysis of the temperature dependent data. Since the disappearance of this avoided level crossing gap is being studied in this chapter, the former method cannot be utilised for this data.

Instead, the background contribution is determined by fitting the undisturbed cavity resonance far from the resonant external field and subtracting that signal from the baseline. That subtraction removes the cavity resonance from the data and the remaining signal denotes the background signal. The background can then be subtracted from the data around resonance without disturbing the resonant line shapes. This comparison is illustrated in Figure 5.13 showing the raw data and the background corrected data for a relative phase of $\phi = \pi$ and attenuation of $8\,\mathrm{dB}$ ($\delta_0 = 1.02 \pm 0.09$) on the cavity path. Despite the ability to identify small signals by removing the background oscillations, for relative phases and amplitudes close to the collapse of the avoided level crossing gap, i.e. around resonance, the influence of the correction on the signal's line shapes can no longer be neglected. For instance, if the linewidth or amplitude of the fit of the Lorentzian is overestimated, the background correction can remove a significant part of the signal or completely distort the signal at level merging. Thus, the background correction is only used to determine small signals far from resonance and not for most of the data in the case of a level merging.

As a next step, after the background correction, the algorithm for extracting values of the coupling strength for different combinations of ϕ and δ_0 is explained in more detail in the next section.

5.6.1 Algorithm for peak detection

In order to find the minimal distance between the upper and lower polariton branch when the relative phase and amplitude are tuned, both the amplitude and phase of the complex scattering parameter $S_{11}(\omega)$ need to be taken into account. As shown in Figure 5.14 b.) for the slightly off-resonant dataset (black, dotteed line), the signals already overlap. Therefore, the determination of the minimal coupling strength is limited by the sum of the linewidths of both dips. However, the distance between the dips, i.e. the coupling strength, is still resolvable if one also considers the signal's phase. At the frequency of

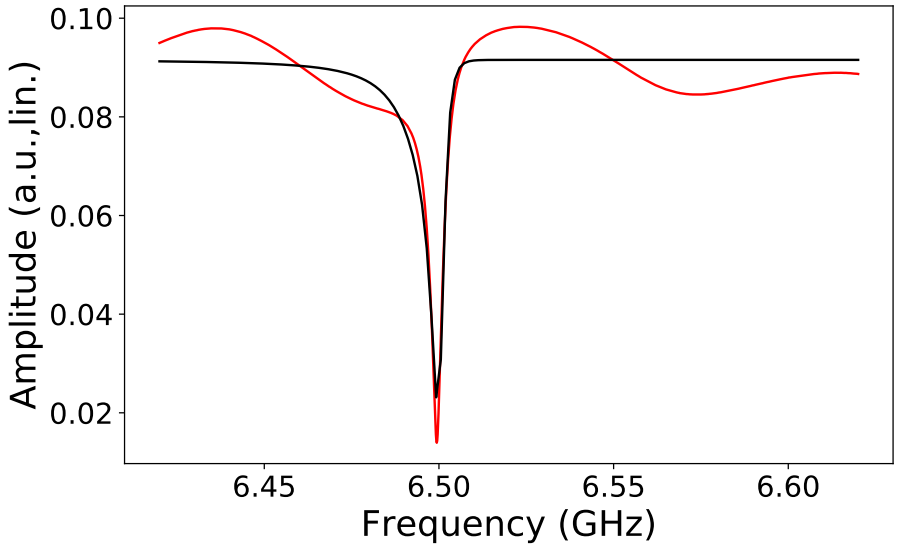

Figure 5.13: Illustration of the algorithm for background removal of the data in the experiment towards level merging. Picture of the raw data with the background (solid red line) and the Lorentzian fit (solid black line) of the cavity resonator. The fit yielded $\omega_r/2\pi = (6.498 \pm 0.00006)\,\mathrm{GHz}$ and $\kappa_r/2\pi = (3.85 \pm 0.15)\,\mathrm{MHz}$.

the cavity resonator and each branch, a phase jump in the phase can be observed. The magnitude of the phase jump depends on the individual quality, i.e. coupling factors of each component. Towards a complete collapse of the frequency gap of the avoided level crossing, i.e. level merging, the coupling or excitation of one branch is more and more suppressed. As a result, the magnitude in the phase eventually shifts below the baseline. The frequency of the respective dip can no longer be identified unambiguously in order to determine the coupling strength. Hence, in the final data analysis, the phase gradient is utilised as it is more sensitive to small changes in the resonance frequency (c.f. Figure 5.14 a.)). Utilising the above described scheme, the size of the gap between the upper and lower polariton branch is typically calculated for a window in the dispersion spectrum of $\pm 1\,\mathrm{mT}$ around the external field necessary for resonant coupling as it is shown in Figure 5.15 for the smallest, experimentally observed value ($\phi = \pi, \delta_0 = 1.02 \pm 0.09$ (corresponding to an attenuation of the cavity port of 8 dB), c.f. Appendix). Since the coupling strength corresponds to the minimum distance in the avoided level crossing, the value is found as the minimum in the respective data array. For the observation of a collapse of the coupling strength at a fixed phase ϕ, a sweep over almost three magnitudes of the relative amplitude ratio from $\delta_0 = 0.04 \pm 0.01$ to $\delta_0 = 11.79 \pm 1.97$ was made. If the cavity port's amplitude is further attenuated, i.e. the value for δ_0 is increased from $\delta_0 = 1$ to larger $\delta_0 > 1$ ($\delta_0 = 11.79 \pm 1.97$ was the highest value in this experiment), another regime is entered. Instead of the revival of a normal anticrossing gap along the frequency axis is a single external field value, the dispersion spectrum takes an entirely different shape. Instead, in a region around resonance with a certain width both along the field and frequency axis with a single solution for the dispersion of the hybrid state is observed. For a certain field interval, which is symmetric around resonance and for which the width depends on δ_0, the dispersion spectrum decomposes into two branches. As already discussed analytically and will be shown later on for the experimental data, the dispersion spectrum decomposes into two triangular shaped parts with an amplitude

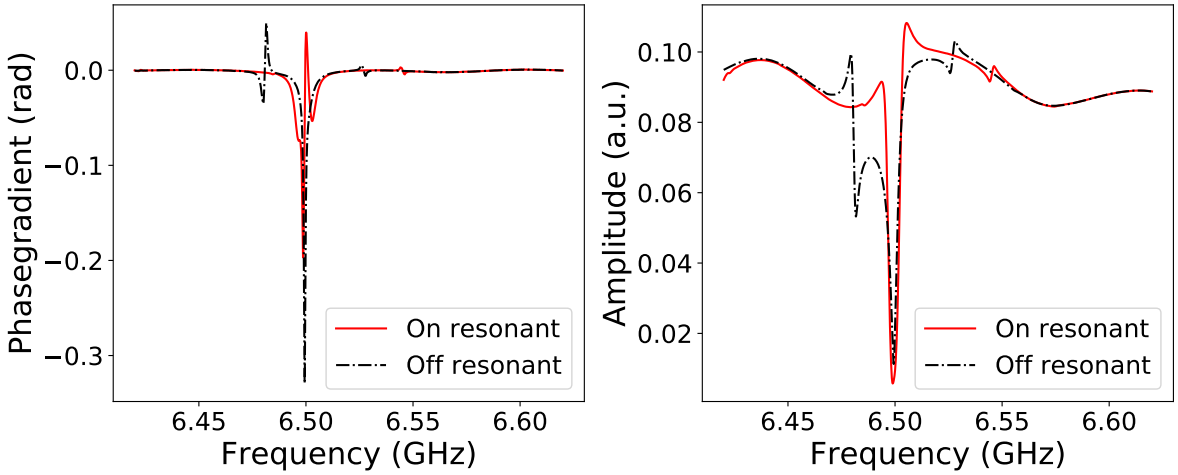

Figure 5.14: Example, illustrating the algorithm for the determination of the frequency gap between the upper and lower polariton branch for $\phi = \pi$ and an attenuation of 8 dB along the path P_1, corresponding to $\delta_0 = 1.02 \pm 0.09$. It is shown both for an off (black, dotted line)and on resonant (red, solid line) signal. a.) Phase gradient of the signal. The phase data has been unwrapped previously, i.e. the phase offset due to the finite path of the microwave signal from the source to the resonator has been removed. The frequency of each branch corresponds to the maximal absolute value b.) Off- and on-resonant linear uncorrected amplitude of the signal. This plot shows, why it is crucial to include the phase in the analysis. In the region of level merging, the respective coupling strengths are smaller than the individual linewidth. Therefore, although they can no longer be resolved any longer in the amplitude representation, they are still separable in the phase. As a result, the more sensitive phase gradient is used for the analysis. However, note that around resonance and level merging, the magnitudes also become small, which becomes problematic for a higher attenuation of the cavity port (c.f. Section 5.12)

maximum at the apex of each (c.f. Figure 5.9, Figure 5.10). The higher the attenuation, the more the apexes move away from the resonant field and frequency. Thus, the region in which the upper and lower CMP branch collapsed connects the apexes. This region grows with higher attenuation denoting the regime of level merging around resonance.

However, if the crosstalk is too large, the extracted values for the coupling strength can be distorted by the crosstalk. Hence, in order to estimate the reliability of the extracted values, it is necessary to identify the magnitude and influence of the crosstalk in these measurements. Therefore, the next section examines the crosstalk in greater detail.

5.7 Crosstalk

In the following analysis the crosstalk can be separated into two significant contributions which are denoted as the “baseline crosstalk” and the “signal crosstalk”. Whilst the first describes the changes in the baseline, i.e. influence for all frequencies in the respective dataset due to varying the phase from 0 to π, the latter refers to the influence on the resonance signal such as the amplitude.

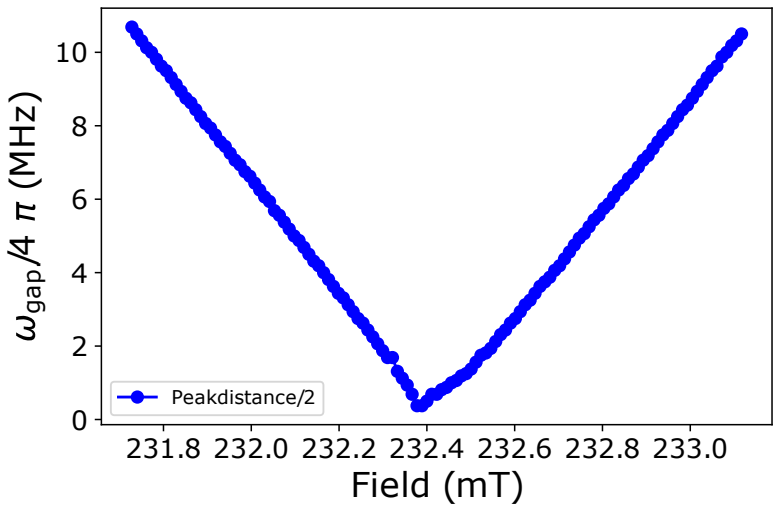

Figure 5.15: Result from the algorithm which calculates the distance between the upper and lower CMP branch. The minimal distance corresponds to resonant coupling and twice the coupling strength $g'(\delta_0, \phi)/2\pi$. In this figure, the result for $\phi = \pi$ and $(\delta = 1.02 \pm 0.09)$ (8 dB attenuation set in the path P_2), the distance is already divided by two, showing the coupling strength at the minimum which is $g'(\delta_0 = 1.02 \pm 0.09, \phi = \pi)/2\pi = (0.375 \pm 0.3)$ MHz.

5.7.1 Baseline crosstalk

In order to exclude local variations of the amplitude at different frequencies, the amplitude value which is shown in Figure 5.16 is averaged over a large window of frequencies. Of course, the region of the cavity resonance is excluded from this averaging process. Since the collapse of the anticrossing can be observed for a relative phase shift of π whilst a "classical" avoided level crossing occurs for $\phi = 0$, the greatest change due to crosstalk should be observable between $\phi = 0$ to $\phi = \pi$. Hence, the mean amplitude value of the baseline for $\phi = 0$ is compared to the one for $\phi = \pi$ as a function of the attenuation at the cavity port (c.f. Figure 5.16). The difference between the baseline amplitudes is also added (Figure 5.16 b.)) showing that this difference is below 0.7 %. Therefore, the baseline is not perturbed by a phase dependent crosstalk.

5.7.2 Signal crosstalk

In order to estimate the impact of the crosstalk on the cavity resonance, the changes in the loaded quality factor, resonance frequency and total amplitude are determined. Since the crosstalk denotes the direct interaction of the magnon port with the cavity resonator photons, it suffices to consider the off-resonant signal of the cavity resonator. At resonance, the crosstalk should not change, as although the desired coupling of the magnons to the cavity photons sets in, the magnon port interacts only indirectly with the cavity resonator.

Influence on the quality factor and resonance frequency

Both the loaded quality factor Q_l and the resonance frequency $\omega_r/2\pi$ including the error bars are extracted from a circle fit to the off-resonant cavity resonator's resonance for the

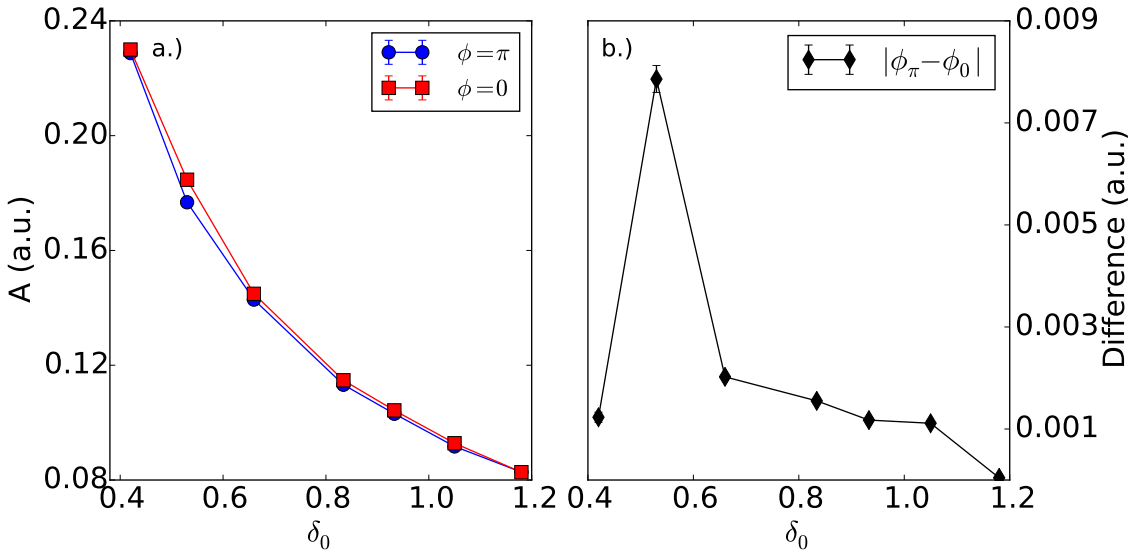

Figure 5.16: a.) Changes of the amplitude A of the baseline due to a contribution of the crosstalk as a function of δ_0 of the cavity port for two different relative phase shifts until the onset of level merging ($\delta_0 = 1$). The amplitudes for $\phi = 0$ (red, squares) and $\phi = \pi$ (blue, circles) decrease due to the increasing attenuation. The black data points denote the difference between the former two. For all displayed attenuation values, it does not exceed 0.7 % of the respective amplitude values. As a result, the crosstalk has a negligible effect on the signal's baseline. The error bars of the amplitudes originate from the standard deviation of the mean amplitudes and in the order of 0.2 % for both phases. b.) Difference between the amplitude values for $\phi = 0$ and $\phi = \pi$. The error bars for the amplitude difference are derived from Gaussian error propagation and in the order of 2 % except the first and last value In the figure, they are covered by the data points as the absolute magnitudes are much smaller. The solid lines in a.) and b.) serve as a guide for the eye, connecting the data points.

two relative phase shifts $\phi = 0$ and $\phi = \pi$. As illustrated in Figure 5.17, the resulting values (blue (red) for $\phi = 0(\phi = \pi)$) for Q_l (a.)) and $\omega_r/2\pi$ (b.)) are examined as a function of the attenuation at the cavity port. In order to quantify the variation due to a relative phase change of π, the difference between each case is plotted in Figure 5.17 c.) for Q_l (cyan) and for $\Delta\omega_r/2\pi$ (magenta). Referring to Figure 5.17 a.), within the error bars Q_l remains constant over the analysed range of attenuation of the signal arriving at the cavity port. The total variation of Q_l does not exceed $\Delta Q_l = 50$ which is less than 5 % of the absolute value. A similar observation also applies to the resonance frequency, where there is a small deviation between the two phases but considering the absolute value of this difference, the change is negligibly small. As shown in Figure 5.17 c.) and d.) for the difference, the resonance frequency does not change by more than 0.4 MHz which occurs for an attenuation of 7 dB ($\delta_0 = 0.93 \pm 0.08$). The small outlier close to $\delta_0 = 1$ for $\phi = 0$ is still the same within the error bars and not significant for level merging with $\phi = \pi$, where no such change is observed. These small phase-dependent changes demonstrate that there is a contribution from crosstalk in this system. However, the observed shifts are small compared to the absolute magnitude of the values. The resonance frequency is within the error bars constant for attenuating the cavity port's power and does not vary significantly between different phases. The linewidth of the resonance is also not

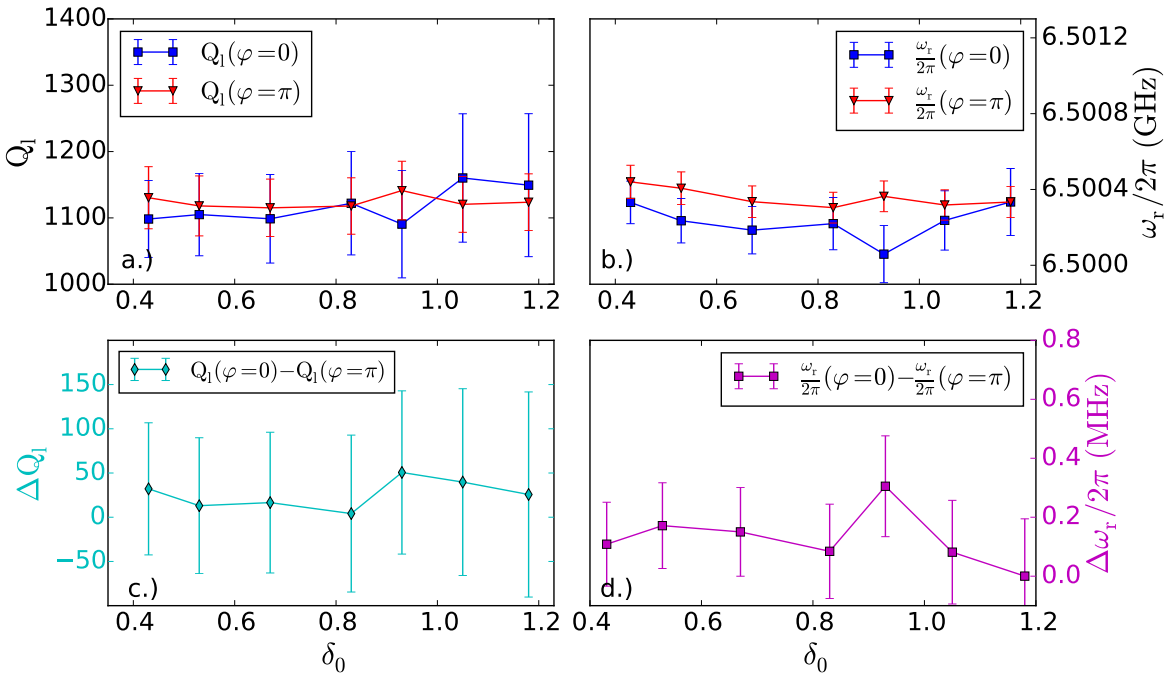

Figure 5.17: Change in loaded quality factor and resonance frequency of the cavity response out of resonance for two different phases ($\phi = 0$, $\phi = \pi$) as a function of the attenuation of the cavity port's amplitude. a.) Loaded quality factor as a function of the attenuation value for $\phi = 0$ (blue) and $\phi = \pi$ (red). Within the error bars, there is no significant change in Q_l. b.) Resonance frequency of the cavity resonator's "bright" mode for $\phi = 0$ (blue) and $\phi = \pi$ (red). For each phase setting, the frequency remains constant as a function of the attenuation within the error bars. Although the resonance frequency changes by turning the phase, the total difference is on the order of 0.004 % and hence is negligibly small. c.) Illustration of the total difference ΔQ_l (cyan) between the values for $\phi = 0$ and $\phi = \pi$. d.) Analogous calculation of the difference $\Delta\omega/2\pi$ (magenta) between the resonance frequency for $\phi = 0$ and $\phi = \pi$ from b.). The maximal change in quality factor does not exceed 50, which yields changes below 4.5 % and the total shift in frequency is less than 1 MHz. Within the error bars, there is no change. This small value shows that the crosstalk is not affecting the recorded signal. Hence, the discussed changes in amplitude and phase of the dispersion spectra can be attributed to level merging and not interference effects. The solid lines in a.) - d.) serve as a guide for the eye, connecting the data points.

influenced by the crosstalk since the quality factor does not change within the error bars either. Since the question of an amplitude enhancement for the case of level merging will be addressed later on, the change in the amplitude due to a change in relative phase will be now quantified.

Influence on amplitude

In order to quantify the impact of crosstalk on the signal's amplitude which is originating from the cavity photon out of resonance, the dependence of the maximal amplitude of the cavity resonance is determined as a function of the attenuation at the cavity port. Similar to Section 5.7.1, the amplitude values for $\phi = 0$ and $\phi = \pi$ are determined, and

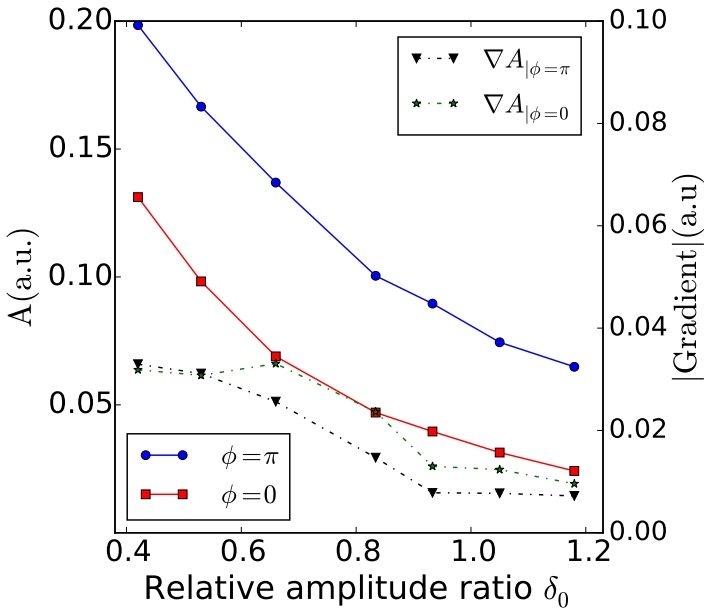

Figure 5.18: Change in the maximum amplitude of the cavity resonator's signal far from resonant coupling to the Kittel magnons, shown for two different phase values ($\phi = 0$ (red, squares) and $\phi = \pi$ (blue, circles)). In addition, the gradient for both curves illustrating the different slopes of both values for ϕ at the same attenuation value is plotted (black, triangles($\phi = \pi$), stars ($\phi = 0$)). The dotted lines connect the points and serve as a guide for the eye. Due to the increased attenuation at the cavity port, both amplitude curves decrease. The associated gradient shows similar behaviour for both, although it is higher for $\phi = 0$. This can be attributed to the changing relative orientation of $h_{\mathrm{AC}}^{\mathrm{crosstalk}}$ to $h_{\mathrm{AC}}^{\mathrm{cavity}}$. With a phase shift of π, there is no gain from the crosstalk. Hence this curve decreases faster. As a result, the difference between both curves decreases as well. Towards $\delta_0 = 1$, the gradient becomes almost constant. Errors in the determination of the amplitude are smaller than the data points and covered.

the corresponding gradients are calculated showing the change in slope between these curves as illustrated in Figure 5.18. In contrast to the negligible change of the baseline's amplitude (c.f. Figure 5.16), the peak amplitude varies substantially when the relative phase is shifted by $\phi = \pi$. The amplitudes decrease relative to the increase in attenuation of the cavity port's input power, but the maximum amplitude for $\phi = 0$ constantly remains below the value at $\phi = \pi$. The amplitudes differ by more than 65 % for lower attenuation values, and this difference decreases towards a higher attenuation of the cavity port. However, the gradient becomes constant. This decrease in the difference can be explained if the phase dependent field component's, $h_{\mathrm{AC}}^{\mathrm{crosstalk}}$ (c.f. Figure 5.6), orientation to the cavity field, $h_{\mathrm{AC}}^{\mathrm{cavity}}$, is considered. For $\phi = 0$, these contributions are in phase such that the absorption of energy at the cavity port is (partially, $\delta_0 < 1$) compensated by the crosstalk. As a result, the off-resonant dip's amplitude should be lower than for the opposite case, $\phi = \pi$ because, in a reflection measurement, it is the amount of absorption that is recorded. For the other case, the crosstalk leads to destructive interference with the AC field induced by the cavity port, increasing the absorption of energy. As illustrated in Figure 5.18, the amplitude is higher for $\phi = \pi$ and in line with the above picture. The attenuation of the cavity port is increased whereas the crosstalk's contribution remains

constant. Since the number of photons from the cavity port is lower, the signal amplitude for both phases decreases. However, the gradient of the amplitude change for $\phi = \pi$ is higher because there is no compensation by the photons from the crosstalk as there is for $\phi = 0$. Therefore, the difference between the maximal amplitudes for $\phi = 0$ and $\phi = \pi$ decreases towards higher attenuation values.

In conclusion, the baseline is not affected by crosstalk. Furthermore, the changes of the reflection signal recorded at the cavity port are at least one order of magnitude (less than 5 %) smaller than the quality factor or the maximal, off-resonant amplitude. Therefore, the different types of observed dispersion spectra which are shown in the next section can indeed be attributed to a control of the CMP's coupling strength by relative phase and amplitude changes.

5.8 Dispersion spectra

How the spectroscopic data is recorded is similar to the previous chapter where, for each temperature point, the dispersion spectrum for the CMP as a function of the externally applied field has been measured. However, instead of the temperature as the additionally varied parameter, the dispersion spectrum is now recorded for various combinations of relative phase and amplitude ratio between the cavity and magnon port. In view of the previous discussion on the coupling strength (c.f. Section 5.5.6), three different regimes of the relative amplitude ratio can be identified. These are $\delta_0 < 1$, $\delta_0 = 1$, and $\delta_0 > 1$ for all relative phases. Moreover, the relative phases of $\phi = 0$ and $\phi = \pi$ are found to be special cases in the two-tone CMP system, showing the greatest difference in the dispersion spectra. Hence, after discussing the limit for $\delta_0 \to 0$ (c.f. Figure 5.19), the changes of the above mentioned spectra are shown for the three different regimes of δ_0 both for $\phi = 0$ (left column) and $\phi = \pi$ (right column) in Figure 5.20 to Figure 5.22. In total, the relative phase is swept over more than one period, and the relative amplitude ratio is varied from $\delta_0 = 0.04 \pm 0.01$ to $\delta_0 = 11.79 \pm 1.97$. These three different regimes for δ_0 are shown in the following.

5.8.1 Dispersion spectra for $\delta_0 \to \delta_0 = 0$

Starting from the limit of $\delta_0 \to 0$, the dispersion spectrum of the CMP should correspond to the "classical" avoided level crossing at the external field value for resonant coupling to excited magnons. This is confirmed for an attenuation at the magnon port of 20 dB, i.e. $\delta_0 = 0.04 \pm 0.01$ where both in amplitude (a.)) and phase (b.)) are displayed in Figure 5.19. Similar to the previous chapter, the hybridisation of the cavity photon with the Kittel mode represents the dominant feature with the largest frequency gap in the avoided level crossing. Here, the resonance field is at $\mu_0 H_{\mathrm{res}} \approx 232\,\mathrm{mT}$ and as the upper (anti-symmetric) and lower (symmetric) frequency branch are well separated this hybridisation is in the strong coupling regime. Despite the Kittel mode's avoided level crossing, there are other weakly coupled avoided level crossings in the spectrum. Ordered for decreasing coupling strength, the most visible ones occur at $\mu_0 H_{\mathrm{MS}} \approx (229.75, 230.75, 234)\,\mathrm{mT}$, respectively. These modes represent higher order magnetostatic modes which depending on the externally applied field are also resonantly coupling to the cavity photons. Compared to the "cleaner" spectra at room temperature in terms of other modes for the temperature dependent study on the CMP even the dispersion spectrum for a strongly suppressed

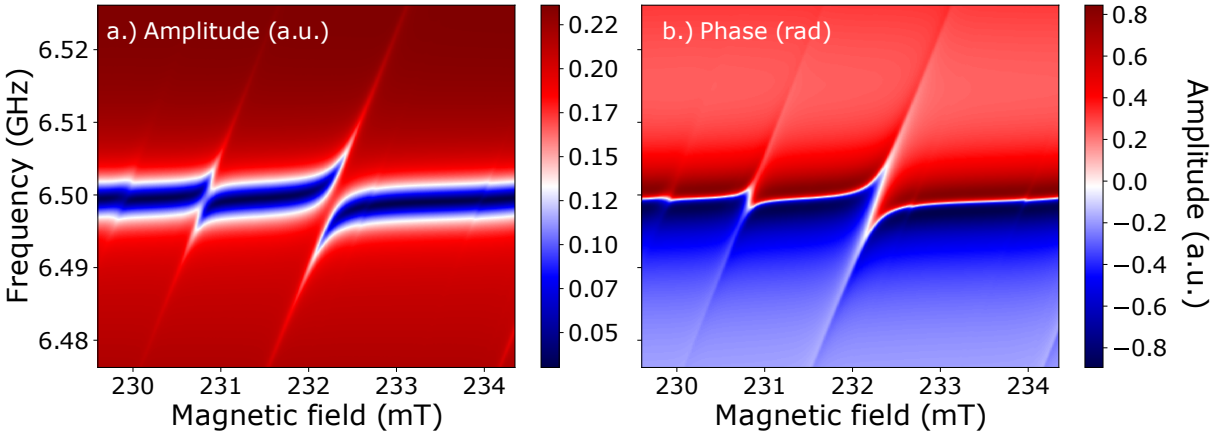

Figure 5.19: Dispersion spectrum of both the signal's amplitude (a.)) and phase (b.)) for a relative phase of $\phi = \pi$. The magnon port is attenuated by 20 dB as compared to the cavity port. This attenuation yields $\delta = 0.04 \pm 0.01$, and there is effectively no influence of the phase shift on the avoided level crossing. In this limit, the hybridised system can hence be described as a standard CMP with an avoided level crossing between the symmetric and the antisymmetric solution at resonance. The resonant coupling of the Kittel mode magnons occurs at an external field mode of $\mu_0 H_{\text{ext}} = 232.25\,\text{mT}$ with a coupling strength of $g'(\delta_0 = 0.04 \pm 0.01, \phi = 0)/2\pi = (3.24 \pm 0.3)\,\text{MHz}$. The additionally visible avoided level crossings of lower coupling strength correspond to the hybridisation with of the cavity photons with magnons in higher order magnetostatic modes.

magnon is more complex (c.f. Chapter 4, Section 4.6.7). Hence, for this experiment, a smaller YIG sphere is used in order to decrease the number of strongly coupled modes in the vicinity of the Kittel mode. As shown previously (c.f. Section 5.14), such additional coupling also influences the coupling strength of the Kittel mode. However, such additional changes in the coupling strength can heavily influence the study of the coupling strength of the Kittel mode as a function of the relative phase and amplitude ratio. For instance, it is not clear whether higher order magnetostatic modes with a non-uniform precession pattern follow the changes in phase and amplitude in the same fashion as the Kittel mode's precession which precesses uniformly. Hence, distinguishing between a decrease in coupling strength due to an increased parasitic coupling to other modes close in a resonant field or the change in phase or amplitude ratio cannot be performed unambiguously. Thus, this contribution should be suppressed as much as possible. As a result, the size of the YIG sphere is changed from one with a diameter $d = 0.5\,\text{mm}$ to one with $d = 0.2\,\text{mm}$. Hence, the probability for additionally strongly coupled modes next to the Kittel mode is decreased because the smaller sphere exhibits a lower number of available spins.

The dependence on the relative phase and amplitude for the mode with the highest coupling strength next to the Kittel mode are the subject of Section 5.13.

5.8.2 Dispersion spectra for $\delta_0 < 1$

In the intermediate regime, i.e. $0 < \delta_0 < 1$, the gap of the avoided level crossing either groww for $\phi = 0$ or decreases for $\phi = \pi$. However, there is no complete level merging in this

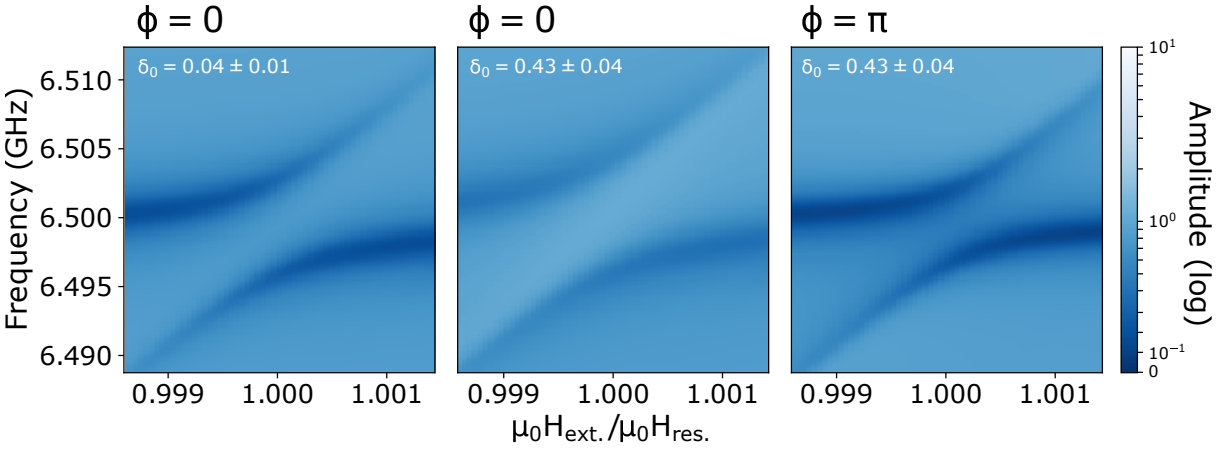

Figure 5.20: Comparison of the dispersion spectra for $\delta_0 = 0.43 \pm 0.04$, i.e. lower than 1 for $\phi = 0$ and $\phi = 0$ with the case for a strongly suppressed magnon port. There the system behaves effectively as a "single-tone" driven CMP. For $\delta_0 = 0.43 \pm 0.04$, $\phi = 0$, the gap increases and decreases for $\phi = \pi$ but no coalescence is seen yet.

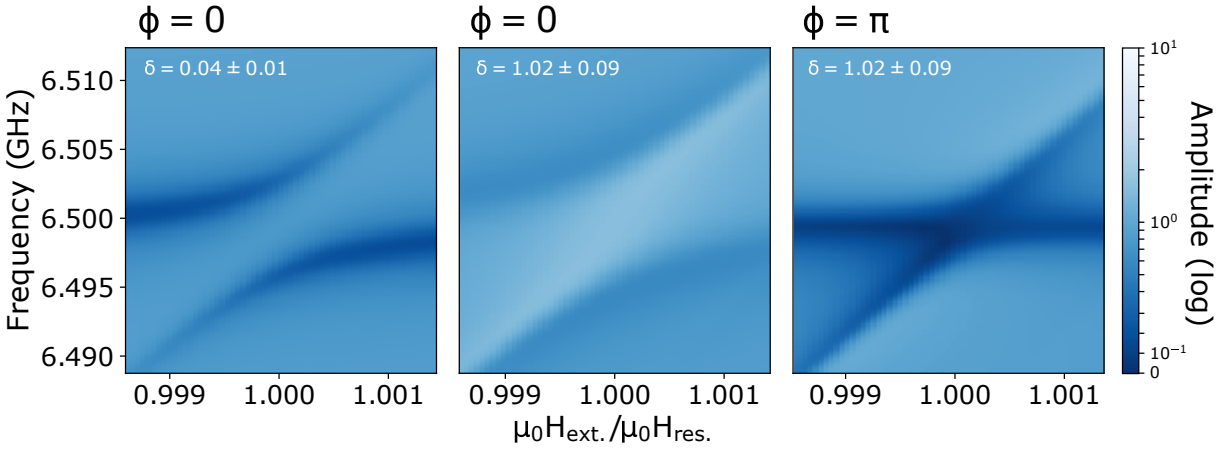

Figure 5.21: Dispersion spectra for $\delta_0 = 1.02 \pm 0.09$, i.e. at the transition to level merging for $\phi = 0$ and $\phi = \pi$. The case for a "standard" avoided level crossing with $\delta_0 = 0.04 \pm 0.01 \ll 1$ and $\phi = 0$ is plotted for direct comparison as it represent a "classical" avoided level crossing.

regime. Thus, increasing the relative amplitude ratio only performs a phase dependent modulation of the coupling strength. From $\delta_0 = 0.04 \pm 0.01$ to $\delta_0 = 0.43 \pm 0.04$, the coupling strength is enhanced by $\Delta g'/2\pi = (0.63 \pm 0.42)\,\mathrm{MHz}$ for $\phi = 0$, and decreased by $\Delta g'/2\pi = (0.69 \pm 0.42)\,\mathrm{MHz}$ for $\phi = \pi$. Within the error bars, the magnitude of the increase and decrease is the same and has also been indicated in the previous discussion of the simulations (c.f. Section 5.5.6). As illustrated in Figure 5.20, even for $\phi = \pi$ one can still observe a well separated avoided level crossing in the strong coupling regime. Hence, the repulsive part of the interaction between the cavity photon and the magnon is reduced but yet dominates the dispersion spectrum.

5.8.3 Dispersion for $\delta_0 = 1$

It is expected that the onset of level merging should occur for a value of the relative amplitude ratio $\delta_0 = 1$ for $\phi = \pi$. However, for $\phi = 0$, the frequency gap of the avoided

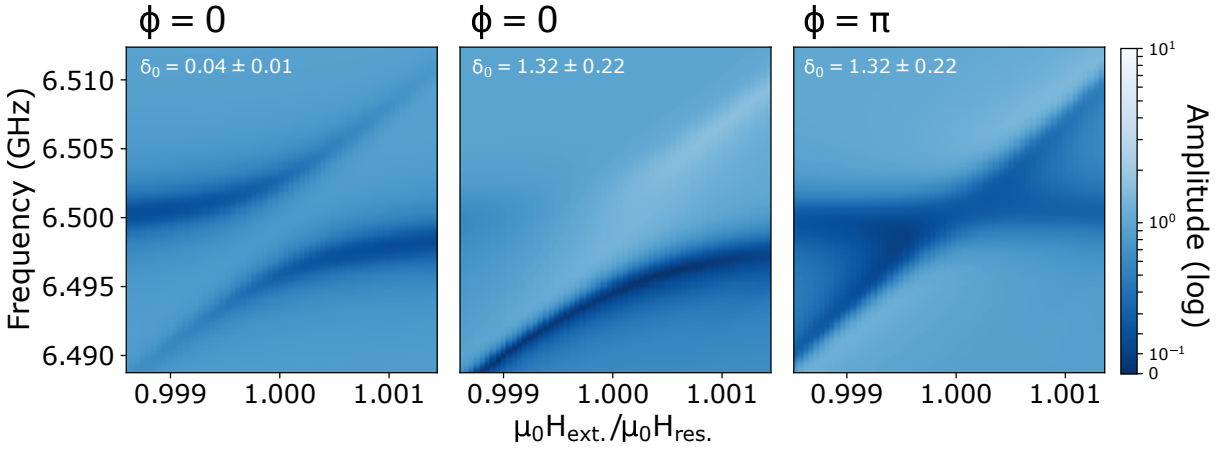

Figure 5.22: Dispersion spectra for $\delta_0 = 1.31 \pm 0.22$ within the regime of level merging for $\phi = 0$ and $\phi = \pi$. The case for a "standard" avoided level crossing with $\delta_0 = 0.04 \pm 0.01 \ll 1$ and $\phi = 0$ is plotted for direct comparison.

level crossing should further open, as the real part of $g'(\delta_0, \phi)$ continues to grow. Thus, with the two-ton driven CMP experiment, one can confirm the theoretical expectation for an increasing gap for $\phi = 0$ and decrease for $\phi = \pi$ as displayed in Figure 5.21. Compared to the coupling strength $g'(\delta_0 = 0.43 \pm 0.04, \phi = 0)$, it further increases by $\Delta g'/2\pi = (1 \pm 0.42)\,\mathrm{MHz}$ for $g'(\delta_0 = 1.02 \pm 0.09, \phi = 0)$, resulting in a total increase from $\delta_0 = 0.04 \pm 0.01$ of $\Delta g'/2\pi = (1.63 \pm 0.42)\,\mathrm{MHz}$. The slightly higher amplitude in the avoided level crossing region compared to $\delta_0 = 0.43$ (c.f. Figure 5.20, centre image) is attributed to the contributions from crosstalk. Since the total amplitude at the cavity port is lowered, the relative strength of the crosstalk amplitude compared to the signal amplitude increases. Thus, the amplitude appears "brighter", i.e. with a larger value, in the spectrum than before. If the phase is now changed to $\phi = \pi$, the antisymmetric and symmetric solution of the avoided level crossing has collapsed to a single solution at resonance field. The real part of the coupling strength becomes zero and, thus, one enters the regime of level merging. The minimal value of the coupling strength is hereby determined to be $g'(\delta_0 = 1.02 \pm 0.09, \phi = \pi)/2\pi = (0.37 \pm 0.3\,\mathrm{MHz})$.

5.8.4 Dispersion spectra for $\delta_0 > 1$

As illustrated in Figure 5.22, above the threshold to level merging, the dispersion spectrum exhibits two triangular shaped halves whose apexes point towards each other. At these apexes, the signal's amplitude is increased concering the amplitude far from the apexes. The general shape of this dispersion spectrum corresponds to the simulated dataset of the $S_{11}(\omega)$ parameter. For a further increase of δ_0, the triangles move both vertically and horizontally away from the resonance field and frequency in opposite directions. The horizontal separation of the apexes is proportional to the imaginary part of the coupling strength. Thus, extracting this difference as a function of δ_0 allows one to find an experimental estimate of the coupling strength above $\delta_0 = 1$ for $\phi = \pi$ where the coupling strength is purely imaginary (c.f. Section 5.5.6).

After the consideration of exemplary dispersion spectra for the three distinct regimes for δ_0, the dependence of the coupling strength on δ_0 ($\phi = \mathrm{const}$) and ϕ ($\delta_0 = \mathrm{const}$) is now going to be discussed. However, in order to exclude a power dependence of the ampli-

tudes at the magnon and the cavity port, respectively, the coupling strength is recorded for different output powers of the VNA, as well. This dependence is shown in the next section before the phase and amplitude dependence of the coupling strength.

5.9 Dependence on VNA output power

For this experiment, the microwave output power level of the VNA is set to $P_{\text{out}} = -5\,\text{dBm}$ for all spectroscopic measurements of level merging. In addition, the relative amplitude ratio is varied by attenuating one signal path relative to the other. Thus, in this regime, no non-linear effects due to high input powers are expected to occur. However, in order to quantify this assumption, two dispersion spectra at the intermediate phase of $\phi = \pi/2$ and $\delta_0 = 0.93 \pm 0.08$, with a microwave output power level of either $P_{\text{out},1} = -10\,\text{dBm}$, or $P_{\text{out},2} = +10\,\text{dBm}$ have been recorded. As described in Section 5.6, the values for the coupling strength are determined to be $g'(0.93 \pm 0.08, \pi/2)/2\pi = (3.49 \pm 0.25)\,\text{MHz}$ for $P_{\text{out},1}$ and $g'(0.93 \pm 0.08, \pi/2)/2\pi = (3.87 \pm 0.06)\,\text{MHz}$ for $P_{\text{out},2}$. Note that, the error bars correspond to the frequency resolution of the respective dataset. Within the error bars, there is no dependence of the observed spectra on the microwave output power level on the spectrum, at least up to $P_{\text{out},2} = 10\,\text{dBm}$. Hence, the changes in the effective coupling strength can only be attributed to the variation of the relative amplitude ratio.

5.10 Dependence on the relative amplitude

In order to examine the dependence of the coupling strength on the relative amplitude, the real and, if the SNR is still in a reasonable range, for $\delta_0 \geq 1$ and $\phi = \pi/2, \pi$ the imaginary part of the complex coupling strength is also determined. Thus, the real part of the complex coupling strength is determined by the peak-search algorithm presented in Section 5.6 as half of the size of the gap. However, for the imaginary part, the determination of the value is different, as discussed now.

5.10.1 Determination of the imaginary part of the amplitude

In the regime of level merging, one observes the formation of a region around the resonant coupling field, where the magnon and the cavity photon are at the same frequency. In other words, there is only one solution for the polaritonic mode, i.e. the CMP, because the symmetric and antisymmetric solutions have collapsed. The width of this region in terms of the applied external magnetic field depends on δ_0 and increases for larger δ_0. Therefore, this width is determined by identifying the field value above and below the resonant coupling field where the frequencies of the Kittel mode magnon and the cavity photon match. As a result, the previous algorithm that employs the phase gradient is not usable, because that algorithm searches for the distance between two peaks in the gradient which do not exist in this regime. As will be shown in the next section, the previous analysis scheme needed to be modified in order to determine the imaginary part of the complex coupling strength in the regime of level merging.

Second scheme for data analysis for the imaginary part of the coupling strength

Instead, the amplitude data are fitted by the sum of two Lorentzian functions. It is shown in Chapter 3, Section 3.2 that the CMP can be modelled as a system of two coupled

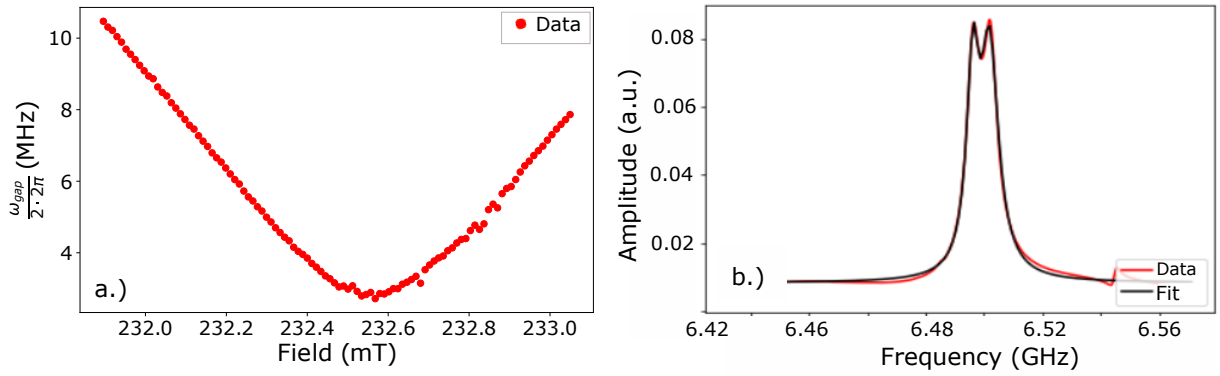

Figure 5.23: Illustration of the algorithm utilising the sum of two Lorentzian functions as the objective function in the fit to the amplitude. This method is used for the determination of the imaginary part of the coupling strength and linewidth analysis instead of a peak-search based on the phase gradient of the datasets. a.) The fit returns the positions of the peaks, i.e. the cavity resonance and the field dependent Kittel mode. Hence, the coupling strength can be extracted from the minimum distance between these peaks. Here, the parasitic avoided level crossing from the crosstalk has been analysed, yielding $g'(\delta_0 = 11.79 \pm 1.97, \phi = \pi)/2\pi \approx (2.8 \pm 0.3)\,\mathrm{MHz}$ b.) Example of the result from the fitting of the sum of two Lorentzians with unique resonance frequencies. It corresponds to the minimal value of the coupling strength shown in a.).

oscillators which justifies the above model of a sum of two Lorentzian functions [160]. Hence, the real part of the coupling strength is determined by the distance between the positions of the resonance peaks of each Lorentzian. An example for the determination of $\Re(g'(\delta_0, \phi))$ with the respective fit at the field value where the distance is minimal, is displayed in Figure 5.23. For this dataset one can identify an avoided level crossing, which yields $\Re(g'(\delta_0, \phi)) \approx (2.8 \pm 0.3)\,\mathrm{MHz}$. However, for this dataset $\phi = \pi$ and $\delta_0 = 11.79 \pm 1.97$, which should correspond to the level merging regime. Thus, no avoided level crossing should be visible. Therefore, together with the spectrum in Figure 5.22 where one can see slightly "brighter" amplitudes around the level merging spectrum, the above Figure 5.23 indicates that the experimental data towards higher δ_0 exhibits more than a single contribution from level merging. These additional contributions will be discussed in the next section.

Avoided level crossings: Increasing relative strength of crosstalk for higher δ_0

As already indicated in the spectra in Figure 5.21 and Figure 5.22, the dispersion spectra for higher δ_0 do not only show level merging for $\phi = \pi$. Instead, they exhibit a superposition of a level merging spectrum with an avoided level crossing at the same resonance frequency instead of pure level merging. Compared to the data for $\delta_0 = 1.31 \pm 0.22$ in Figure 5.22 for $\phi = \pi$, the relative intensity of this avoided level crossing increases towards larger values of δ_0 as shown in Figure 5.24 a.) for the amplitude and b.) phase data for $\phi = \pi$ and $\delta_0 = 11.79 \pm 1.97$. The phase and amplitude of this dataset are shown because without knowing the physical system, the amplitude data of this spectrum can also be attributed to a "classical" avoided level crossing in the weak coupling regime. However, the addition of the phase data shows that the spectrum is indeed a superposition of a level merging and an (unwanted) avoided level crossing. For $\delta_0 = 11.79 \pm 1.97$, the cavity

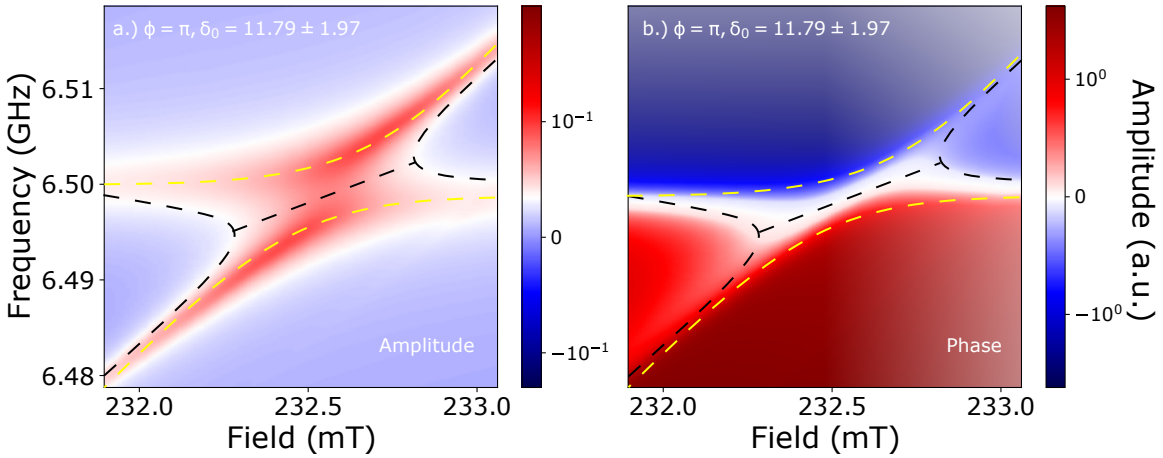

Figure 5.24: Dispersion spectra of the amplitude (a.)) and phase (b.)) for $\phi = \pi$ and $\delta_0 = 11.79 \pm 1.97$. The spectra are a superposition of two signals, as indicated by the dotted lines, which serve as a guide for the eye. Therefore, they are comprised of a level merging spectrum (black) with an additional avoided level crossing (yellow) at the same resonance frequency. This dataset represents the highest measured value for δ_0. As a result, the cavity port is so strongly attenuated, that the relative strength from the avoided level crossing is far higher than when $\delta_0 = 1.31 \pm 0.22$ (c.f. Figure 5.22). This additional avoided level crossing is attributed to a transmission measurement of the crosstalk at the cavity port and its relative weight increases as the cavity port is further attenuated. However, for the complex-valued coupling strength, this avoided level crossing adds a parasitic real-valued contribution, which decreases the field distance between the apexes of the level merging signal. Hence, this additional input has to be considered in the calculation of $\Im(g'(\delta_0, \phi))$

resonator port is attenuated by 29 dB which lowers the SNR. In order to ensure $\phi = \pi$ is set correctly, the phase signal is shown for a lower relative amplitude ratio with a higher SNR for $\phi = 0$ and $\phi = \pi$ in Section 8.1.3, Figure 8.1 a.) and b.), respectively. This comparison confirms that the displayed phase in Figure 5.24 b.) corresponds to a phase shift of $\phi = \pi$ with level merging and the above-discussed contribution and does not refer to an avoided level crossing such as the ones in Chapter 4.

The existence of the additional avoided level crossing is attributed to a transmission measurement of the crosstalk at the cavity port. Although it has been shown before that for the data for $\delta_0 \lesssim 1$, the crosstalk has no substantial impact on the signal: However, if the amplitude at the cavity port is substantially smaller than the one at the magnon port, the crosstalk has to be taken into account towards higher δ_0. In the course of the measurement at the cavity port, this crosstalk corresponds to a "classical" transmission measurement of an avoided level crossing as there is no relative phase shift. The values for the coupling strength which are determined with fitting two Lorentzians are listed in Table 5.2. Since the level merging signal and this avoided level crossing are superimposed, they mutually influence each other. If the cavity port is strongly attenuated the contribution from this (unwanted) anticrossing is relatively stronger, but at the same time, the attractive coupling is higher as the imaginary part of the coupling grows. This explains why the values from Table 5.2 decrease to larger δ_0. Thus, in order to minimise

δ_0	4.17	5.25	8.32	11.79
$\Re g'(\delta_0)/2\pi$ (MHz)	3.38	3.19	2.72	2.89
$\overline{\Re g'(\delta_0)/2\pi}$ (MHz)	3.04 ± 0.25			

Table 5.2: Values of the coupling strength for $\delta_0 > 4$ for the avoided level crossing due to a crosstalk transmission measurement where there is no dependence on the relative phase. Below this value, the signal from the level merging is dominant, i.e. the cavity port's amplitude is not too weak. The last row displays the geometric mean. Taking the mutual influence of level merging and avoided level crossing into account, this geometric mean yields an average value for the coupling strength which is used to find an estimate for $\Im(g'(\delta_0, \phi))$. The error denotes the standard deviation.

the uncertainty, the geometric mean including the standard deviation has been calculated to find an average value for the contribution to the real part of the coupling strength.

Calculation of the contribution of the parasitic coupling to $\Im(g'(\delta_0, \phi))$

As indicated before, the level merging and the avoided level crossing from crosstalk mutually influence each other. Hence, even for $\phi = \pi$, the contributions to the effective coupling strength as measured at the cavity port are not purely imaginary. Instead, the crosstalk's avoided level crossing results in a non-zero real component. As shown in Section 5.5.6, the presence of a non-zero real part corresponds to an enhancement of the frequency gap of the avoided level crossing. In turn, it counteracts the growth of the area of level merging around resonance. Thus, the horizontal distance between the apexes (c.f. Figure 5.22, $\phi = \pi$) is diminished by the additional real-valued part. As a result, the contribution from the real part has to be added to the values for $\Im(g'(\delta_0, \phi))$ extracted from the horizontal distance in the following section.
Hence, in the experiment, for $\phi = \pi$ and $\delta_0 > 1$, one measures a smaller imaginary part $|\Im(z)_{\text{meas}}|$ instead of the true modulus, denoted by $|\Im(z)_0|$.
The relation between both is given by $|\Im(z)_0| = \sqrt{|\Re(g'(\delta_0)_{\text{crosstalk}})|^2 + |\Im(z)_{\text{meas}}|^2}$, where $z = g'(\delta_0, \phi)$. Since the relative weight of the avoided level crossing distorting the level merging spectrum is proportional to δ_0, the real part of the average value of the crosstalk's avoided level crossing (c.f. Table 5.2) is calculated by:

$$\Re(g'(\delta_0)_{\text{crosstalk}}) = \delta_0 \overline{\Re g'(\delta_0)} \tag{5.9}$$

Correspondingly, the offset $\Delta\Im(z)_{\text{crosstalk}}$ on the imaginary part due to the presence of the crosstalk's avoided level crossing can be estimated by:

$$\Delta\Im(z)_{\text{crosstalk}} = |\Im(z)_{\text{meas}}| - |\Im(z)_0|, \tag{5.10}$$

where the values for this experiment are shown in Table 5.3

5.10.2 Threshold for the determination of $\Im(g'(\delta_0, \phi))$

For the determination of the imaginary part of the coupling strength, the finite linewidth of the response of each constituent necessitates the introduction of a threshold. This

δ_0	1.31	2.63	3.71	8.32	11.79
$\Delta\Im(z)_{\text{crosstalk}}$	0.365	0.539	0.896	2.778	4.538

Table 5.3: Offset which has to be added to the directly measured values of $\Im(g'(\delta_0, \phi))$ calculated by Equation (5.10).

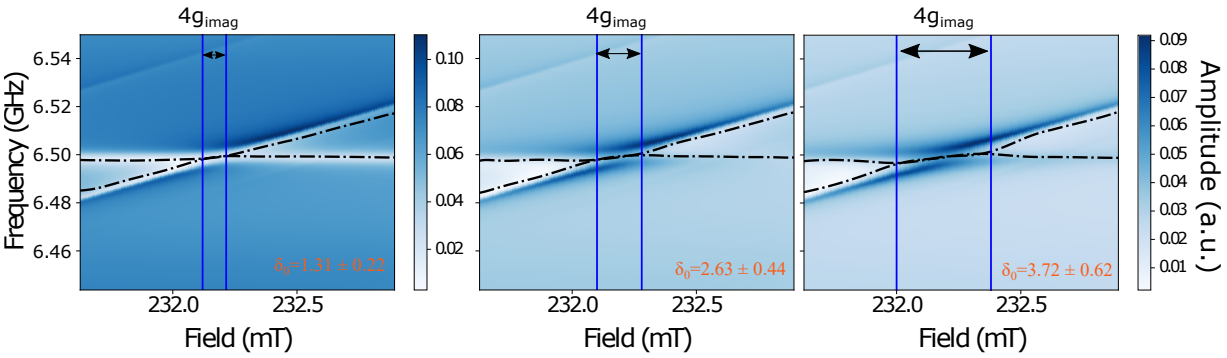

Figure 5.25: Illustration of the determination of the imaginary part for $\phi = \pi$ and increasing values of $\delta_0 > 1$. The final thresholds $g_{\text{threshold}}$ used for the identification of $|\Im(z)|_{\text{meas}}|$ are a.) $g_{\text{threshold}}/2\pi = 1.15\,\text{MHz}$, b.) $g_{\text{threshold}}/2\pi = 1.5\,\text{MHz}$, and c.) $g_{\text{threshold}}/2\pi = 2.5\,\text{MHz}$. Hence, the distances are $\mu_0\Delta H_{\text{merging}}$. The dotted lines are the result from the determination of the resonance frequencies using the respective threshold value and a Savitzky-Golay filter. The filter removes possible outliers from the fit result [207]. The solid (blue) lines serve as a guide for the eye and indicate the horizontal distance between the apexes.

threshold is defined as the minimum distance between the peaks where still the sum of two Lorentzians can be fitted to the data. If the distance is lower than the threshold value, a single Lorentzian is fitted to the composite signal in the regime of level merging. Specifically, this means that for the field entries where the threshold has to be applied, the magnon and the cavity photon frequencies match by definition. The determination of the specific threshold value is illustrated in Figure 5.25 (c.f. Section 8.1.4). The threshold value increases towards larger δ_0 because of two reasons. First, the width $\mu_0\Delta H_{\text{merging}}$ grows and the coalescence of the magnon and cavity photon frequencies at the identified apex takes place less abruptly. As also seen from the phase representation of the data (c.f. Section 8.1.5, Figure 8.3), this increases the frequency difference where both peaks can be still clearly identified. Second, the higher attenuation of the cavity port and enhanced influence of the crosstalk's avoided level crossing needs to be taken into account.
Furthermore, the individual off-resonant linewidths and the linewidth in the regime of level merging have to be considered when setting the threshold. The highest threshold cannot exceed the sum of the magnon and cavity photon linewidth, because above that the individual peaks should be resolvable again. As discussed in more detail later on, this corresponds to the geometric mean of the off-resonant linewidth of the cavity resonator and Kittel mode magnon, i.e. $g_{\text{threshold}}/2\pi = ((3.79\pm0.003)+(1\pm0.5))/2\,\text{MHz} = (2.4\pm0.25)\,\text{MHz}$. Thus, the lowest threshold should not be below half the linewidth of the merged spectrum, which is in the order of 1 MHz(c.f. Section 5.12).

δ_0	1.31	2.63	3.71	8.32	11.79
$\lvert\Im(z)_{\text{meas}}\rvert/2\pi$ (MHz)	1.176	3.44	3.99	5.81	6.58
$\Delta\lvert\Im(z)_{\text{meas}}\rvert/2\pi$ (MHz)	0.575	0.75	1.25	1.25	1.25

Table 5.4: Values for $|\Im(z)_{\text{meas}}|$ for five different values of δ_0.

Following the derivation in Ref. [205], the horizontal distance $\mu_0\Delta H_{\text{merging}}$ between the apexes, where only one solution for the coupled system exists in the regime of level merging, corresponds to

$$\mu_0\Delta H_{\text{merging}} = 4\Im g'(\delta_0, \phi) \equiv 4g_{\text{imag}}. \tag{5.11}$$

In order to compare the field distance with the coupling strength, which is given in frequency units, the corresponding frequency of this splitting is calculated via the Kittel mode's dispersion relation for a spherical sample. The corresponding results are shown in Table 5.4. Now, by utilizing Equation (5.10), the imaginary part of the coupling strength, $\Im(g'(\delta_0, \phi))$, can be determined. Furthermore, the dependence of the complex coupling strength for different combinations of δ_0 and ϕ can be examined and compared to the simulations.

5.10.3 Combined dependence of $\Re(g'(\delta_0, \phi))$ and $\Im(g'(\delta_0, \phi))$

The result from sweeping the relative amplitude ratio δ_0 while keeping the relative phase fixed is displayed in Figure 5.26 a.) and b.) for $\phi \in (0, \pi/2, \pi)$. Whilst the top one (a.)) shows the real part for $\phi = 0, \pi$ and the modulus for $\pi = \pi/2$, the bottom one illustrates the imaginary part extracted from the data analysis both for the regimes $0 < \delta_0 < 1$ and $\delta_0 > 1$. Whereas in Figure 5.26 a.), the solid lines correspond to fits of Equation (5.8), in b.) they correspond to a calculation using this equation as the number of available data points was too low. Since the coupling strength is a complex quantity now, only the real part for $\phi = 0$ and $\phi = \pi$ (because the imaginary part is zero in these cases) and the modulus for the intermediate phase values of the coupling strength can be extracted from the experimental data. Thus, except in the regime for level merging ($\phi = \pi$ and $\delta_0 > 1$) where the coupling strength is purely imaginary, it is not possible to directly extract the imaginary part of $g'(\delta_0, \phi)$. It can also be partially derived from the data for $\phi = \frac{\pi}{2}$, where the modulus contains a contribution from both real *and* imaginary parts. Comparing the experimental data with the analytical expression for $g'(\delta_0, \phi)$ demonstrates an excellent agreement with the calculated values from Figure 5.11 a.) for the real and b.) for the imaginary part. For a relative phase of $\phi = 0$, $\Im g'(\delta_0, \phi) = 0$ (red, circles), and the coupling strength increases continuously as δ_0 grows. The coupling strength changes from $\Re g'(\delta_0, \phi)|^{\phi=0}_{\delta_0=0.04\pm0.01}/2\pi = (3.24 \pm 0.3)$ MHz to $\Re g'(\delta_0, \phi)|^{\phi=0}_{\delta_0=3.71\pm0.62}/2\pi = (7 \pm 1.5)$ MHz. On the contrary, when the relative amplitude ratio approaches $\delta_0 = 1$, the coupling strength decreases for $\phi = \pi$ (blue, squares) reaching zero when $\delta_0 = 1$. Then, being in the regime of level merging, only the imaginary component is non-zero and correspondingly increases with δ_0.

Hence, in this regime, the modulus corresponds only to the contribution from the imaginary part. As a result, one can extract the data points shown in Figure 5.26 b.). Taking

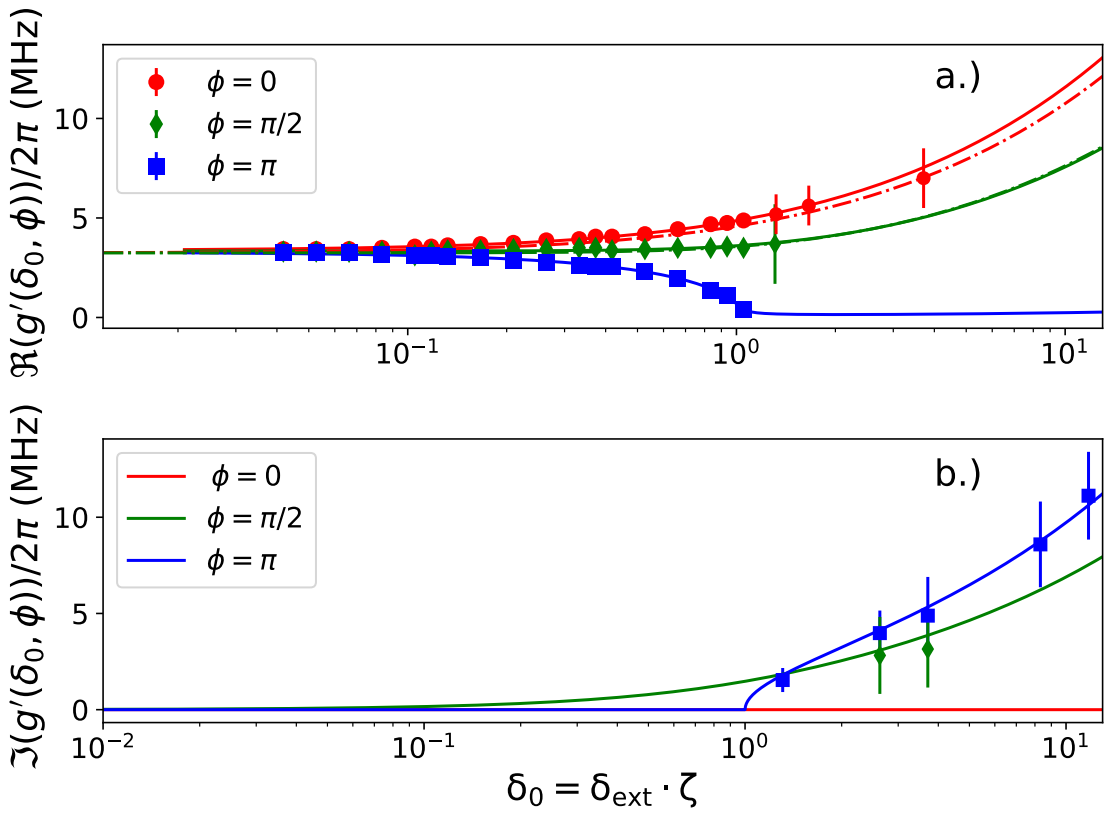

Figure 5.26: Real (top, a.)) and imaginary part (bottom, b.)) of the effective coupling strength for three different values of fixed relative phase as a function of the relative power level. Top: The experimental values (points) match well with the fits (solid lines), $\mathcal{R}(g'(\delta_0, \phi)) = 0$ for $\delta_0 \geq 1$ and $\phi = 0$. The dotted red (green) line corresponds to a calculation based on Equation (5.8) for $\phi = 0\,(\pi/2)$. Bottom (b.)): Imaginary part as extracted from Figure 5.25. These values are also consistent with the developed model although the error bars are much larger. This increase of the error bars is attributed to the lower SNR for higher attenuations at the cavity port (c.f. Section 5.10.1). Thus, the number of data points is also lower. Due to the lower number of data points the solid lines represent a calculation based on Equation (5.8). The parameters extracted from the analysis have been utilised.

both extremal cases $\phi = 0$ and $\phi = \pi$ into account, one can deduce that the observable spectra at certain δ_0 and ϕ most likely depend on the ratio between the real and imaginary part of the coupling strength. Whilst the real part can be associated with the existence of an avoided level crossing, i.e. level repulsion, the imaginary part refers to an attraction of the previous symmetric and antisymmetric solutions, i.e. level merging. Thus, for intermediate phases between $\phi = 0$ and $\phi = \pi$, such as $\phi = \pi/2$ (green, diamonds), one enters a regime where there is a coexistence between an avoided level crossing (level repulsion) and level merging. In this case, the final spectrum contains the features from both level repulsion and attraction as shown in Figure 5.27. This figure also shows a further feature which can be seen in several spectra, especially those with an intermediate phase value between $\phi = 0$ and $\phi = \pi$. The amplitude sign of the Kittel mode's dispersion undergoes a change when the resonance frequencies match, i.e. $\omega_r = \omega_m$. In this specific case, the

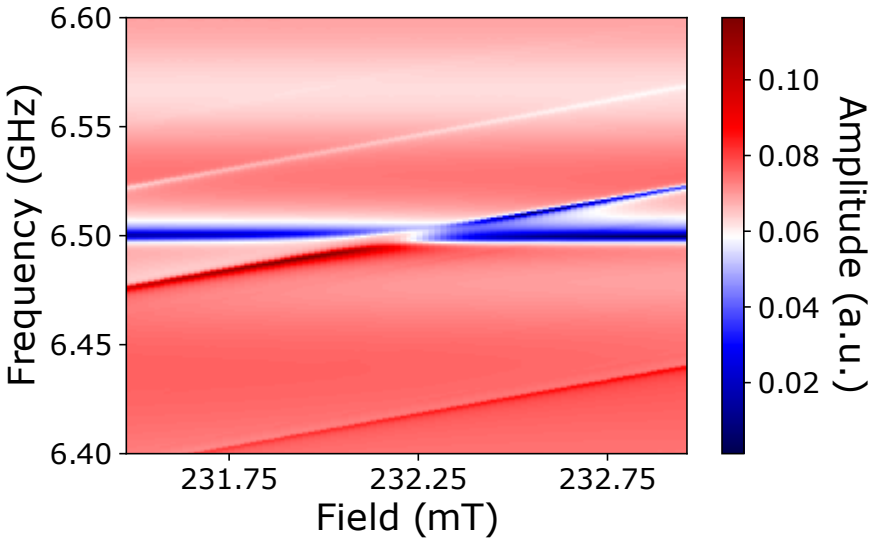

Figure 5.27: Experimental data showing the "interaction" of level repulsion and attraction for $\delta_0 = 1.31 \pm 0.22$ and $\phi = -\frac{3}{8}\pi$. The counteracting repulsion and attraction at resonance lead to a partial extinction and partial enhancement of the signal. One can see both the characteristic features. First, the signal's curvature corresponding to the symmetric and antisymmetric mode of a "classical" avoided level crossing. Second, the existence of the triangular structure with the right apex more dominant than the left one.

signal turns from a resonance peak to a resonance dip. Initially, the Kittel mode is not a dip, as one would expect from a reflection measurement. This observation is attributed to the fact that here the relative phase for Figure 5.27 is $\phi = \pi + \frac{3}{8}\pi$, i.e. a value higher than $\phi = \pi$, which changes the form of the resonance. However, when the Kittel mode magnon is dressed with a cavity resonator photon, in the phase representation of the dispersion a phase jump of π is observed. As a result, the signal towards the higher external magnetic field, i.e. beyond a resonant coupling to the Kittel mode, changes from a peak to a dip.

Therefore, using this two-tone controlled CMP, it is not only possible to switch the interaction "on" or "off" but also to have a tunable control over the amount of coherent information exchange.

5.11 Dependence of $g'(\delta_0, \phi)$ on the relative phase

Despite the strong dependence of the coupling strength on δ_0 with a constant relative phase, the value of $g'(\delta_0, \phi)$ also changes when the relative phase is varied. Therefore, measurements have also been made where the relative amplitude ratio is kept fixed, and the relative phase is changed in an interval of $\phi \in (-\frac{\pi}{2}, \frac{7}{4}\pi)$. In combination with a solid line from a fit to Equation (5.8), the real part of the coupling strength is displayed in Figure 5.28 for four different values of δ_0. This plot shows how increasing the relative amplitude ratio from $\delta_0 \ll 1$ to $\delta \approx 1$, enhances the variation of the coupling strength as a function of the relative phase. If the magnon port is strongly attenuated, the influence of the relative phase should be suppressed. The data points for $\delta_0 = 0.04 \pm 0.01$ (black) confirm this expectation and are in line with the data and calculations for $\delta_0 \ll 1$ in Fig-

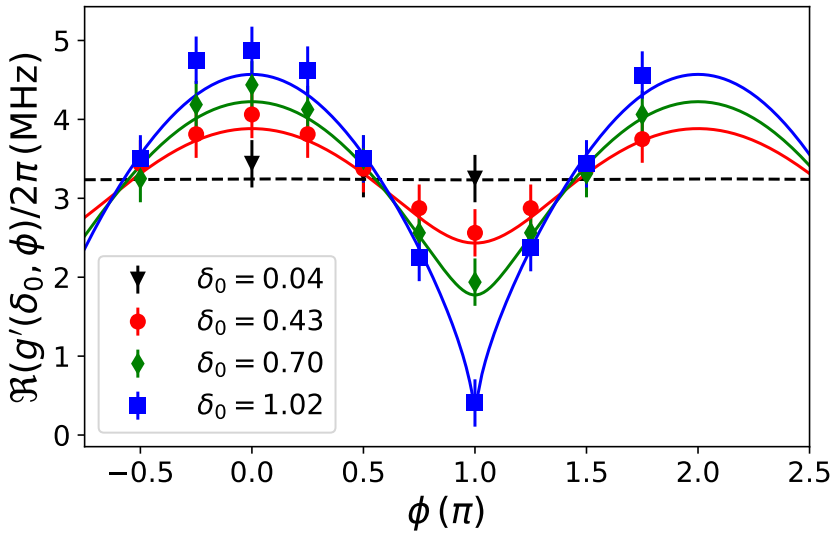

Figure 5.28: Real part of coupling strength as a function of the relative phase for four different relative power level ratios δ_0. The solid lines represent fits based on Equation (5.8), from which the values for δ_0 in the legend are extracted. Due to the low number of data points, the dotted black line serves as a guide for the eye and is not a fit. For $\delta_0 = 0.04 \pm 0.01$, there is only a small phase dependence of the coupling strength as it changes by 6 % from $\phi = 0$ to $\phi = \pi$. Increasing δ_0 but remaining in the intermediate regime for δ_0 ($0 < \delta_0 < 1$), the modulation on the coupling strength grows, but the gap does not close for $\phi = 0$. The decrease is comparable to the increase of $\phi = 0$. However, for $\delta_0 = 1.02$, the coupling strength decreases to zero at $\phi = \pi$, which marks the transition to level merging.

ure 5.28. The coupling changes only by 6% from $g'(\delta_0,\phi)|^{\phi=0}_{\delta_0=0.04\pm0.01}/2\pi = (3.44\pm0.3)$ MHz to $g'(\delta_0,\phi)|^{\phi=0}_{\delta_0=0.04\pm0.01}/2\pi = (3.25 \pm 0.3)$ MHz. Please note that, due to only a few data points for $\delta = 0.04 \pm 0.01$, the dotted line does not represent a fit. Rather, it serves as a guide for the eye to show the minimal variations. As expected from the discussion in Section 5.11, the coupling strength is periodically modulated for $0 < \delta_0 = 0.43, 0.7 < 1$ for $\phi = 0$ and $\phi = \pi$ but the amplitude of the modulation increases for $\delta_0 \to 1$. Whilst for the first, the size of the frequency gap of the avoided level crossing increases by 25 %, the latter increases by 21 %, which is in the same range within the error bars. Just as with $\phi = \pi$ in Figure 5.26, the transition from level repulsion to level merging is reached for $\delta_0 = 1$. In the experiment, a minimal value of $g'(\delta_0,\phi)|^{\phi=0}_{\delta=1.02\pm0.09}/2\pi = (0.37 \pm 0.3)$ MHz is measured for $\phi = \pi$ which yields the fit result of $\delta_0 = 1.02 \pm 0.09$ (c.f. Section 8.1.2). The maximal value of the coupling strength,$g'(\delta_0,\phi)|^{\phi=0}_{\delta=1.02\pm0.09}/2\pi = (4.88 \pm 0.3)$ MHz, is also observed for $\phi = 0$ and $\delta_0 = 1.02 \pm 0.09$. Moreover, the experimental data is in good agreement to the analytical expectation for $\Im(g'(\delta_0,\phi))$ shown in Figure 5.11 b.).

The data displayed in Figure 5.26 and Figure 5.28 shows full control of the coupling strength by purposefully tuning the relative phase and amplitude. Such control allows the coherent exchange of information to be either turned off or strongly enhanced. The control over the coupling strength is realised by moving from a cavity port only driven CMP to a two-tone CMP through the introduction of a second (magnon) port with relative phase and amplitude to the cavity port.

In contrast to related experiments at room temperature, the system is completely externally controllable which makes this two-tone driven approach attractive for further experiments [75]. Furthermore, all measurements are conducted with the same resonator and YIG sphere and there is no need to change different types of resonators such as in Ref. [193]. For instance, the addition of a non-linear component such as a qubit similar to the one used in Ref. [27] could enable one to "turn off or on" the interaction between the magnon based memory and the qubit based processing unit.

5.12 Amplitude enhancement

Usually, in CMP experiments, the spin wave excitation, i.e. magnons, in the sample is given by the coupling of cavity resonator photons to the magnonic system. As a result, from the photons perspective, the coupling represents an additional channel of energy dissipation for the resonator. Here, most of the spectroscopic data is obtained from a microwave reflection measurement of the cavity resonator. Consequently, changes in the cavity resonator's signal amplitude and hence losses comprise the experimental data from the hybridised cavity photon-magnon system. Therefore, in order to fully understand the influence of the additional magnon port leading to another AC magnetic field with a relative phase and amplitude to the previous single-tone, CMP experiment, the amplitude and the corresponding losses need to be also discussed. Whilst the study of the coupling strength for different values of δ_0 and ϕ demonstrates the existence of different coupling regimes and control over the cavity photon-magnon interaction, the amplitude and linewidth can give experimental insight into the coupling mechanism itself. Recently, it has been predicted that in the regime of level merging, i.e. $\delta_0 \geq 1, \phi = \pi$, the signal amplitude at resonance should be strongly enhanced and the FMR linewidth decreased [77]. In this regard, the amplitude enhancement denotes the amplitude difference between the off-resonant and the on-resonant signal amplitude at the resonance frequency of the cavity resonator. To this end, a horizontal cut of the data at the cavity resonance of $\omega_r/2\pi = 6.4985\,\mathrm{GHz}$ is made which allows one for the extraction of the dependence of the amplitude as a function of the externally applied field for this specific frequency. As shown in Figure 5.29 a.), in addition to the amplitude enhancement at resonance (red, squares), the change in the signal's amplitude is also studied for frequencies both slightly below (green, stars) and above (blue, circles) the resonance frequency. The solid lines correspond to fits based on Equation (5.7), and the two dotted vertical lines (green) mark the field interval yielding an amplitude enhancement of more than 10 dB for the on-resonant case. Furthermore, the inset exemplarily illustrates the method for the determination of the values given in the main. It displays both the off- and on-resonant signal for the most significant value of an enhancement. Hence, it corresponds to a maximal amplitude change of 30 dB. For this specific case, one can also infer an asymmetry both for whether the chosen frequency value is above or below the resonance frequency and in the dataset itself as the external field is varied. Starting from the latter, as the Kittel mode approaches resonance, the hybridisation sets in and hence, there is an additional phase jump for this mode before and after passing resonance. Thus, the Kittel dispersion can here also change from a dip to a peak before and after resonance. Since the enhancement is determined by comparing the signal to the cavity resonator *dip*, this changes the shape of the result for the increasing amplitude. The difference in amplitude enhancement for the same distance below and above the resonance frequency is attributed to the small uncertainty in setting the phase value to $\phi = \pi$. As illustrated in Figure 5.30 for $\phi = \pi + \pi/8$, the part

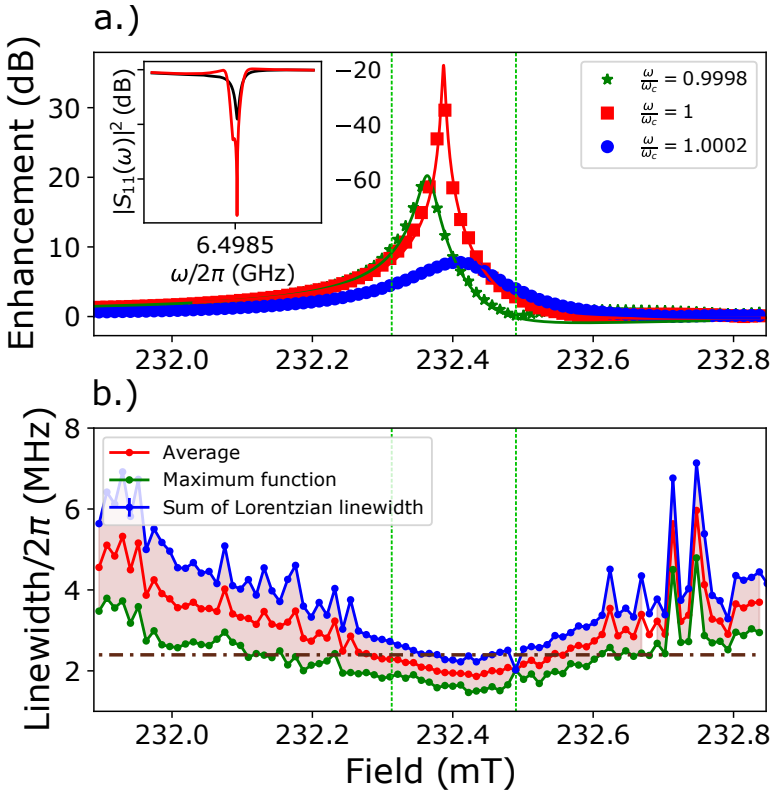

Figure 5.29: a.) Change of the maximal amplitude at three different frequencies normalised to the resonance frequency of $\omega_r/2\pi = 6.4985\,\mathrm{GHz}$ as a function of the applied magnetic field below (green, stars), at (red, squares), and above (blue, circles) resonance. The solid lines refer to fitting the data by Equation (5.7). Both the magnon and the resonator linewidth output parameters are in a similar range and do not strongly fluctuate (c.f. Section 8.1.6). As illustrated by the inset, the data points in the main figure correspond to the difference of the off-resonant ($\mu_0 H_{\mathrm{ext}} \neq \mu_0 H_{\mathrm{res}}$, black) and on-resonant ($\mu_0 H_{\mathrm{ext}} = \mu_0 H_{\mathrm{res}}$) amplitude. The small kink to the left of the on-resonant signal is due to the asymmetry in the level merging spectrum (c.f. Figure 5.22). The vertical dotted green lines denote the field interval where the amplitude enhancement at resonance exceeds 10 dB. At resonance, the amplitude is enhanced by 30 dB which is equivalent to a gain of 1000. b.) Estimate of the linewidth using an interval (red shaded area) given by an upper (blue) and lower (green) bound as a function of the field. The average (red) is then an estimated value for the linewidth. The dotted horizontal line (dark brown) denotes the average value between the cavity resonator and magnon linewidths $((\kappa_r/2\pi + \kappa_m/2\pi)/2 = (3.8 \pm 0.003 + 1 \pm 0.5)/2\,\mathrm{MHz} = (2.4 \pm 0.25)\,\mathrm{MHz})$. The mean of the linewidth below this value is $\kappa_{\mathrm{ges}} = (2.12 \pm 0.21)\,\mathrm{MHz}$. Thus, on average, the linewidth further decreases by $(14.28 \pm 8)\,\%$ due to the effect level merging

of the spectrum left from the resonance field generally exhibits a higher amplitude than the right half. On the contrary, for $\phi = \pi - \pi/8$, the situation is reversed. Therefore, this asymmetry is mostly due to the systematic error in the phase of $\Delta\phi = 0.02\frac{\pi}{8}$. As previously mentioned, this error originates from the uncertainty in repeatedly setting the mechanically tunable phase shifter to the same value.

In general, an enhancement of the amplitude of the recorded microwave signal corresponds to a higher amount of energy being stored in the resonator, i.e. a higher number of photons

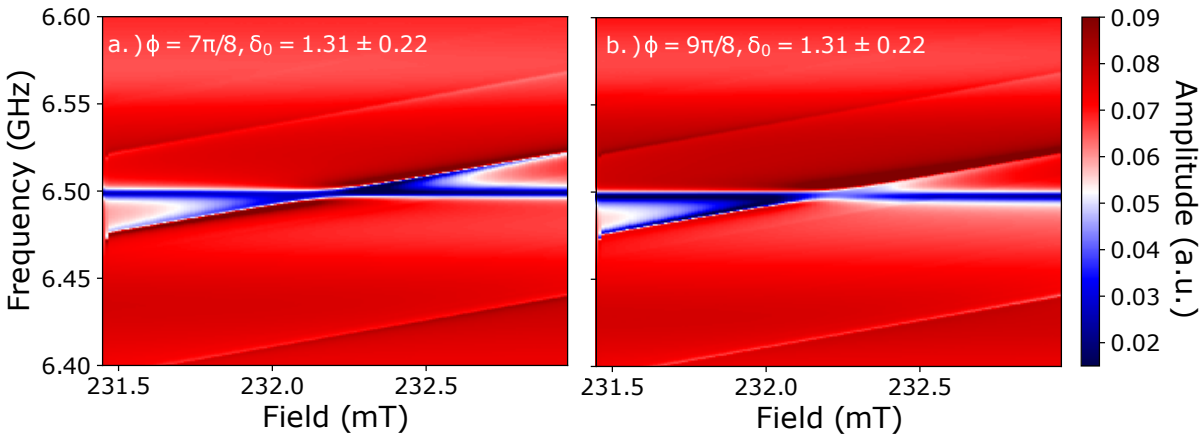

Figure 5.30: Unprocessed spectroscopic amplitude data for $\delta = 1.31 \pm 0.22$ for $\phi = \pi \pm \pi/8$. If the phase difference from π is increased the asymmetry increases. The branch exhibits a higher intensity which depends on whether the phase is detuned in the positive or negative direction.

[99]. Due to the presence of the second AC magnetic field being generated by the magnon port, an additional torque is exerted on the precessing magnetisation. Depending on the relative phase and amplitude, this torque can compensate for the damping torque and, hence, the dissipation of the precession. The losses due to the coupling can therefore also be compensated. Instead of acting as a new dissipation channel in the presence of the coupling at resonance, the magnonic constituent of the hybrid system can rather serve as a new driving source for the cavity resonator photons [77].

In addition, aside from resulting in an enhancement of the signal's magnitude, the (at least partial) compensation of the dissipation should also have an impact on the linewidth of the CMP at resonance. The linewidth of the strongly coupled magnon photon system has been previously studied in a single tone driven CMP experiment [60]. For this work, they instead observed an increase of the FMR linewidth at the condition for resonant coupling This data is obtained through a spin pumping experiment of YIG coupled to a cavity resonator photon where the increase in linewidth is attributed to "non-resonant cavity photon-magnon coupling" [60, 61]. Therefore, the analysis of the linewidth around resonance can give further insight into or even confirm the predicted mechanism. The change in the linewidth is displayed in Figure 5.29 b.). Due to the high number of free parameters in Equation (5.7), the individual linewidths of the coupled system cannot be unambiguously determined. Since a model of two coupled oscillators can describe the hybridised system, the linewidth can also be extracted from fitting a sum of two Lorentzian functions to the data. However, in the regime of level merging the two curves overlap. Therefore, instead of a single value, the linewidth is estimated within an interval with a lower and upper bound.

Especially in the case of overlap, the linewidth cannot exceed the sum of both individual widths. Thus, the upper bound (blue) is given by the sum of the Lorentzian linewidth. The lower bound is estimated employing the Maximal function [208]. The application of the Maximal function on the linewidth returns the higher value of the two Lorentzian linewidths [209]. Since the result from fitting both curves simultaneously,

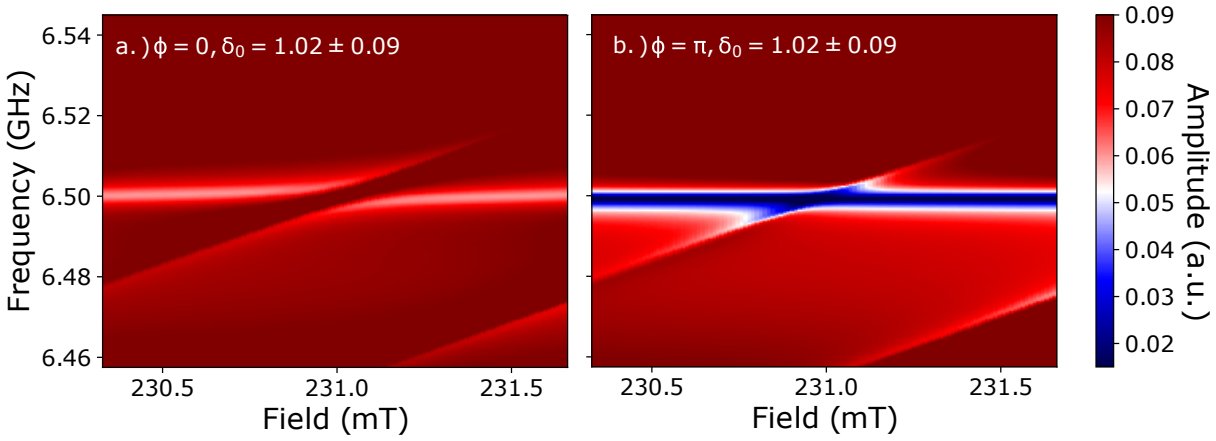

Figure 5.31: Spectrum of the magnetostatic mode which resonantly couples to the cavity resonator at $\mu_0 H_{\text{ext}} = 231\,\text{mT}$ for $\phi = 0$ (a.)) and $\phi = \pi$ (b.)) whilst δ_0 is set to $\delta_0 = 1.02 \pm 0.09$. Analogously to the observation of level merging for the Kittel mode, the frequency gap of the avoided level crossing at $\phi = 0$ decreases at $\phi = \pi$ to zero within the available resolution. On the right lower half of the figure, the dispersion of the Kittel mode is already visible.

i.e. the composite linewidth, cannot be lower than the individual linewidths, the Maximal function represents a reasonable lower bound. Moreover, all signals are recorded by means of the response at the cavity resonator's frequency and signals below the linewidth at this frequency can no longer be resolved. In order to quantify an amplitude enhancement due to level merging and not just due to the overlap of the magnon and photon dispersions, the linewidth should be below the average of the off-resonant magnon and cavity resonator linewidths. For the case of level merging, the off-resonant linewidth of the cavity resonator is determined from the loaded quality factor $Q_l = (858.11 \pm 40.63)$ to be $\kappa_r = (3.787 \pm 0.003)\,\text{MHz}$, and the linewidth of the Kittel mode magnon to be $\kappa_m \approx (1 \pm 0.5)\,\text{MHz}$. The high error in the linewidth is due to the spread of different (off-resonant) values of the magnon linewidth for different datasets. As the dotted, line graphically shows in Figure 5.29, only a few values of the average linewidth between the Maximal function and the sum are below this threshold corresponding to a value of $(2.39 \pm 0.25)\,\text{MHz}$. The mean value in the interval marked by the vertical lines, is $(2.12 \pm 0.21)\,\text{MHz}$. As a result, the linewidth is on average narrowed by $(14.28 \pm 8)\%$ due to the effect of level merging in this system.

5.13 Level merging as a collective effect: Coalescence of other magnetostatic modes (MS)

The previous discussion considered the impact on the coupling strength due to the extension of the "classical" experimental setup by introducing a relative phase and amplitude for the Kittel mode only. The Kittel mode refers to a uniform precession of the excited spins in the sample and typically has the highest coupling strength, which is advantageous for reaching the strong coupling regime. Thus, it usually represents the first choice for the study of effects related to the coupling strength between a cavity resonator photon and a magnon. However, as in the previous chapter, depending on the homogeneity of the

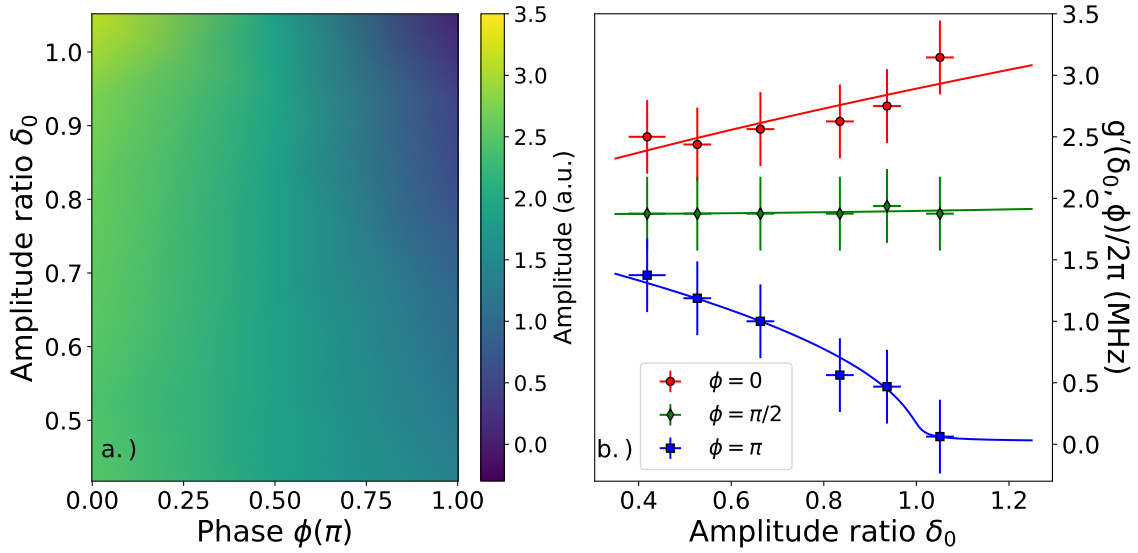

Figure 5.32: Dependence of the higher order MS mode at $\mu_0 H_{\text{ext}} = 231\,\text{mT}$ on the relative phase and amplitude, and showing the transition from level repulsion to the regime of level merging for this mode. a.) Colour coded dependence of the coupling strength on the relative phase (x-axis) and amplitude (y-axis). b.) Analogous plot to Figure 5.26, but only in the region between $\delta_0 = 0.43 \pm 0.04$ to $\delta_0 = 1.02 \pm 0.09$, where one can observe said transition. Again, the solid line represents fits to the experimental data. The error bars for the y-axis represent the uncertainty in the peak detection algorithm. Furthermore, the error bars for δ_0 are from the fit result of Figure 5.28. This is the analysis for a higher order magnetostatic mode from the same dataset, and the signal amplitudes much lower, hence increasing the error. The values for the real part of the coupling strength evolve similarly to the Kittel mode, but the net change is lower.

magnetic field throughout the sample and its size, higher order magnetostatic modes are also excited. The observation of additional couplings at different resonant coupling field raises the question of whether the effect of level merging is restricted to a single mode or is simultaneously applied to all other higher order magnetostatic modes as well.

Therefore, such modes are visible in several of the shown spectra as field dependent lines above and below the cavity resonator's resonance frequency (c.f. Figure 5.19, for instance). In Figure 5.31 the spectra for $\phi = 0$ (a.)) and $\phi = \pi$ (b.)) for $\delta_0 = 1.02 \pm 0.09$ are displayed. The former avoided level crossing spectrum transforms into one exhibiting level merging when the relative phase is shifted by π as has been discussed previously for the Kittel mode. This observation demonstrates that the control over the coupling strength provided by a relative phase shift and amplitude ratio is not restricted to a specific mode, but level attraction also occurs for higher order magnetostatic modes. However, in order to qualitatively quantify the behaviour of higher order magnetostatic modes when the relative phase and amplitude are altered, the mode at $\mu_0 H_{\text{ext}} = 231\,\text{mT}$ has been also examined. Please note that, due to the single band nature of cavity based spectroscopic experiments, the exact mode numbers (n, m, r) cannot be determined here. Hence, that is the same situation as in the previous chapter on the temperature dependent properties of a "classical" CMP. In a similar fashion to Figure 5.26a.) and Figure 5.28, this mode is analysed for three different phases ($\phi \in (0, \pi/2, \pi)$) but over a smaller interval of δ_0,

namely $\delta_0 = 0.43 \pm 0.04 - 1.02 \pm 0.09$, as this interval for δ_0 marks the transition from level repulsion to level merging. The dependence of the coupling strength on the relative phase and amplitude for this specific mode is displayed in Figure 5.32 a.) as a colour scale. In order to better compare the change from level repulsion to attraction with the corresponding data of the Kittel mode, the values of the coupling strength are also shown in Figure 5.32 b.). As before the coupling strength increases for $\phi = 0$ for higher δ_0 and decreases to zero for $\phi = \pi$ and $\delta_0 \geq 1$. Although the functional behaviour of the coupling strength is qualitatively the same, small differences remain. In general, the gradient of the curves is lower which is attributed to the lower value for $g_{\text{eff}}(\delta_0 \to 0, \phi)$ in Equation (5.8) which serves as a proportionality factor. The coupling strength is lower because fewer spins are found in this higher order magnetostatic mode than in the Kittel mode (c.f. Chapter 4).

In conclusion, this shows that the functional response of the coupling strength via changes in the relative phase and amplitude applies simultaneously to all modes which hybridise with the cavity photons at their respective resonance fields. This result confirms that the control of the coupling is applied to all modes as the relative phase shift between the AC magnetic fields which excite the magnons in the magnetic sphere are applied "globally" over the entire sample. Nevertheless, as a direct consequence, this not only allows one to suppress the coherent exchange of information for the Kittel mode, where there may still be information exchange through other modes but for the whole hybridised system.

5.14 YIG spheres of different size

The experimental data presented in the previous section is recorded with a YIG sphere of 0.2 mm diameter, which is sufficiently strongly coupled for the spectroscopic measurements but the oscillation time ($t \propto 1/4\pi g_{\text{eff}}$) is too short for time-resolved measurements. The interaction after one excitation pulse to the cavity will decay before other operations can be performed. Thus, bigger samples would enhance the coupling strength since $g_{\text{eff}} \propto \sqrt{N} \propto V_{\text{sample}}$. However, by increasing the sample size, possible inhomogeneities in the magnetic field strength across the sample can result in the excitation of additional magnetostatic modes. If their resonance frequency, and so the value of the externally applied magnetic DC field, is close to that of the Kittel mode, the coupling to each mode will be influenced by the presence of the others (c.f. Chapter 4). In addition, since the number of available spins is also increased, the parasitic avoided level crossings will exhibit a larger gap as the number of spins in these modes is altered. The first experimental data has been taken with a YIG sphere of 0.5 mm or 1 mm diameter. Although the coupling strength of the Kittel mode is enhanced, the resulting dispersion spectra are not "clean" in the sense that the Kittel mode's avoided level crossing intersects with other avoided level crossings. This intersection is shown in Figure 5.33 by the dotted lines which serve as a guide for the eye in this spectrum. Regarding the internal relative amplitude ratio, the small number of data points for different phases and the distorted avoided level crossing of the Kittel mode with the resonator made an estimate of δ_0 impossible for this dataset. However, given the previous analysis, δ_0 should be below one, because the avoided level crossings from higher order magnetostatic modes close whilst the gap for the Kittel mode yet does not close completely. Hence, in principle, this new two-tone setup to introduce dynamic control over the coupling strength can be utilised for different samples. However, this setup is restricted to the ratio of the homogeneity of the AC magnetic field at the

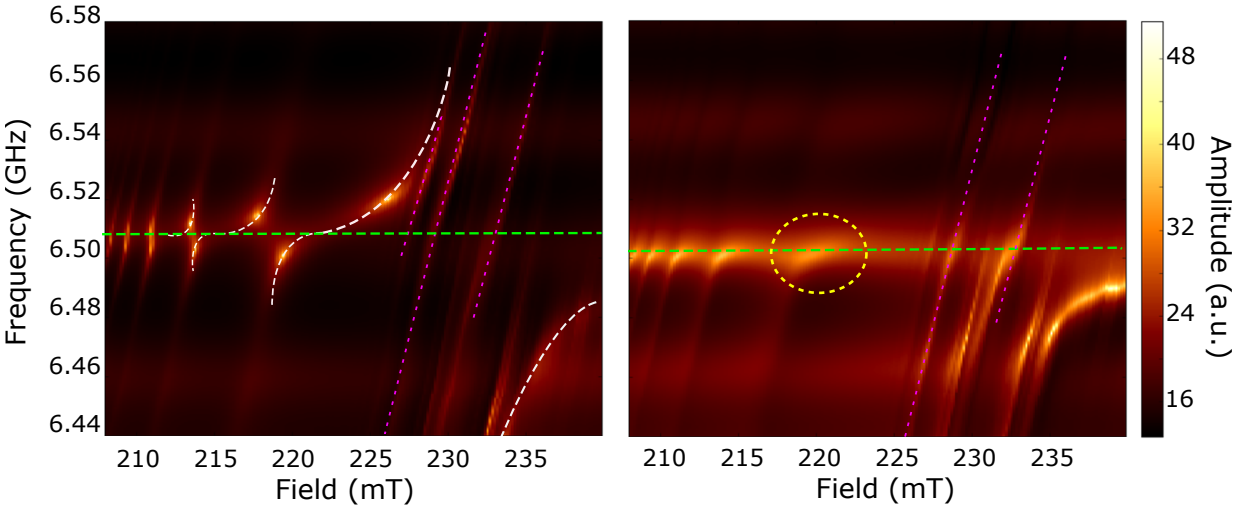

Figure 5.33: Example for the transition of a CMP with a YIG sphere of 1mm diameter between an avoided level crossing to level merging. a.) Several avoided level crossings at a relative phase of $\phi = 0$. Since there are multiple avoided level crossings, the dotted lines have been added as a guide for the eye. The green line refers to the field independent dispersion of the cavity resonator, the white from the right to the left to the Kittel modes avoided level crossing and two weaker coupled ones, and the magenta line indicates the dispersion from other magnetostatic modes which intersect the avoided level crossing from the Kittel mode. b.) The avoided level crossings partially collapsed (c.f. Section 5.13) in the former signal region of the avoided level crossing as exemplarily shown for the encircled mode. Presumably, the value for δ_0 is too low for full coalescence, i.e. reaching level merging for the Kittel mode's avoided level crossing. Although the gap closes as the resonance signal is attracted towards the cavity resonance frequency but still has the typical shape of an avoided level crossing, especially for the lower, symmetric branch. The phase shift

sample's position and across the sample volume.

5.15 Summary

In summary, a completely externally tunable, first experimental realisation of control over the coupling strength of a cavity photon magnon-polariton in a three-dimensional system has been demonstrated in this chapter. Following a theoretical proposal from Grigoryan *et al.*, the reentrant cavity resonator from the previous temperature-dependent study on the CMP has been modified [77]. Apart from the previous inductive coupling loop to excite the cavity resonator photons, called the cavity port, a second input port has been added. This second port, called the magnon port, is shifted in phase and amplitude with respect to the cavity port. However, the second AC magnetic field from the second input only directly couples to the magnons in the magnetic sample, delivering an additional AC magnetic field that acts on the precessing spins. Hence, the only interaction with the cavity photons occurs indirectly via the coupling of the magnons to the cavity photons at resonance. It is of major importance that a direct excitation of the cavity resonator photons, called crosstalk, should be suppressed as much as possible. The presence of strong crosstalk would result in interference effects that obscure the observation

of level merging. The *relative* phase is denoted by ϕ and amplitude ratio by $\delta_0 = \frac{|h_{\mathrm{AC}}^{\mathrm{magnon}}|}{|h_{\mathrm{AC}}^{\mathrm{cavity}}|}$. These are the quantities used to control the new expression for the coupling strength $g'(\delta_0, \phi) = g_{\mathrm{eff}}(\delta_0 = 0)\sqrt{1 + \delta_0 e^{i\phi}}$.

One signature of a "typical" CMP in a one-tone driven system is the formation of an avoided level crossing. At resonance, the coupled system exhibits two solutions with frequencies $\omega_{1,2} = \omega_0 \pm g_{\mathrm{eff}}$. Since, the coupling strength is typically a real, positive valued quantity, this results in the opening of a frequency gap $\Delta\omega_{1,2} = 2g_{\mathrm{eff}}$. This behaviour is also called level repulsion. Hence, if the squared coupling strength changes its sign or the coupling strength becomes a complex quantity, the shape of the CMP spectra can change dramatically. Thus, in order to analytically model the experimental data, a modified expression for the reflection scattering parameter $S_{11}(\omega)$ from the previous one-tone driven CMPs needed first to be derived from Input-Output theory. The dependence on the relative phase and amplitude for the coupling strength can be found to be $g'(\delta_0, \phi) \propto \sqrt{1 + \delta_0 e^{i\phi}}$. This relation shows that, under certain combinations of δ_0 and ϕ, the term under the square root changes such that the coupling strength indeed is a complex quantity. Then, the experimental data can be analysed in view of the dependence of this new coupling strength in both the relative amplitude ratio δ_0 and relative phase ϕ as discussed in Section 5.10.3 and Section 5.11. In line with analytical calculations it has been found that, for $\phi = \pi$, $\delta_0 = 1$, the above changes in the coupling strength transform the interaction between the cavity photons and the magnons in the magnetic sample such that instead of an avoided level crossing an attraction of the levels, i.e. for certain combinations of ϕ and δ_0 level merging is observed. In addition, the coupling strength can be enhanced or suppressed when the value of the relative phase is varied. However, level merging occurs only for $\phi = 0$ *and* $\delta_0 \geq 1$, where, experimentally, the onset of level merging was observed for $\delta_0 = 1.02 \pm 0.09$ with the minimal observed gap of (0.37 ± 0.3) MHz. Furthermore, an enhancement of 30 dBm of the signal's amplitude, along with a decrease in the linewidth of $14.28 \pm 8\%$ in the region of level merging has been shown. In this regime, not only has been the coupling strength of the Kittel mode manipulated, but all higher order magnetostatic modes which may also be excited, were too. Such control over all observable couplings shows that externally tuning the coupling strength by employing this two-tone driven system can be collectively applied to the whole system. To this end, the coherent exchange of information can now be controlled and intentionally enhanced or completely switched off.

Chapter 6

Conclusion and Outlook

6.1 Conclusion

Cavity magnon-polariton spectroscopy refers to the investigation of the characteristics of cavity magnon-polaritons (CMPs) which are the associated quasiparticles of hybridised cavity photon-magnon states. The hybridised state originates from the resonant coupling between magnons and photons in the strong coupling regime, where the macroscopic coupling strength g_{eff} exceeds both the individual dissipation from the magnons (κ_m) and the cavity resonator (κ_r), i.e. $g_{\text{eff}} \gg \kappa_m, \kappa_r$. The coupling strength denotes a measure of the coherent exchange of information between the coupled constituents. Hence, understanding and controlling this quantity is of central interest in the prospect of using CMPs in information processing technologies. The signature of a CMP from such hybridisation is the observation of an avoided level crossing in the dispersion spectrum which refers to the dependence of the system's frequency to an external sweep parameter. At resonance, the coupled cavity photon-magnon state exhibits two normal modes with frequencies $\omega_{1,2} = \omega_0 \pm g_{\text{eff}}$, where ω_0 denotes the resonance frequency of the uncoupled system where the dispersions of magnon and cavity resonator photon would cross in the absence of coupling.

The experimental realisation of cavity magnon-polariton spectroscopy both at millikelvin temperatures ($T \simeq 10\,\text{mK}$) and room temperature ($T \simeq 300\,\text{K}$) opened new avenues [54, 56, 58]. The millikelvin temperatures can be associated with the quantum regime and the classical regime can be associated with room temperature. These experiments resulted in the emergence of the field of quantum magnonics and cavity spintronics, respectively [27, 28, 55, 61]. In the field of quantum magnonics, a new hybrid quantum circuit (HQC) between a qubit and a magnon placed in the same resonator, with a coupling between them mediated by the cavity resonator photon could be successfully realised [27]. Therefore, the resonator serves as a data bus between the fast processing (qubit) and the storage (magnon, i.e. macroscopic spin ensemble) unit. Hence, the above experiments represent a crucial step towards the realisation of quantum computers based on HQCs [46, 210]. On the other end of the temperature scale investigated in this thesis, i.e. at room temperature, the utilisation of hybridised cavity photon-magnon states in the field of cavity spintronics, links concepts from circuit quantum electrodynamics (CQED) to applications in information processing. In spintronics, alongside the electronic charge, the usage of the electronic spin serves as an additional degree of freedom by which information can be carried and processed, has the potential to supersede conventional electronics with

spin-based devices [16, 24, 187]. For instance, such spin-based devices could allow one to process data faster and store data in a non-volatile manner [24, 187].

However, at this point, despite this recent progress, the nature of the cavity photon-magnon coupling and the associated coupling strength requires further investigations. There are two distinct, separated temperature regimes which need to be further studied. Although they exhibit similar dispersion spectra, the origin of the strong coupling turns out to be different [27, 60, 61]. At room temperature, the observation of strong coupling with features such as "classical Rabi-like oscillations" originates from a classical coherence instead of quantum coherence. As explained in Ref. [60] and [61], it originates from a phase correlation of macroscopic electromagnetic fields from classical electrodynamics described by Maxwell's equations.
Thus, in order to further understand the behaviour of the coupling strength in the transition from the quantum regime at millikelvin temperatures to room temperature, it is necessary to connect the temperature regimes and study the coupling strength over the entire temperature range. In addition, the realisation of strong coupling resulting in a CMP only represents the first steps towards full control over this kind of system. Despite the characterisation of the coupling strength, it is key to develop new experimental methods which allow for the manipulation of the coupling such that it can be deliberately switched on and off.

In the course of this doctoral thesis, an experimental apparatus for temperature dependent magnon-polariton spectroscopy across a temperature range of 2 K to 290 K has been set up at the Johannes Gutenberg-University Mainz (JGU). As a result, in collaboration with co-workers from the Karlsruhe Institute of Technology (KIT) providing the data at 30 mK, the temperature dependence of the cooperativity $C = \frac{g_{\text{eff}}^2}{\kappa_m \kappa_r}$, i.e. the coupling strength and the magnon linewidth of a CMP, could be studied from 30 mK to 290 K in the course of this thesis [67]. The results of this experiment have been presented in Chapter 4. This temperature dependent study not only connects two formerly distinct temperature regimes but also represents a detailed characterisation of the specific system comprised of a purposefully designed three-dimensional reentrant cavity resonator with a field enhancement ([159]) at the position of a Yttrium-Iron-Garnet (YIG) sphere for future experiments. The knowledge about the key properties of the system and components allows for an extension of the current setup towards the realisation of control over the coupling strength. As recently theorised in Ref. [77], the gap of the avoided crossing, i.e. the coupling strength, can be tuned by the introduction of a second microwave feed line. The second drive is shifted in phase and amplitude relative to the first and only couples to the magnons of the hybrid system. Thus, the coupling strength is completely and externally controllable by tuning the relative phase ϕ and amplitude $\delta_0 = \frac{|h_{x,AC}^{\text{magnon}}|}{|h_{AC}^{\text{cavity}}|}$ between both inputs, where $|h_{x,AC}^{\text{magnon}}|$ and $|h_{AC}^{\text{cavity}}|$ correspond to the internal alternating current (AC) magnetic field amplitudes of the magnon and the cavity inputs.

Hence, the first experimental chapter of this doctoral thesis presents the temperature dependent study of the coupling strength between a Kittel mode magnon and a cavity resonator photon. To this end, it has been found that the temperature dependence of the coupling strength has to be divided into one temperature regime for $T > 100$ K and a second for $T \leq 100$ K. From room temperature to $T = 100$ K, the changes of the coupling

strength are governed by the temperature dependent increase of the saturation magnetisation according to Bloch's $T^{3/2}$ law. However, for $10\,\mathrm{K} < T < 100\,\mathrm{K}$, the coupling strength deviates from Bloch's law and decreases due to the presence of a simultaneous coupling to higher order magnetostatic modes. Around $T \sim 40 - 50\,\mathrm{K}$, the probability for such parasitic coupling is maximal and the decrease most prominent. For lower temperatures, it increases to a plateau value in the millikelvin temperature regime. Additional examination of the Kittel mode magnon linewidth showed that it corresponds to the linewidth of the uncoupled system. Despite small contributions from the surface roughness of the sample, the presence of rare earth impurities governs the temperature dependence of the linewidth. At particular temperatures ($T = 43\,\mathrm{K}$ and $T = 90\,\mathrm{K}$), the crystal field splitting of the two lowest energy levels of the impurities coincides with the CMP's resonance frequency. Thus, the scattering from these impurities is enhanced and leads to peaks in the linewidth. These peaks in the linewidth can differ in width and amplitude depending on the specific impurity contributing at a given temperature.

In order to improve the experimental data, it is desirable to strongly suppress parasitic coupling to other modes as much as possible. Thus, excitation fields which are as homogeneous as possible should preferably be employed and the highest possible purity and polishing for the sample utilised. However, most importantly, along with studying $\kappa_r(t)$ of the cavity resonator, the cooperativity should be examined. It is a dimensionless quantity yielding a measure of the coherent information exchange in the presence of losses. It can be shown that, for the entire temperature range, $C > 20$ which means that the coherent information exchange and the strong coupling regime, i.e. the existence of CMPs prevails from 30 mK to 290 K.

After having shown the persistence and robustness of the coherent information exchange over a broad temperature range, it is possible to think about methods to deliberately manipulate the system such as turning on or off the flow of information. A control of the coupling strength such that for full "transmission" of information the gap of the avoided crossing is maximised or minimised represents one possible solution. As mentioned previously, the manipulation of the gap of the avoided crossing would correspond to tuning the coupling strength. Then, a complete collapse of the anticrossing can occur, called level merging. Such control over the coupling strength of a CMP in a three-dimensional system has been realised in the course of this doctoral thesis in the second experimental chapter (c.f. Chapter 5). Please note that, for the experiment on level merging the same reentrant cavity resonator was utilised but a smaller YIG sphere with a diameter of $d = 0.2\,\mathrm{mm}$ has been used. That decrease in the sample size allowed for the suppression of parasitic higher order magnetostatic modes close to the Kittel mode's resonance frequency which are also strongly coupled.

As mentioned previously, the coupling strength is controlled by tuning the relative phase ϕ and amplitude ratio δ_0 between two intracavity AC magnetic fields induced by two microwave inputs, where the second one couples only to the magnons. The only interaction between the new input field with the one from the cavity photons occurs indirectly via the coupling of the magnons and the cavity photons at resonance. It is of prime importance that a direct excitation of the cavity resonator photons, called crosstalk, is suppressed as much as possible. Otherwise, the presence of large crosstalk would result in interference effects instead of the observation of level merging. The additional input

exerts an additional torque on the magnetisation and, depending on its orientation, that torque can enhance or compensate the dissipation of the system, including the coupling of the photons of the magnons. The anticrossing is enhanced for $\phi = 0$, and all δ_0 but collapses for $\phi = \pi$ and $\delta_0 \geq 1$, where the latter results in the regime of level merging. However, for single-tone driven CMPs, the coupling strength is typically a real, positive valued quantity, which results in the opening of a frequency gap of $\Delta\omega_{1,2} = 2g_{\text{eff}}$. Hence, if the coupling strength becomes a complex quantity, the shape of the CMP spectra can change dramatically. For the work performed in this thesis, the introduction of the two-tone driven system results in a complex-valued coupling strength. From Input-Output theory, the dependence of the complex valued coupling strength on the relative phase and amplitude can be found to be $g'(\delta_0, \phi) = g_{\text{eff}}\sqrt{1 + \delta_0 e^{i\phi}}$, where g_{eff} corresponds now to the "single-tone" coupling strength, i.e. the coupling strength in the limit for $\delta_0 \to 0$. At resonance, the coupling between the cavity photons and the magnons can be considered as an additional dissipation channel. For $\phi = \pi$ and $\delta_0 = 1$, the additional torque is oriented such that it compensates the losses of the system. Therefore, a strong enhancement of the signal's amplitude can be expected, which is accompanied by a decrease of the linewidth of the signal at resonance due to the onset of the regime of level merging. Such a decrease will then be in contrast to previous works employing a single-tone driven CMP, where, instead, an increase of the linewidth around and maximum at resonance has been reported by Bai *et al.* [60].
Indeed, in the experiment on level merging, an enhancement of the signal's amplitude of 30 dB, and a decrease in the linewidth of $14.28 \pm 8\%$ for $\phi = \pi$ and $\delta_0 \sim 1$ which represents the onset of level merging can be shown. Furthermore, level merging is simultaneously observed for the Kittel mode and higher order magnetostatic modes which are still present in the smaller sphere. Thus, the coupling strength of all observable couplings of magnon modes in the magnetic sample can be controlled simultaneously. This control shows that externally tuning the coupling strength through this two-tone driven system can be collectively applied to the whole system. To this end, the coherent exchange of information can be now controlled and enhanced or completely switched off at will.

In summary, by first establishing an experimental apparatus for magnon polariton spectroscopy, the full system could be characterised and the two distinct temperature regimes from previous works connected. Then, the system can be extended in order to obtain a fully tunable, experimental control over the coupling strength of the CMP at room temperature. Such a two-tone driven system could be further applied to different systems which also employ the (strong) coupling between different types of samples and a cavity resonator photon leading to other polaritons, because the control of the coupling strength is completely externally. In addition, the control of the coupling strength could be extended to a two-dimensional waveguide resonator and a YIG film instead of the three-dimensional system employed in this thesis [189]. However, these measurements serve only as a proof of principle. The control of the coupling strength with two-dimensional systems or even with magnetic samples other than YIG requires further measurements and analysis beyond the scope of this work. In addition, such a two-tone driven experimental setup employing the same cavity resonator but a larger YIG sphere and a microstrip line in place of the second inductive loop of the second port has recently been used from Tim Wolz at KIT to perform time-resolved studies on the CMP. Specifically, the aim is to examine the influence of ϕ_0 and δ_0 on the coupling mechanism as a function of time at the KIT. The addition of time-resolved studies on CMPs allows one to study the onset

and related limits of spin-photon interactions directly. In turn, the time-resolved control could later be used for precisely timed operations in information and data processing on that regime turning on or off the coupling. Despite such extensions which continue to employ a similar system comprised of a three-dimensional reentrant cavity resonator and a YIG sphere, the field of cavity spintronics is currently moving in many other directions which will be detailed out in the following.

6.2 Outlook

The field of cavity spintronics is a recent and quickly growing field of active research. As such, it has started to develop branches and establishing new connections to other areas of physics. The usage of cavities in the optical or microwave frequency range as employed in this thesis enhances the interaction of the magnons with electromagnetic radiation which can enable the observation of magneto-optical effects. For example, in the field of cavity optomagnonics, the coherent coupling of light to magnons in the uniform or other higher order magnetostatic modes is actively discussed. Specifically, the interaction between whispering gallery mode cavities and magnons is investigated both theoretically such as in Refs. [211, 212] and experimentally such as in Refs. [213, 214]. Furthermore, in cavity magnomechanics, the phonon-magnon interaction utilising ferrimagnetic spheres is studied [215]. Another direction is to use similar systems as discussed in this thesis but with antiferromagnetic samples, serving as the magnonic component in the coupling, where only a few other works exist to the moment [216, 217]. As will be shown later on, the study of such CMPs also is a perspective for further measurements with the experimental apparatus used for the findings discussed in this work. Despite the above branches, further development of utilising a cavity resonator such as the ones utilised in this doctoral thesis which can mediate a coherent information exchange between samples in the cavity resonator is ongoing work. This includes qubit-magnon coupling, i.e. linking cavity spintronics to quantum magnonics [27, 69] and related applications, or the distant manipulation of spin currents mediated by cavity resonator photons [71]. In this regard, the long-distance transport and, hence, manipulation of spin currents is also of central interest in spintronics. Due to their sensitivity to and tunability by external magnetic fields, ferromagnetic materials are currently the preferred employed components for spintronic applications [218, 219, 220]. However, ferromagnetic resonance is limited to the GHz frequency regime constraining the development of ultrafast data processing devices by utilising ferromagnetic materials [219]. The replacement of ferromagnets with antiferromagnets, which typically exhibit resonance frequencies in the high GHz and THz frequency regime, would be advantageous [218]. Furthermore, their insensitivity to external magnetic fields, the absence of strays fields and recent experimental observation of long-distance spin transport in antiferromagnets makes them a promising candidate to overcome the limitations of ferromagnetic based devices [219, 221]. However, at the same time, these advantages aggravate the study and manipulation of antiferromagnets. For additional information on various works in antiferromagnetic spintronics, the reader may refer to Ref. [218, 219] and the references therein. Despite the recent progress, the necessity for the development of new experimental methods is still one of the open questions to truly utilise antiferromagnets for spintronic applications [219].

In the above context, hybrid systems employing CMPs in the field of cavity spintronics could represent a promising candidate. However, this calls for the development of cavity resonators which resonate at much higher resonance frequencies and coupling them with antiferromagnetic magnons. It could open an avenue to obtain further insight into spin-photon interactions. For instance, utilising the previously presented two-tone driven ferromagnetic magnon polariton experiment could allow one to study and manipulate the phase correlation between antiferromagnetic magnons and photons. Currently, for cavity spintronics, mostly the ferrimagnetic insulator YIG is utilised. Its excellent magnetic properties such as the lowest known Gilbert damping and high spin net density render YIG a well-suited candidate not only for magnonics, but also for reaching the strong coupling regime for cavity spintronics [24, 100, 222]. Furthermore, the demonstration of the long distant manipulation of spin currents of two ferromagnets mediated by a cavity, allows one to enhance the long-distance transport of magnons for spintronic applications through cavity spintronics [71]. In the transition from ferromagnets to antiferromagnets, it has been theoretically shown that strong spin-photon coupling with an antiferromagnet is possible and, just as a ferromagnet, scales as $g_{\text{eff}} \propto \sqrt{N}$, where N is the total number of available spins [223]. For instance, one could replace one of the ferromagnets in the system shown in Ref. [71] with an antiferromagnet or use synthetic antiferromagnets for magnonics as proposed in Ref. [222] to integrate antiferromagnets within an existing ferromagnetic system. Nevertheless, as a first step, strong cavity photon-magnon coupling between a high-frequency cavity resonator and an antiferromagnet needs to be experimentally demonstrated. However, at this moment, resonators for THz frequencies are mostly all optical or are too small to use larger samples which come with a higher number of available spins (e.g. [224] and the references therein). Thus, an antiferromagnetic sample with a resonance frequency in the order of several tens of GHz would represent an excellent first choice. For instance, one might use the antiferromagnetic insulator hematite (α-Fe_2O_3) which shows a weak ferromagnetic phase and, at certain temperatures, can be tuned to exhibit a resonance frequency on the order of 30 GHz [225]. In addition, long-distance spin propagation in a single crystal of this material has recently been observed [221], making hematite a promising candidate for spintronic applications. Thus, it may be sufficient to design a corresponding cavity resonator which resonates around 30 GHz.

Towards the end of this thesis, the design of such a resonator has been realised. Utilising the simulation software CST, the new cavity resonator is designed such that it would (i) still enable DC experiments on the antiferromagnetic sample under investigation by openings at the sides and (ii) resonates at $\omega_r/2\pi = 33.07$ GHz. Such resonance frequency would allow a resonant coupling to the respective antiferromagnet such as hematite. The result from the simulation is shown for the electric and magnetic field distribution in Figure 6.1 a.) and b.), respectively. As a first approach, a small rectangular cavity resonator is chosen and the resonance was measured by M. Kewenig from the Technische Universität Kaiserslautern. As illustrated in Figure 6.1 c.) it could be shown that that new cavity resonator exhibits a resonance $\omega_r/2\pi = 32.314$ GHz which is in agreement with the simulations. The dimensions of this resonator are shown in Figure 6.1 d.). In order to minimise distortions of the small resonating space of the resonator by the coupling loop, it is designed for reflection measurements and exhibits a single port. In addition, in contrast to the reentrant resonator, the microwave signal is coupled capacitively to the resonator. Due to the small cavity resonator's mode volume, these changes in the resonator geometry are important. The next step would be to insert a single crystal

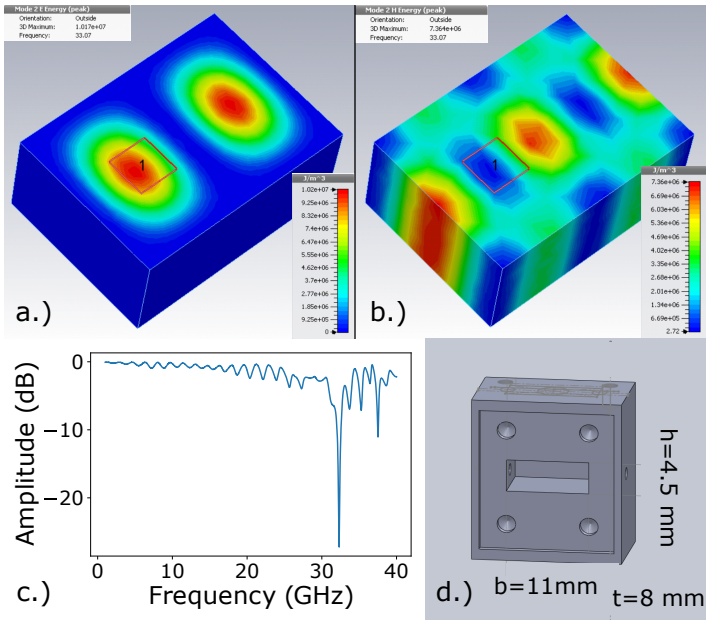

Figure 6.1: Overview of the result from the simulations, design and the measurement of the resonance frequency for a high-frequency cavity resonator. a.) Electric and b.) magnetic field distribution of the chosen resonator mode at a simulated resonance frequency of $\omega_r/2\pi = 33.07\,\text{GHz}$. c.) Reflection measurement of the cavity resonator at room temperature. The resonance frequency is at $\omega_r/2\pi = 32.314\,\text{GHz}$ with a signal amplitude of more than 20 dB and in line with the simulations. Measurement courtesy of M. Kewenig. d.) Sketch of the technical drawing for the construction of the cavity. As for the reentrant cavity resonator, the lid (not shown such that the inner part is seen) serves to close the resonator's volume. The correct alignment of the lid is supported by the outer lip which fixes it along the xy-plane.

hematite sample into the cavity and perform the first spectroscopic measurements on this system in an external magnetic field starting from room temperature for the first tests and characterisations. However, due to the small net magnetic moment of the antiferromagnet and the low number of spins, it is not clear whether a clear anticrossing could be observed. Instead, presumably, a weakly coupled system where some changes may be seen in the phase representation of the reflection signal will be one of the first observations. Currently, this is ongoing work.

Given the new experimental scheme using two microwave inputs with a relative phase and amplitude (c.f. Chapter 5), the work presented in this thesis yields another perspective for further measurements. Towards the implementations of hybrid quantum circuits for realising quantum computation [46], a coupling between a qubit and a magnon which is mediated by a cavity resonator has already been demonstrated [27]. However, in this experiment, the coupling strength refers to a fixed parameter determined from the cavity resonator geometry and the choice of the magnetic sample. In the course of the temperature dependent study from Chapter 4, I showed with my co-workers, that the coherent exchange of information exists across the entire temperature range from 30 mK to 290 K, since $C > 1$ for all temperatures. Therefore, as a next step, one could extend the two-tone driven CMP to the millikelvin temperature regime where one could then examine the regime of level merging in the single photon regime. Such a study would allow one to

study the coupling on a microscopic scale instead of the macroscopic one at room temperature. As a second step, in a similar manner to Ref. [27], the addition of a qubit to the cavity photon-magnon system could open an avenue to control the qubit-magnon interaction at will. To this end, the control over the coupling strength could also be utilised for the study of (quantum) entanglement between magnons and (cavity) photons for both ferro- or antiferromagnetic CMPs. For the latter, such entanglement has been recently theorised in Ref. [226].

Finally, the study of central characteristics of a CMP such as the coupling strength as a function of temperature to connect the classical with the quantum regime and the development of a new experimental method to control the spin-photon coupling contributes to understanding the nature of the CMP and opens new directions for cavity spintronics. Specifically, the control over the coupling strength opens a new route towards a deliberate control of various systems. As discussed, one could extend the current concepts of cavity spintronics to antiferromagnetic cavity spintronics or implement tunable qubit-cavity photon-magnon systems for the realisation of hybrid quantum circuits by such two-tone driven cavity magnon-polariton spectroscopy.

Chapter 7

Acknowledgements

The realisation the described experimental work on cavity magnon polariton spectroscopy and writing this document would not have been possible without the contribution of numerous people.

First of all, I want to thank my supervisors for giving me the opportunity to enter the exciting field of magnetism and spintronics in general and cavity spintronics in particular. In this regard, I want to thank them for their help and support which was always available when I needed it. I highly appreciate their trust in giving me the freedom to work on my own, develop myself, gain more and more knowledge in the course of my thesis and being able to contribute to this project with my own ideas. Further, I am thankful for the possibility of presenting my work at national and international workshops or conferences, meeting other people working on the same or related topics and learning more about their work. However, the work in the laboratory is not the same without my colleagues who became friends. Jokes of all kind, coffee breaks and our regular "socialising" events cheered me up when the experiment was (again) not working and helped me a lot in keeping the motivation to try and try again until it works. They were also a source of help and advice due to their experience in slightly different topics from mine giving ideas from another perspective. I enjoyed the sometimes heated discussions, gossiping, goofing around about almost everything with where some thought they need to teach me sarcasm. They state they did progress, but I should note sometimes they did not understand my dry irony and took some things at face value which I found then funny. I also thank my french friend for discussions on my work on level merging and for his crowded, chaotic desk making me feel better when I looked at mine. I also want to deeply thank him for arranging the contact with his french colleagues where I can continue research in magnonics and (re)learn French. I want to thank my whisky loving friend for having the patience to read the entire thesis, correcting and polishing my sometimes germanised english writing and starting to enjoy good whiskey after our whiskey tastings. I will remember a lot of great, and sometimes really drunk evenings.
An experimental work is not possible without the technical staff of our group and mechanical workshop which brings the designs one it thinking of into reality. Hence, here, I want to thank our main technician for his immense help, patience, explanations sharing his experience and laughter regarding any problem I had with the cryostat or the probe station. I also want to thank the "grey eminence" for our software, accounts, the secretary staff for their administrative support and patience they answer questions which are presumably asked over and over again. Last but not least I thank the mechanical workshop and the

entire team there for their support and unbureaucratic help when something needed to be quickly fixed.

I want to gratefully acknowledge my collaborators I had the chance to work within the course of my joint work located at the JGU and the KIT for conducting experiments and discussions. Specifically, I want to thank them for the fruitful work in respectively strongly contributing to the development of the reentrant cavity resonator, providing for the millikelvin temperature data and discussions. Special thanks go here to a former master student, which I met as a co-supervisor of her Master thesis but we became friends in the process. She was patient when I was not, all the "girls talk" was much fun during the long measurement times, and thanks for trying delicious Chinese food in Germany. I also want to gratefully thank her for taking a lot of the experimental data again in better quality as a HIWI after she finished with her thesis.

I want to thank the university orchestra in Mainz under where the director puts so much passion into everything he does and makes us all better musicians. I learned so much, and when thinking over physics challenges my mind, music lets me dream and deeply affects my soul giving me the motivation for doing more physics. Especially, I want to thank my dear friends of our group five violins and a bugle with my desk neighbour, who understands stupid "Bönnsch" and Cologne area jokes, and the others for the great times and the opportunity to learn that musicians and other professions are as geek as physicists. I want to thank my dearest friend in Berlin for all these deep discussions about philosophical questions; she is my "sister in spirit".

I want to thank my parents for always supporting me always on my way. They contributed a lot to what I am now and to say it in ancient words: "Δεν είμαι Αθηαίος ούτε Έλλινας πολίτης, αλλά πολίτης του κόσμου (Σωκράτης, 469-399 π.Ξ., Φιλόσοφος)".
I want to thank my brother for having the ability in telling me truths, I might not want to hear in the beginning, being as stubborn as myself and opening different views on various things in the course of our discussions.

In the end, my most special thanks go to my husband, who is also my best friend. He believed in me when I lost the confidence in myself, keeps me motivated by making me smile, and shares some of his computational skills with me and most importantly is giving me most of the happiest moments I can remember and understands the emotional challenges during a PhD.
¡Todo tuanis! y al final ...
"*Por una mirada, un mundo;*
por una sonrisa, un cielo;
por un beso ...
yo no sé qué te diera por un beso"
(Gustavo Adolfo Bécquer)

In the course of this doctoral thesis the following publications based on the presented results or from collaboration with my colleagues from KIT are published or submitted to a peer-reviewed journal:

- I. Boventer, M. Pfirrmann, J. Krause, Y. Schön, M. Kläui and M. P. Weides
  "Complex temperature dependence of coupling and dissipation of cavity-magnon polaritons from milliKelvin to room temperature" [1]
  Phys. Rev. **B** 97, 184420 (2018)

- I. Boventer, C. Dörflinger, T. Wolz, R. Macêdo, R. Lebrun, M. Kläui and M. P. Weides "*Control of the Coupling Strength and Linewidth of a Cavity-Magnon Polariton*"
  arXiv:1904.00393v1 (2019)
  submitted and under review for Physical Review Letters

- M. Pfirrmann, I. Boventer, A. Schneider, T. Wolz, M. Kläui, A.V. Ustinov and M. P. Weides
  "*Magnons at low excitations: Observation of incoherent coupling to a bath of two-level-systems*"
  arXiv:1903.03981v1 (2019)
  submitted to Physical Review Letters

Publications to which I contributed with FMR measurements and FMR data analysis (c.f. A.) or code for the datanalysis of data within a large background signal such as in Chapter 4 (c.f. B.).

A. P. Krautscheid, R. M. Reeve, D. Schönke, I. Boventer, A. Conca, A. V. Chumak, B. Hillebrands, J. Ehrler, J. Osten, J. Fassbender and M. Kläui
   "*Direct observation of spin diffusion enhanced nonadiabatic spin torque effects in rare-earth-doped permalloy*"
   Phys. Rev. **B** 98,21 , 214406 (2018)

B. P. Yang, J. D. Brehm, J. Leppäkangas, L. Guo, M. Marthaler, I. Boventer, A. Stehli, T. Wolz, A. V. Ustinov and M. P. Weides
   "*Probing the Tavis-Cummings level splitting with intermediate-scale superconducting circuits*"
   arXiv:1810.00652v1 (2018)

[1] The values of the single spin coupling strength were wrongly calculated in the first version. It does not change any of the given statements and was reported to the editorial desk and in the thesis the correct values are given.

Chapter 8

Appendix

8.1 Supplementary information to Chapter 5

In this section, additional information on the analysis is given such as a remark on the determination for the relative amplitude ratio δ_0 or the threshold for the identification of the imaginary part of the coupling strength in the regime of level merging.

8.1.1 Control of the CMP's coupling with 2D resonators

The above-presented system with a cavity and magnon port to control the coupling strength employing their relative phase and amplitude represent a three-dimensional approach. However, concerning experiments with thin films and further applications, a two dimensional, waveguide resonator based approach would be more advantageous. In principle, such control is possible and it has been shown in terms of a "proof of prinicple" measurement in the course of the Master's thesis from C. Dörflinger [189]. There, experimental data for this two dimensional control is presented but for a qualitative statement this system requires further characterization, measurements and last but not least optimizations. Nevertheless, these preliminary results demonstrate the universal applicability of this two-tone system once again.

Cavity port (dB)	Magnon port (dB)	δ_{ext}	δ_0
0	20	0.1	0.042
2	20	0.125	0.052
4	20	0.158	0.066
6	20	0.199	0.083
8	20	0.251	0.105
9	20	0.282	0.118
0	10	0.316	0.132

2	10	0.398	0.166
4	10	0.501	0.209
6	10	0.631	0.263
8	10	0.794	0.331
9	10	0.891	0.372
0	0	1	0.417
2	0	1.259	0.525
4	0	1.585	0.661
6	0	1.995	0.832
7	0	2.239	0.933
8	0	2.512	1.047
9	0	2.818	1.175
10	0	3.162	1.319
12	0	3.981	1.660
14	0	5.012	2.090
16	0	6.31	2.631
19	0	8.913	3.717
20	0	10	4.17
26	0	19.953	8.320
29	0	28.134	11.753

Table 8.1: Overwiew over the experimentally set values for the combination of attenuators in the cavity and magnon port. In addition, the externally determined amplitude ration, δ_{ext} and the corresponding internal amplitude ratio δ_0 are given. The conversion factor ($\delta_0 = \zeta\delta_{ext}$) is $\bar{\zeta} = (0.417 \pm 0.07)$, and is determined from fitting of Equation (5.8).

8.1.2 Determination of δ_0

In the current setup, it is not possible to directly measure the amplitudes of the internal alternating current (AC) magnetic fields from the magnon and the cavity port, respectively. Thus, experimentally, the internal amplitude ratio of δ_0 cannot be directly determined. As previously mentioned, it is only possible to determine an external relative amplitude ratio δ_{ext} before the signal is coupled to the cavity port and magnon port, respectively. However, the internal amplitude ratio can be extracted from the external one via $\delta_0 = \zeta\delta_{\text{ext}}$ (c.f.Section 5.5.2). From fitting to $g'(\delta_0, \phi)|_{\phi=\text{const}}$ to (c.f. Figure 5.26) and $g'(\delta_0, \phi)|_{\delta_0=\text{const}}$ (c.f. Figure 5.28), values for δ_0 are also found which are compared to the previous fit result. As can be inferred from Table 8.2, the values are in the same order of magnitude and within the errorbars in accordance with each other. The value for ζ is determined to $\zeta = 0.418 \pm 0.065$. In order to minimize the error on the determination of δ_0 the geometric average including the errorbars is calculated. The result is also given in Table 8.2 and these values for δ_0 are utilized in the discussion of the results and distinction of the regimes for avoided level crossings or occurrence of level merging. Note, that in both cases, the error bars are calculated from the covariance matrix. Then, the geometric mean for the result for ζ for $\phi = 0, \pi/2, \pi$ and the error of the mean value utilising Gaussian error propagation are calculated. This procedure results in $\zeta = 0.418 \pm 0.065 \approx 0.42 \pm 0.07$. For the data with higher δ_0, the respective value and corresponding error again employing Gaussian error propagation are calculated from the relation $\delta_0 = \zeta\delta_{\text{ext}}$. Thus, only the values for δ_0 correspond to the mean of both fit results from Table 8.2 for less than 10 dB attenuation of the cavity port. Please note, that the dimensionless values for δ_0 including error bars were given without curly brackets, whereas curly brackets are used for parameters with error bars with a unit.

(a) δ_0	0.436	0.555	0.700	0.867	0.913	0.99
(b) δ_0	0.417	0.525	0.661	0.832	0.923	1.047
$\bar{\delta_0}$	0.426	0.540	0.681	0.850	0.923	1.019
δ_{ext}	1	1.259	1.585	1.995	2.239	2.512

Table 8.2: Comparison of the fitresults . (a) Values for δ_0 determined from a direct fit to $g'(\delta_0, \phi)|_{\delta_0=\text{const}}$ (b) Values for δ_0 calculated from the values for δ_{ext} and the determination of ζ from a fit to the data from $g'(\delta_0, \phi)|_{\phi=\text{const}}$

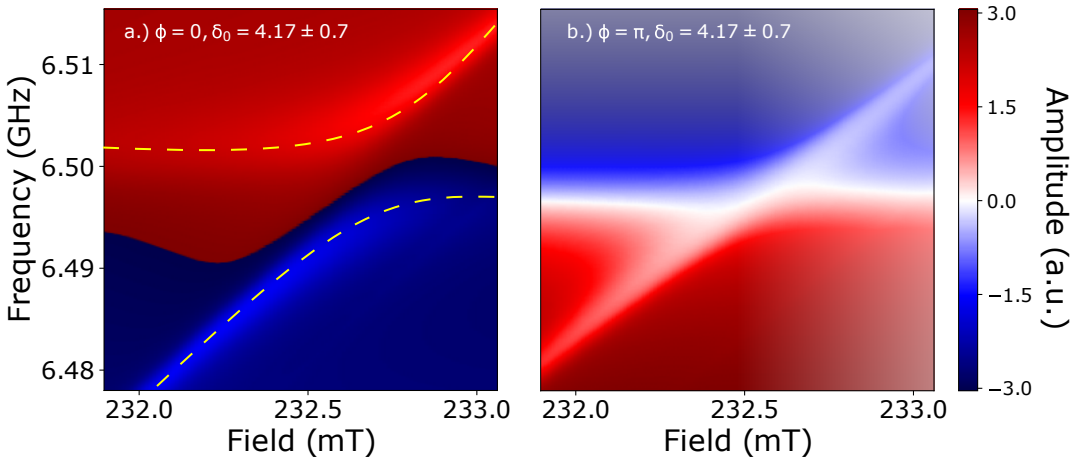

Figure 8.1: Phase spectrum for a.) $\phi = 0$ and b.) $\phi = \pi$ for $\delta_0 = 4.17 \pm 0.7$. This data is from the same dataset as the data displayed in Figure 5.24. a.) Observation of the avoided level crossing. The separation in the middle into a blue and red area is attributed to cable background oscillations. They have not been removed via a background correction, because, otherwise, the resolution of the avoided level crossing is of poor quality. The yellow lines serve as a guide to the eye only. b.) Illustration of the phase for level merging. The separation into two triangles and a region of level merging is visible. Thus, the data from Figure 5.24 corresponds to $\phi = \pi$ but includes the artifact from a transmission measurement of the crosstalk at the cavity port.

8.1.3 Identification of phase shift of π for highly attenuated signals ($\delta_0 > 4$)

In Section 5.10.1, Figure 5.24 shows that the peak search algorithm cannot be utilised for the determination of the imaginary part of the coupling strength. Towards higher values of δ_0, the relative strength of the residual contribution from direct crosstalk becomes larger because, for $\delta_0 \gg 1$, the cavity port's amplitude is further and further decreased. As a result, in the reflection measurement from the cavity port, the signal is a superposition of a transmission measurement from the crosstalk and the signal of interest. Due to the high attenuation of 29dB of the cavity port in Figure 5.24, one may argue that the phase-in Figure 5.24 b.) is not correctly set at $\phi = \pi$. Thus, the following plot compares the phase values for $\phi = 0$ (a.)) and $\phi = \pi$ (b.)) for $\delta_0 = 4.17 \pm 0.7$, where the attenuation of the cavity port is still lower.

8.1.4 Determination of the threshold

As shown in Figure 5.25, the threshold is chosen such that there are neither strong fluctuations of the identified resonance frequencies (peaks) around the resonant coupling field and sharp jumps. The latter would indicate an overestimation of the threshold.

8.1.5 Increase of threshold: Phase representation

For the determination of the imaginary part, it is necessary to increase the threshold towards higher values of δ_0. As shown in Figure 8.3 for the data for $\phi = \pi$ and two values

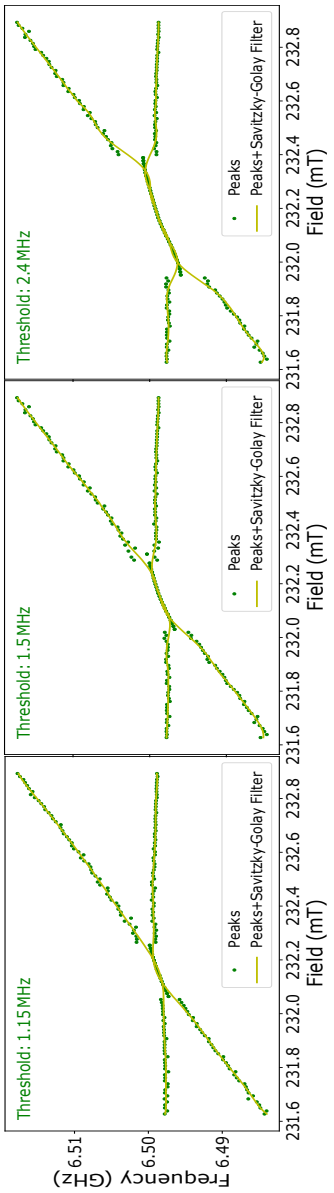

Figure 8.2: Determination of the correct threshold for data in the regime of level merging. Exemplary, it is shown for $\delta_0 = (1.31 \pm 0.22)$, corresponding to an attenuation of 10 dB of the path P_1 to the cavity port. Here, for a threshold of 2.4MHz, the jump to the area of level merging around the resonance is significant. Hence, for this dataset, this threshold value represents an overestimation. On the contrary, a threshold of 1.15 MHz is too low because the spread of the values on the right side from the resonant coupling field indicates that the peak search algorithm does not identify two clear peaks.

of δ_0, the transition point to the region with a single solution, i.e. level merging, becomes blurred for higher values of δ_0.

8.1.6 Amplitude enhancement: Linewidths from fits

The solid lines for the amplitudes are determined by a fit of Equation (5.7) for a constant frequency as a function of the studied field interval. From the fit, the parameters for each frequency entry are determined and utilised to generate the solid lines. Around

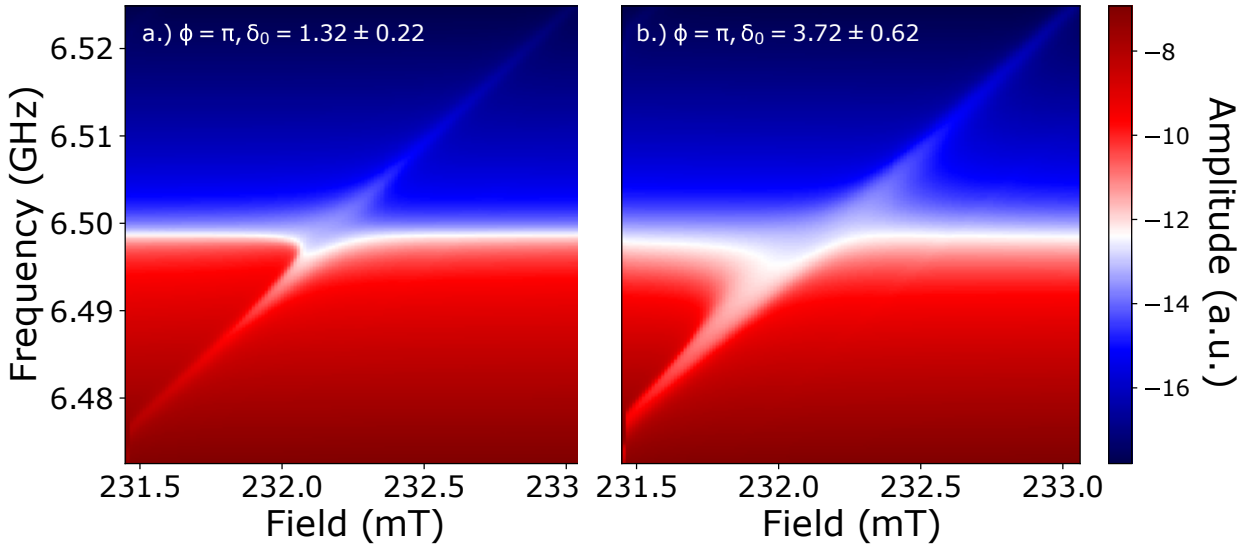

Figure 8.3: Phase representation for $\phi = \pi$ and $\delta_0 = 1.31 \pm 0.22$ (a.)) and $\delta_0 = 3.71 \pm 0.62$ (b.)), respectively. From a.) to b.) the area of level merging increases. However, the transition is less sharp in b.) and thus the area where two peaks are still clearly identifiable is lower. As a result, the threshold is set higher after it is compared to these phase datasets.

the resonance frequency of $\omega_r/2\pi = 6.4985\,\text{GHz}$, the values for the linewidth are all in the order of 2 MHZ for the curves displayed in Figure 5.29 a.). Towards resonance, the losses of the resonator increase as the coupling to the magnons become more and more resonant. It increases further for a slightly higher value of resonance but the values of the linewidth also start to fluctuate, and these fit results are not in agreement with the ones from fitting a sum of two Lorentzian. In addition, there is a small asymmetry in spectra of level merging if the phase is not set exactly at $\phi = \pi$ (c.f. Figure 5.30).

8.2 Technical drawings

In the following, several technical drawings used for the construction of the two sample rods for the cryogenic setup in Mainz in the course of this doctoral thesis, are shown. The electronical files (Solidworks construction files etc.) are copied to a USB stick and given to the administrative staff. Please note, that for the first rod, apart from the sample holder, no further design and construction in the mechanical workshop was necessary, as the parts were found in the lab or bought commercially (such as the cross piece from Vacom) in the beginning.

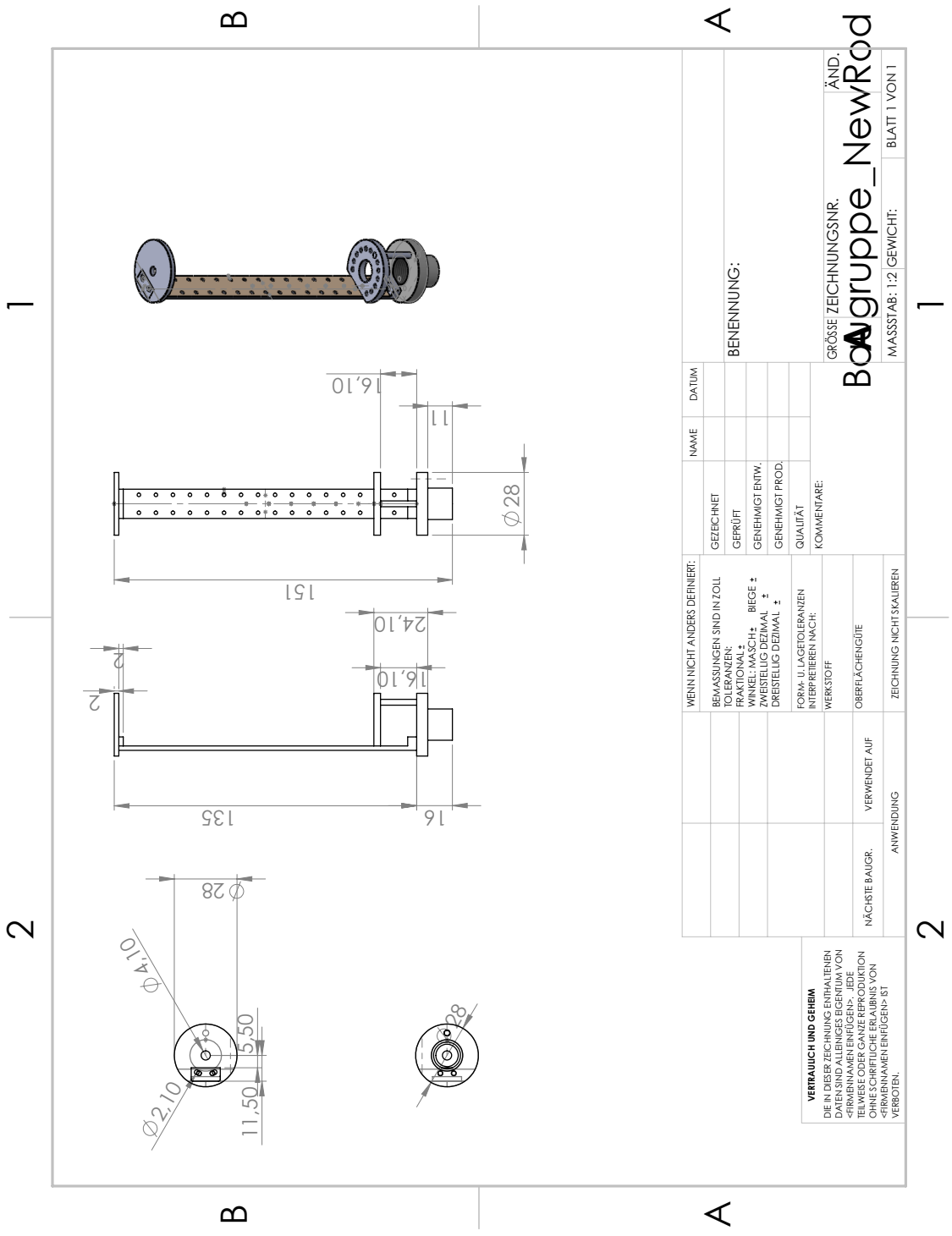

Figure 8.4: Drawing for the assembled main components (the copper cap is excluded for better visibility) of the second rod.Units are given in mm. As mention in the main, the material is copper for all parts. The different colours are for better visibility of the single components.

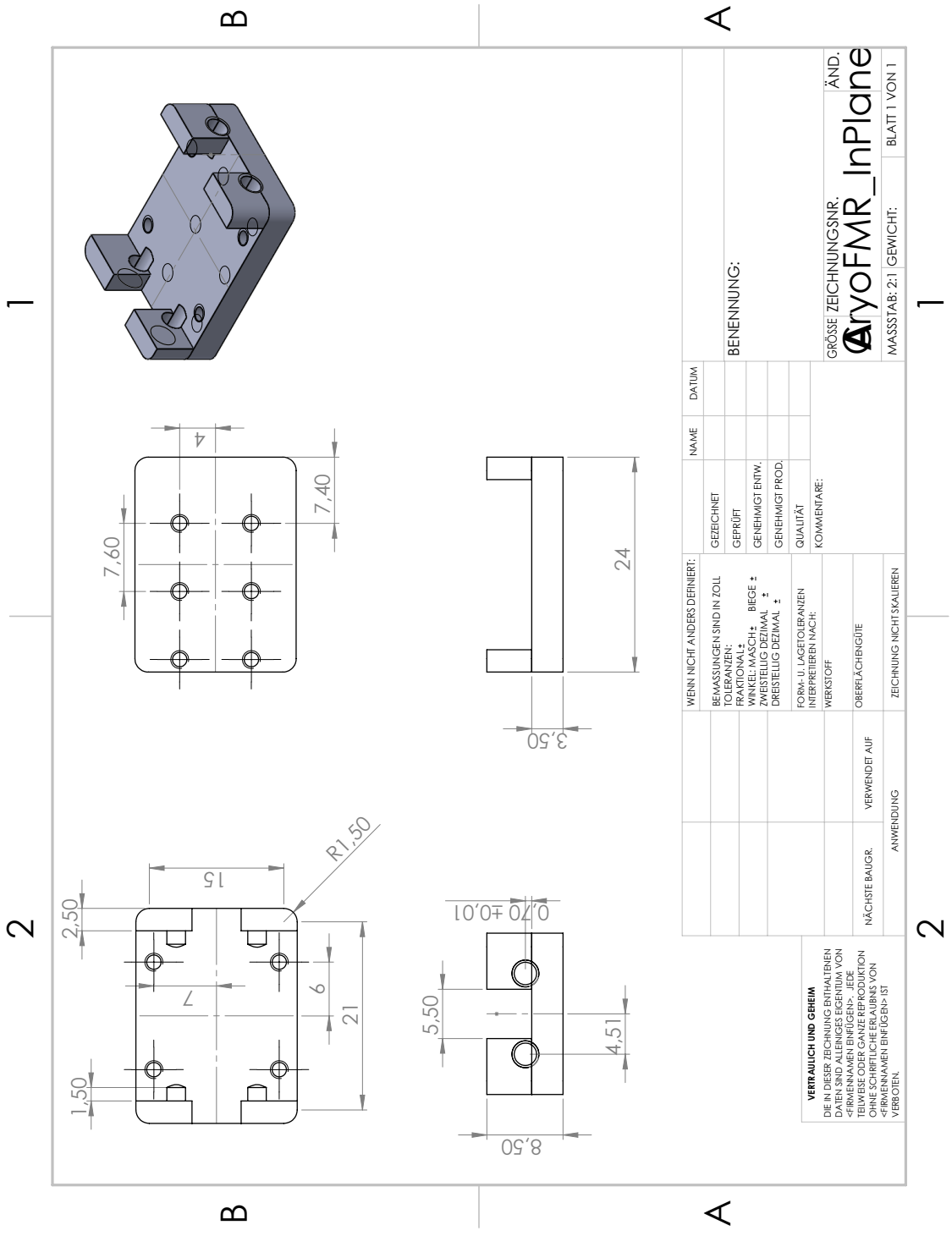

Figure 8.5: In plane holder for a stripline or coplanar waveguide for FMR measurements with the second rod. Units are given in mm. As mention in the main, the material is copper for all parts. The different colours are for better visibility of the single components. Note: This is the basis file, in discussions with the mechanical workshop small changes were made, which are

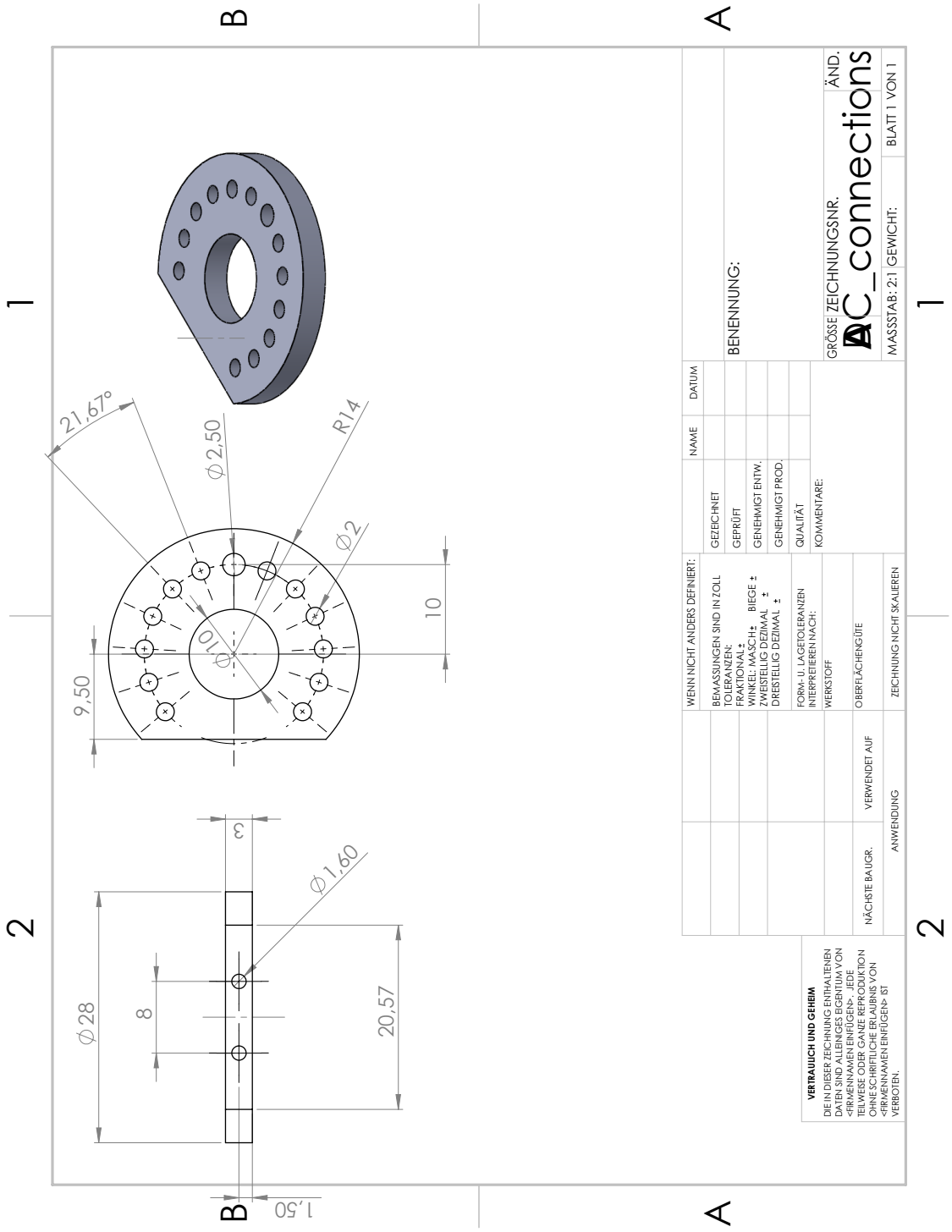

Figure 8.6: Feed through for the DC connections of the second rod which allows to separate them well and remove stress from the thin cables which are wired to the gold pads of the stripline. Small, double sided pins are inserted into each hole of the DC connector and soldered. The DC-cables coming from the top are soldered to the upper side of this pin, and the shorter going to the sample to the bottom . Units are given in mm. As mention in the main, the material is copper for all parts. The different colours are for better visibility of the single components.

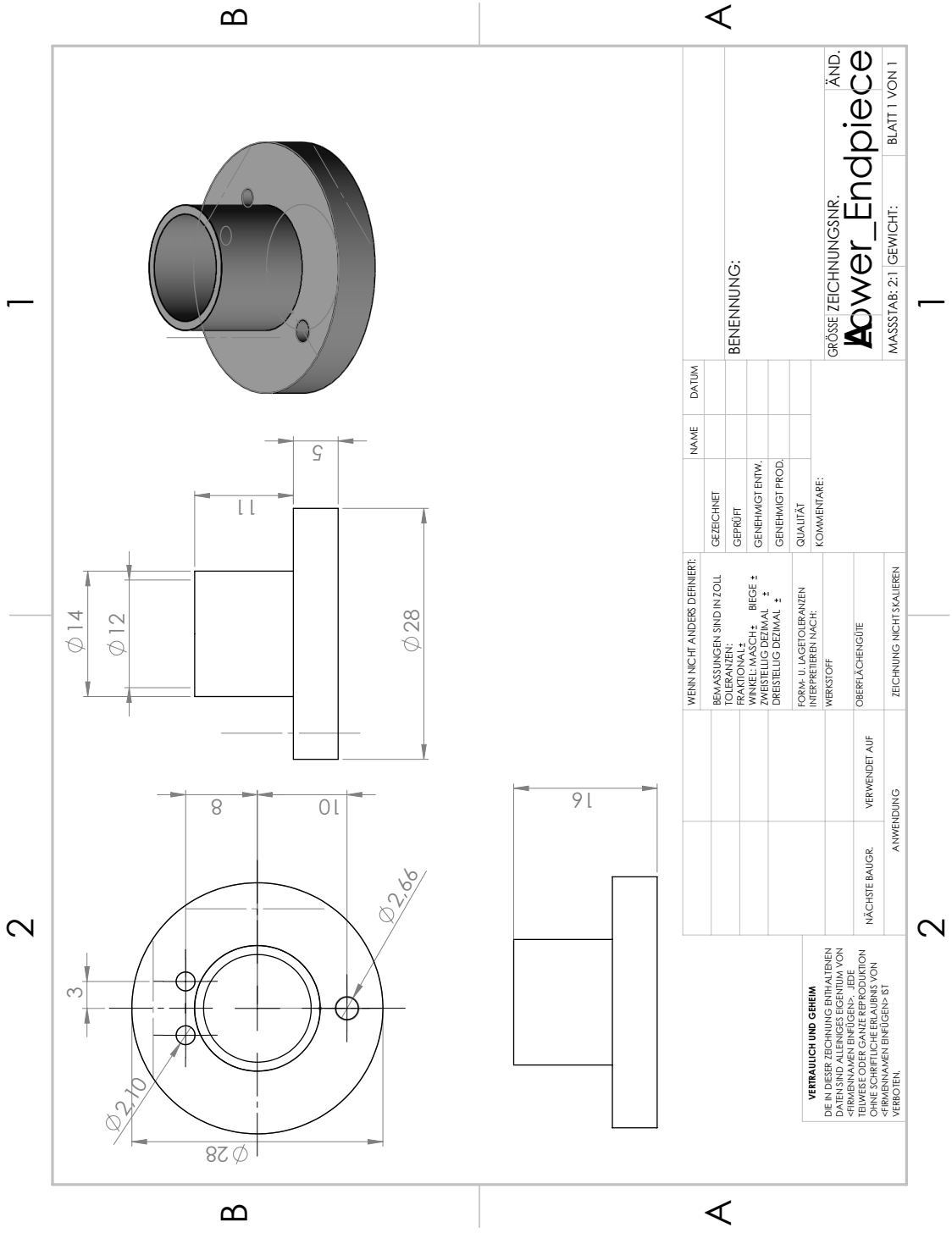

Figure 8.7: Dimensions of the lower end of the second sample rod.

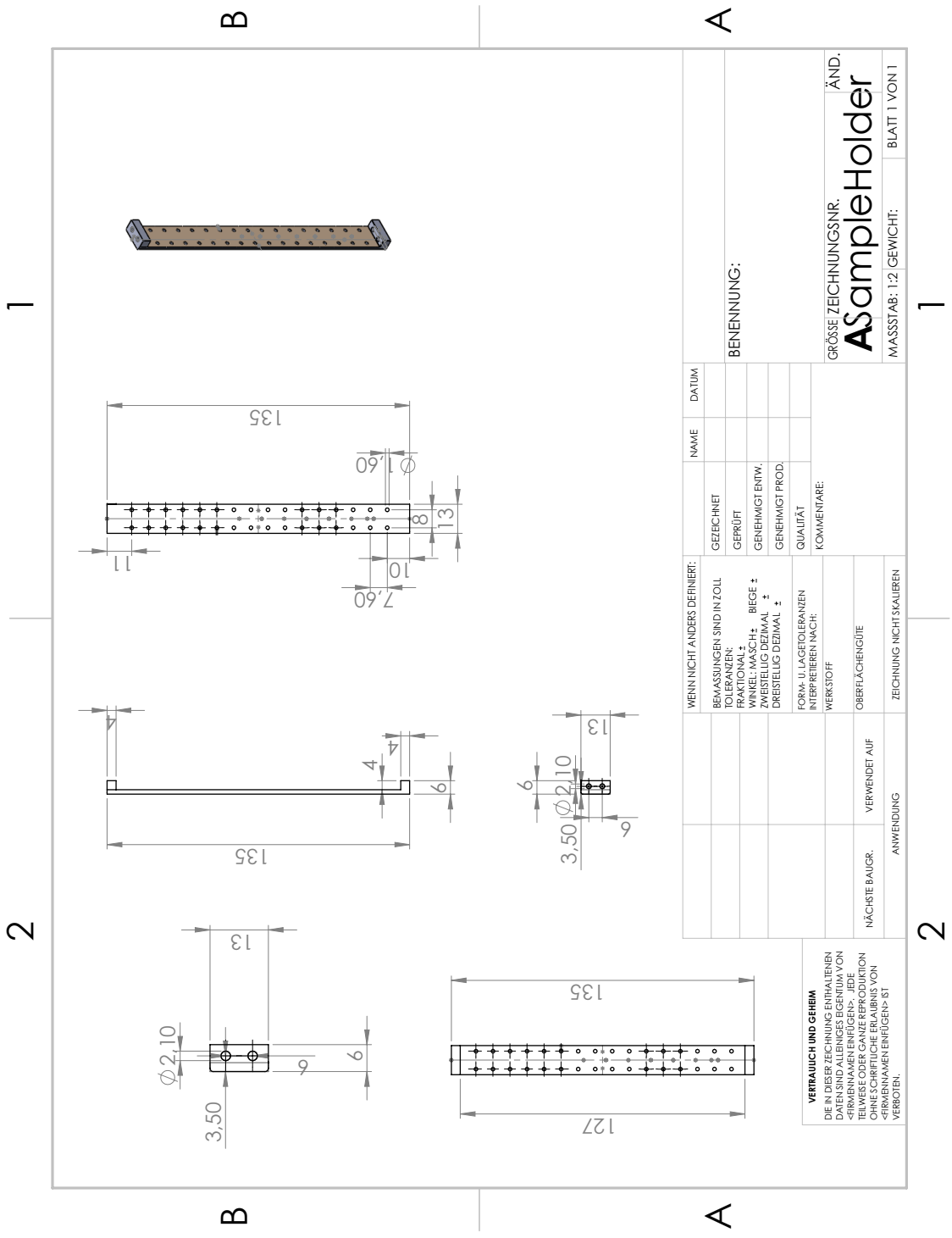

Figure 8.8: Dimensions of the second sample holder. The first one is shorter.It has got a length of 35.4 mm and does not contain the lips at the top and the bottom. Instead it is recessed into the baseplate. Therfore, the whole sample holder of the first rod become more instable by time.

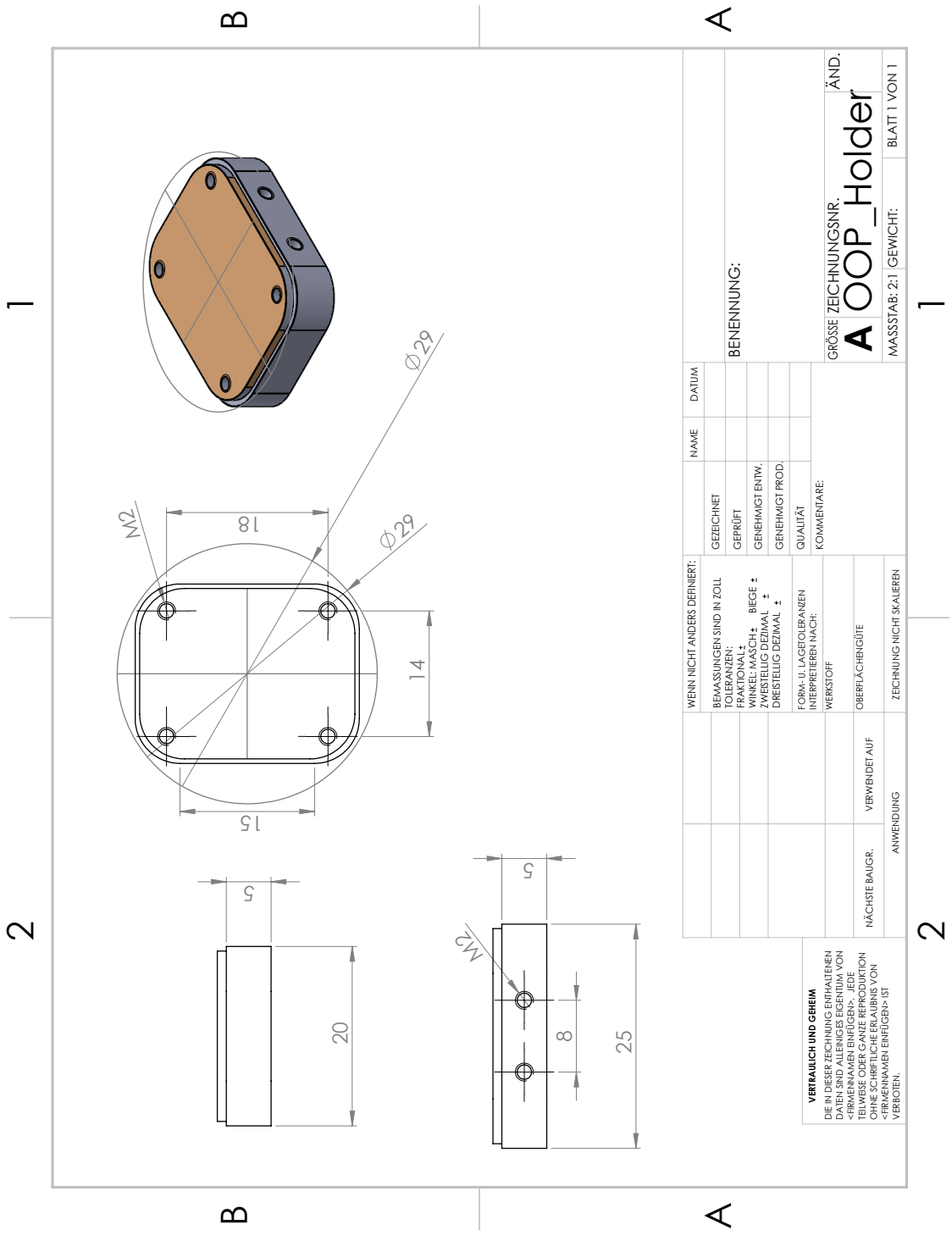

Figure 8.9: Dimensions of the stripline holder for out-of-plane FMR measurements with the second sample rod. The brown part respresents a sketch for the stripline dimensions.

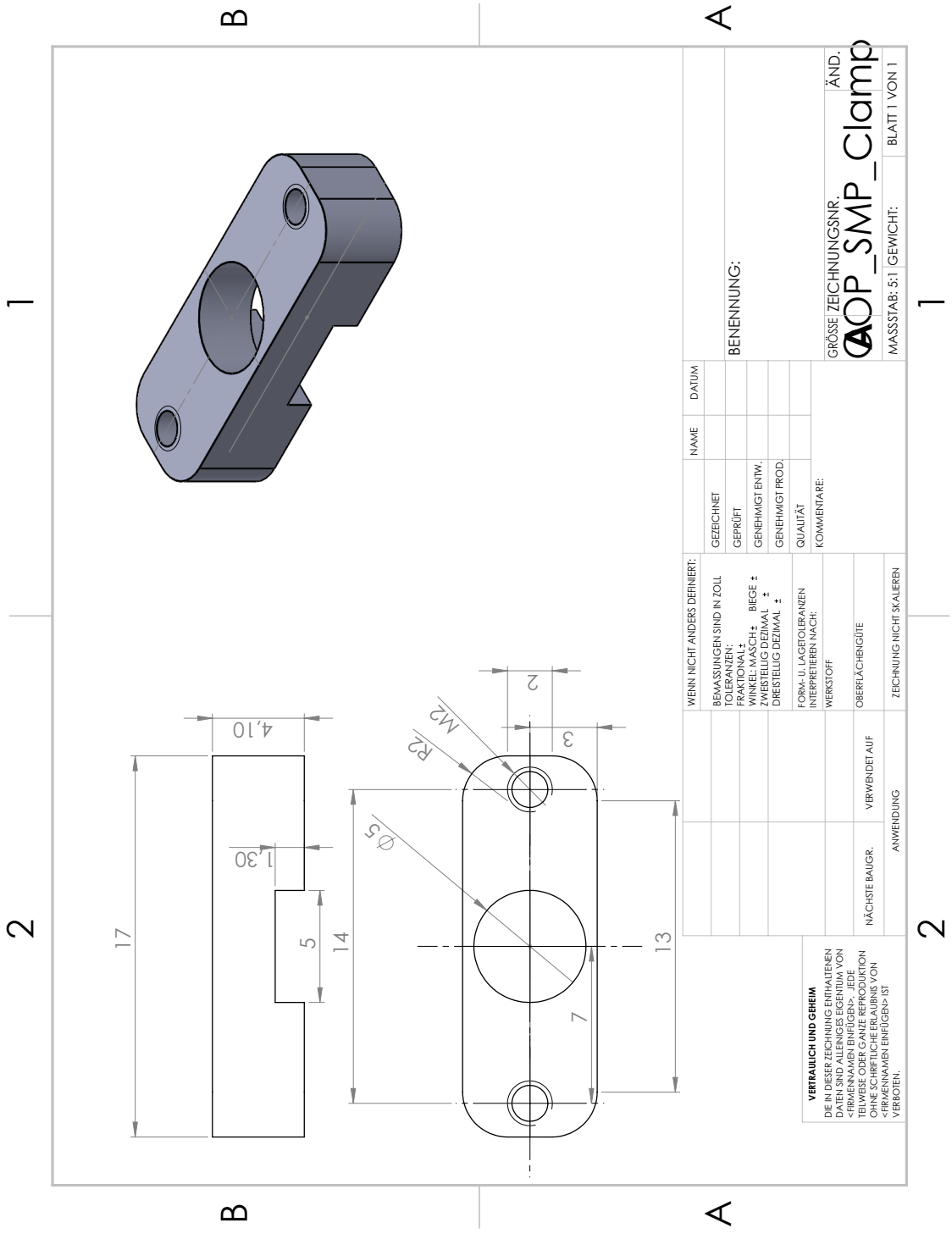

Figure 8.10: Dimensions of the piece to clamp, i.e. fix the position of the SMP connectors and remove additional stress on the soldering connections.

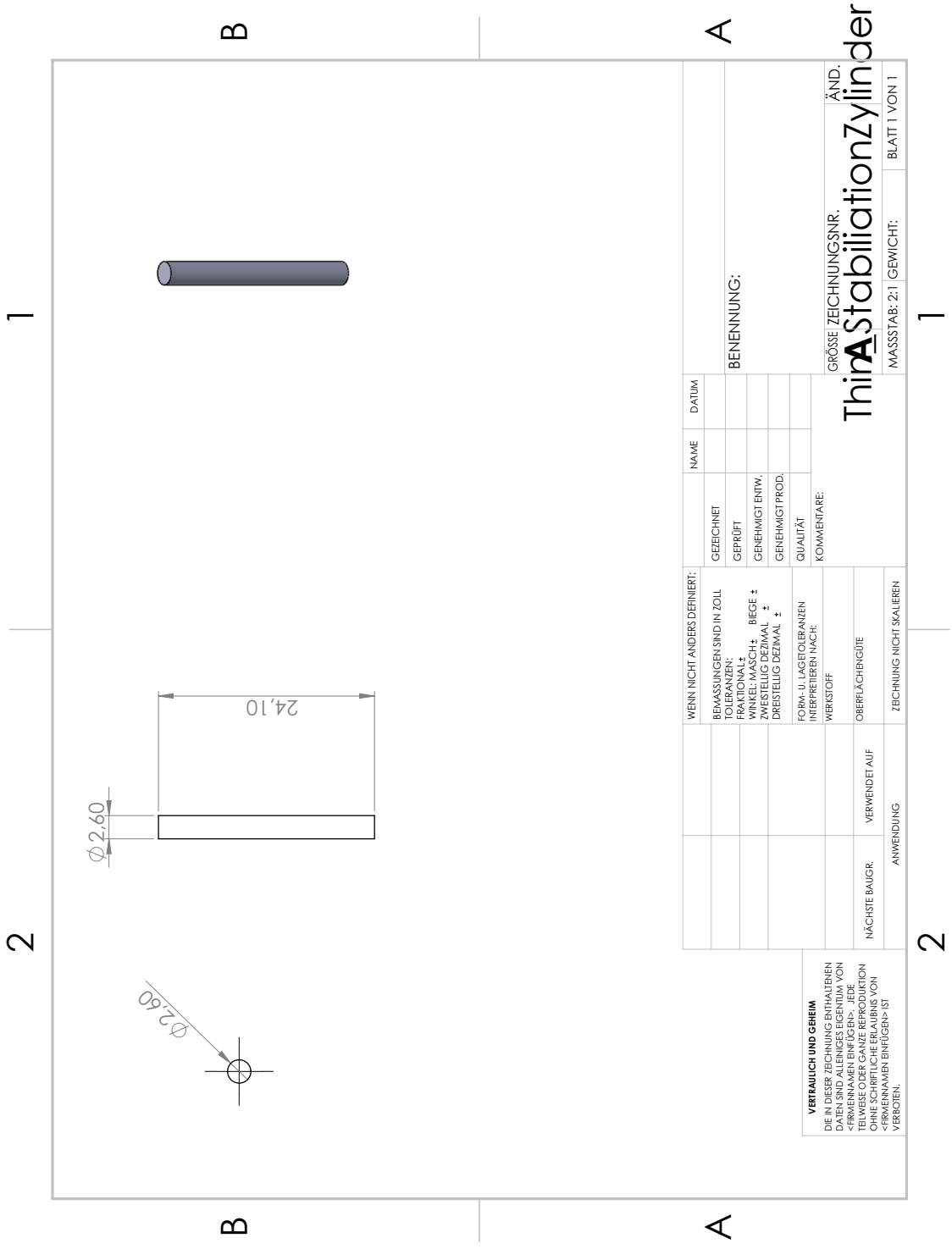

Figure 8.11: Dimensions of the zylindrical piece to stabilize the piece for the DC connections (c.f. Figure 8.4 and Figure 8.6)

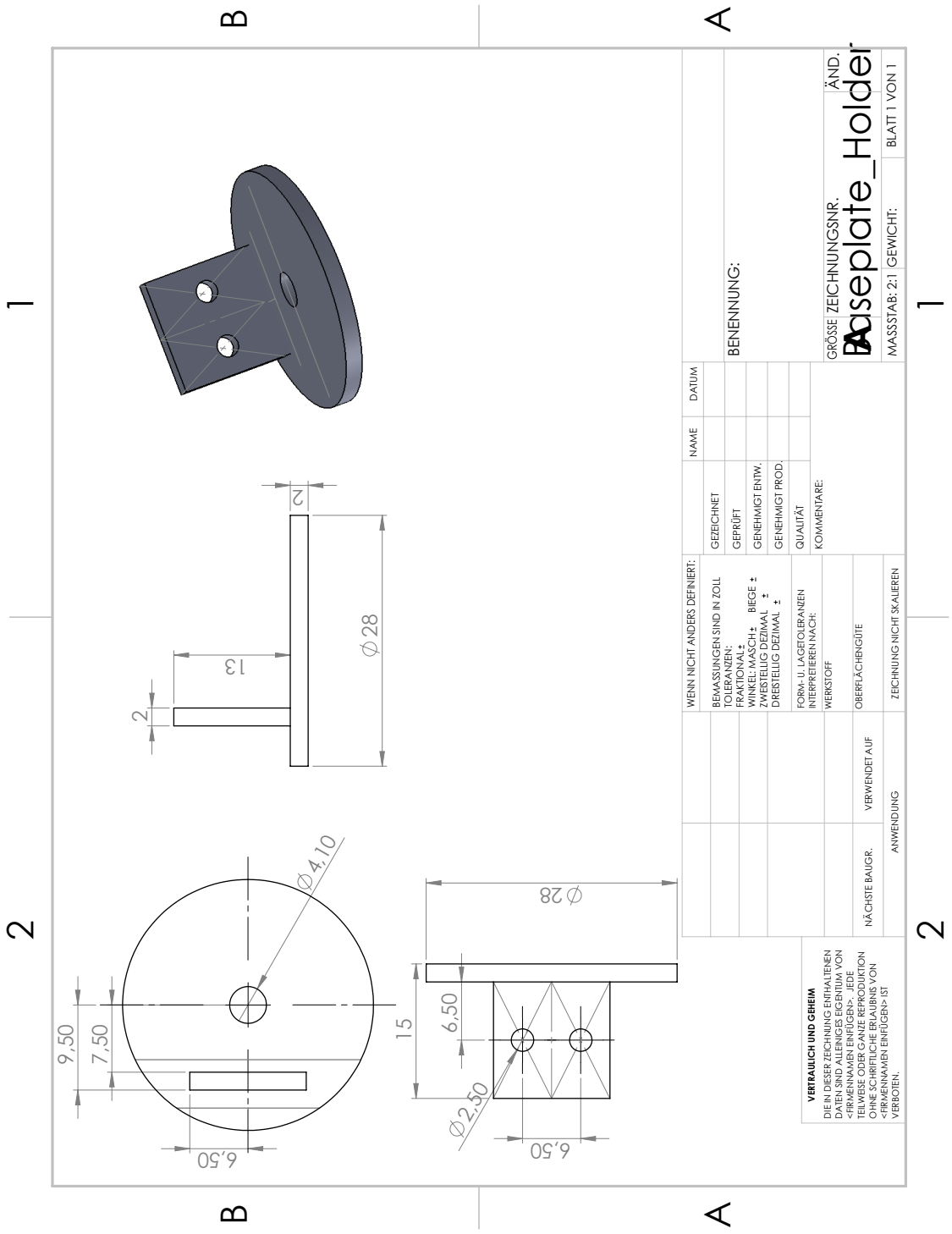

Figure 8.12: Dimensions of the baseplate at the bottom of the sample holder (c.f. Figure 8.4). The difference to the base plate of the first rod is that instead of the rectangular extrusion where the sample holder is screwed to, the sample holder has a small notch of the same dimension of 1 mm. The drilling in the centre is for the attachment of the outer screw which fixes the copper cap to the sample holder when everything is inserted into the cryostat.

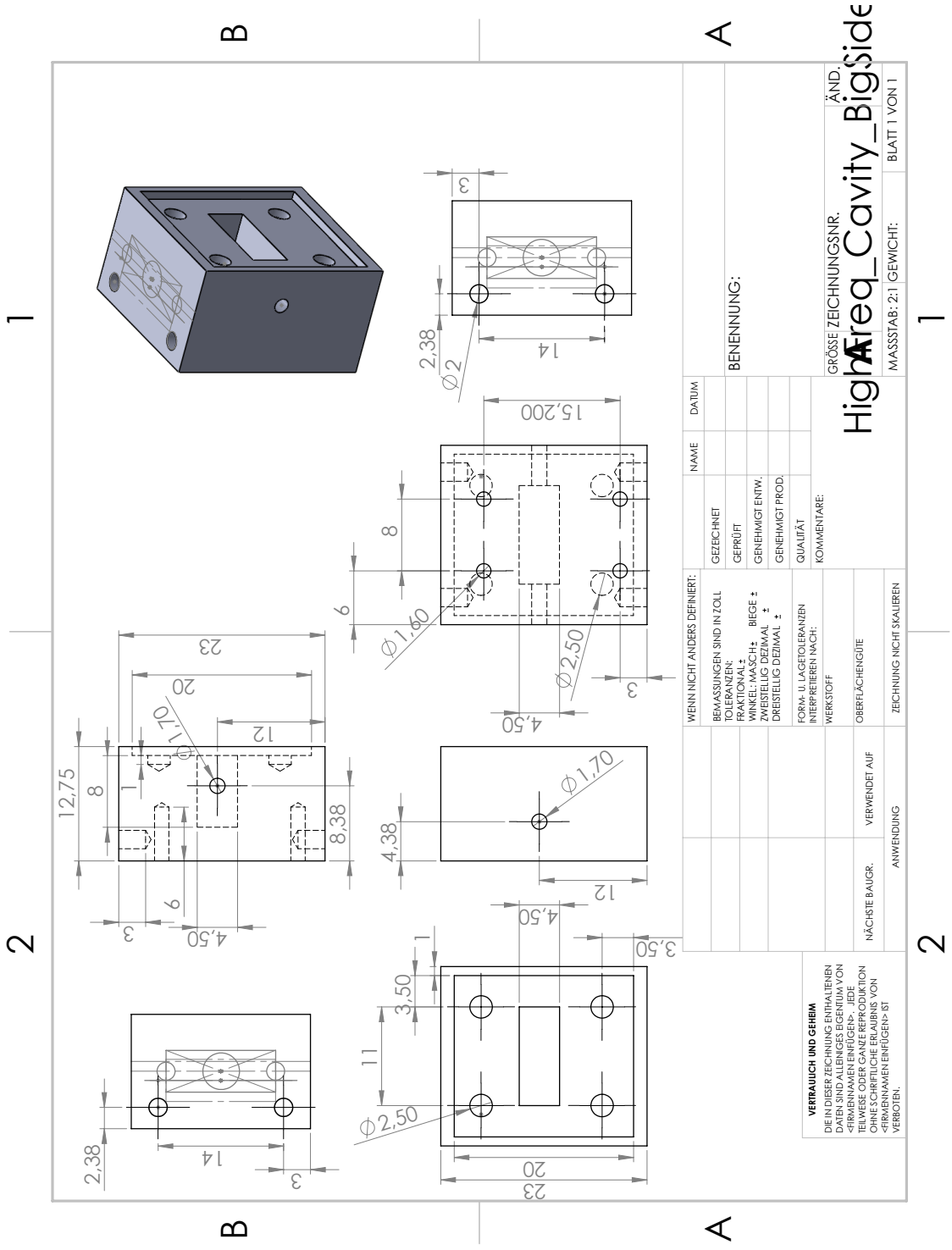

Figure 8.13: Dimensions of the "big" side of the new high frequency cavity resonator with a resonance frequency of $\omega_r \simeq 33\,\text{GHz}$ for the planned measurements of CMP's in weak ferromagnets (c.f. Figure 6.1). The material is copper and all dimensions are given in units of mm.

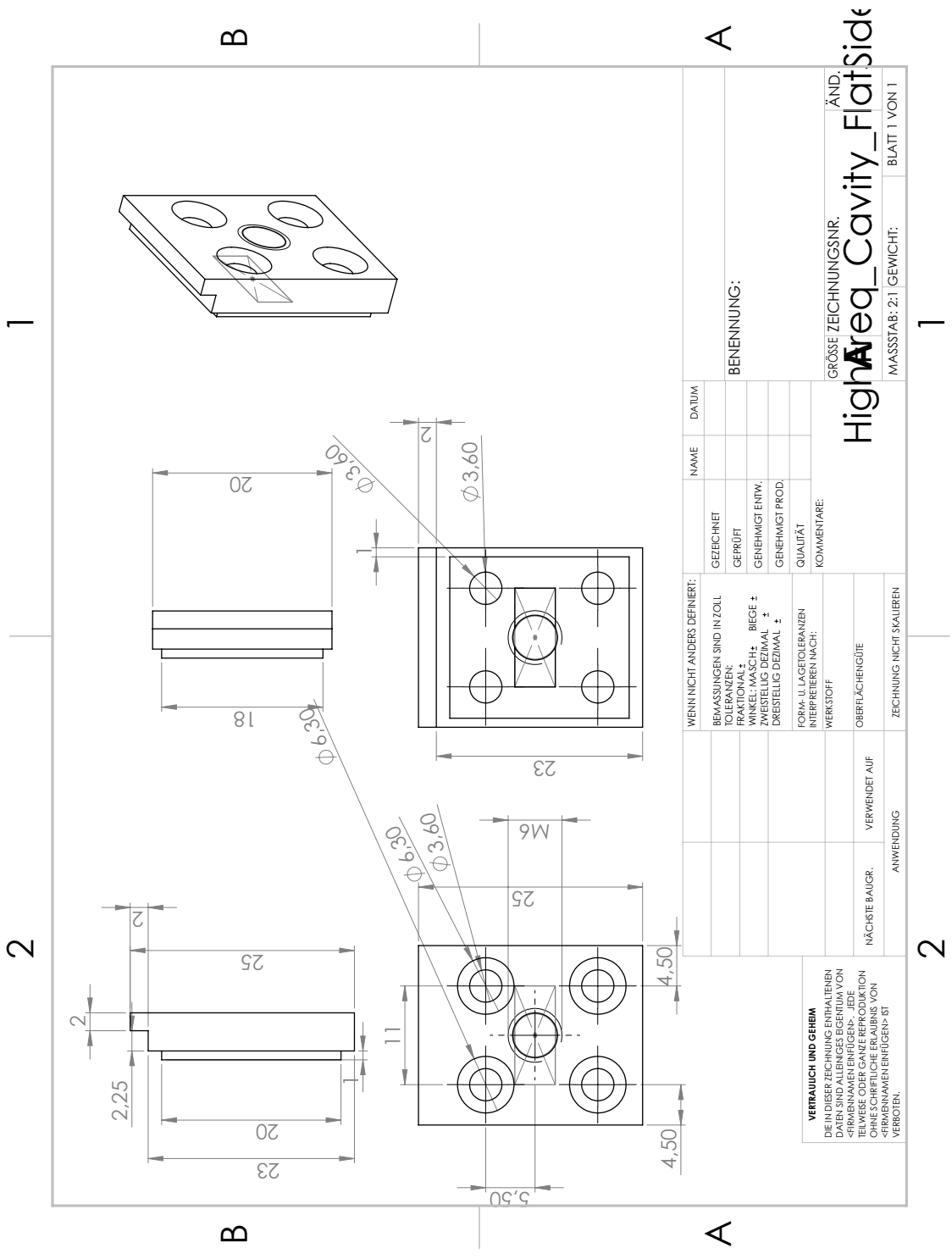

Figure 8.14: Dimensions of the "small" side of the new high frequency cavity resonator with a resonance frequency of $\omega_r \simeq 33\,\mathrm{GHz}$ for the planned measurements of CMP's in weak ferromagnets (c.f. Figure 6.1). The material is copper and all dimensions are given in units of mm.

Bibliography

[1] Collins, *Collins English Dictionary: Complete and Unabridged*. Collins; 7 Rev Ed edition, (2005).

[2] G. S. Hurst, J. O. Stoner, J. D. Graybeal, and S. Chu, "Spectroscopy." Encyclopaedia Britannica, inc. last access: February 2018.

[3] J. Weiner and F. Nunes, *Light-Matter Interaction*. Oxford University Press, (2017).

[4] H. J. Kimble, "Strong interactions of single atoms and photons in cavity QED," *Physica Scripta* **T76** (1), p. 127 (1998).

[5] G. Rempe, T. Fischer, M. Hennrich, A. Kuhn, T. Legero, P. Maunz, P. W. H. Pinkse, and T. Puppe, "Single atoms and single photons in cavity quantum electrodynamics," in *Coherence and Quantum Optics VIII*, pp. 241–248, Springer US, (2003).

[6] R. P. Feynman, *QED: The Strange Theory of Light and Matter*. Princeton University Press, (2014).

[7] J. Maxwell, "VIII. a dynamical theory of the electromagnetic field," *Philosophical Transactions of the Royal Society of London* **155**, pp. 459–512 (1865).

[8] D. L. Mills and E. Burstein, "Polaritons: the electromagnetic modes of media," *Reports on Progress in Physics* **37** (7), pp. 817–926 (1974).

[9] E. Hecht, "Einstein on mass and energy," *American Journal of Physics* **77** (9), pp. 799–806 (2009).

[10] B. Povh, K. Rith, C. Scholz, F. Zetsche, and W. Rodejohann, *Teilchen und Kerne*. Springer Berlin Heidelberg, (2013).

[11] D. F. Walls and G. F. Milburn, *Quantum Optics*. Springer-Verlag GmbH, (2008).

[12] M. Litinskaya, "Polaritons," in *Reference Module in Materials Science and Materials Engineering*, Elsevier, (2016).

[13] K. Cho, *Excitons*. Springer Science & Business Media, 2012, (2012).

[14] V. L. Safonov, *Nonequilibrium Magnons*. Wiley VCH Verlag GmbH, (2012).

[15] A. G. Gurevich and G. A. Melkov, *Magnetization Oscillations and Waves*. CRC PR INC, (2000).

[16] I. Žutić, J. Fabian, and S. D. Sarma, "Spintronics: Fundamentals and applications," *Reviews of Modern Physics* **76** (2), pp. 323–410 (2004).

[17] Editorial, "Memory with a spin," *Nature Nanotechnology* **10** (3), pp. 185–185 (2015).

[18] F. Matsukura, Y. Tokura, and H. Ohno, "Control of magnetism by electric fields," *Nature Nanotechnology* **10** (3), pp. 209–220 (2015).

[19] J. Jeske, Á. Rivas, M. H. Ahmed, M. A. Martin-Delgado, and J. H. Cole, "The effects of thermal and correlated noise on magnons in a quantum ferromagnet," *New Journal of Physics* **20** (9), p. 093017 (2018).

[20] M. Johnson and R. H. Silsbee, "Interfacial charge-spin coupling: Injection and detection of spin magnetization in metals," *Physical Review Letters* **55** (17), pp. 1790–1793 (1985).

[21] A. Khitun, M. Bao, and K. L. Wang, "Magnonic logic circuits," *Journal of Physics D: Applied Physics* **43** (26), p. 264005 (2010).

[22] T. Fischer, M. Kewenig, D. A. Bozhko, A. A. Serga, I. I. Syvorotka, F. Ciubotaru, C. Adelmann, B. Hillebrands, and A. V. Chumak, "Experimental prototype of a spin-wave majority gate," *Applied Physics Letters* **110** (15), p. 152401 (2017).

[23] V. V. Kruglyak, S. O. Demokritov, and D. Grundler, "Magnonics," *Journal of Physics D: Applied Physics* **43** (26), p. 264001 (2010).

[24] A. V. Chumak and H. Schultheiss, "Magnonics: spin waves connecting charges, spins and photons," *Journal of Physics D: Applied Physics* **50** (30), p. 300201 (2017).

[25] T. Holstein and H. Primakoff, "Field Dependence of the Intrinsic Domain Magnetization of a Ferromagnet," *Physical Review* **58** (12), pp. 1098–1113 (1940).

[26] F. J. Dyson, "General theory of spin-wave interactions," *Physical Review* **102** (5), pp. 1217–1230 (1956).

[27] Y. Tabuchi, S. Ishino, A. Noguchi, T. Ishikawa, R. Yamazaki, K. Usami, and Y. Nakamura, "Quantum magnonics: The magnon meets the superconducting qubit," *Comptes Rendus Physique* **17** (7), pp. 729–739 (2016).

[28] D. Lachance-Quirion, Y. Tabuchi, A. Gloppe, K. Usami, and Y. Nakamura, "Hybrid quantum systems based on magnonics." arXiv:1902.03024v2 [quant-ph], (2019).

[29] R. P. Feynman, "Simulating physics with computers," *International Journal of Theoretical Physics* **21** (6–7), pp. 467–488 (1982).

[30] A. Imamoglu, D. D. Awschalom, G. Burkard, D. P. DiVincenzo, D. Loss, M. Sherwin, and A. Small, "Quantum information processing using quantum dot spins and cavity-qed," *Physical Review Letters* **83** (20), pp. 4204–4207 (1999).

[31] J. Stolze and D. Suter, *Quantum Computing: A Short Course from Theory to Experiment*. Wiley-VCH Verlag, (2004).

[32] D. Deutsch, "Quantum theory, the church-turing principle and the universal quantum computer," *Proceedings of the Royal Society A: Mathematical, Physical and Engineering Sciences* **400** (1818), pp. 97–117 (1985).

[33] D. Deutsch and R. Jozsa, "Rapid solution of problems by quantum computation," *Proceedings of the Royal Society A: Mathematical, Physical and Engineering Sciences* **439** (1907), pp. 553–558 (1992).

[34] P. W. Shor, "Polynomial-time algorithms for prime factorization and discrete logarithms on a quantum computer," *SIAM Journal on Computing* **26** (5), pp. 1484–1509 (1997).

[35] J. I. Cirac and P. Zoller, "Quantum computations with cold trapped ions," *Physical Review Letters* **74** (20), pp. 4091–4094 (1995).

[36] H. Haffner, C. Roos, and R. Blatt, "Quantum computing with trapped ions," *Physics Reports* **469** (4), pp. 155–203 (2008).

[37] Q. A. Turchette, C. S. Wood, B. E. King, C. J. Myatt, D. Leibfried, W. M. Itano, C. Monroe, and D. J. Wineland, "Deterministic entanglement of two trapped ions," *Physical Review Letters* **81** (17), pp. 3631–3634 (1998).

[38] S. Olmschenk, D. N. Matsukevich, P. Maunz, D. Hayes, L.-M. Duan, and C. Monroe, "Quantum teleportation between distant matter qubits," *Science* **323** (5913), pp. 486–489 (2009).

[39] J. M. Raimond, M. Brune, and S. Haroche, "Manipulating quantum entanglement with atoms and photons in a cavity," *Reviews of Modern Physics* **73** (3), pp. 565–582 (2001).

[40] C. J. Hood, "The atom-cavity microscope: Single atoms bound in orbit by single photons," *Science* **287** (5457), pp. 1447–1453 (2000).

[41] D. P. DiVincenzo, "The physical implementation of quantum computation," *Fortschritte der Physik* **48** (9-11), pp. 771–783 (2000).

[42] A. Wallraff, D. I. Schuster, A. Blais, L. Frunzio, R.-S. Huang, J. Majer, S. Kumar, S. M. Girvin, and R. J. Schoelkopf, "Strong coupling of a single photon to a superconducting qubit using circuit quantum electrodynamics," *Nature* **431** (7005), pp. 162–167 (2004).

[43] M. A. Sillanpää, J. I. Park, and R. W. Simmonds, "Coherent quantum state storage and transfer between two phase qubits via a resonant cavity," *Nature* **449** (7161), pp. 438–442 (2007).

[44] J. Koch, T. M. Yu, J. Gambetta, A. A. Houck, D. I. Schuster, J. Majer, A. Blais, M. H. Devoret, S. M. Girvin, and R. J. Schoelkopf, "Charge-insensitive qubit design derived from the cooper pair box," *Physical Review A* **76** (4), p. 042319 (2007).

[45] I. Georgescu, S. Ashhab, and F. Nori, "Quantum simulation," *Reviews of Modern Physics* **86** (1), pp. 153–185 (2014).

[46] Z.-L. Xiang, S. Ashhab, J. Q. You, and F. Nori, "Hybrid quantum circuits: Superconducting circuits interacting with other quantum systems," *Reviews of Modern Physics* **85** (2), pp. 623–653 (2013).

[47] M. H. Devoret, A. Wallraff, and J. M. Martinis, "Superconducting qubits: A short review." arXiv:cond-mat/0411174v1 [cond-mat.mes-hall], (2004).

[48] Y. Kubo, C. Grezes, A. Dewes, T. Umeda, J. Isoya, H. Sumiya, N. Morishita, H. Abe, S. Onoda, T. Ohshima, V. Jacques, A. Dréau, J.-F. Roch, I. Diniz, A. Auffeves, D. Vion, D. Esteve, and P. Bertet, "Hybrid quantum circuit with a superconducting qubit coupled to a spin ensemble," *Physical Review Letters* **107** (22), p. 220501 (2011).

[49] Y. Nakamura, Y. A. Pashkin, and J. S. Tsai, "Coherent control of macroscopic quantum states in a single-cooper-pair box," *Nature* **398** (6730), pp. 786–788 (1999).

[50] M. Hofheinz, E. M. Weig, M. Ansmann, R. C. Bialczak, E. Lucero, M. Neeley, A. D. O'Connell, H. Wang, J. M. Martinis, and A. N. Cleland, "Generation of fock states in a superconducting quantum circuit," *Nature* **454** (7202), pp. 310–314 (2008).

[51] Y. Kubo, F. R. Ong, P. Bertet, D. Vion, V. Jacques, D. Zheng, A. Dréau, J.-F. Roch, A. Auffeves, F. Jelezko, J. Wrachtrup, M. F. Barthe, P. Bergonzo, and D. Esteve, "Strong coupling of a spin ensemble to a superconducting resonator," *Physical Review Letters* **105** (14), p. 140502 (2010).

[52] R. Amsüss, C. Koller, T. Nöbauer, S. Putz, S. Rotter, K. Sandner, S. Schneider, M. Schramböck, G. Steinhauser, H. Ritsch, J. Schmiedmayer, and J. Majer, "Cavity QED with magnetically coupled collective spin states," *Physical Review Letters* **107** (6), p. 060502 (2011).

[53] Ö. O. Soykal and M. E. Flatté, "Strong field interactions between a nanomagnet and a photonic cavity," *Physical Review Letters* **104** (7), p. 077202 (2010).

[54] H. Huebl, C. W. Zollitsch, J. Lotze, F. Hocke, M. Greifenstein, A. Marx, R. Gross, and S. T. B. Goennenwein, "High cooperativity in coupled microwave resonator ferrimagnetic insulator hybrids," *Physical Review Letters* **111** (12), p. 127003 (2013).

[55] C.-M. Hu, "Dawn of Cavity Spintronics," *Physics in Canada* **72** (2), p. 76 (2016).

[56] Y. Tabuchi, S. Ishino, T. Ishikawa, R. Yamazaki, K. Usami, and Y. Nakamura, "Hybridizing ferromagnetic magnons and microwave photons in the quantum limit," *Physical Review Letters* **113** (8), p. 083603 (2014).

[57] D. Lachance-Quirion, Y. Tabuchi, S. Ishino, A. Noguchi, T. Ishikawa, R. Yamazaki, and Y. Nakamura, "Resolving quanta of collective spin excitations in a millimeter-sized ferromagnet," *Science Advances* **3** (7), p. e1603150 (2017).

[58] X. Zhang, C.-L. Zou, L. Jiang, and H. X. Tang, "Strongly coupled magnons and cavity microwave photons," *Physical Review Letters* **113** (15), p. 156401 (2014).

[59] E. M. Purcell, "Spontaneous emission probabilities at radio frequencies," in *Confined Electrons and Photons*, pp. 839–839, Springer US, (1995).

[60] L. Bai, M. Harder, Y. Chen, X. Fan, J. Xiao, and C.-M. Hu, "Spin pumping in electrodynamically coupled magnon-photon systems," *Physical Review Letters* **114** (22), p. 227201 (2015).

[61] M. Harder and C.-M. Hu, "Chapter Two - Cavity Spintronics: An Early Review of Recent Progress in the Study of Magnon–Photon Level Repulsion," in *Solid State Physics* (R. E. Camley and R. L. Stamps, eds.), vol. 69, pp. 47–121, Elsevier, (2018).

[62] J. A. Haigh, N. J. Lambert, A. C. Doherty, and A. J. Ferguson, "Dispersive readout of ferromagnetic resonance for strongly coupled magnons and microwave photons," *Physical Review B* **91** (10), p. 104410 (2015).

[63] S. Klingler, H. Maier-Flaig, C. Dubs, O. Surzhenko, R. Gross, H. Huebl, S. T. B. Goennenwein, and M. Weiler, "Gilbert damping of magnetostatic modes in a Yttrium Iron Garnet sphere," *Applied Physics Letters* **110** (9), p. 092409 (2017).

[64] R. G. E. Morris, A. F. van Loo, S. Kosen, and A. D. Karenowska, "Strong coupling of magnons in a YIG sphere to photons in a planar superconducting resonator in the quantum limit," *Scientific Reports* **7** (1), p. 11511 (2017).

[65] H. Maier-Flaig, M. Harder, S. Klingler, Z. Qiu, E. Saitoh, M. Weiler, S. Geprägs, R. Gross, S. T. B. Goennenwein, and H. Huebl, "Tunable magnon-photon coupling in a compensating ferrimagnet – from weak to strong coupling," *Applied Physics Letters* **110** (13), p. 132401 (2017).

[66] H. Maier-Flaig, S. Klingler, C. Dubs, O. Surzhenko, R. Gross, M. Weiler, H. Huebl, and S. T. B. Goennenwein, "Temperature-dependent magnetic damping of yttrium iron garnet spheres," *Physical Review B* **95** (21), p. 214423 (2017).

[67] I. Boventer, M. Pfirrmann, J. Krause, Y. Schön, M. Kläui, and M. Weides, "Complex temperature dependence of coupling and dissipation of cavity magnon polaritons from millikelvin to room temperature," *Physical Review B* **97** (18), p. 184420 (2018).

[68] M. Pfirrmann, I. Boventer, A. Schneider, T. Wolz, M. Kläui, A. V. Ustinov, and M. Weides, "Magnons at low excitations: Observation of incoherent coupling to a bath of two-level-systems." arXiv:1903.03981v1 [quant-ph], (2019).

[69] X. Zhang, C.-L. Zou, N. Zhu, F. Marquardt, L. Jiang, and H. X. Tang, "Magnon dark modes and gradient memory," *Nature Communications* **6** (1), p. 8914 (2015).

[70] B. Yao, Y. S. Gui, J. W. Rao, S. Kaur, X. S. Chen, W. Lu, Y. Xiao, H. Guo, K. P. Marzlin, and C. M. Hu, "Cooperative polariton dynamics in feedback-coupled cavities," *Nature Communications* **8** (1), p. 1437 (2017).

[71] L. Bai, M. Harder, P. Hyde, Z. Zhang, C.-M. Hu, Y. Chen, and J. Q. Xiao, "Cavity mediated manipulation of distant spin currents using a cavity-magnon-polariton," *Physical Review Letters* **118** (21), p. 217201 (2017).

[72] J. Li, S.-Y. Zhu, and G. Agarwal, "Magnon-photon-phonon entanglement in cavity magnomechanics," *Physical Review Letters* **121** (20), p. 203601 (2018).

[73] D. Zhang, X.-Q. Luo, Y.-P. Wang, T.-F. Li, and J. You, "Observation of the exceptional point in cavity magnon-polaritons," *Nature Communications* **8** (1), p. 1368 (2017).

[74] Ø. Johansen and A. Brataas, "Nonlocal coupling between antiferromagnets and ferromagnets in cavities," *Physical Review Letters* **121** (8), p. 087204 (2018).

[75] M. Harder, Y. Yang, B. Yao, C. Yu, J. Rao, Y. Gui, R. Stamps, and C.-M. Hu, "Level attraction due to dissipative magnon-photon coupling," *Physical Review Letters* **121** (13), p. 137203 (2018).

[76] B. M. Yao and Y. S. Gui and T. Yu and J. W. Rao and Y. T. Zhao and W. Lu and C. M. Hu, "Coherent control of magnon radiative damping with local photon states." arXiv:1902.06795 [cond-mat.mes-hall], (2019).

[77] V. L. Grigoryan, K. Shen, and K. Xia, "Synchronized spin-photon coupling in a microwave cavity," *Physical Review B* **98** (2), p. 024406 (2018).

[78] I. Boventer, C. Dörflinger, T. Wolz, R. Macêdo, M. K. Romain Lebrun, and M. Weides, "Control of the Coupling Strength and Linewidth of a Cavity Magnon-Polariton." arXiv:1904.00393v1 [cond-mat.mes-hall], (2019).

[79] W. Demtröder, *Experimentalphysik 2: Elektrizität und Optik*. Springer, (2004).

[80] R. Feynman, *Feynman Lectures on Physics 2: Mainly Electromagnetism and Matter*. Hachette Book Group USA, (2015).

[81] J. D. Jackson, *Klassische Elektrodynamik*. Walter de Gruyter GmbH, (2013).

[82] S. J. Blundell, *Magnetism: A Very Short Introduction*. Oxford University Press, (2012).

[83] R. Gross and A. Marx, *Festkörperphysik: Aufgaben und Lösungen*. De Gruyter Oldenbourg, (2014).

[84] J. M. D. Coey, *Magnetism and Magnetic Materials*. Cambridge University Press, (2010).

[85] D. C. Mattis, *The Theory of Magnetism Made Simple: An Introduction To Physical Concepts And To Some Useful Mathematical Methods*. World Scientific Publishing Company, (2006).

[86] N. M. Neil W. Ashcroft, *Solid State Physics*. Cengage Learning, Inc, (1976).

[87] P. A. M. Dirac and R. H. Fowler, "The Quantum Theory of the Electron," *Proceedings of the Royal Society A: Mathematical, Physical and Engineering Sciences* **117** (778), pp. 610–624 (1928).

[88] Schmidt-Böcking, Horst, Schmidt, Lothar, Lüdde, Hans Jürgen, Trageser, Wolfgang, Templeton, Alan, and Sauer, Tilman, "The Stern-Gerlach experiment revisited," *The European Physical Journal H* **41** (4-5), pp. 327–364 (2016).

[89] F. Schwabl, *Statistische Mechanik*. Springer-Verlag GmbH, (2006).

[90] J.-J.-V. Leeuwen, "Problémes de la théorie électronique du magnétisme," *Journal de Physique et Le Radium* **2** (12), pp. 361–377 (1921).

[91] A. Aharoni, *Introduction to the Theory of Ferromagnetism*. Oxford University Press, (2001).

[92] G. F. Dionne, *Magnetic Oxides*. Springer US, (2010).

[93] P. Weiss, "L'hypothèse du champ moléculaire et la propriété ferromagnétique," *Journal de Physique Théorique et Appliquée* **6** (1), pp. 661–690 (1907).

[94] N. Majlis, *The Quantum Theory of Magnetism*. World Scientific, (2007).

[95] F.Bloch, "Zur Theorie des Austauschproblems und der Remanenzerscheinung der Ferromagnetika," *Zeitschrift für Physik* **74** (5), pp. 295–335 (1932).

[96] A. J. Princep, R. A. Ewings, S. Ward, S. Tóth, C. Dubs, D. Prabhakaran, and A. T. Boothroyd, "The Full Magnon Spectrum of Yttrium Iron Garnet," *npj Quantum Materials* **2** (1), p. 63 (2017).

[97] J. Xiao, G. E. W. Bauer, K.-c. Uchida, E. Saitoh, and S. Maekawa, "Theory of magnon-driven spin seebeck effect," *Physical Review B* **81** (21), p. 214418 (2010).

[98] V. Cherepanov, "The saga of YIG: Spectra, thermodynamics, interaction and relaxation of magnons in a complex magnet," *Physics Reports* **229** (3), pp. 81–144 (1993).

[99] D. M. Pozar, *Microwave Engineering*. John Wiley and Sons Ltd., (2011).

[100] B. Z. Rameshti, Y. Cao and G. E. W. Bauer, "Magnetic spheres in microwave cavities," *Physical Review B* **91** (21), p. 214430 (2015).

[101] J. Helszajn, *YIG Resonators and Filters*. John Wiley & Sons, (1985).

[102] E. Mallmann, A. Sombra, J. Goes, and P. Fechine, "Yttrium Iron Garnet: Properties and Applications Review," *Solid State Phenomena* **202**, pp. 65–96 (2013).

[103] Ferrisphere Inc. 15 Falcon Rd. Flanders, NJ 07836. United States.

[104] T. L. Gilbert, "A Lagrangian formulation of the gyromagnetic equation of the magnetic field," *Physical Review* **100**, p. 1243 (1955).

[105] D. Polder, "On the theory of ferromagnetic resonance," *Physica* **15** (1-2), pp. 253–255 (1949).

[106] S. Kusminskiy, "Quantum magnetism, spin waves, and light." Notes to lecture: Friedrich-Alexander Universität Erlangen/Nürnberg, (2018).

[107] C. Tim, "Theory of magnetism." International Max Planck Research School for Dynamical Processes in Atoms, Molecules and Solids, (2010).

[108] F. Bloch, "Über die Quantenmechanik der Elektronen in Kristallgittern," *Zeitschrift für Physik* **52** (7-8), pp. 555–600 (1929).

[109] L. Landau, "ON THE THEORY OF THE DISPERSION OF MAGNETIC PERMEABILITY IN FERROMAGNETIC BODIES," in *Collected Papers of L.D. Landau*, pp. 101–114, Elsevier, (1965).

[110] J. H. E. Griffiths, "Anomalous high-frequency resistance of ferromagnetic metals," *Nature* **158** (4019), pp. 670–671 (1946).

[111] C. Kittel, "On the Theory of Ferromagnetic Resonance Absorption," *Physical Review* **73** (2), pp. 155–161 (1948).

[112] S. S. Kalarickal, P. Krivosik, M. Wu, C. E. Patton, M. L. Schneider, P. Kabos, T. J. Silva, and J. P. Nibarger, "Ferromagnetic resonance linewidth in metallic thin films: Comparison of measurement methods," *Journal of Applied Physics* **99** (9), p. 093909 (2006).

[113] B. K. Kuanr, A. V. Kuanr, P. Grünberg, and G. Nimtz, "Swept-frequency FMR on Fe/Cr/Fe trilayer ultrathin films, microwave giant magnetoresistance," *Physics Letters A* **221** (3-4), pp. 245–252 (1996).

[114] T. J. Silva, C. S. Lee, T. M. Crawford, and C. T. Rogers, "Inductive measurement of ultrafast magnetization dynamics in thin-film permalloy," *Journal of Applied Physics* **85** (11), pp. 7849–7862 (1999).

[115] M. Sparks and R. Loudon and C. Kittel, "Ferromagnetic Relaxation. I. Theory of the Relaxation of the Uniform Precession and the Degenerate Spectrum in Insulators at Low Temperatures," *Physical Review* **122** (3), pp. 791–803 (1961).

[116] T. Kasuya and R. C. LeCraw, "Relaxation mechanisms in ferromagnetic resonance," *Physical Review Letters* **6** (5), pp. 223–225 (1961).

[117] J. Nemarich, "Contribution of the Two-Magnon Process to Magnetostatic-Mode Relaxation," *Physical Review* **136** (6A), pp. A1657–A1664 (1964).

[118] R. Loudon, "Theory of ferromagnetic relaxation by two-magnon processes," *Solid State Communications* **7** (17), pp. 1163–1166 (1969).

[119] C. E. Patton, "Linewidth and relaxation processes for the main resonance in the spin-wave spectra of ni–fe alloy films," *Journal of Applied Physics* **39** (7), pp. 3060–3068 (1968).

[120] B. Kuanr, R. E. Camley, and Z. Celinski, "Narrowing of the frequency-linewidth in structured magnetic strips: Experiment and theory," *Applied Physics Letters* **87** (1), p. 012502 (2005).

[121] I. Neudecker, G. Woltersdorf, B. Heinrich, T. Okuno, G. Gubbiotti, and C. Back, "Comparison of frequency, field, and time domain ferromagnetic resonance methods," *Journal of Magnetism and Magnetic Materials* **307** (1), pp. 148–156 (2006).

[122] M. C. Hickey and J. S. Moodera, "Origin of Intrinsic Gilbert Damping," *Physical Review Letters* **102** (13), p. 137601 (2009).

[123] M. Sparks and C. Kittel, "Ferromagnetic Relaxation Mechanism for Mz in Yttrium Iron Garnet," *Physical Review Letters* **4** (5), pp. 232–234 (1960).

[124] M. Sparks, "Ferromagnetic Resonance Porosity Linewidth Theory in Polycrystalline Insulators," *Journal of Applied Physics* **36** (5), pp. 1570–1573 (1965).

[125] L. R. Walker, "Magnetostatic modes in ferromagnetic resonance," *Physical Review* **105** (2), pp. 390–399 (1957).

[126] P. Röschmann and H. Dötsch, "Properties of magnetostatic modes in ferrimagnetic spheroids," *Physica Status Solidi (b)* **82** (1), pp. 11–57 (1977).

[127] R. E. Arias, "Spin-wave modes of ferromagnetic films," *Physical Review B* **94** (13), p. 134408 (2016).

[128] A. Barman and A. Haldar, "Time-domain study of magnetization dynamics in magnetic thin films and micro- and nanostructures," in *Solid State Physics*, vol. 65, pp. 1–108, Elsevier, (2014).

[129] P. C. Fletcher and R. O. Bell, "Ferrimagnetic resonance modes in spheres," *Journal of Applied Physics* **30** (5), pp. 687–698 (1959).

[130] W. Demtröder, *Experimentalphysik 4.* Springer-Verlag GmbH, (2017).

[131] J. F. Dillon and J. W. Nielsen, "Effects of Rare Earth Impurities on Ferrimagnetic Resonance in Yttrium Iron Garnet," *Physical Review Letters* **3** (1), pp. 30–31 (1959).

[132] E. G. Spencer, R. C. LeCraw, and A. M. Clogston, "Low-temperature line-width maximum in yttrium iron garnet," *Physical Review Letters* **3** (1), pp. 32–33 (1959).

[133] A. M. Clogston, "Relaxation phenomena in ferrites," *Bell System Technical Journal* **34** (4), pp. 739–760 (1955).

[134] R. Teale and K. Tweedale, "Ytterbium-ion relaxation in ferrimagnetic resonance," *Physics Letters* **1** (7), pp. 298–300 (1962).

[135] J. F. Dillon, "Ferrimagnetic Resonance in Rare-Earth-Doped Yttrium Iron Garnet. III. Linewidth," *Physical Review* **127** (5), pp. 1495–1501 (1962).

[136] C. Kittel, "Theory of ferromagnetic resonance in rare earth garnets. i.gValues," *Physical Review* **115** (6), pp. 1587–1590 (1959).

[137] P.-G. De Gennes, C. Kittel, and A. Portis, "Theory of ferromagnetic resonance in rare earth garnets. II. line widths," *Physical Review* **116** (2), pp. 323–330 (1959).

[138] H. Suhl, *Relaxation Processes in Micromagnetics.* OXFORD UNIV PR, (2007).

[139] J. S.-Y. Wang, "Energy Width of Ferromagnetic-Exchange Magnons in a Magnetic Field," *Physical Review B* **6** (5), pp. 1908–1912 (1972).

[140] M. Sparks, "Two-Magnon Processes in Ferromagnetic Relaxation," *Physical Review Letters* **8** (2), pp. 54–55 (1962).

[141] G. R. Jones, "Surface Dependence of Magnetostatic-Mode Linewidths in Yttrium Iron Garnet," *Journal of Applied Physics* **36** (12), pp. 3702–3703 (1965).

[142] Y. Lam, "Magnetostatic-mode linewidths in Yttrium Iron Garnet," *Solid-State Electronics* **8** (12), pp. 923–930 (1965).

[143] J. V. Vleck, "Ferromagnetic resonance," *Physica* **17** (3-4), pp. 234–252 (1951).

[144] K. Barmak and K. Coffey, *Metallic films for electronic, optical and magnetic applications*. Woodhead Publishing Limited, (2014).

[145] W. K. Chen, *The Electrical Engineering Handbook*. Elsevier Inc., (2005).

[146] J. A. Pierce, "MIT Radiation Laboratory Series," *Physics Today* **1** (2), pp. 19–19 (1948).

[147] S. Schelkunoff, "Electromagnetic waves in conducting tubes," *Physical Review* **52** (10), pp. 1078–1078 (1937).

[148] P. Chakravorty, "Analysis of rectangular waveguides – an intuitive approach," *IETE Journal of Education* **55** (2), pp. 76–80 (2014).

[149] M. Zahn, "Electromagnetic Field Theory: A Problem Solving Approach, Chapter 8: Guided electromagnetic waves." MIT Open Course Ware.

[150] M. Mechaik, "Signal attenuation in transmission lines," in *Proceedings of the IEEE 2001. 2nd International Symposium on Quality Electronic Design*, pp. 191–196, IEEE Comput. Soc, (2001).

[151] P. K. Chaturvedi, "Microwave cavity resonators," in *Microwave, Radar & RF Engineering*, pp. 81–99, Springer Singapore, (2018).

[152] T. K. Ishii, *Handbook of Microwave Technology*. Elsevier S&T, (1995).

[153] D. H. Staelin, "Electromagnetics and Applications." MIT Open Course Ware, (2011).

[154] J. Whitaker, ed., *The Electronics Handbook (Electrical Engineering Handbook)*. CRC Press, (2005).

[155] M. Aspelmeyer, *Cavity Optomechanics*. Springer Berlin Heidelberg, (2014).

[156] D.Angelakis, *Quantum Simulations with Photons and Polaritons: Merging Quantum Optics with Condensed Matter Physics (Quantum Science and Technology)*. Springer, (2017).

[157] Y. Yamamotoa, J. Jacobson, S. Pau, H. Cao, and G. Björk, "Exciton-polaritons in microcavities," in *Nanostructures and Quantum Effects*, pp. 157–164, Springer Berlin Heidelberg, (1994).

[158] M. O. Scully and M. S. Zubairy, *Quantum Optics*. Cambridge University Press, (2012).

[159] M. Goryachev, W. G. Farr, D. L. Creedon, Y. Fan, M. Kostylev, and M. E. Tobar, "High-cooperativity cavity QED with magnons at microwave frequencies," *Physical Review Applied* **2** (5), p. 054002 (2014).

[160] W. Demtröder, *Experimentalphysik 1: Mechanik und Wärme (Springer-Lehrbuch)*. Springer, (2005).

[161] N. Bloembergen and R. V. Pound, "Radiation damping in magnetic resonance experiments," *Physical Review* **95** (1), pp. 8–12 (1954).

[162] M. Harder, L. Bai, C. Match, J. Sirker, and C. Hu, "Study of the cavity-magnon-polariton transmission line shape," *Science China Physics, Mechanics & Astronomy* **59** (11), p. 117511 (2016).

[163] M. Tavis and F. W. Cummings, "Exact Solution for an N-Molecule–Radiation-Field Hamiltonian," *Physical Review* **170** (2), pp. 379–384 (1968).

[164] J. Krause, "Ferromagnetic resonance measurements at milli-Kelvin temperatures," Master's thesis, Karlsruhe Institute of Technology (KIT), (2016).

[165] F. Pobell, *Matter and Methods at Low Temperatures*. Springer-Verlag GmbH, (2007).

[166] CST-Computer Simulation Technology AG. Bad Nauheimer Str. 19, 64289 Darmstadt, Germany.

[167] K. Uenakada, "Equivalent circuit of reentrant cavity (short papers)," *IEEE Transactions on Microwave Theory and Techniques* **21** (1), pp. 48–51 (1973).

[168] W. W. Hansen and R. D. Richtmyer, "On resonators suitable for klystron oscillators," *Journal of Applied Physics* **10** (3), pp. 189–199 (1939).

[169] R. H. Varian and S. F. Varian, "A high frequency oscillator and amplifier," *Journal of Applied Physics* **10** (5), pp. 321–327 (1939).

[170] K. Z. Dejie Li, *Electromagnetic Theory for Microwaves and Optoelectronics*. Springer-Verlag Berlin Heidelberg, (2013).

[171] M. Kelly, "Design of cylindrical re-entrant cavity resonators," in *IEE Colloquium on Effective Microwave CAD*, IEE, (1997).

[172] M. M. Denner, "3D cavity resonators for magnon polariton experiments." Bachelor thesis at Karlsruhe Institute of Technology (KIT), (2016).

[173] P. J. Petersan and S. M. Anlage, "Measurement of resonant frequency and quality factor of microwave resonators: Comparison of methods," *Journal of Applied Physics* **84** (6), pp. 3392–3402 (1998).

[174] "Qkit – a quantum measurement suite in python", https://github.com/qkitgroup/qkit." last access: January 2019.

[175] S. Probst, F. B. Song, P. A. Bushev, A. V. Ustinov, and M. Weides, "Efficient and robust analysis of complex scattering data under noise in microwave resonators," *Review of Scientific Instruments* **86** (2), p. 024706 (2015).

[176] B. Josephson, "Possible new effects in superconductive tunnelling," *Physics Letters* **1** (7), pp. 251–253 (1962).

[177] R. C. Jaklevic, J. Lambe, A. H. Silver, and J. E. Mercereau, "Quantum interference effects in josephson tunneling," *Physical Review Letters* **12** (7), pp. 159–160 (1964).

[178] J. Clarke and A. I. Braginski, *The SQUID Handbook: Fundamentals and Technology of SQUIDs and SQUID Systems*. Wiley-VCH, (2004).

[179] M. M. Elfresh, "Fundamentals of magnetism and magnetic measurements featureing quantum design's magnetic property measurement system," *Quantum Design* **11578**, p. 132 (1994).

[180] D. Jiles and D. Atherton, "Ferromagnetic hysteresis," *IEEE Transactions on Magnetics* **19** (5), pp. 2183–2185 (1983).

[181] I. Mayergoyz and G. Friedman, "Generalized preisach model of hysteresis," *IEEE Transactions on Magnetics* **24** (1), pp. 212–217 (1988).

[182] L. Tauxe, H. N. Bertram, and C. Seberino, "Physical interpretation of hysteresis loops: Micromagnetic modeling of fine particle magnetite," *Geochemistry, Geophysics, Geosystems* **3** (10), pp. 1–22 (2002).

[183] W. H. Meiklejohn, "Exchange anisotropy—a review," *Journal of Applied Physics* **33** (3), pp. 1328–1335 (1962).

[184] K. Binmore and J. Davis, *Calculus: Concepts and Methods*. Cambridge University Press, (2001).

[185] G. Münster, *Quantentheorie*. Walter de Gruyter GmbH, (2010).

[186] R. LeCraw, E. Spencer, and C. Porter, "Ferromagnetic resonance line width in yttrium iron garnet single crystals," *Physical Review* **110** (6), pp. 1311–1313 (1958).

[187] V. K. Joshi, "Spintronics: A contemporary review of emerging electronics devices," *Engineering Science and Technology, an International Journal* **19** (3), pp. 1503–1513 (2016).

[188] A. M. Zaki, H. J. Blythe, S. M. Heald, A. M. Fox, and G. A. Gehring, "Growth of high quality yttrium iron garnet films using standard pulsed laser deposition technique," *Journal of Magnetism and Magnetic Materials* **453**, pp. 254–257 (2018).

[189] C. Dörflinger, "Implementing synchronized magnon-photon coupling," Master's thesis, Karlsruhe Institute of Technology (KIT), (2018).

[190] A. Berrier, R. Cools, C. Arnold, P. Offermans, M. Crego-Calama, S. H. Brongersma, and J. Gómez-Rivas, "Active control of the strong coupling regime between porphyrin excitons and surface plasmon polaritons," *ACS Nano* **5** (8), pp. 6226–6232 (2011).

[191] K. Sivalertporn and E. A. Muljarov, "Controlled strong coupling and absence of dark polaritons in microcavities with double quantum wells," *Physical Review Letters* **115** (7), p. 077401 (2015).

[192] W. Gao, X. Li, M. Bamba, and J. Kono, "Continuous transition between weak and ultrastrong coupling through exceptional points in carbon nanotube microcavity exciton–polaritons," *Nature Photonics* **12** (6), pp. 362–367 (2018).

[193] B. Bhoi, B. Kim, S.-H. Jang, J. Kim, J. Yang, Y.-J. Cho, and S.-K. Kim, "Abnormal anti-crossing effect in photon-magnon coupling." arXiv:1901.01729v2 [cond-mat.mes-hall], (2019).

[194] J. J. Hopfield, "Theory of the contribution of excitons to the complex dielectric constant of crystals," *Physical Review* **112** (5), pp. 1555–1567 (1958).

[195] M. Harder, Y. Gui, and C.-M. Hu, "Electrical detection of magnetization dynamics via spin rectification effects," *Physics Reports* **661**, pp. 1–59 (2016).

[196] J. Brehm, "Towards superconducting quantum interfaces for tunneling system," Master's thesis, Karlsruhe Institute of Technology (KIT), (2016).

[197] D. S. Lemons and A. Gythiel, "Paul Langevin's 1908 paper "On the Theory of Brownian Motion" ["Sur la théorie du mouvement Brownien," C. R. Acad. Sci. (Paris) 146, 530–533 (1908)]," *American Journal of Physics* **65** (11), pp. 1079–1081 (1997).

[198] C. M. Bender, D. C. Brody, and H. F. Jones, "Complex extension of quantum mechanics," *Physical Review Letters* **89** (27), p. 270401 (2002).

[199] C. M. Bender, P. E. Dorey, C. Dunning, A. Fring, D. W. Hook, H. F. Jones, S. Kuzhel, G. Lévai, and R. Tateo, *PT Symmetry*. WORLD SCIENTIFIC (EUROPE), Jun (2018).

[200] C. M. Bender and S. Boettcher, "Real spectra in non-hermitian hamiltonians HavingPTSymmetry," *Physical Review Letters* **80** (24), pp. 5243–5246 (1998).

[201] J. Wen, X. Jiang, L. Jiang, and M. Xiao, "Parity-time symmetry in optical microcavity systems," *Journal of Physics B: Atomic, Molecular and Optical Physics* **51** (22), p. 222001 (2018).

[202] A. Galda and V. M. Vinokur, "Parity-time symmetry breaking in spin chains," *Physical Review B* **97** (20), p. 201411 (2018).

[203] M. Harder, L. Bai, P. Hyde, and C.-M. Hu, "Topological properties of a coupled spin-photon system induced by damping," *Physical Review B* **95** (21), p. 214411 (2017).

[204] Y. Cao and P. Yan, "Pt-symmetric cavity magnon polaritons." arXiv:1901.10685v1 [cond-mat.mes-hall], (2019).

[205] N. R. Bernier, L. D. Tóth, A. K. Feofanov, and T. J. Kippenberg, "Level attraction in a microwave optomechanical circuit," *Physical Review A* **98** (2), p. 023841 (2018).

[206] A. Stehli, "Experiments with coupled concentric transmons," Master's thesis, Karlsruhe Institute of Technology (KIT), (2016).

[207] G. S. Per-Olof Persson, *Mathematical Systems Theory in Biology, Communications, Computation and Finance*. Springer-Verlag New York Inc., (2003).

[208] E. M. Stein, *Harmonic Analysis (PMS-43)*. Princeton University Press, (2016).

[209] L. Grafakos, *Classical and Modern Fourier Analysis*. Prentice Hall, (2003).

[210] G. Kurizki, P. Bertet, Y. Kubo, K. Mølmer, D. Petrosyan, P. Rabl, and J. Schmiedmayer, "Quantum technologies with hybrid systems," *Proceedings of the National Academy of Sciences* **112** (13), pp. 3866–3873 (2015).

[211] F. M. Jasmin Graf, Hannes Pfeifer and S. V. Kusminskiy, "Cavity optomagnonics with magnetic textures: Coupling a magnetic vortex to light," *Physical Review B* **98** (24), p. 241406 (2018).

[212] S. Sharma, B. Z. Rameshti, Y. M. Blanter, and G. E. W. Bauer, "Optimal mode matching in cavity optomagnonics." arXiv:1903.01718v1 [cond-mat.mes-hall], (2019).

[213] A. Osada, R. Hisatomi, A. Noguchi, Y. Tabuchi, R. Yamazaki, K. Usami, M. Sadgrove, R. Yalla, M. Nomura, and Y. Nakamura, "Cavity optomagnonics with spin-orbit coupled photons," *Physical Review Letters* **116** (22), p. 223601 (2016).

[214] J. A. Haigh, N. J. Lambert, S. Sharma, Y. M. Blanter, G. E. W. Bauer, and A. J. Ramsay, "Selection rules for cavity-enhanced brillouin light scattering from magnetostatic modes," *Physical Review B* **97** (21), p. 214423 (2018).

[215] X. Zhang, C.-L. Zou, L. Jiang, and H. X. Tang, "Cavity magnomechanics," *Science Advances* **2** (3), p. e1501286 (2016).

[216] M. Mergenthaler, J. Liu, J. J. L. Roy, N. Ares, A. L. Thompson, L. Bogani, F. Luis, S. J. Blundell, T. Lancaster, A. Ardavan, G. A. D. Briggs, P. J. Leek, and E. A. Laird, "Strong coupling of microwave photons to antiferromagnetic fluctuations in an organic magnet," *Physical Review Letters* **119** (14), p. 147701 (2017).

[217] M. Bialek, A. Magrez, and J.-P. Ansermet, "Magnon-polaritons in dystrosium ferrite." arXiv:1903.09590v1 [cond-mat.mes-hall], (2019).

[218] T. Jungwirth, J. Sinova, A. Manchon, X. Marti, J. Wunderlich, and C. Felser, "The multiple directions of antiferromagnetic spintronics," *Nature Physics* **14** (3), pp. 200–203 (2018).

[219] V. Baltz, A. Manchon, M. Tsoi, T. Moriyama, T. Ono, and Y. Tserkovnyak, "Antiferromagnetic spintronics," *Reviews of Modern Physics* **90** (1), p. 015005 (2018).

[220] X. Marti, I. Fina, and T. Jungwirth, "Prospect for antiferromagnetic spintronics," *IEEE Transactions on Magnetics* **51** (4), pp. 1–4 (2015).

[221] R. Lebrun, A. Ross, S. A. Bender, A. Qaiumzadeh, L. Baldrati, J. Cramer, A. Brataas, R. A. Duine, and M. Kläui, "Tunable long-distance spin transport in a crystalline antiferromagnetic iron oxide," *Nature* **561** (7722), pp. 222–225 (2018).

[222] R. A. Duine, K.-J. Lee, S. S. P. Parkin, and M. D. Stiles, "Synthetic antiferromagnetic spintronics," *Nature Physics* **14** (3), pp. 217–219 (2018).

[223] H. Y. Yuan and X. R. Wang, "Magnon-photon coupling in antiferromagnets," *Applied Physics Letters* **110** (8), p. 082403 (2017).

[224] V. Astley, B. McCracken, R. Mendis, and D. M. Mittleman, "Analysis of rectangular resonant cavities in terahertz parallel-plate waveguides," *Optics Letters* **36** (8), p. 1452 (2011).

[225] F. J. Morin, "Electrical properties of αFe_2O_3 and αFe_2O_3 containing titanium," *Physical Review* **83** (5), pp. 1005–1010 (1951).

[226] H. Y. Yuan, S. Zheng, Q. Y. He, and M.-H. Yung, "Enhancement of antiferromagnetic magnon-magnon entanglement inside a cavity." arXiv:1903.02484v1 [cond-mat.mes-hall], (2019).